Novel applications of the Josephson effect: Ferroelectric characterisation and capacitively shunted grain boundary junctions

Philip Francis McBrien

Pembroke College, Cambridge

A dissertation submitted for the degree of Doctor of Philosophy at the University of Cambridge

September 2000

Summary: Novel applications of the Josephson effect: Ferroelectric characterisation and capacitively shunted grain boundary junctions

This thesis describes applications of the ac Josephson effect. Firstly, results are presented from bicrystal grain boundary $YBa_2Cu_3O_{7-\delta}$ junctions shunted with a $YBa_2Cu_3O_{7-\delta}/SrTiO_3/Au$ multilayer external capacitor, to make a junction with a hysteretic current voltage characteristic operating at high temperatures. A hysteretic junction with a McCumber parameter of 1.01 at 72.3K, with a critical current of 451μA and a resistance of 0.56Ω was achieved for a junction shunted with a $150\mu m^2$ external capacitor with a 50nm $SrTiO_3$ dielectric. The measured capacitance was less than that expected from a calculation of the parallel plate shunt capacitance. The explanation was thermal noise suppression of the hysteresis and the junction saw the shunt capacitor as a distributed impedance rather than a lumped circuit element.

It was found during these investigations that the influence of the $SrTiO_3$ substrate on the intrinsic junction capacitance was poorly understood. The permittivity of $SrTiO_3$ is 24000 at 4.2K. A series of $YBa_2Cu_3O_{7-\delta}$ Josephson junctions of lengths from 2μm to 20μm was patterned on a $SrTiO_3$ bicrystal and the Fiske resonance dispersion relation was measured. The dispersion relation consisted of two branches, one at low frequencies with a high resonator capacitance per unit length and a high frequency branch with a low resonator capacitance per unit length. This was due to the frequency dependence of the permittivity of bulk $SrTiO_3$, which drops above the soft optic phonon frequency. From the dispersion relation, the permittivity of bulk $SrTiO_3$ was 750 and the soft optic phonon frequency was 145GHz.

The ac Josephson effect was exploited to measure the permittivity of thin films of $SrTiO_3$ at microwave frequencies using Josephson junctions coupled to external resonators. The permittivity of 50nm, 100nm and 200nm $SrTiO_3$ films was frequency independent between 100GHz and 900GHz and to decrease with film thickness. The permittivity of the 50nm film was 35 and that of the 200nm film was 187 at 4.2K. The permittivity of the 200nm film was tunable with a dc voltage bias between 245 and 112 at 30K and 116GHz.

The grain boundary capacitance was used to probe grain boundary current transport. The capacitance per unit area scaled inversely with resistance area product and increased linearly with critical current density, for undoped and Ca doped $YBa_2Cu_3O_{7-\delta}$ grain boundaries on 24° bicrystals. This behaviour could not be explained by tunneling models of grain boundary current transport, and requires current flow over a fraction of the area of the grain boundary.

Preface

This dissertation is submitted for the degree of Doctor of Philosophy in the University of Cambridge. Except where specific reference is made, this work is entirely the result of my own work and includes nothing that is the outcome of work done in collaboration. No part of this work has been or is being submitted for any other qualification at this or any other university. Some of the work contained in this dissertation has been published. This dissertation does not exceed the limit of length.

Philip McBrien

Device Materials Group, Department of Materials Science and IRC in Superconductivity, University of Cambridge.

September 2000

Acknowledgements

Firstly and most importantly I would like to thank my supervisor Dr. Ed Tarte. He has been a constant source of inspiration, help and enthusiasm over the past three years. I would also like to thank Dr. Mark Blamire and the head of the research group, Professor Jan Evetts, for providing the use of the laboratory. Dr. Dae-Joon Kang deserves thanks for his patience when teaching me photolithography and electrical characterisation of devices. Two other members of the group deserve a special mention for their help: Dr. Wilfred Booij and Dr. Gavin Burnell whose support with device processing, measurements and software proved to be indispensable.

The project would not have been possible without the people who grew me films: Dr. Ed Tarte, Dr. Alex Moya and Dr. Frank Kahlmann at the University of Cambridge, Dr Ed. Romans at the University of Strathclyde and the Mannhart Group at the University of Augsburg. At the University of Strathclyde I would like to thank Dr. Colin Pegrum for his advice with the project, and Dr. Chris Carr, Dr. Ed Romans and Dr. Pete Maas for their welcome during my time in Glasgow.

I should also acknowledge my colleagues and fellow students in the group, life in the lab would not be the same without you….. In strictly alphabetical order: John Durrell, Cliff

Elwell, Rob Hadfield, Mike Hogg, Rob Kinsey, Debbie Morecroft, Richard Moseley, James Ransley, Noel Rutter, Rachel Speaks and Neil Todd. And everyone else as well.

I spent many happy hours in pubs in Cambridge and bars all over the world with Alastair Bradley, James McCrone and Steve Rycroft. At Pembroke College, Rachel Quirk, Helen Storey,. Rowan Stewart and Heather Linton (now Stewart!) gave much needed support and friendship.

The Engineering and Physical Sciences Research Council and ultimately the Great British taxpayer funded this project and provided my maintenance during my time in Cambridge.

Final thanks goes to my parents and my younger brother, Matthew.

TABLE OF CONTENTS

Chapter 1: Introduction

1.1 Motivation and objectives of this thesis

One of the most promising areas for applications of superconductivity has been the Josephson effect. This is the observation of a supercurrent between two superconductors separated by a weak link. The Josephson junction is a natural voltage tunable microwave oscillator in a region of the frequency spectrum where there are few alternative sources. The junction can be configured to act both as a microwave source and a detector. Two Josephson junctions in parallel are known as a Superconducting QUantum Interference Device (SQUID). The SQUID is a very sensitive detector of magnetic flux, with applications in biomagnetism and other areas where non-destructive evaluation is required.

The first experiment described in this thesis is the coupling of an external shunt capacitor to a$YBa_2Cu_3O_{7-\delta}$ grain boundary Josephson junction, with the aim of creating a device with a hysteretic current voltage characteristic at high temperatures (>50K). Most Josephson junctions fabricated from cuprate superconductors to date have not had hysteretic current voltage characteristics. The primary application of such a device is the relaxation oscillation SQUID, which oscillates with a frequency dependent on the applied flux. Hysteretic Josephson junctions are also a useful element for Josephson junction based logic circuits.

As a result of these investigations it was apparent that the influence of the $SrTiO_3$ bicrystal substrate on the capacitance of the grain boundary Josephson junctions was not well understood. The permittivity of $SrTiO_3$ is very large (24000) at 4.2K. However, the capacitance determined from the hysteresis in the current voltage characteristics of the junctions was not consistent with that calculated for the co-planar contribution to the junction capacitance from the $SrTiO_3$ substrate with its large permittivity. The permittivity of bulk $SrTiO_3$ is known to be strongly frequency dependent in the same frequency range as the Josephson oscillations. Therefore, experiments were performed on a series of Josephson junctions of various lengths with the aim of ascertaining the influence of the $SrTiO_3$ substrate on the junction capacitance.

The Josephson oscillations were exploited to measure the permittivity of thin films of $SrTiO_3$ at microwave frequencies. An external resonator coupled to a Josephson junction perturbs the

current voltage characteristic of that junction. The parameters of the resonator, such as the permittivity of its dielectric, can be extracted from the position and shape of the perturbation in the current voltage characteristic of the junction. The frequency dependence of the permittivity of thin film and bulk $SrTiO_3$ could then be compared and contrasted.

Having obtained a more thorough understanding of the influence of the $SrTiO_3$ substrate on the capacitance of $YBa_2Cu_3O_{7-\delta}$ grain boundary Josephson junctions, their capacitance was used as a probe of the current transport mechanism across the grain boundary. Over a decade after the discovery that grain boundaries limit the critical current of polycrystalline cuprate superconductors, the mechanism of current transport across the grain boundary still remains controversial.

The thesis is organised as follows. The remainder of this chapter is devoted to the Josephson effect and transmission lines. The resistively and capacitively shunted model of the Josephson junction is presented, followed by an examination of the effect of an applied magnetic field on the Josephson behaviour. An overview of transmission line theory is given, in terms of a model consisting of distributed circuit elements. The effect of a transmission line on the Josephson junction is then discussed. Chapter 2 reviews the properties of $YBa_2Cu_3O_{7-\delta}$ and $YBa_2Cu_3O_{7-\delta}$ Josephson junctions. The structural and electrical properties of $YBa_2Cu_3O_{7-\delta}$ grain boundaries are described. Chapter 3 reviews the dielectric properties of ferroelectrics and incipient ferroelectrics such as $SrTiO_3$. The differences between bulk, single crystal $SrTiO_3$ and thin film $SrTiO_3$ are highlighted. The experimental techniques and apparatus needed for the study are described in Chapter 4. The operation of the relaxation oscillation SQUID and results from $YBa_2Cu_3O_{7-\delta}$ grain boundary junctions coupled to external capacitors are presented in Chapter 5. Chapter 6 reports the experiment to determine the influence of the $SrTiO_3$ substrate on the capacitance of the grain boundary. Chapter 7 presents measurements of the permittivity of a series of thicknesses of $SrTiO_3$ films at microwave frequencies, using Josephson junctions coupled to external resonators. The scaling of the $YBa_2Cu_3O_{7-\delta}$ grain boundary resistance area product, critical current density and capacitance per unit area for a series of junctions is described in Chapter 8. Finally, Chapter 9 concludes the work.

1.2 Basic concepts of superconductivity

The resistance of a superconductor vanishes abruptly to zero when it is cooled below its

critical temperature T_c. Below T_c a superconductor exhibits perfect diamagnetism, whereby magnetic and electric fields are completely excluded its bulk. This is the Meissner effect and it is reversible. The magnetic field decays exponentially in the superconductor over a characteristic length known as the London penetration depth. Screening supercurrents flow within a penetration depth of the surface which prevent any magnetic field from penetrating the bulk of the superconductor.

A complete microscopic theory of superconductivity was developed by Bardeen, Cooper and Schreiffer (BCS theory). As a result of a strong interaction between the electrons and the phonons in the superconductor it becomes energetically favourable for the electrons to condense into pairs, known as Cooper pairs. The pairs are bosons and can therefore be described by a single macroscopic quantum wavefunction with an amplitude and a phase. The squared amplitude of this wavefunction can be interpreted as the fraction of the conduction electrons in the superconducting state. The theory predicts a maximum T_c for superconductivity, but the T_c of the cuprates is higher than this maximum. Therefore, BCS theory cannot be directly applied to the cuprates. However, the concept of a macroscopic quantum wavefunction is still valid for describing the properties of the cuprate superconductors, even though the detail of the pairing mechanism remains unclear.

1.3. The Josephson Effect

1.3.1 Introduction and Feynman derivation

In 1962 Josephson[1] predicted that a supercurrent would flow across a weak link between two superconductors. The effect is the result of the decaying of the superconducting order parameter Ψ into the weak link. If the order parameters on either side of the weak link overlap a supercurrent can flow through the weak link. Josephson effects were first convincingly observed experimentally by Anderson[2].

Here, a derivation of the Josephson effect due to Feynman[3] is given. The superconducting order parameter is considered as a macroscopic wavefunction and the time dependent Schrodinger equation $i\hbar d\Psi/dt=\hat{H}\Psi$ is applied to the superconducting weak link. This gives (1.1) for the time evolution of the wavefunction on each side of the weak link, where K is a coupling constant for the interaction of the wavefunction between the two superconductors and

$U_{1,2}$ is the energy of the wavefunction in each superconductor.

$$\begin{aligned} i\hbar\frac{\partial\Psi_1}{\partial t} &= U_1\Psi_1 + K\Psi_2 \\ i\hbar\frac{\partial\Psi_2}{\partial t} &= U_2\Psi_2 + K\Psi_1 \end{aligned} \tag{1.1}$$

If the weak link is insulating then a constant voltage bias V applied across it produces a difference in potential energy of $-2eV$, where $-2e$ is the charge on a superconducting pair. If the zero of energy is taken as $(U_2\text{-}U_1)/2$, then (1.1) becomes,

$$\begin{aligned} i\hbar\frac{\partial\Psi_1}{\partial t} &= -eV\Psi_1 + K\Psi_2 \\ i\hbar\frac{\partial\Psi_2}{\partial t} &= eV\Psi_2 + K\Psi_1 \end{aligned} \tag{1.2}$$

Next, a superconducting wavefunction (1.3) with a phase $\varphi_{1,2}$ on either side of the weak link can be substituted into (1.2). The square of the amplitude of the wavefunction $n_{1,2}$ is interpreted as the superconducting pair density.

$$\Psi_{1,2} = \left(n_{1,2}\right)^{1/2} e^{i\varphi_{1,2}} \tag{1.3}$$

Substitution of (1.3) into (1.2) and equating the imaginary and real parts respectively gives (1.4) and (1.5).

$$\begin{aligned} \frac{\partial n_1}{\partial t} &= \frac{2}{\hbar}K\left(n_1 n_2\right)^{1/2}\sin\left(\varphi_2-\varphi_1\right) \\ \frac{\partial n_2}{\partial t} &= -\frac{2}{\hbar}K\left(n_1 n_2\right)^{1/2}\sin\left(\varphi_2-\varphi_1\right) \end{aligned} \tag{1.4}$$

$$\begin{aligned} \frac{\partial\varphi_1}{\partial t} &= -\frac{K}{\hbar}\left(\frac{n_2}{n_1}\right)^{1/2}\cos\left(\varphi_2-\varphi_1\right)+\frac{eV}{\hbar} \\ \frac{\partial\varphi_2}{\partial t} &= -\frac{K}{\hbar}\left(\frac{n_1}{n_2}\right)^{1/2}\cos\left(\varphi_2-\varphi_1\right)-\frac{eV}{\hbar} \end{aligned} \tag{1.5}$$

From (1.4), it can be seen that the rate of increase of the pair density in the first superconductor is the rate of decrease of pair density in the second. If there is a circuit connected to the junction, then (1.4) gives the rate of change of pair density or the supercurrent flow J_s across

the junction (1.6).

$$J_s = J_c \sin(\phi) \tag{1.6}$$

This is the dc Josephson relation. A supercurrent can flow through the weak link up to a maximum value J_c. For currents larger than J_c, a potential difference is developed across the junction. The difference between the phases of the wavefunctions of the superconductors is $\phi=\varphi_2-\varphi_1$.

The term in $\cos(\varphi)$ in (1.5) can be eliminated by subtraction to give (1.7).

$$\frac{\partial \phi}{\partial t} = \frac{2e}{\hbar} V \tag{1.7}$$

This is the ac Josephson relation. Integration of (1.7) and substitution into (1.6) gives (1.8), where ϕ_0 is a constant of integration. The phase difference between the order parameters of the two superconductors increases linearly with time.

$$J_s = J_c \sin\left(\frac{2e}{\hbar} Vt + \phi_0\right) \tag{1.8}$$

Therefore, when the junction is voltage biased an ac current flowes at an angular frequency ω given by (1.9).

$$\omega = \frac{2e}{\hbar} V \tag{1.9}$$

The Josephson junction therefore acts as a natural voltage tunable microwave oscillator. A dc voltage of 1mV across the junction produces a frequency of 483.6 GHz.

1.3.2 The shunted junction model

1.3.2.1 A junction shunted by a resistor

The resistively shunted junction (RSJ) model provides a phenomenological approach to the determination of the current voltage (*IV*) characteristics of the Josephson junction. It was devised independently by Stewart[4] and McCumber[5]. The junction is modelled as a Josephson element shunted by a resistor in parallel. In the RSJ model the junction is current

biased, which is the most straightforward way to measure the *IV* characteristic. The current flowing through the junction can be broken down into two components. The supercurrent arises from the dc Josephson effect and is given by (1.6). A finite voltage across the junction gives rise to the quasiparticle current I_n, given by (1.10), where R_n is the junction normal state resistance.

$$I_n = V/R_n \tag{1.10}$$

The addition of (1.6) and (1.10) combined with the ac Josephson relation (1.7) gives (1.11) for the total current I flowing through the junction.

$$I = I_c \sin(\phi) + \frac{\hbar}{2eR_n}\frac{d\phi}{dt} \tag{1.11}$$

Equation (1.11) can be solved analytically[6],[7]. The mean voltage across the junction is determined by the averaging of the time derivative of the phase, which no longer increases linearly with time. It is given by (1.12), which determines the form of the dc *IV* characteristic of a resistively shunted junction, as shown in Fig. 1.1.

$$\overline{V} = 0 \qquad I<I_c$$

$$\overline{V} = R_n\sqrt{I^2 - I_c^2} \qquad I>I_c \tag{1.12}$$

For $I>I_c$ the time dependent voltage is given by (1.13)[6].

$$V(t) = \overline{V} + \sum_{m>0} V_m \sin(m\omega t) \tag{1.13}$$

The amplitudes of the time dependent voltages V_m, determined by Fourier analysis are (1.14).

$$V_m = I_c R_n \frac{2\left(\left(I/I_c\right)^2 - 1\right)^{1/2}}{\left(\left(I/I_c\right) + \left(\left(I/I_c\right)^2 - 1\right)^{1/2}\right)^m} \tag{1.14}$$

The time dependent voltage in turn generates microwave currents flowing in the resistor.

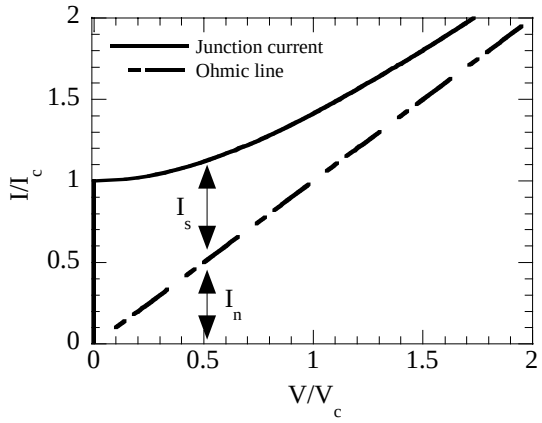

Figure 1.1 A normalised RSJ *IV* characteristic, showing the time averaged ac supercurrent I_s flowing in the resistor and the quasiparticle current I_n flowing in the resistor.

When biased just above the critical current, the higher harmonics of the ac Josephson oscillations are significant and their average dominates the voltage drop across the junction. At higher currents, the oscillations become monochromatic and their average voltage tends to zero, as shown in Fig 1.2. The normal current in the junction resistance dominates and the junction *IV* characteristic tends towards the ohmic line.

The characteristic voltage of the junction V_c is equal to the I_cR_n product. It is the maximum amplitude of the first harmonic of the ac supercurrent. The normalised amplitudes of the first four harmonics of the Josephson oscillations are shown in Fig. 1.3. For voltages greater than ~V_c, the oscillations are approximately monochromatic.

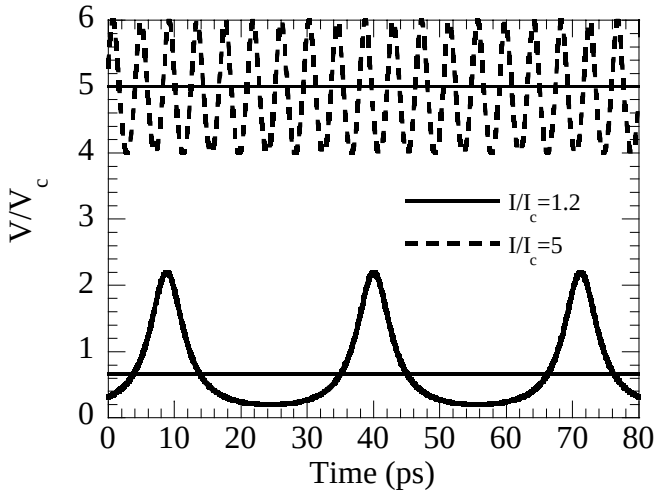

Figure 1.2. The time dependent voltage across the Josephson junction for I/I_c=1.2 and 5.

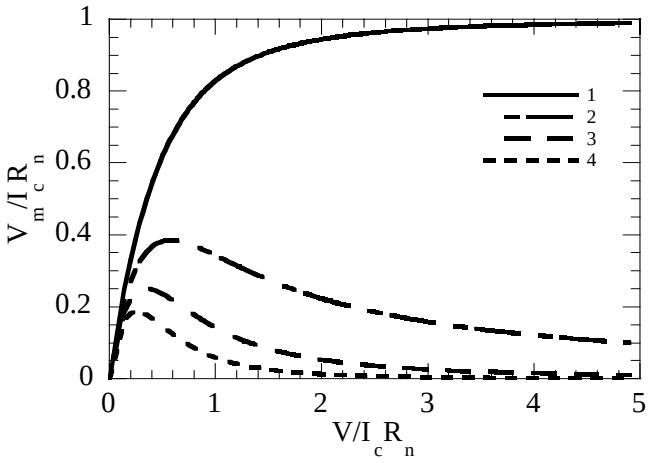

Figure 1.3. The normalised amplitude of the first four harmonics of the ac supercurrent versus normalised voltage.

1.3.2.2 A junction shunted by a resistor and a capacitor

The RSJ model can be developed to include the junction capacitance. The equivalent circuit is shown in Fig 1.4, with a capacitor in parallel with the Josephson element and the resistor. This is the resistively and capacitively shunted junction (RCSJ) model.

The displacement current flowing through the capacitance C is given by $C(dV/dt)$. The displacement current is added to (1.11) for the RSJ model and expressed in terms of the phase difference across the junction with (1.7) to give (1.15).

$$I = I_c \sin\phi + \frac{\hbar}{2eR_n}\frac{d\phi}{dt} + \frac{\hbar C}{2e}\frac{d^2\phi}{dt^2} \tag{1.15}$$

The model can no longer be solved analytically. The McCumber parameter β_c determines whether or not the capacitance term in (1.15) drives the IV characteristic hysteretic. It is defined by (1.16), where $\Phi_0=h/2e$ is the flux quantum.

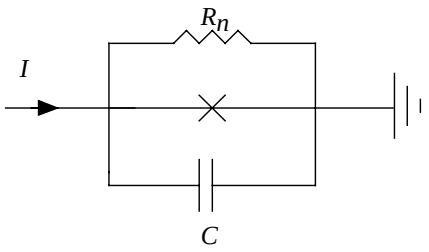

Figure 1.4. An equivalent circuit for a Josephson junction. The cross represents the Josephson element.

$$\beta_c = \frac{\tau_{RC}}{\tau_J} = \frac{R_n C}{\Phi_0 / 2\pi I_c R_n} = \frac{2\pi I_c R_n^2 C}{\Phi_0} \tag{1.16}$$

The McCumber parameter is the ratio of the two characteristic time constants of the system. These are the RC time constant of the resistor and the capacitor τ_{RC} and the period of the Josephson oscillations at the frequency corresponding to I_cR_n.

When β_c<<1 the time constant of the capacitor is much less than the period of the Josephson oscillations. The charge stored on the capacitor relaxes much faster than the time taken for the junction to switch into the zero voltage state. The *IV* curve is single valued for all voltages. Junctions with β_c<<1 are also referred to as overdamped.

When β_c>>1 the time constant of the capacitor is much larger than the period of the Josephson oscillations. Consider biasing the junction with a slowly increasing dc current, starting from I=0. As the magnitude of the current increases the junction switches into the voltage state in the normal way. However, if the current is decreased back past the critical current there is still charge stored on the capacitor. The charge relaxes causing the junction to remain in the voltage state until it returns to the zero voltage state at some current I_r. Junctions with β_c>>1 are referred to as underdamped. The *IV* characteristic is therefore hysteretic as shown in Fig. 1.5.

A junction with β_c<<1 has I_c=I_r and is not hysteretic. A junction with β_c>>1 has I_c>I_r and is hysteretic. A junction with β_c=∞ has I_r=0.

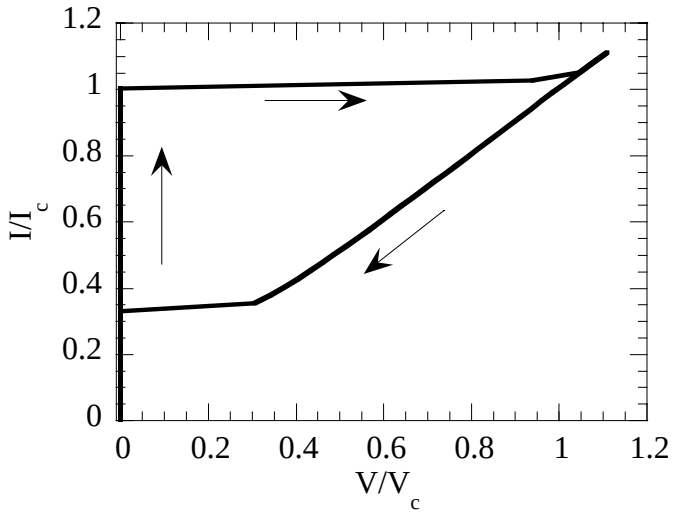

Figure 1.5 A normalised hysteretic IV characteristic with β_c=15.

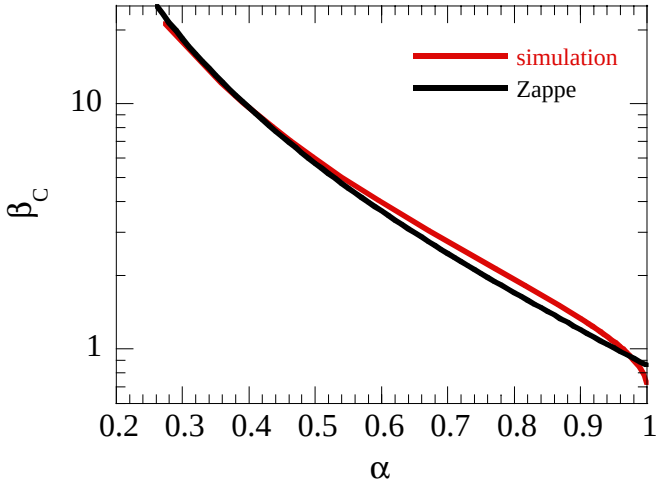

Figure 1.6 Zappe's approximation (1.17) and numerical simulations of β_c versus α.

McCumber[5] solved (1.16) numerically to give β_c as a function of $\alpha=I_c/I_r$. Zappe[8] determined an approximate expression for β_c as a function of α, given in (1.17).

$$\beta_c = \frac{(2-(\pi-2)\alpha)}{\alpha^2} \tag{1.17}$$

The form of β_c versus α from Zappe's approximation is given in Fig. 1.6, together with numerical simulations (from JSIM) to determine the real value of β_c. The majority of junctions in this study had $1<\beta_c<10$. Zappe's approximation underestimates β_c by ~10% for $\alpha<0.96$, and overestimates β_c for $\alpha>0.96$.

In summary, there are three important parameters that can be determined from the *IV* characteristic of the Josephson junction. These are the junction critical current, the junction resistance, from a fit to the *IV* characteristic at high current biases and the junction capacitance from the hysteresis in the *IV* characteristic. Resonances which cause perturbations in the *IV* characteristic at particular voltages can also be used to determine junction parameters, and these are discussed in section 1.4 and Chapters 5, 6 and 7.

1.3.2.3 Josephson coupling energy and noise fluctuations

In the zero voltage state no energy is dissipated within the junction. However, some energy is stored in the junction. This can be found by considering the work done by an external system on the ac supercurrent when the junction is in the voltage state causing a phase change from ϕ_1

to ϕ_2[6]. Using both the dc and ac Josephson relations (1.6) and (1.7) the work done is therefore given by (1.18).

$$W = \frac{\hbar I_c}{2e}\int_{\phi_1}^{\phi_2}\sin(\phi)d\phi = \frac{\hbar I_c}{2e}\left(\cos\phi_1 - \cos\phi_2\right) \tag{1.18}$$

For a Josephson junction, this is interpreted as a potential energy. The maximum energy that can be stored in the junction is therefore given by $\hbar I_c/2e = \Phi_0 I_c/2\pi$.

The primary source of noise in the high T_c superconducting junctions in this study was thermal fluctuations in the critical current. These fluctuations are quantified with the noise parameter Γ, defined in (1.19) which is the ratio of the thermal energy k_BT, where T is the temperature and k_B is Boltzmann's constant, to the Josephson coupling energy.

$$\Gamma = \frac{2\pi k_B T}{\Phi_0 I_c} \tag{1.19}$$

When $\Gamma \sim 0$, thermal noise has little effect on the *IV* characteristic. However, when $\Gamma > 1$, the critical current step in the *IV* characteristic becomes rounded. Thermal noise also suppresses the hysteresis of a junction with $\beta_c > 1$. This effect is discussed in more detail in section 3.5. External electromagnetic interference suppresses the junction critical current in the same way as thermal noise.

1.3.3 Magnetic field effects

The discussion of the Josephson effect in sections 1.2.1 and 1.2.2 tacitly ignored the presence of any magnetic fields. In this section, the influence of a magnetic field on the behaviour of a Josephson junction is discussed. Magnetic field effects on Josephson behaviour are discussed in more detail in the book by Barone and Paterno[9].

1.3.3.1 Flux quantisation

The current density $\mathbf{J_s}$ of a superconductor with an order parameter of the form (1.3) is given by (1.20).

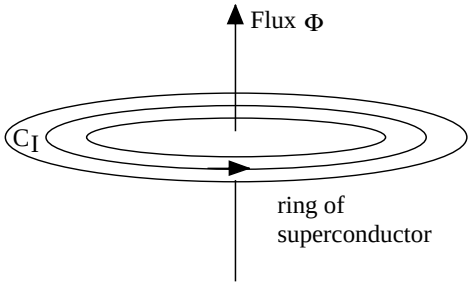

Figure 1.7. A ring of superconductor in a magnetic field.

$$\mathbf{J}_s = \frac{2en_s}{m}(\hbar\nabla\varphi + 2e\mathbf{A}) \tag{1.20}$$

The magnetic vector potential **A** is defined by **B**=∇x**A** where **B** is the magnetic field. The mass of the charge carriers is m and n_s is the superconducting pair density. A ring of superconductor in a magnetic field is shown in Fig. 1.7. Screening currents flow only on the surface of the superconductor, so deep inside the ring, no supercurrents flow and $\mathbf{J_s}$=0. Integration of $-\nabla\varphi$ around the contour C_I in Fig. 1.7 gives:

$$\oint \hbar\nabla\varphi.\mathbf{dl} = \oint 2e\mathbf{A}.\mathbf{dl} \tag{1.21}$$

For a complete circuit of the contour, the phase change must either be zero or a multiple of 2π, otherwise the order parameter will not be single valued at the start and finish of the circuit. The line integral of the magnetic vector potential around the contour is equal to the magnetic flux Φ enclosed by that contour. The flux through the ring is therefore quantised in integer multiples of the flux quantum Φ_0.

$$\hbar 2\pi = 2e\Phi_0 \Rightarrow \Phi_0 = \frac{h}{2e} \tag{1.22}$$

The flux quantum is equal to $2.07\text{x}10^{-15}$ Tm^2.

1.3.3.2 Quantum interference in a single junction

Next, consider a weak link placed in the superconducting ring in Fig 1.7. The phase difference between the superconducting electrodes is now defined as (1.23) to preserve gauge invariance.

$$\phi = \varphi_2 - \varphi_1 - \frac{2e}{\hbar}\oint \mathbf{A}.\mathbf{dl} \tag{1.23}$$

Integration of $-\nabla\varphi$ around the contour C_I as for the ring without a weak link gives (1.24).

$$\varphi = \varphi_0 - 2\pi\frac{\Phi}{\Phi_0} \tag{1.24}$$

The phase difference across the weak link is therefore proportional to the flux through the ring. A flux in the *y* direction applied directly through a weak link in a superconducting film of thickness *h* is shown in Fig. 1.8. The film thickness is much greater than the penetration depth of the magnetic field **B** into the superconducting electrodes λ_L. From (1.24), at a distance *z* along the weak link the phase difference is given by (1.25). The thickness of the weak link is t_J, and the screening supercurrents and the overall bias current flow in the *x* direction.

$$\varphi = \varphi_0 - \frac{2\pi\mathbf{B}_\mathbf{y} z\left(t_J + 2\lambda_L\right)}{\Phi_0} \tag{1.25}$$

The critical current at a given flux through the junction is found by substituting (1.25) into the dc Josephson relation for the critical current density (1.6). This expression is then integrated along the length *l* of the weak link to give (1.26). The critical current at zero applied flux is I_{c0}.

$$I_c(\Phi) = \int_{-l/2}^{l/2} \mathbf{J_c} \sin\left(\varphi_0 - \frac{2\pi B_y z\left(2\lambda_L + t_J\right)}{\Phi_0}\right) dz = I_{c0}\left|\frac{\sin\left(\pi\Phi/\Phi_0\right)}{\pi\Phi/\Phi_0}\right| \tag{1.26}$$

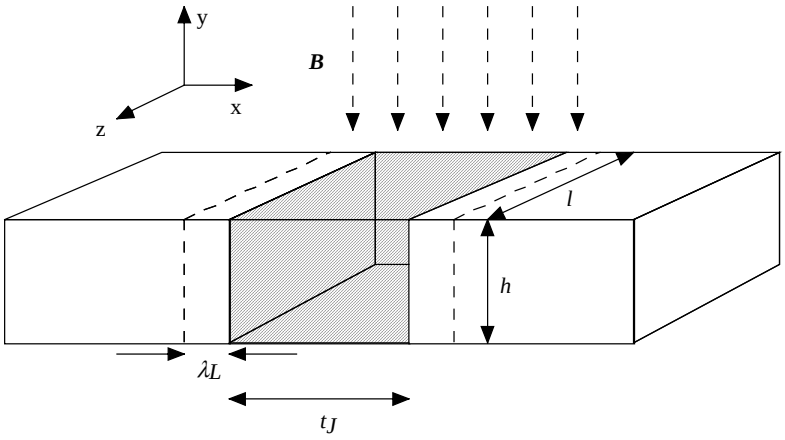

Figure 1.8 A Josephson junction in an applied magnetic field in the *y* direction.

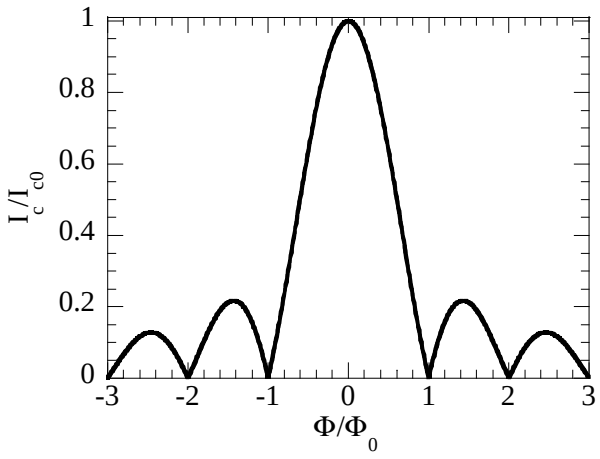

Figure 1.9. The characteristic Fraunhofer pattern for the modulation of the Josephson critical current by an applied flux.

This is the analogue of the Fraunhofer pattern for the intensity of diffracted light from a single slit. It is characteristic Josephson behaviour and is shown in Fig. 1.9. The minima and maxima in the modulation of the critical current with applied flux can be explained as follows. At zero applied flux, the phase difference between the order parameters of the superconducting electrodes is constant across the length of the weak link. When flux is applied, there is a phase gradient along the length of the weak link such that the supercurrent flows both backwards and forwards across it. When exactly one flux quantum is applied the forward and back components of the supercurrent cancel and the critical current is zero. The variation of critical current density with position along the *z* axis of the junction is shown in Fig. 1.10, for zero, half and one flux quantum through the junction.

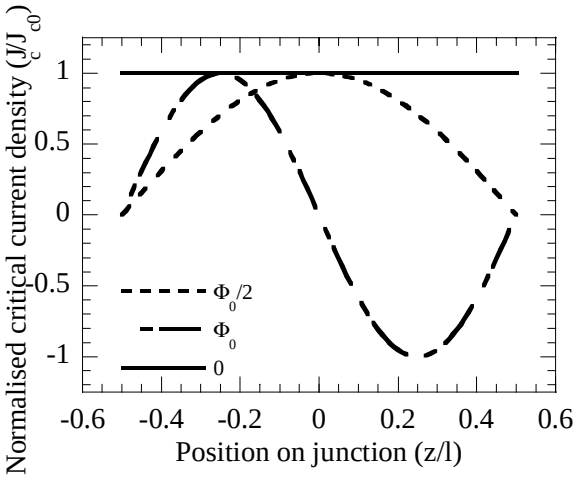

Figure 1.10. The dependence of normalised critical current density J_c/J_{c0} with position along the *z* axis of the junction, for zero, half and one flux quantum through the junction.

1.3.3.3 Quantum interference for two Josephson junctions

The argument that led to (1.24) can be repeated to show that the phase difference between two Josephson junctions connected in parallel threaded by a flux Φ is given by $2\pi\Phi/\Phi_0$. The total current flowing through the two junctions is given by the sum of the currents through each one and is found to be $2I_c\cos(\pi\Phi/\Phi_0)$, where I_c is the critical current of one junction. The critical current varies periodically with the applied flux. The two junctions in parallel are known as a superconducting quantum interference device (SQUID) and provide a very sensitive detector of magnetic flux. The SQUID is the most widely used application of the Josephson effect (see for example Kang[10]).

1.3.3.4 Long Josephson junctions

The above analysis of a Josephson junction in a magnetic field assumed that the junction was short and that the magnetic field completely penetrated the entire weak link. This situation is not necessarily true for longer (in the *z* direction) Josephson junctions. In this case, the electrodynamics of the junction must be considered with use of the Maxwell equation (1.27)[7,11,12].

$$\nabla \times \mathbf{B} = \mu_0 \mathbf{J_c} + \mu_0 \varepsilon_0 \varepsilon_R \frac{d\mathbf{E}}{dt} \tag{1.27}$$

In (1.27), μ_0 and ε_0 are the permeability and permittivity of free space, ε_R is the relative permittivity (dielectric constant) of the junction barrier and **E** is the electric field across the junction. In the geometry in Fig. 1.8, the current flows in the *x* direction and the magnetic field is in the field is in the *y* direction. Initially assuming time independence, (1.27) reduces to (1.28), which is Ampere's law in the *x* direction.

$$\frac{\partial \mathbf{B_y}}{\partial z} = -\mu_0 \mathbf{J_c} \tag{1.28}$$

The phase gradient is given by (1.25). Differentiating (1.25) twice with respect to *z* gives $\partial\mathbf{B_y}/\partial z$. Again, substitution of (1.25) into (1.6) gives $\mathbf{J_c}$, enabling (1.28) to be written as (1.29), where λ_J is the Josephson penetration depth given by (1.30).

$$\frac{\partial^2 \varphi}{\partial z^2} = \frac{\sin \varphi(z)}{\lambda_J^2} \tag{1.29}$$

$$\lambda_J^2 = \frac{\Phi_0}{2\pi\mu_0 J_c (2\lambda_L + t_J)} \tag{1.30}$$

In the limit where l is small compared to λ_J, $\partial^2\varphi/\partial z^2 \approx 0$, and therefore $\partial\varphi/\partial z$ is a constant. This is the short junction limit described in section 1.3.3.2. It is clear from (1.29) that λ_J is a penetration depth (consider small φ where $\sin(\varphi) \approx \varphi$). It is the distance over which the external magnetic field penetrates into the weak link, or the distance over which the Josephson currents flow. It arises because the currents flowing in the junction produce a self field which screens the external field. There are two important consequences of the self field. These are that the critical current of a junction does not increase indefinitely with its area and that for a long junction with $l >> \lambda_J$ a magnetic field cannot completely suppress the Josephson critical current. Furthermore, the critical current density is non uniform along the z axis of a long junction even in zero applied field.

Next, time dependence can be introduced. The electric field across the parallel plate structure in Fig. 1.8. is given by $-V/t_J$. With the aid of the ac Josephson relation (1.7), the Maxwell equation (1.27) can therefore be written as (1.31).

$$\frac{\partial^2 \varphi}{\partial z^2} = \frac{2\pi(2\lambda_L + t_J)}{\Phi_0}\left(\mu_0 J_c \sin\varphi + \frac{\varepsilon_0 \varepsilon_R \Phi_0}{2\pi t_J}\frac{\partial^2 \varphi}{\partial t^2}\right) \tag{1.31}$$

A wave equation (also known as the sine-Gordon equation) can therefore be written for the junction as (1.32), where c_J is the speed of a plane wave propagating in the cavity between the superconducting electrodes, given by (1.33). It is known as the Swihart[13] velocity for waves propagating in a superconducting transmission line.

$$\frac{\partial^2 \varphi}{\partial z^2} - \frac{1}{c_J^2}\frac{\partial^2 \varphi}{\partial t^2} = \frac{\sin\varphi}{\lambda_J^2} \tag{1.32}$$

$$c_J = \frac{c_0}{\sqrt{\varepsilon_R\left(\frac{2\lambda_L + t_J}{t_J}\right)}} \tag{1.33}$$

In (1.33), c_0 is the velocity of light in free space. Substituting plane wave solutions of the form $\varphi=\exp(i(\omega t+k_z z))$ yields the dispersion relation (1.34) for electromagnetic waves in the Josephson junction.

$$\omega^2 = c_J^2 k_z^2 + \omega_p^2 \tag{1.34}$$

The dispersion relation (1.34) shows that electromagnetic waves do not propagate in the junction below the plasma frequency ω_p. However, if there is no Josephson current there is no final term in (1.32) and Swihart modes can propagate with a linear dispersion relation. The form of the dispersion relation for the Josephson junction is shown in Fig. 1.11.

1.4 Transmission lines

In this section a review of transmission line theory is presented. The effect on the *IV* characteristic of waves propagating in the Josephson junction cavity is discussed. Furthermore, the wavelength of the Josephson oscillations in any external circuit connected to the junction can be short enough to be comparable to the dimensions of the components in the circuit themselves. In this situation a distributed circuit model is required.

1.4.1 Transmission line theory

Following Collin[14] the equivalent circuit of a differential length of transmission line is shown in Fig. 1.12.

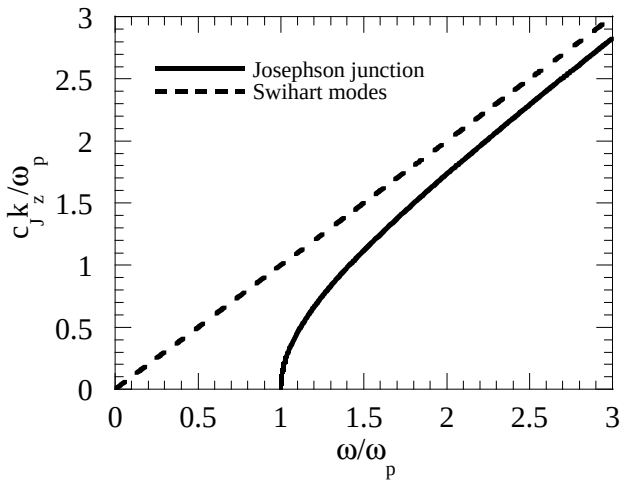

Figure 1.11. The dispersion relation for electromagnetic waves propagating in the cavity formed by the Josephson junction. Swihart modes can propagate in the absence of a Josephson current.

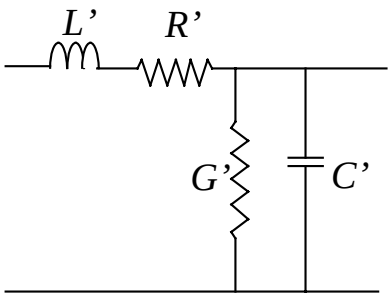

Figure 1.12. A differential length of transmission line.

The inductance and capacitance per unit length of the line are given by *L'* and *C'* respectively. The resistive losses in the inductor and the dielectric losses in the capacitor are given by *R*' and *G'* per unit length respectively. Application of Kirchoff's laws to the current *I* and the voltage *V* at either end of the circuit yields (1.35).

$$\begin{aligned} V-\left(V+\frac{\partial V}{\partial z}dz\right) &= L'\,dz\frac{\partial I}{\partial t}+IR'\,dz \Rightarrow \frac{\partial V}{\partial z}=-\left(L'\frac{\partial I}{\partial t}+IR'\right) \\ I-\left(I+\frac{\partial I}{\partial z}dz\right) &= C'\,dz\frac{\partial V}{\partial t}+VG'\,dz \Rightarrow \frac{\partial I}{\partial z}=-\left(C'\frac{\partial V}{\partial t}+VG'\right) \end{aligned} \tag{1.35}$$

Assuming that the current and voltage vary sinusoidally with time so that $I=I_0\exp(\mathrm{i}\omega t)$ and $V=V_0\exp(\mathrm{i}\omega t)$ reduces (1.35) to (1.36).

$$\begin{aligned} \frac{\partial V}{\partial z} &= -(R'+i\omega L')I \\ \frac{\partial I}{\partial z} &= -(G'+i\omega C')V \end{aligned} \tag{1.36}$$

Elimination of *I* or *V* from (1.36) gives a wave equation for the with a general solution (1.37) for the variation of current and voltage along the length of the transmission line.

$$\begin{aligned} V &= V^+e^{-\gamma z}+V^-e^{+\gamma z} \\ I &= I^+e^{-\gamma z}+I^-e^{+\gamma z} \end{aligned} \tag{1.37}$$

The propagation constant for the transmission line γ is given by (1.38).

$$\gamma=\sqrt{(R'+i\omega L')(G'+i\omega C')}=\alpha+i\beta \tag{1.38}$$

This equation describes the dispersion relation for the transmission line. The characteristic

impedance of the transmission line Z_0 is defined in (1.39).

$$Z_0 = \frac{V^{\pm}}{I^{\pm}} = \sqrt{\frac{R' + i\omega L'}{G' + i\omega C'}} \tag{1.39}$$

An ideal lossless transmission line has $R'=G'=0$ and so $\gamma = i\omega(L'C')^{1/2}$. Hence a wave propagates through the line with wave number $\omega(L'C')^{1/2}$ and phase velocity $c=(L'C')^{1/2}$. The boundary condition for (1.37) in the case of an open ended transmission line (such as the cavity in a Josephson junction) is that no current flows at the ends. Electromagnetic waves propagating through it are reflected at each end. The forward and backward propagating waves combine to give resonant standing wave modes of the field with the form (1.40), where l is the length of the transmission line and n is an integer.

$$V(z,t) = e^{i\omega t}\cos\left(\frac{n\pi z}{l}\right) \tag{1.40}$$

The resonant modes have frequencies (1.41).

$$\omega_n = \frac{n\pi c}{2l} \tag{1.41}$$

1.4.2 The Josephson junction as a transmission line

1.4.2.1 Fiske resonances

Fiske resonances[15] appear as a peak the *IV* characteristic of the Josephson junction. The Fiske resonances are caused by the excitation of electromagnetic modes in the cavity formed by the superconducting electrodes of the junction. The form of the standing wave mode is described by (1.40). The resonances are excited by the Josephson oscillations. The peaks appear at the voltages in the *IV* curve which correspond to the resonant frequencies of the cavity from (1.41). The resonant voltages V_n of order n are therefore determined by substitution of (1.41) into the ac Josephson relation (1.9).

$$V_n = \frac{n\Phi_0 c_J}{2l} \tag{1.42}$$

The Fiske resonances only appear upon application of a magnetic field to the junction, because

a non uniform distribution of the current density is required to excite the modes. The maximum amplitude of the first order resonance is close to a flux of $\Phi_0/2$. Intuitively, this is because the spatial variation of the current density in the junction at $\Phi_0/2$ (see Fig. 1.10) is the same as the spatial distribution of the current at the first order resonance. The dependence of the amplitude of the first order Fiske resonance on the applied flux is shown in Fig. 1.13. The Fiske resonance voltage does not vary with the applied flux.

The speed of light in the junction can also be derived from the transmission line theory in section (1.3.1) from the inductance and capacitance per unit length of the Josephson cavity. The cavity shown in Fig. 1.8 is a parallel plate resonator so its capacitance per unit length is given by (1.43).

$$C' = \varepsilon_0 \varepsilon_R h / t \tag{1.43}$$

The inductance per unit length is given by (1.44). The magnetic field penetrates into the superconducting electrodes for a distance of one penetration depth on either side of the cavity.

$$L' = \frac{\mu_0}{h}\left(t + 2\lambda_L\right) \tag{1.44}$$

For a cuprate grain boundary Josephson junction the film thickness is comparable to or much less than the penetration depth of the magnetic field. In the situation where $\lambda_L >> h$ the correction to the penetration depth is $\lambda_{eff} = \lambda_L^2/h$. In this study, this correction was also used in the limit $\lambda_L \approx h$. The speed of light in the junction c_J is given by $(L'C')^{-1/2}$ and found to be equal to the Swihart velocity (1.33).

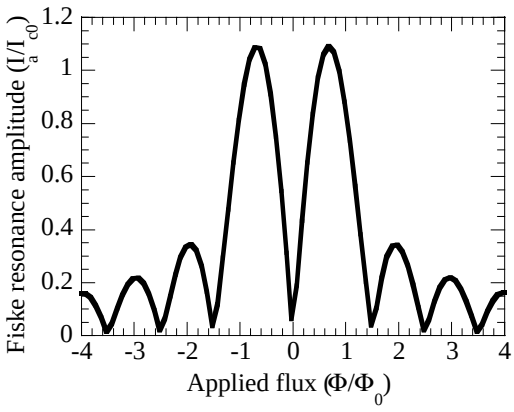

Figure 1.13. The dependence of the amplitude of the first order Fiske resonance on the applied flux[16].

1.4.2.2 Flux flow resonances

Flux flow resonances occur for Josephson junctions in the long limit and are also known as Eck peaks[12]. Above a certain critical magnetic field the Josephson currents cannot screen the external field from the interior of the weak link. The spatial distribution of the Josephson current density in the weak link is no longer sinusoidal as in Fig. 1.10 but instead consists of Josephson vortices. The distribution of the vortices remains periodic. When a voltage is applied across the weak link the vortices acquire a velocity c_v given by (1.45).

$$c_v = \frac{V}{B(2\lambda_L + t_J)} \tag{1.45}$$

A resonance is observed in the *IV* characteristic when the velocity of the Josephson vortices is equal to the velocity of electromagnetic waves in the cavity formed by the Josephson junction. Combining (1.45) with (1.33) thus gives the voltage V_{ff} of the flux flow resonance.

$$V_{ff} = c_0\left(\frac{t_J(2\lambda_L + t_J)}{\varepsilon_R}\right)^{1/2} \tag{1.46}$$

The voltage of the flux flow resonance is therefore dependent on the magnetic field applied to the junction.

A unified theory of Fiske modes and Eck peaks in long junctions has recently been presented by Cirillo *et al*[17]. The sine-Gordon equation is solved numerically by treating the Josephson oscillation as a perturbation phase of the voltages of the resonant modes. However, the Fiske

resonance voltages are still given by (1.42) regardless of whether the junctions are in the long or the short limit.

1.4.3 Josephson junctions coupled to external transmission lines

The Josephson oscillations can also be used to drive a resonator other than that formed by the junction cavity itself. The external resonator presents a shunt impedance to the Josephson junction. The impedance of the resonator is real at its resonant frequencies. Therefore, at the resonance microwave power from the Josephson oscillation is coupled out of the junction into the resonator giving rise to a dip in the current at the resonant voltage. The resonant voltages are given by (1.42), with c_J replaced by the speed of light in the resonator, which is determined by its inductance and capacitance per unit length. A magnetic field is not required for the Josephson oscillations to excite resonances in external transmission lines. The position of the resonances in the *IV* characteristic can be used to extract the dielectric properties of the transmission line. A more detailed discussion of the effect of an external resonator on the *IV* characteristic of the Josephson junction can be found in Chapter 7.

1.4.4 A summary of types of resonances in Josephson junctions

It is therefore possible to observe 3 types of resonance in the *IV* characteristics of Josephson junctions. Fiske resonances are propagated by currents and voltages in the superconducting electrodes of the Josephson junction, which must be separated by an insulating cavity. Flux flow resonances are propagated in the distribution of the Josephson current in the weak link itself. Fiske resonances and flux flow resonances both require magnetic fields to excite them. They can be distinguished by observing the dependence of the resonant voltage on the applied magnetic field. The Fiske resonant voltage is independent of the applied magnetic field whereas the flux flow voltage is proportional to it (see (1.46)).

External transmission line resonances and Fiske resonances can be distinguished by their presence or absence with zero applied magnetic field. The most reliable method of distinguishing Fiske resonances from external transmission line resonances is to determine whether the resonant voltage is inversely proportional to the junction length or to the length of the external resonator.

1.4.5 Losses

In this section, the origins of losses in transmission lines are briefly discussed. In this study, microstrip transmission lines with normal metal electrodes have also been used, so high frequency losses in the normal metal are also reviewed. Resistive losses in a normal metal at high frequencies result from the penetration of the tangential component of the electric field into the metal. The conduction current in the metal is given by Ohm's law, so that $\mathbf{J}=\sigma\mathbf{E}$, where σ is the conductivity, and the displacement current is assumed to be small compared to the conduction current. Assuming sinusoidal variation of the electric field with time, a combination of Faraday's law and the Maxwell equation (1.27) yields (1.47). An equivalent relation can be derived for both the magnetic field and the current density.

$$\nabla^2\mathbf{E} = i\omega\mu_0\sigma\mathbf{E} \tag{1.47}$$

The electric field therefore decays exponentially into the metal, with a decay length known as the skin depth δ_s given by (1.48).

$$\delta_s = \sqrt{\frac{2}{\omega\mu_0\sigma}} \tag{1.48}$$

The surface resistance R_s of a conductor is defined as the resistance per unit length per unit width, or resistance per square, and given by (1.49).

$$R_s = \frac{1}{\sigma\delta_s} \tag{1.49}$$

The resistance per unit length *R'* in section 1.3.1 can be recovered by multiplying by the length of the element and dividing by its width as the width elements are in parallel. For a normal metal, the resistance per unit length is proportional to the square root of the frequency of the electromagnetic waves.

For a superconductor, using the two fluid model, the conductivity is complex and given by $\sigma=\sigma_1-i\sigma_2$. The real and imaginary components represent electrons in the unpaired (normal) and paired (superconducting) states respectively. The conductivity components are given by (1.50) assuming that $\sigma_1<<\sigma_2$. The number of pairs and conductivity in the normal state are n_n and σ_n

respectively.

$$\sigma_1 = \sigma_n \, n_n / n$$
$$\sigma_2 = 1/\omega\mu_0\lambda_L^2 \tag{1.50}$$

A superconductor therefore has a surface impedance Z_s given by (1.51)[11].

$$Z_s = \frac{\omega^2\mu_0^2\lambda_L^3 n_n \sigma_n}{2n} + i\omega\mu_0\lambda_L \tag{1.51}$$

The surface resistance of a superconductor is therefore proportional to the square of the frequency. The temperature dependence of the surface resistance of the superconductor is determined by the temperature dependence of the penetration depth. In the two fluid model of superconductivity this is modelled by (1.52).

$$\lambda_L(T) = \frac{\lambda_L(0)}{\sqrt{1-(T/T_c)^4}} \tag{1.52}$$

Dielectric losses are modelled with a complex permittivity so that $\varepsilon=\varepsilon_1+i\varepsilon_2$. A loss tangent is defined as $\tan\delta=\varepsilon_2/\varepsilon_1$ and the conductance per unit length of the transmission line G' is given by (1.53).

$$G' = \omega C' \tan\delta \tag{1.53}$$

Chapter 2: The properties of $YBa_2Cu_3O_{7-\delta}$ and $YBa_2Cu_3O_{7-\delta}$ Josephson junctions

2.1 Introduction

The cuprate 'high T_c' superconductors were discovered in 1986 by Bednorz and Muller[18]. A barium doped lanthanum cuprate was found to have a superconducting transition temperature T_c of 36K. This result was of great significance as the T_c value measured was higher than the maximum predicted by the BCS theory for conventional superconductors. In 1987 a material with a T_c of 93K was discovered by Wu *et al*[19]. The material was $YBa_2Cu_3O_7$ (YBCO), a cuprate related to the initial compound studied by Bednorz and Muller, and its T_c was much higher than any which had been observed up to that point. The Josephson junctions used in this study were fabricated from YBCO thin films, so the properties of YBCO are reviewed in this chapter.

2.2 Physical properties and crystal structure

The $YBa_2Cu_3O_{7-\delta}$ crystal structure is shown in Fig. 2.1. The structure consists of three perovskite unit cells stacked along the c-axis. The structure contains a layer of yttrium atoms sandwiched between copper oxide planes, followed by a barium oxide layer, copper oxide chains and another barium oxide layer. The oxygen content of the copper oxide chains can be varied, and YBCO undergoes an orthorhombic to tetragonal phase transition at an oxygen content δ between 0.32 and 0.5. When the oxygen content is saturated such that δ=0, YBCO is orthorhombic.

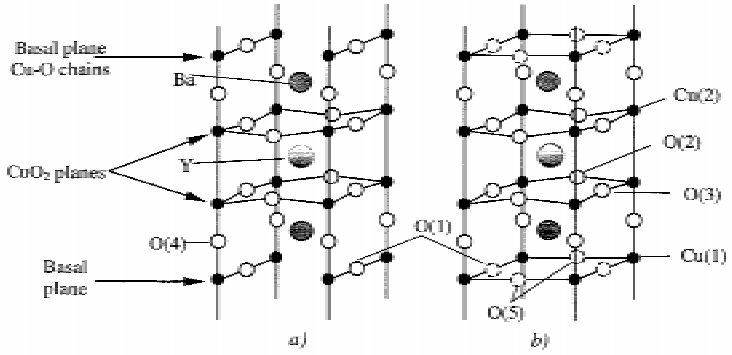

Figure 2.1 The crystal structure of YBCO. Dashed circles indicate partially filled oxygen sites. In the orthorhombic phase, a=0.381nm, b=0.388nm and c=1.18nm.

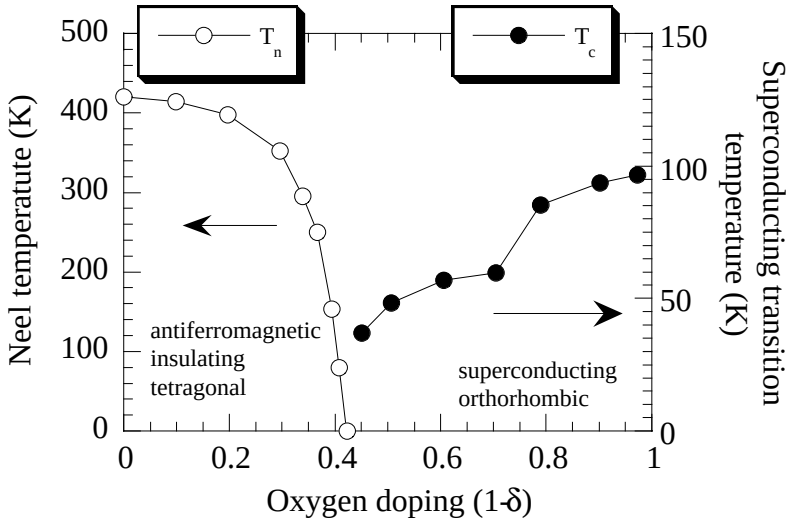

Figure 2.2 The oxygen doping phase diagram for YBCO[20].

The critical temperature of YBCO is also strongly dependent on the oxygen doping. A combination of neutron scattering and electrical transport measurements on single crystals of YBCO led to the doping phase diagram shown in Fig. 2.2. The orthorhombic to tetragonal structural phase transition corresponds to a transition from a metallic, superconducting phase to an insulating antiferromagnetic phase. The Neel temperature for the onset of antiferromagnetic ordering is also strongly dependent on the oxygen doping.

The electrical properties of YBCO are highly anisotropic depending on which direction relative to the crystallographic axes they are measured. The normal state resistivity perpendicular to the c-axis is much larger than that parallel to it[21], as shown in Fig. 2.3. The penetration depth of the magnetic field is also anisotropic. Values at 4.2K are approximately 140nm in the ab-plane[22] perpendicular to the c-axis and 900nm parallel to the c-axis[23]. The coherence length is 2nm in the ab-plane and 0.4nm parallel to the c-axis[23]. YBCO is therefore a type II superconductor where flux vortices can penetrate above a certain magnetic field before superconductivity is destroyed.

The charge carriers in YBCO are holes in the copper oxide layers. The hole concentration n is controlled by the oxygen doping and YBCO has $n=4/3-2\delta/3$ holes per unit cell. The localisation of the holes in the copper oxide planes provides an explanation for the differences between the c-axis and ab-plane transport properties.

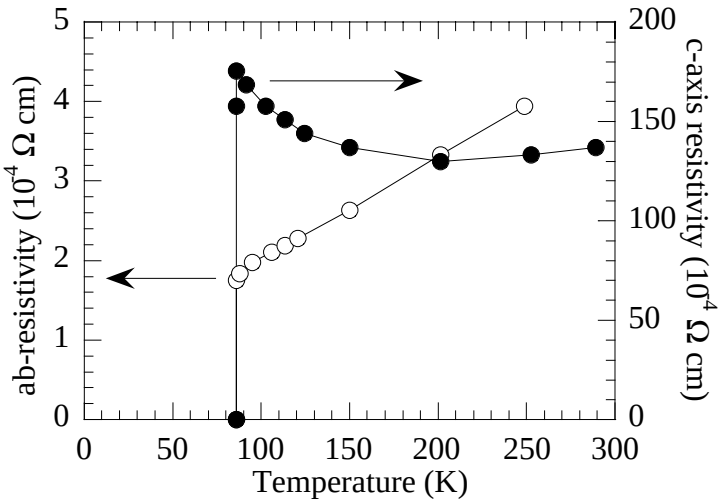

Figure 2.3 The normal state resistivity of single crystal YBCO perpendicular and parallel to the c-axis versus temperature[21].

The order parameter of YBCO has been shown to contain a d-wave component. The most convincing initial experiment was performed by Tsuei *et al*[24]. A d-wave order parameter consists of lobes which have both positive and negative signs as in Fig. 2.4. In the tricrystal geometry used by Tsuei *et al*, the lobes of the d-wave order parameter could overlap in such a way as to produce a Josephson junction which causes an additional π phase shift in the order parameter at the weak link. This type of Josephson junction is known as a π junction where the dc Josephson relation (1.6) is modified to become $J_S=J_C\sin(\phi+\pi)$. A π junction formed at a facet in a grain boundary is shown in Fig. 2.8. The π phase shift gives rise to half integer flux quantisation in the loop around the 3 junctions, which was observed with a scanning SQUID microscope.

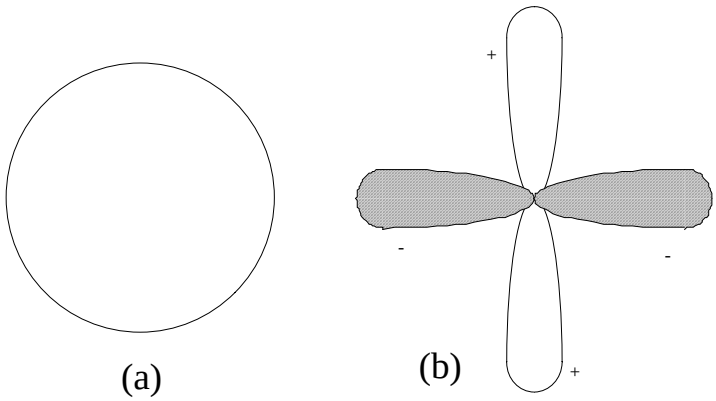

Figure 2.4 A superconducting order parameter with (a) s-wave and (b) $d_{x^2-y^2}$ symmetry.

A subsequent experiment by Wollman *et al*[25] gave more evidence for $d_{x^2-y^2}$ symmetry of the order parameter. Josephson junctions were manufactured from YBCO-gold-lead interfaces. The gold layer acts as the weak link and the lead is a conventional superconductor with an s-wave order parameter. A junction was made parallel to the edge of a YBCO single crystal with the current flowing in the ab-planes. Standard Fraunhofer modulation of the critical current with a magnetic field was observed (see Fig.1.8). Another junction was manufactured around a 90° corner in the YBCO single crystal. At the a-c crystal face the signs of the order parameters in the YBCO and the lead are both positive, but at the b-c face the YBCO order parameter is negative. A π junction is formed at the junction with the b-c crystal face, so the supercurrent flows in the opposite direction to that through the a-c interface. At zero applied flux, the supercurrent tunneling from the b-c face of the crystal into the gold-lead cancels that flowing through the a-c face, so no critical current is observed. The modulation of the critical current with applied flux showed the splitting of the central peak of the Fraunhofer pattern. Half integer flux quantisation and the corner YBCO-Au-Pb junctions give clear evidence for $d_{x^2-y^2}$ order parameter symmetry.

The YBCO order parameter is currently believed to consist of a mixture of s and d wave components[26].

More recently, SQUIDs consisting of one standard junction at one π junction have been fabricated from YBCO tricrystal Josephson junctions. The periodic modulation of the critical current with flux is shifted by $\pi/2$ for the π-SQUID[27].

2.3 YBCO Josephson junctions

2.3.1 Josephson junction categories

Josephson junctions can in general be divided into 3 groups depending on the method of current transport across the weak link. The supercurrent transport across a junction with an insulating barrier occurs by quantum mechanical tunneling. These are superconductor-insulator-superconductor (SIS) junctions. SIS junctions with niobium electrodes and an aluminium oxide weak link are fabricated commercially[28]. The second category consists of junctions with a normal metal weak link, or superconductor-normal-superconductor (SNS) junctions. The weak link in a SNS junction could also be a superconductor above its transition temperature, in which the junction is known as SS'S. The transport mechanism in a SNS

junction is the proximity effect where the supercurrent diffuses into the metal. An example of a SNS junction is the planar niobium copper niobium junction fabricated with a focused ion beam[29]. The third junction category is that where the weak link is a constriction of a size much less than the coherence length of the superconductor. The niobium point contact junction is an example of a junction in the constriction category[30].

2.3.2 Types of YBCO Josephson junction

The fabrication of YBCO Josephson junctions suitable for applications has proved to be challenging. However, the ease of refrigeration of circuits manufactured from high T_c as opposed to from low T_c compounds has stimulated a large research effort. There are several stringent criteria for Josephson junctions from which commercial circuits can be manufactured. The junctions require a high I_cR_n product, reproducible on chip and from chip to chip plus suitability for dense packing. Hysteretic and non-hysteretic junctions should be available on the same chip. The junctions should also be chemically stable and be able to withstand infinite thermal cycling.

The requirements described above are difficult to satisfy. The small coherence length of YBCO and related compounds means that the interface between the weak link and the superconductor must be controlled on an atomic scale. Furthermore, the cuprates are highly anisotropic and extremely chemically reactive. Only metals such as gold and silver and certain other perovskite compounds do not undergo a chemical reaction with YBCO.

Josephson junctions which have been developed for YBCO fall roughly into 3 types[31]:

1) Ion or electron beam implanted junctions (junctions without interfaces)

These junctions exploit the dependence of the superconducting transition temperature of the YBCO on oxygen doping and defects. A film is grown epitaxially on a single crystal substrate and junctions are fabricated via the irradiation of a small area of the film with either electrons[32] or ions[33]. The irradiated area thus has a lower T_c and the junctions are SNS in character[34]. The positioning of junctions on the chip is very flexible and ion implanted junctions can potentially be mass produced. The I_c and R_n of the junctions is also controllable via the energy of the beam and the total irradiation time. The fabrication of resistors is also possible with either technique[35,36]. Ion and electron beam implanted junctions also

overcome the problems with establishing a good interface between the superconducting electrodes and the weak link.

2) Junctions with a barrier of non-superconducting material (junctions with extrinsic interfaces)

Junctions can be manufactured using a normal metal bridge, e.g. gold[37], or with a $PrBa_2Cu_3O_{7-\delta}$ barrier layer on an a-axis film[38]. These junctions require complex multilayer fabrication techniques and careful control of the barrier superconductor interface. The junction critical currents and resistances are less reproducible than those of implanted junctions.

3) Junctions with intrinsic interfaces

A Josephson junction is formed at a grain boundary in YBCO due to its short coherence length, which is comparable to the length of the structurally disordered region of the grain boundary. Junctions with reproducible I_c and R_n can be formed on an epitaxial film grown on a bicrystal substrate. A bicrystal consists of two single crystals fused together at a well defined misorientation angle θ, as shown in Fig. 2.5. The YBCO film growth is epitaxial so the grain boundary in the substrate propagates into the film. Two other misorientations are possible apart from that in Fig 2.5. These are a twist of the [010] axes whilst keeping the [100] axes parallel and a tilt of the [001] axes. The rotation of the axes may be either symmetric or antisymmetric with respect to the boundary.

Grain boundary junctions were first fabricated by Chaudhari *et al*[39]. Epitaxial YBCO films were grown on polycrystalline $SrTiO_3$ substrates with 100μm grains and tracks were patterned

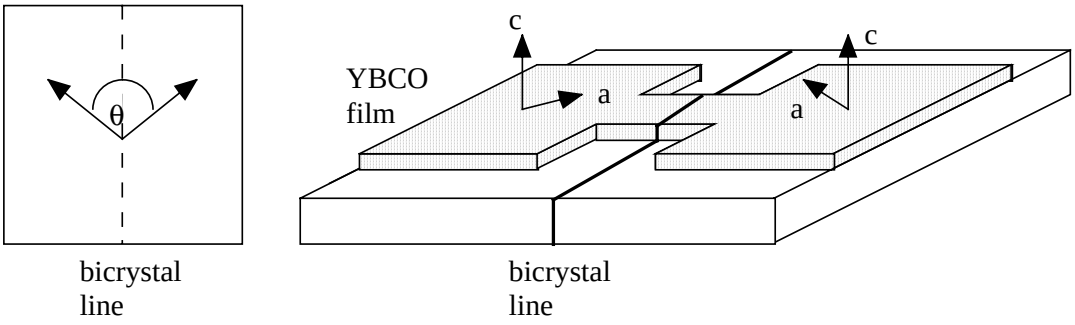

Figure 2.5 A tilt bicrystal grain boundary with misorientation angle θ. The arrows represent the relative orientation of the [100] lattice planes. The [001] planes remain parallel to one another. The YBCO film is grown epitaxially on the bicrystal.

across a single grain boundary. The *IV* characteristics observed were *RSJ* like, as shown in Fig. 1.1. The magnetic field modulation of the critical current was Fraunhofer like for a single grain boundary and periodic for two grain boundaries in parallel. This confirmed that the grain boundaries were Josephson coupled.

Another type of intrinsic barrier junction is the step edge junction. A film is grown epitaxially across a substrate which has had a step etched into it. A grain boundary forms at the top and bottom of the step.

Bicrystal YBCO Josephson junctions are the most straightforward to fabricate, especially when multilayer deposition is required, and so they were used in this study. The critical current and resistance of grain boundary junctions has been found to be stable over a period of years[40]. The properties of grain boundaries are discussed in the next section. The disadvantage of bicrystal junctions is the restriction that all the junctions must be placed along the bicrystal line in the centre of the substrate. Bicrystal junctions are therefore most suitable for applications which only require a few junctions, such as SQUIDs. The most promising junction technology for circuits with many junctions is implantation.

2.4 YBCO grain boundaries

2.4.1 Microstructure and angular dependence of the critical current

The decrease of the critical current density with grain boundary misorientation angle was observed in the first bicrystal junctions manufactured by Dimos *et al*[41]. The most recent study was carried out by Hilgenkamp and Mannhart[42]. The trend is shown in Fig. 2.6. Gurevich and Pashitskii[43] have postulated that there is a transition with misorientation angle in the coupling behaviour of the supercurrent across the grain boundary. Grain boundaries with a greater than 10° misorientation angle (high angle grain boundaries – HAGB) exhibit Josephson coupled behaviour whilst flux flow coupled behaviour is observed in grain boundaries with less than 10° misorientation angles (low angle grain boundaries – LAGB). For a 10° grain boundary, the transition from flux flow to Josephson coupled grains has been found to be temperature dependent, occurring at 75K[44].

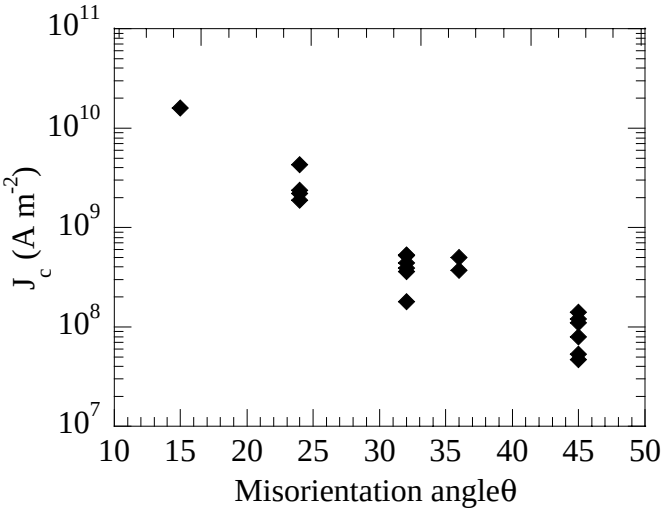

Figure 2.6. The dependence of critical current density on grain boundary misorientation angle[42].

The origins of the decrease in critical current density with grain boundary misorientation angle and the LAGB-HAGB transition can be traced to the grain boundary microstructure. Scanning transmission electron microscopy studies indicate that the grain boundary consists of arrays of dislocations[45]. Gurevitch and Pashitskii[43] propose that the YBCO in the dislocation cores is driven into the antiferromagnetic insulating state by strain. The size of the dislocation cores increases with increasing misorientation angle. At a certain critical angle the dislocation cores overlap to form a continuous region of structural disorder and the crossover from flux flow LAGB coupling to Josephson HAGB coupling occurs. In the LAGB regime the current transport is via superconducting channels in between the dislocation cores. Scanning electron transmission microscopy also indicates that the width of the structurally disordered region in the HAGB regime increases linearly with the misorientation angle[45]. If the current transport across this region were by tunnelling, this would account for the exponential decrease of the critical current density with misorientation angle. Current transport across the grain boundary is discussed in more detail in Chapter 8.

Another contribution to the decrease in critical current density with grain boundary microstructure is the combination of grain boundary faceting and the d-wave symmetry of the order parameter. Grain boundary faceting occurs as a natural consequence of the growth mechanism of YBCO films. The misorientation angle of the YBCO does not necessarily follow that of the grain boundary in the bicrystal substrate, but rather has a sawtooth pattern across the bicrystal line. A transmission electron microscope image of faceting in a 6°

misoriented grain boundary is shown in Fig. 2.7[46]. The length scales of the facets are between 10 to 100nm. Depending on the orientation of the facets with respect to the grain boundary the d-wave symmetry of the order parameter means that either 0 or π junctions can be formed at the facet, as shown in Fig 2.8. The π junctions have a negative critical current density, so the current flows in the opposite direction to the current bias. This leads to an inhomogeneous critical current density across the width of the grain boundary. The overall critical current density of the grain boundary is thus reduced. Hilgenkamp *et al*[47] estimated that the π facets cover 5% of the junction area for a 24° grain boundary and up to 20% of the area of a 36° grain boundary from transmission electron microscope images.

2.4.2 Electrical properties of high angle grain boundaries

The critical current of a HAGB YBCO junction decreases approximately linearly with temperature[49]. However, the temperature dependence of the critical current cannot be used to unambiguously determine whether the current transport across the boundary is by tunneling or by a proximity effect mechanism[50]. The mechanism of current transport across the grain boundary is still controversial and the various models are reviewed in Chapter 8. The normal state resistance and the capacitance of the grain boundary are temperature independent[51,52]. The *IV* characteristics of the grain boundaries can be modelled with the RCSJ model. At 4.2K, the I_cR_n products are approximately equal to 1mV for a 24° grain boundary junction and β_c is approximately equal to 1[31]. Grain boundary junctions therefore have an intrinsic capacitance

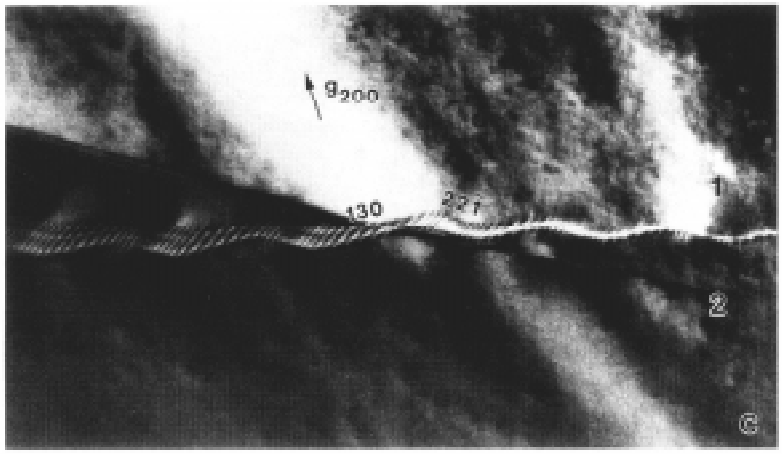

Figure 2.7 Faceting in a 6° YBCO grain boundary[46]. The length of each facet is on the order of a few tens of nanometres. Sub-faceting on length scales of a few nanometres was also observed.

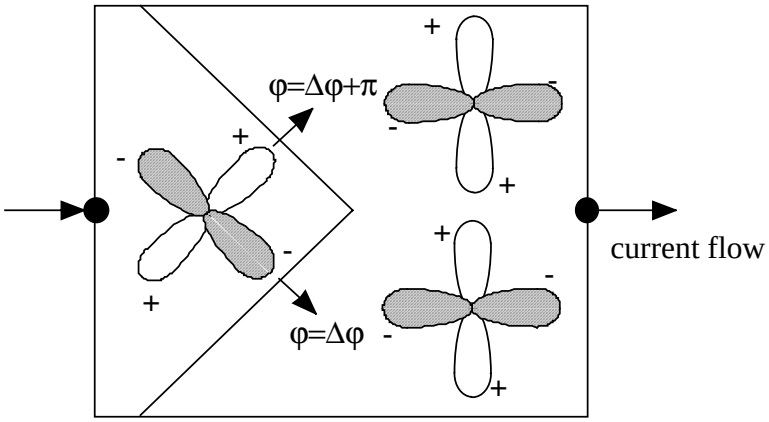

Figure 2.8. A facet at a grain boundary. The facet may cause an additional phase difference of π between the two superconducting grains[48].

and this points towards the existence of an insulating barrier layer within the grain boundary. The McCumber parameter decreases with temperature as it is proportional to the critical current. Hence, for temperatures above approximately 40K grain boundary junctions have $\beta_c<1$.

There are two possible contributions to the intrinsic capacitance of a bicrystal grain boundary junction: the junction cavity itself behaves as a parallel plate capacitor with the barrier layer as the dielectric and the substrate can provide a co-planar shunt capacitance (see Fig 5.4, the equvialent circuit in Fig. 5.5 and Fig 6.8). An attempt to make this contribution to the junction capacitance dominate is described in section 3.4.1. There are two methods to measure the intrinsic capacitance of the grain boundary. It can be obtained directly from the hysteresis in the *IV* characteristic followed by the use of Zappe's approximation (1.17) to determine the McCumber parameter. The critical current and the normal state resistance can also be read directly from the *IV* curve and hence the capacitance can obtained using (1.16). The capacitance per unit length of the barrier can also be obtained via the position of the Fiske resonance in the *IV* curve, with (1.42), (1.43) and (1.44). However, a reliable estimate of the penetration depth is also needed. Using both the hysteresis and the Fiske resonance the penetration depth can be calculated[53]. It is assumed that the structural width of the grain boundary is negligible compared to the effective penetration depth in (1.44) for the inductance per unit length. This is true for all YBCO grain boundaries which have a maximum structural width of 1nm[45] and a minimum a-b penetration depth of 140nm at 4.2K[22].

Table 2.1 The dielectric constants of substrates using for YBCO film growth.

Substrate	Dielectric constant (T=4.2K)	Reference
$SrTiO_3$	24000	Neville *et al*[54]
MgO	9.7	Krupka *et al*[55]
Yttria stabilised zirconia	27	Scheel *et al*[56]
$LaAlO_3$	23.5	Krupka *et al*[55]

A comparison of the total capacitance per unit area of grain boundary junctions grown on different substrates can be used to see whether or not the substrate makes a contribution to the capacitance. It is difficult to measure the dielectric constant of the boundary itself as this requires a measurement of its thickness. The dielectric constant of the different substrates used for growing YBCO films varies over several orders of magnitude, see Table 2.1. Assuming the barrier thickness remains relatively constant between different substrates the capacitance per unit area should give a useful measure of the substrate contribution to the grain boundary capacitance. Strontium titanate ($SrTiO_3$) substrates were used in this study and its properties are discussed in more detail in Chapter 3.

Table 2.2 gives a summary of measurements of the capacitance per unit area of grain boundary YBCO junctions together with the substrate, the method used to obtain the capacitance and the type of junction. It can be seen from Table 2.2 that there is a possible contribution to the intrinsic capacitance of the grain boundary from the substrate, but only over one order of magnitude, whereas the substrate permittivity varies over several orders of magnitude.

Tarte *et al* presented convincing evidence against a large substrate contribution to the intrinsic capacitance of the grain boundary[57]. The capacitance per unit length of a series of different junctions with different YBCO film thicknesses on $SrTiO_3$ bicrystal substrates was measured. The capacitance was determined from both hysteresis and Fiske resonance measurements. The plot of capacitance per unit length versus film thickness obtained is shown in Fig. 2.9.

Table 2.2 The capacitance per unit area of YBCO grain boundary junctions at 4.2K.

Substrate	Junction Type	Capacitance per unit area pF μm^{-2}	Method used to obtain capacitance	Reference
$SrTiO_3$	36.8° bicrystal	0.295	Hysteresis	Nakajima, Yokota *et al*[58]
$SrTiO_3$	24° bicrystal	0.126	Fiske resonance and hysteresis	Tarte *et al*[59]
$SrTiO_3$	24° bicrystal	0.246	Fiske resonance	Beck *et al*[60]
$SrTiO_3$	36° bicrystal	0.295	Fiske resonance	Beck *et al*[60]
MgO	24° bicrystal	0.0520	Fiske resonance	Beck *et al*[60]
$LaAlO_3$	Step edge	0.0239	Fiske resonance and hysteresis	Yi, Winkler *et al*[61]
YSZ	0-32° bicrystal	0.0492	Fiske resonance	Zhang, Winkler *et al*[62]
YSZ	0-32° bicrystal	0.0221	Fiske resonance	Winkler, Zhang *et al*[63]

If the substrate and intrinsic grain boundary capacitances add in parallel then the plot in Fig. 2.28 has an equation of the form (2.1).

$$C' = \frac{\varepsilon_0 \varepsilon_R h}{t_J} + \frac{\varepsilon_0 \varepsilon_{RSTO}}{\pi} \ln\left(\pi\left(\frac{a}{t_J} - \frac{1}{2}\right)\right) \qquad (2.1)$$

In (2.1), h is the film thickness, t_J is the thickness of the grain boundary barrier layer, ε_R and ε_{RSTO} are the dielectric constants of the grain boundary and the $SrTiO_3$ substrate respectively and a is the length of the track containing the junction. The gradient of the line should give the grain boundary contribution and its intercept the substrate contribution. The upper limit on the STO dielectric constant was found to be 60, far below that of 24000 reported by Neville *et al*[54]. This discrepancy is thought to be due to the frequency dependence of the permittivity of STO,

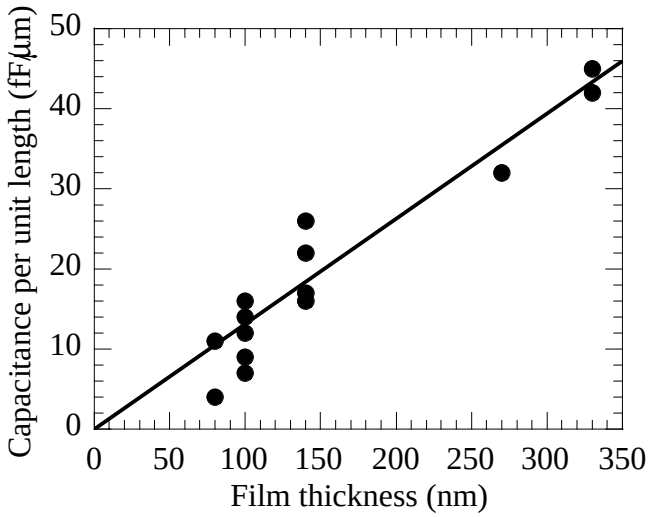

Figure 2.9 Junction capacitance per unit length at 4.2K versus film thickness from hysteresis and Fiske resonance measurements[57].

which is discussed in Chapters 3 and 6.

The dielectric constant of $SrTiO_3$ is also strongly temperature dependent in the region from 4.2K to 90K[54]. Therefore, if the substrate were contributing to the grain boundary capacitance, it would be expected that the total capacitance should be temperature dependent. However, the grain boundary capacitance is effectively independent of temperature for junctions on $SrTiO_3$ bicrystals[52].

The evidence is therefore against a substrate contribution to the grain boundary capacitance. However, the dielectric constant of $SrTiO_3$ is strongly frequency dependent in the domain of the frequency of the Josephson oscillations, as discussed in Chapter 3. This should be taken into account when shunt capacitance from the substrate is calculated, as discussed in Chapter 6.

Chapter 3: The dielectric properties of strontium titanate

3.1 Introduction

Strontium titanate substrates were used for the YBCO grain boundary junctions in this study. As discussed in section 2.4.2, the influence of strontium titanate on the capacitance of grain boundary Josephson junctions is not fully understood. In this chapter, a review of the dielectric properties of bulk single crystal strontium titanate paying particular attention to temperature and frequency dependencies is presented. Thin films of strontium titanate were used as a dielectric both in shunt capacitors and microstrip resonators coupled to the YBCO Josephson junctions. The dielectric properties of thin film strontium titanate are also reviewed and contrasted with the behaviour of bulk single crystal strontium titanate.

3.1.1 Strontium titanate

In recent years there has been a renewal of interest in dielectrics such as strontium titanate ($SrTiO_3$ - STO) and related ferroelectrics (e.g. $Ba_xSr_{1-x}TiO_3$). This has been driven by the need for a higher dielectric constant ε_R material for use in random access memory[64] in order to increase the density of capacitors whilst retaining the same amount of charge stored on the capacitor. Ferroelectric memories are also being developed[65], where the 'bit' is represented by the direction of spontaneous polarisation in the ferroelectric and the memory is 'non-volatile' – i.e. the contents of the memory are not lost when no electrical power is supplied. STO also has a lattice constant compatible with YBCO, and this leads to applications in low loss cryogenic filters for cellular communications[66]. Furthermore, the ε_R of STO can be tuned with an applied voltage bias and hence frequency agile microwave filters can be constructed as well as other microwave devices[67,68].

An obstacle to the realization of these applications has been the difference in dielectric properties between single crystal bulk and thin film STO, and particularly the decrease in the ε_R of thin film as compared to single crystal bulk STO. A value of 1800 at 20K has been reported for a 400nm thick film[69], whereas for single crystal STO the ε_R is 24000 at 4.2K, and is 16000 at 20K for 1x1x1.5mm samples[54]. The variation of ε_R with temperature T is also very different for the thin film and bulk regimes. As the temperature is decreased, $\varepsilon_R(T)$ for bulk STO rises monotonically to 24000 at 4.2K and then saturates[70] which is behaviour

characteristic of an incipient ferroelectric, but $\varepsilon_R(T)$ for thin film STO displays relaxor ferroelectric behaviour with a peak either around 40K or 90K[71]. Furthermore, for applications both in filters and memories it is important to have a thorough understanding of dielectric losses in STO, and particularly at microwave frequencies there exists neither a large volume of experimental data nor a complete understanding of the loss mechanisms involved for either thin film or bulk STO[72].

3.2 Background theory

3.2.1 Definition of a ferroelectric

A ferroelectric crystal is one which possesses two or more stable states with spontaneous polarisation, or electric dipole moment, even in the absence of an applied electric field. On application of a large enough electric field the crystal can be made to switch between the two states. However, the crystal structure of the two states is otherwise indistinguishable. The first ferroelectric to be discovered was Rochelle salt in 1920, and in this compound the spontaneous polarisation is the result of the ordering of hydrogen bonds below a certain temperature, called the Curie temperature. At this temperature there is a sudden decrease in ε_R and the crystal is said to have undergone a ferroelectric phase transition. Hysteresis is exhibited in curves of electric field versus polarisation in an analogous manner to the hysteresis seen in the permanent magnetisation of a ferromagnet. The phase change to the ferroelectric state below the Curie temperature is always accompanied by a structural phase transition, and in fact the ferroelectric phase transition is a subgroup of crystals which undergo a structural phase transition.

Oxygen octahedral ferroelectrics form the largest single class of ferroelectrics, and the first to be discovered was barium titanate in 1945. These ferroelectrics are based around the perovskite crystal structure, shown in Fig. 3.1. Above its Curie temperature, 393K, barium titanate has the cubic perovskite structure shown in Fig. 3.1. Below 393K barium titanate undergoes a structural phase transition to a ferroelectric tetragonal crystal with a permanent dipole moment or spontaneous polarisation formed by the displacement of the Ti^{4+} ion with respect to the octahedron of O^{2-} ions[73].

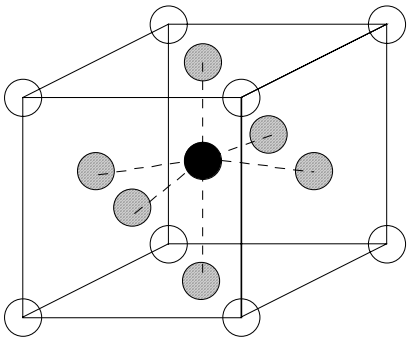

Figure 3.1 The cubic perovskite lattice structure. The strontium / barium atoms are white, the oxygens are grey shaded and the titanium is black (for temperatures greater than the Curie temperature).

3.2.2 Ginzburg-Landau-Devonshire (GLD) theory for ferroelectric phase transitions

For a linear, isotropic and homogeneous (LIH) dielectric an applied electric field ***E*** gives rise to an induced dipole moment with polarisation ***P***. The displacement field ***D*** is then defined (in SI units) as $\boldsymbol{D}=\varepsilon_0\boldsymbol{E}+\boldsymbol{P}$. The dielectric constant (permittivity) is defined as $\varepsilon_R = (1/\varepsilon_0)(d\boldsymbol{D}/d\boldsymbol{E})$, so for the LIH dielectric with $\boldsymbol{P}=\varepsilon_0\chi\boldsymbol{E}$, where χ is the electric susceptibility, $\varepsilon_R=(1+\chi)$. To correctly describe non-linear dielectrics such as ferroelectrics, however, higher order ***P*** terms are required in the definition of the displacement field.

GLD theory provides a phenomenological understanding of ferroelectricity in terms of the macroscopic electric fields and the free energy. Following Lines and Glass[73], it is assumed that an expression for the free energy of the system can be written in terms of an order parameter, in this case ***P***. For the situation where all stresses on the crystal are zero, and on the assumption that ***E*** and ***P*** are directed along one of the crystallographic axes, the free energy F can be expressed in the polynomial form (3.1).

$$F = C_1(T)P^2 + C_2(T)P^4 + \ldots\ldots - EP \tag{3.1}$$

Differentiating F with respect to P to find thermodynamic equilibrium and setting $dF/dP=0$ gives (3.2) for the electric field in terms of the polarisation.

$$E = A_1(T)P + A_2(T)P^3 \tag{3.2}$$

When $A_1(T)$ is positive there is a single minimum in F at $P=0$, but when $A_1(T)$ is negative there are two minima in $F(P)$ at non zero P, i.e. the stable state has a spontaneous polarisation. So, P undergoes a continuous second order phase transition when $A_1(T)=0$. In the paraelectric phase

above the Curie temperature T_{cf} it can be seen that $A_1(T)$ is the reciprocal of $\varepsilon_R/\varepsilon_0$ for large ε_R. In the GLD theory it is assumed that near T_{cf} $A_1(T)$ is given by (3.3) for $T>T_{cf}$.

$$A_1(T) = B_1(T - T_{cf}) \qquad T>T_{cf} \tag{3.3}$$

Now, the spontaneous polarisation can be found by setting E=0 in (3.2), and from this the zero field temperature dependence of $A_1(T)$ for $T<T_{cf}$ is given by (3.4).

$$A_1(T) = 2B_1(T_{cf} - T) \qquad T<T_{cf} \tag{3.4}$$

The behaviour of $\varepsilon_R(T)$ predicted by (3.3) and (3.4) is shown in Fig. 3.2(a). Together, (3.3) and (3.4) are known as the Curie-Weiss law for the temperature dependence of the dielectric constant of a ferroelectric. In (3.3) and (3.4), B_1 is a constant.

Close to the ferroelectric phase transition where ε_R is large and $A_1(T)$ is small the two limiting cases for the behaviour of $\varepsilon_R(E)$ are that of large E where the non linear term in (3.2) is dominant,

$$(\varepsilon_0\varepsilon_R)^{-1} = A_1(T) + 3(A_2E^2)^{1/3} \tag{3.5}$$

and small E, where the linear term in (3.2) is dominant, (3.6).

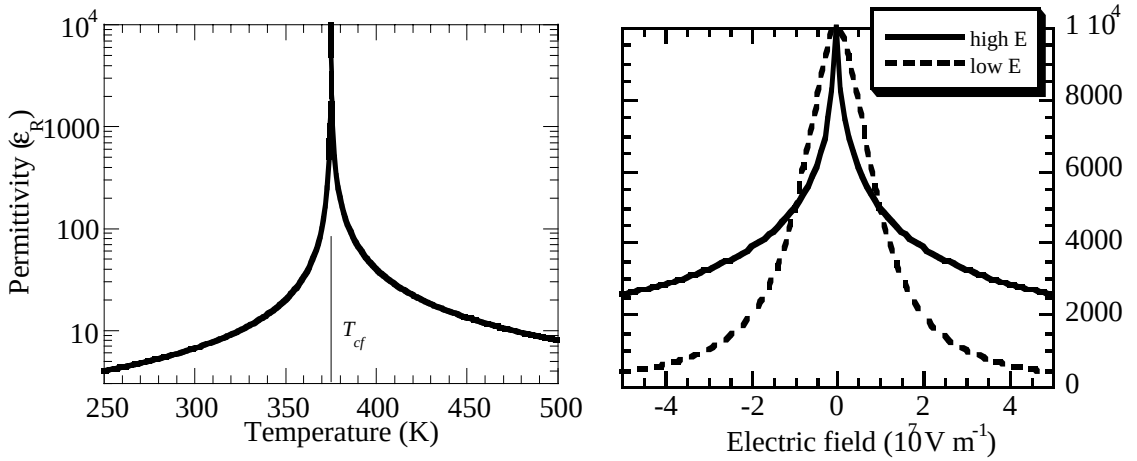

(a) **(b)**

Figure 3.2. Behaviour of (a) $\varepsilon_R(T)$ from (3.3) and (3.4), and (b), $\varepsilon_R(E)$ in the high field and low field limits from (3.5) and (3.6). The scales serve as a guide to the magnitude of the variation.

$$\left(\varepsilon_0 \varepsilon_R\right)^{-1} = A_1(T)\left\{1 + \frac{3A_2}{A_1^3(T)} E^2\right\} \tag{3.6}$$

The form of $\varepsilon_R(E)$ predicted by (3.5) and (3.6) is shown in Fig. 3.2(b).

3.2.3 Lattice dynamics

Ferroelectricity can be interpreted in terms of the softening of a transverse optic phonon mode. For $BaTiO_3$ the mode is associated with the oscillation of the Ti^{4+} ion with respect to the O^{2-} ion octahedron. As $T \rightarrow T_{cf}$ from above, the frequency of the phonon $\omega_{TO} \rightarrow 0$, and the mode freezes completely at T_{cf}. At this temperature there is a structural phase transition and the Ti^{4+} ion becomes permanently displaced with respect to the oxygen octahedron, resulting in a permanent dipole moment in the crystal unit cell and hence spontaneous polarisation. The crystal has undergone a ferroelectric phase transition. The intercell interaction between the dipoles has become stronger than the intracell interactions between the Ti^{4+} and the oxygen octahedron.

It is also evident that for temperatures above T_{cf} there will be a discontinuity in ε_R measured as a function of frequency ω at ω_{TO}, because above ω_{TO} the contribution to ε_R from the dipoles vanishes and so ε_R decreases. $\varepsilon_R(\omega)$ is derived by considering the harmonic oscillations of a lattice of interacting dipoles[73], and is given by (3.7) for the case where a single phonon only is active in the determination of ε_R.

$$\varepsilon_R(\omega) = \varepsilon_R(\infty) + \left(\frac{q^2}{m v \varepsilon_0}\right)\left(\frac{1}{\omega_{TO}^2 - \omega^2 + i\omega\eta}\right) \tag{3.7}$$

In (3.7), $\varepsilon_R(\infty)$ gives the contribution to the dielectric constant from the electronic polarisability, q is a charge coupling constant for the oscillator, m is its reduced mass, v is the volume of the unit cell and η is a damping constant.

The Lyddane-Sachs-Teller relation (3.8) connects the low frequency dielectric constant $\varepsilon_R(0)$ to the high frequency value $\varepsilon_R(\infty)$ via the frequencies of the soft optic phonon and the corresponding longitudinal mode frequency ω_L. It is derived by setting $\varepsilon_R=0$ in (3.7) with no damping, which defines the frequency of the longitudinal optic phonon. In (3.8), A is a

constant of proportionality. The pole of $\varepsilon_R(\omega)$ then defines ω_{TO}.

$$\frac{\varepsilon_R(0)}{\varepsilon_R(\infty)} = A\frac{\omega_L^2}{\omega_{TO}^2} \tag{3.8}$$

The longitudinal phonon corresponds to oscillations whose wave vector is parallel to the direction of the electric field inside the unit cell. The longitudinal optic phonon has a flat dispersion relation with its frequency independent of its wave vector. The transverse optic phonon corresponds to oscillations where the wave vector is perpendicular to the electric field inside the cell. Its dispersion relation is non linear and there are gaps where oscillations are completely suppressed. Combining (3.3) and (3.8) gives (3.9), the variation of the soft mode frequency with temperature. In (3.9), *K* is a constant of proportionality.

$$\omega_{TO} = K(T - T_{cf})^{1/2} \tag{3.9}$$

It should also be noted that the disappearance of a transverse optic phonon is not a necessary criterion for ferroelectricity. There is the possibility of the coupling of two or more phonons to produce a net dipole moment in a crystal, and hence ferroelectricity.

3.2.4 Microscopic theory of ferroelectricity

A more complete microscopic description of ferroelectricity uses a Hamiltonian for the motion of a dipole in a single ferroelectric unit cell. A mean field approximation is applied for the interaction between this cell and the other cells in the crystal and thermodynamic averaging gives measurable properties such as the electric field and temperature dependence of the dielectric permittivity. The theory is described in detail in the book by Lines and Glass[73] and Zhou and Newns[74].

The Hamiltonian in the mean field approximation in terms of the local dipole moment *p* at site *l* is given by (3.10).

$$H = \sum_l \left[V(p_l) - Ep_l - V_0 p_l < p >\right] \tag{3.10}$$

$V(p_l)$ is the local potential well seen by the dipole. For STO, this is given by a harmonic oscillator with a small anharmonic perturbation. *E* is the internal electric field at the site, <*p*>

is the average polarisation per site and thus $V_0<p>$ is the mean field acting on the dipole p_l. The key elements of the model are the interactions between the dipoles and the anharmonic perturbation of the local potential well. Classical thermodynamic averaging of this Hamiltonian recovers the Curie-Weiss law for $\varepsilon_R(T)$. There is a ferroelectric phase transition at $k_B T_{cf}=V_0<p^2>$ when the mean field interaction becomes greater than the depth of the local potential well, and the anharmonicity of the local potential well determines the degree of spontaneous polarisation in the ferroelectric state. The introduction of a small oscillating component into E enables the derivation of (3.9), the linear dependence of the square of the soft mode frequency on temperature.

3.3 Relevant experiments on single crystal bulk strontium titanate

3.3.1 The temperature dependence of the dielectric constant

The dielectric constant of single crystal barium titanate follows the behaviour predicted by GLD theory in (3.3) both above and below its T_{cf}=393K[75]. Neville *et al.*[54] measured the temperature dependence of the dielectric constant of single crystal STO, ε_{RSTO}, and found that (3.3) was followed between 300K and 65K, and extrapolation of $\varepsilon_{RSTO}^{-1}(T)$ gave T_{cf}=30K. This is shown in Fig. 3.3. However, no singularity is found in $\varepsilon_{RSTO}(T)$ and ε_{RSTO} continues to rise up to 4.2K. It was clear therefore that GLD theory was inadequate to explain the behaviour of $\varepsilon_{RSTO}(T)$ at low temperatures. Hence, STO is known as an incipient ferroelectric.

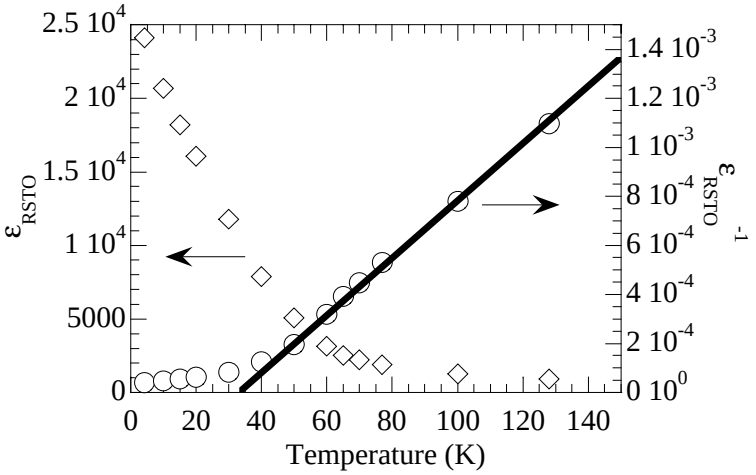

Figure 3.3. The temperature dependence of the dielectric constant of strontium titanate, from Neville *et al.*[54]. The straight line is a fit to the Curie-Weiss law (3.3).

3.3.2 The frequency dependence of the dielectric constant and the transverse soft optic phonon frequency

Only $\varepsilon_R(0)$, $\varepsilon_R(\infty)$, ω_{TO} and η are required to determine the complete form of $\varepsilon_R(\omega)$, so (3.7) can be re-written as (3.11).

$$\varepsilon_{RSTO}(\omega) = \varepsilon_{RSTO}(\infty) + \left(\frac{\omega_{TO}^2 (\varepsilon_{RSTO}(0) - \varepsilon_{RSTO}(\infty))}{\omega_{TO}^2 - \omega^2 + i\omega\eta} \right) \tag{3.11}$$

The form of (3.11) is plotted in Fig. 3.4 for STO at 4.2K with the parameters $\varepsilon_{RSTO}(0)$=24000[54], $\varepsilon_{RSTO}(\infty)$=6[76], ω_{TO}=420GHz[77] and η=30GHz[77]. The form of $\varepsilon_{RSTO}(\omega)$ for STO has also been confirmed to fit to (3.11) using infrared reflectivity measurements of the refractive index[78]. In particular, it was demonstrated that ε_R is positive below ω_{TO} and negative above ω_{TO}.

The temperature dependence of ω_{TO} for single crystal STO has been experimentally measured using neutron scattering by Yamada and Shirane[79]. For single crystal STO, (3.9) was followed from 300K down to 60K, in agreement with the temperature dependence of ε_R from low frequency measurements. An extrapolation of ω_{TO}(T) to ω_{TO}=0 gave T_{cf}=40K. Below 20K ω_{TO} was found to saturate at 450±60GHz so the Lyddane-Sachs-Teller relation (3.8) was found to be valid over all temperatures. Fleury and Worlock[80] performed electric field induced Raman scattering measurements on single crystal STO.

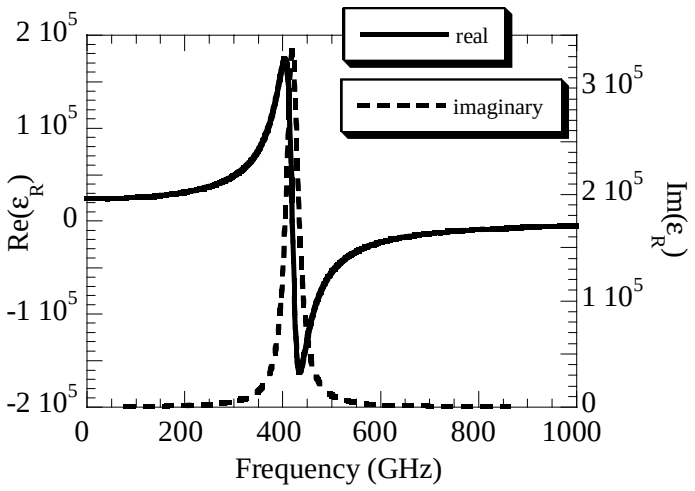

Figure 3.4. Behaviour of $\varepsilon_R(\omega)$ from (4.11) for STO at 4.2K, near the first transverse soft optic phonon frequency.

Again, (3.9) was followed to around 60K. Use of the Lyddane-Sachs-Teller relation (3.8) and (3.2), and measurements of $\omega_{TO}(T)$ at various applied electric fields enabled a calculation of the parameters $A_1(T)$ and $A_2(T)$, which Fleury and Worlock found to be in good agreement with those calculated from measurements of the ε_R of STO at low frequencies. Fleury and Worlock also compared the measured linewidth of the soft optic phonon in STO with theories predicting it based on a ferroelectric phase transition at 32K. The measured linewidth was found to be inconsistent with the theory.

For STO there are 3 further optic phonon frequencies above that of the first transverse optic phonon. The frequency of the second order transverse optic phonon mode is 5.3THz[78], and the other modes have higher frequencies. These higher order modes are not temperature dependent and therefore can be included in *A'* in the Lyddane-Sachs-Teller relation (3.8)[78],[80]. By writing (3.8) as $\varepsilon_R(0)\omega_{TO}^2=B'$ Neville *et al.*[54] were able to verify that the variation of the low frequency dielectric constant with temperature followed quantitatively the behaviour predicted from measurements of the temperature dependence of the soft optic phonon frequency. $B'^{1/2}=n\omega_L(\omega_{L2}/\omega_{TO2})(\omega_{L3}/\omega_{TO3})(\omega_{L4}/\omega_{TO4})$, where ω_{Ln} are the higher optic phonon frequencies and n is the refractive index, and Neville *et al.* calculated $B'=9.65\text{x}10^{28}\text{s}^{-2}$. The agreement between $\omega_{TO}(T)$ for single crystal STO as measured by neutron scattering by Yamada and Shirane[79], and the prediction using the Lyddane-Sachs-Teller relation (3.8) from $\varepsilon_{RSTO}(T)$ from Neville *et al.*, is shown in Fig. 3.5.

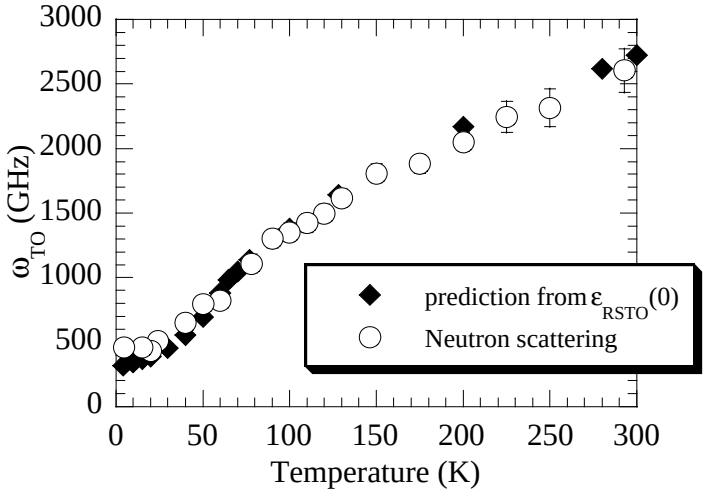

Figure 3.5. $\omega_{TO}(T)$ for STO from neutron scattering measurements[79]and a prediction using (4.8) and low frequency $\varepsilon_{RSTO}(T)$ measurements[54].

STO undergoes a structural phase transition to an antiferrodistortive phase at 105K[81]. The oxygen octahedron in the unit cell rotates a small amount about an axis parallel to one of the faces of the cube. This causes one axis of the unit cell to elongate slightly, so the crystal structure changes from cubic above 105K to tetragonal below 105K. More recent Raman studies by Vogt[77] have shown that the soft mode splits into two components in the antiferrodistortive phase, with the frequencies of each dropping to 540GHz and 270GHz respectively at 4.2K.

3.3.3'Quantum mechanical suppression' of the ferroelectric phase transition in STO

The reason for the absence of a ferroelectric phase transition at 30K in STO was deduced by Muller and Burkard[70]. Using T_{cf}=36K they found that the mean displacement of the Ti^{4+} ion $<p>$ was 0.045Å from the classical theory outlined above, but the mean displacement (or effectively the uncertainty in the position of the Ti^{4+} ion) calculated from the zero point energy of the equivalent quantum mechanical oscillator was found to be 0.077Å. Thus the ferroelectric phase transition in STO is quantum mechanically suppressed.

3.4 Thin film strontium titanate

3.4.1 The contrast between thin film and bulk STO

There are major differences between the dielectric behaviour of thin film and bulk STO. At low frequencies the permittivity of thin film STO, ε_{RTF}, is typically much less than that of bulk STO, ε_{RSTO}. The highest value reported for ε_{RTF} is 5000 at 90K for 200-500nm thick films grown by rf magnetron sputtering[71]. This high value was achieved by a 12 hour anneal at 500°C in oxygen after deposition. Another method to obtain a large ε_{RTF}=1800 at 20K[69] is to cool to room temperature (from a deposition temperature of 760°C) in an oxygen atmosphere after every 50nm STO deposited. However, ε_{RTF} can vary down to 400 for a 500nm film[82], and 80 for a 100nm film[83].

The temperature dependences of the permittivities of thin film and bulk STO are very different. As shown in Fig 3.3, $\varepsilon_{RSTO}(T)$ rises monotonically to 4.2K[54], where it saturates at 24000[70]. However, there is typically a broad peak in $\varepsilon_{RTF}(T)$, either at around 90K[71], or at around 40K[82],[83]. Fig. 3.6 shows the typical form of $\varepsilon_{RTF}(T)$.

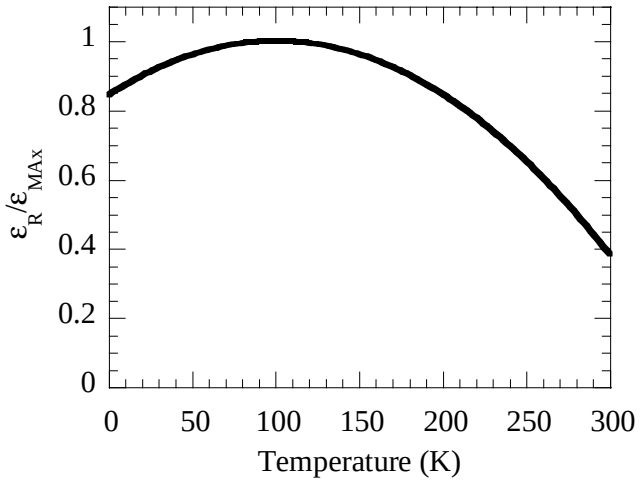

Figure 3.6 The typical form of the temperature dependence of the dielectric constant of thin film strontium titanate.

The broad peak is indicative of a diffuse phase transition[73]. Different regions of the crystal have different Curie temperatures, so there is no longer a sharp discontinuity at one temperature. A diffuse phase transition is a common feature in systems with structural disorder. In a thin film, such structural disorder could arise due to the strain caused by the lattice mismatch between the film and the substrate. Systems which have inhomogeneous compositional disorder also exhibit such behaviour.

For thin film STO, loss tangents between 0.05 and 0.1 are typically reported at low frequencies[71,82]. However, for single crystal STO, the loss tangent is considerably less and has been measured as 10^{-3}[72].

Furthermore, Fuchs *et al.*[71], report hysteretic curves of polarisation as a function of electric field for thin film STO and interpret this spontaneous polarisation with as ferroelectricity with T_{cf}=137K. No evidence of spontaneous polarisation is found for single crystal strontium titanate[83],[54]. However, neither Petrov *et al*[69] or Basceri *et al*[84] report hysteresis in the permittivity as a function of voltage bias for their STO and $Ba_{0.7}Sr_{0.3}TiO_3$ films respectively.

The dielectric properties of incipient ferroelectric thin films have been treated theoretically by Vendik *et al*[85,86]. Vendik introduced a phenomenological dispersion parameter into the equivalents of $A_1(T)$ and $A_2(T)$ to derive a modified version of (3.2). The addition of a dispersion parameter takes into account that the electric field is not necessarily homogeneous

inside the dielectric as a result of defects and mechanical stresses inside the film. A consequence of a non zero dispersion parameter was the introduction of a broad peak into the variation of the dielectric constant with temperature for incipient ferroelectrics without the need for a ferroelectric phase transition. A non zero dispersion parameter also gives rise to hysteretic electric field – polarisation curves due to the redistribution of trapped charge upon reversal of the electric field direction.

Fuchs *et al.*[71] claimed that the peak in the permittivity at 90K of their STO films with temperature was due to a ferroelectric phase transition in contrast to the Vendik theory. Fuchs *et al.* obtained a good fit to the spontaneous polarisation versus temperature measured for their films from standard GLD theory. The peak in permittivity at 40K observed for other STO films was attributed to a tetragonal to trigonal structural phase transition at this temperature.

3.4.2 The causes of the differences between the dielectric properties of thin film and bulk STO

According to Streiffer *et al*[87] there are believed to be three distinct phenomena behind the differences in dielectric behaviour between thin film and single crystal STO. Streiffer *et al.* were able to separate them by making low frequency dielectric measurements on the solid solution $Ba_xSr_{1-x}Ti_{1+y}O_{3+z}$, by independently varying *y*[87].

The phenomena are:-

i. A reduction in film polarisability resulting from Ti non-stoichiometry. An effective dielectric constant for the Streiffer *et al.* films was found to decrease from 900 for y=0.04 to 300 for y=0.15.

ii. The effect of the mechanical constraints imposed by the substrate on the film stress and strain. This leads to structural disorder and a diffuse phase transition. A film removed from the substrate was found to show an increase in dielectric constant from 272 to 378, at room temperature.

iii. A size or interface effect, which is displayed as a decrease in the film dielectric constant with decreasing film thickness.

The causes of the size effect are most relevant for the experiments on a range of thicknesses of

STO thin films described later in this chapter. The size effect was observed by Streiffer *et al.* for $Ba_xSr_{1-x}Ti_{1+y}O_{3+z}$ films for thicknesses between 24 and 160nm over a temperature range between 300K and 480K. The effect was also observed for $Ba_{0.7}Sr_{0.3}TiO_3$ films of thicknesses between 24 and 160nm down to 73K in earlier experiments by the same group[84]. The effect has also been reported by Kotecki *et al.*[64] for $Ba_xSr_{1-x}TiO_3$ films, and by Abe and Komatsu[88] for STO films with thicknesses between 23 and 92nm. All these experiments used metallic electrodes to measure the dielectric constant.

Fuchs *et al.*[71] observed no thickness dependence of the dielectric properties of their STO films for thicknesses between 200 and 500nm. No difference between the properties of the STO films when either Au or YBCO electrodes were used, with the exception of a shift in the maximum of capacitance from zero voltage bias.

Phenomenologically, the size effect can be modelled by modifying (3.2) to give a thickness dependence in the first order polarisation term, as in (3.12).

$$E = \left(\frac{\xi}{d} + A_1(T) \right) P + A_2(T) P^3 \tag{3.12}$$

In (3.12), d is the thickness of the dielectric film and ξ is a constant. Basceri *et al.*[84] found that no modification of $\chi(T)$ was necessary to model the thickness dependence of the dielectric constant of their films. The capacitance of thin film STO has two series contributions, one from the dielectric constant of the bulk, C_b and the other from an interface layer at the boundary between the electrode and the dielectric C_i, as in (3.13).

$$\frac{1}{C} = \frac{1}{C_b} + \frac{1}{C_i} = \frac{d - 2d_i}{\varepsilon_0 \varepsilon_{RSTO} A} + \frac{2d_i}{\varepsilon_0 \varepsilon_i A} \tag{3.13}$$

In (3.13), d_i is the thickness of the interface layer, ε_i is the permittivity of the interface layer and A is the area of the capacitor.

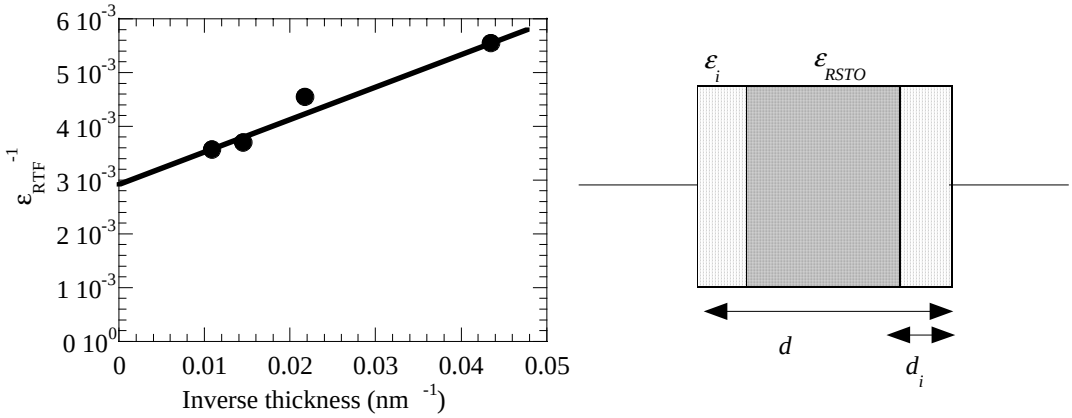

Figure 3.7. The variation of inverse dielectric constant with inverse film thickness for STO films at 295K[88], together with the capacitor geometry for a thin film capacitor with an interface layer.

From (3.13) the effective thin film dielectric constant is given in (3.14).

$$\frac{1}{\varepsilon_{RTF}} = \frac{1}{\varepsilon_{RSTO}} + \frac{2d_i}{d}\left(\frac{1}{\varepsilon_i} - \frac{1}{\varepsilon_{RSTO}}\right) \tag{3.14}$$

Fig. 3.7 shows the capacitor geometry described by (3.13), together with the Abe and Komatsu data[88] for the thickness dependence of ε_{RTF} for STO films at 295K. From the intercept, ε_{RSTO} is found to be 340 in agreement with the Neville *et al*[54] measurement at this temperature.

Streiffer *et al*[87] have summarised the variety of mechanisms that could be responsible for the dependence of ε_{RTF} on film thickness. The mechanisms are either intrinsic or extrinsic to the dielectric film itself. The extrinsic mechanisms consist of contamination of a layer near to the interface, either as a result of chemical species which are not Ba, Sr, Ti or O, or a change in growth mechanism at the interface resulting in a non uniform stoichiometry or grain size across the thickness of the film.

3.4.3 Intrinsic mechanisms for the size effect

The relevant intrinsic mechanisms for the thickness dependence of ε_{RTF} are the formation of an intrinsic dead layer at the surface of an incipient ferroelectric film and the existence of a Schottky barrier at the interface between the metal electrode and the dielectric film.

Zhou and Newns[74] have developed a modified version of the microscopic theory of ferroelectricity, which was described in section 3.2.4, to encompass the effect of finite size on

the dielectric behaviour. A mean field approximation was used as in the bulk case, but the polarisation and the mean field due to the surrounding dipoles were assumed to be dependent on the distance from the surface of the film. The mean field was assumed to decay exponentially at the film surface with a range parameter λ_f, and the polarisation decays exponentially to zero at the surface of the film. The theory leads to two predictions. Firstly, there an exists an intrinsic dead layer at the surface of a ferroelectric with width d_i, and hence the effective dielectric constant scales linearly with film thickness as shown in (3.15).

$$\varepsilon_{RTF} = \frac{T_1}{T + \left(T_0 / d\lambda_f\right) - T_{cf}} \tag{3.15}$$

In (3.15), $T_1=1/\beta$ is the Curie-Weiss constant (see (3.3)) and T_0 is a temperature parameter. For bulk STO T_0 and T_1 can be obtained from the temperature dependences of the frequency of the soft optic phonon and the permittivity. Zhou and Newns found T_0=2060K and T_1=1.01x10^{5}K. By fitting (3.4) to the room temperature Abe and Komatsu data for the size effect in STO films (Fig 3.7), Zhou and Newns found λ_f=1nm^{-1}. From (3.15) it can be seen that below a characteristic film thickness $d_c=(T_0/\lambda_f T)$, ε_{RTF} starts to drop. For STO at 4.2K, this thickness is 490nm. The second prediction, also evident from (3.15) is that T_{cf} decreases with decreasing film thickness, becoming negative for very thin films. This prediction was also verified by experimental data.

The size effect was also treated by Vendik *et al.* by introducing dependence of the film polarisation on position, this time into the modified Ginzburg-Landau-Devonshire expression for $E(P)$. Since the polarisation vector cannot vary within short distances such as one cell of the crystal lattice, below a certain sample size the dielectric properties must become size dependent. An equation equivalent to (3.4) was derived[85], which defined a 'correlation radius', equivalent to T_0/λ_f in (3.15) and approximately equal to 2μm from the Zhou and Newns parameters, or 2.5μm at 78K according to Vendik. The correlation radius is analogous to the coherence length in a superconductor.

Vendik *et al.*[86] identified the electrode material as a further cause of the size effect. It was postulated that the ferroelectric polarisation cannot decay into a metal. Therefore, the ferroelectric polarisation must be zero at the metal – dielectric interface. However, the ferroelectric polarisation can decay into an oxide electrode such as YBCO. The effect was

observed experimentally by Hwang *et al.*. A size effect was observed for $Pt/Ba_{1-x}Sr_xTiO_3/Pt$ capacitors, but not for $IrO_2/Ba_{1-x}Sr_xTiO_3/IrO_2$ capacitors[89]. The intrinsic dead layer was therefore not present for the capacitors with oxide electrodes.

At the interface between a metal and an incipient ferroelectric, a Schottky barrier is formed. Charge carriers diffuse from the incipient ferroelectric into the metal to compensate for the difference between the work function of the metal and the Fermi level of the ferroelectric. The barrier results in a built in voltage at the interface which shifts the maximum of the permittivity versus voltage bias curve (see Fig 3.2(b)) away from the origin[82]. Initially, the film was thought to be depleted only near the electrodes, and so the application of a voltage bias changed the effective length of the depletion region, hence changing the effective dielectric constant[82]. Dietz *et al.* claimed that measurements of the leakage current in $Ba_{0.7}Sr_{0.3}TiO_3$ films showed that films thinner than 162nm were completely depleted, so an applied voltage bias could not change the thickness of the depleted region as described above[90]. Furthermore, the capacitance-voltage curves obtained could be described quantitatively by GLD theory[84], so this was believed to be the correct mechanism responsible for the tuning of the dielectric constant. However, Hwang *et al.*[89] proposed a partially depleted model to explain their leakage current measurements of $Ba_{1-x}Sr_xTiO_3$ films.

Regardless of whether the film is fully or partially depleted, there still exists a small built in field at the electrode-dielectric interface, which could suppress the dielectric constant near the interface and thus appear as an interface capacitance[87].

3.4.4 Frequency dependence of the dielectric constant of thin film ferroelectrics

The frequency dependence of the dielectric constant of $Ba_{0.7}Sr_{0.3}TiO_3$ films has been studied by Baniecki *et al.*[91], between 1mHz and 20GHz at room temperature. The dielectric constant ε_R of the films was found to obey a Curie-von Schweidler relationship with the real part $\varepsilon_R'(\omega)=\varepsilon_R'(0)-A'\omega^p$ and the imaginary part $\varepsilon_R''(\omega)=A''\omega^p$. ε_R' was found to vary by less than 7% in the frequency range studied. For $BaTiO_3$ films, p varies between 0.03 and 0.05[92]. Systems with diffuse phase transitions typically have a frequency dependent dielectric constant, with the dielectric constant maximum occurring at higher temperatures with

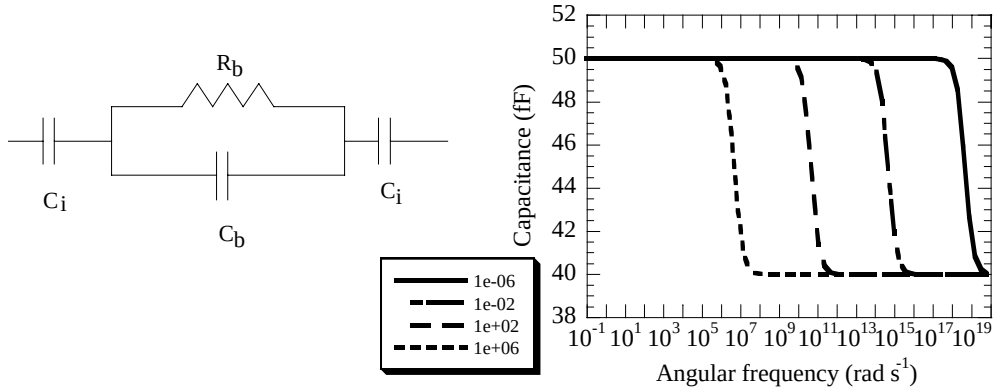

Figure 3.8 The Maxwell – Wagner interface capacitance model and the expected variation of capacitance with frequency for various R_b and C_i=100fF and C_b=200fF.

increasing frequency[73]. In polycrystalline films natural variation in grain sizes could cause the Curie-von Schweidler behaviour[91]. Oxygen vacancies in the depletion region could be a further cause[91]. For epitaxial films, any mismatch of the film to the lattice causes inhomogeneous local strain leading to structural disorder, a further possible cause of the Curie-von Schweidler behaviour[92].

Partially depleted incipient ferroelectric films would exhibit a Maxwell – Wagner relaxation step in the variation of capacitance with frequency. The partially depleted system is modelled as two fully depleted (lossless) interface capacitors C_i in series with a lossy (R_b) bulk capacitor C_b as shown in Fig. 5.3.

The expected variation of capacitance with frequency for the Maxwell – Wagner model is also shown in Fig. 5.3, for various values of R_b and C_i=100fF and C_b=200fF. The limiting values are $C_i/2$ at low frequency and $C_iC_b/(C_i+2C_b)$ at high frequencies, with the step at angular frequency $\omega=2\pi/R_bC_b$. The Baniecki *et al.*[91] measurement of the frequency dependence of the dielectric constant found no evidence for Maxwell Wagner relaxation between 1mHz and 20GHz. Dietz *et al.*[90] claim that this constitutes more evidence for a fully depleted model of $Ba_{1-x}Sr_xTiO_3$ thin films. A step below 1mHz would require carrier densities too low to give the required built in voltage at the dielectric metal interface. A step above 20GHz requires the bulk to be so lossy as to resemble a strongly conducting semiconductor. However, Hwang *et al.*[89] claim that reasonable parameters for the carrier concentration and electron mobility could lead to R_b~1Ω which would give Maxwell – Wagner relaxation in the THz region.

The Zhou and Newns theory also has a third consequence, as mentioned in the original

paper[74], and by Streiffer *et al.*[87]. Since the environment near the surface of the film contains less dipoles, the tendency to drive the transverse optic phonon soft is reduced. Therefore the frequency of the soft optic phonon in thin film STO should be increased with respect to that measured in bulk STO. This would also be expected if the Lyddane-Sachs-Teller relation (3.8) were obeyed in STO thin films.

High frequency measurements (between ~50GHz and 1THz) of the dielectric constant of thin film STO using Josephson junctions coupled to external resonators could therefore provide information regarding the hardening of the soft optic phonon and Maxwell Wagner relaxation.

Chapter 4: Experimental Methods

4.1 Introduction

This chapter describes the fabrication techniques needed to manufacture Josephson junctions, shunt capacitors and YBCO / strontium titanate / gold resonators. The pulsed laser ablation systems that were used to deposit the films are briefly reviewed. Next, descriptions of the photolithography, etching methods and contact deposition procedures are given. Finally, the measurement rig used for the electrical characterisation of the devices at cryogenic temperatures is described.

4.2 Pulsed Laser Deposition

The $YBa_2Cu_3O_7$ (YBCO) / $SrTiO_3$ (STO) bilayers used in this study were from three sources. These were the off-axis laser ablation system at the IRC in Superconductivity at the University of Cambridge and the on-axis system at the Department of Physics and Applied Physics at the University of Strathclyde. Calcium doped YBCO films were grown at the University of Augsburg. The films were grown by Dr. E. Tarte, Dr. A. Moya and Dr. F. Kahlmann at the University of Cambridge, by Dr. E. Romans at the University of Strathclyde and by the Mannhart group at the University of Augsburg. All the films were grown on 24° misorientated STO bicrystal substrates, with the exception of one 36° misorientation angle.

A diagram of the off-axis laser ablation system in Cambridge is shown in Fig. 4.1. A laser is incident on a YBCO target. The substrate on which the film is to be deposited is placed in the plume of ablated material from the target. In principle, the stoichiometry of the film is the same as that of the target. The system uses a KrF excimer laser with a wavelength of 248nm and pulse duration of 10ns. The energy density of the laser at the target surface was 1.8 J cm^{-2}. The targets were water cooled during deposition to prevent excess heating and oxygen depletion. The targets were also rotated to minimise damage to any one part of the surface of the target. The system was pumped to a base pressure of $<10^{-7}$ mbar. The substrate was heated to 780°C during deposition, which took place in a 0.3 mbar oxygen atmosphere. The number of laser pulses controlled film thickness. After deposition of both the YBCO and STO layers, the substrate was cooled to room temperature at 20°C min^{-1} at an oxygen pressure of 1 bar.

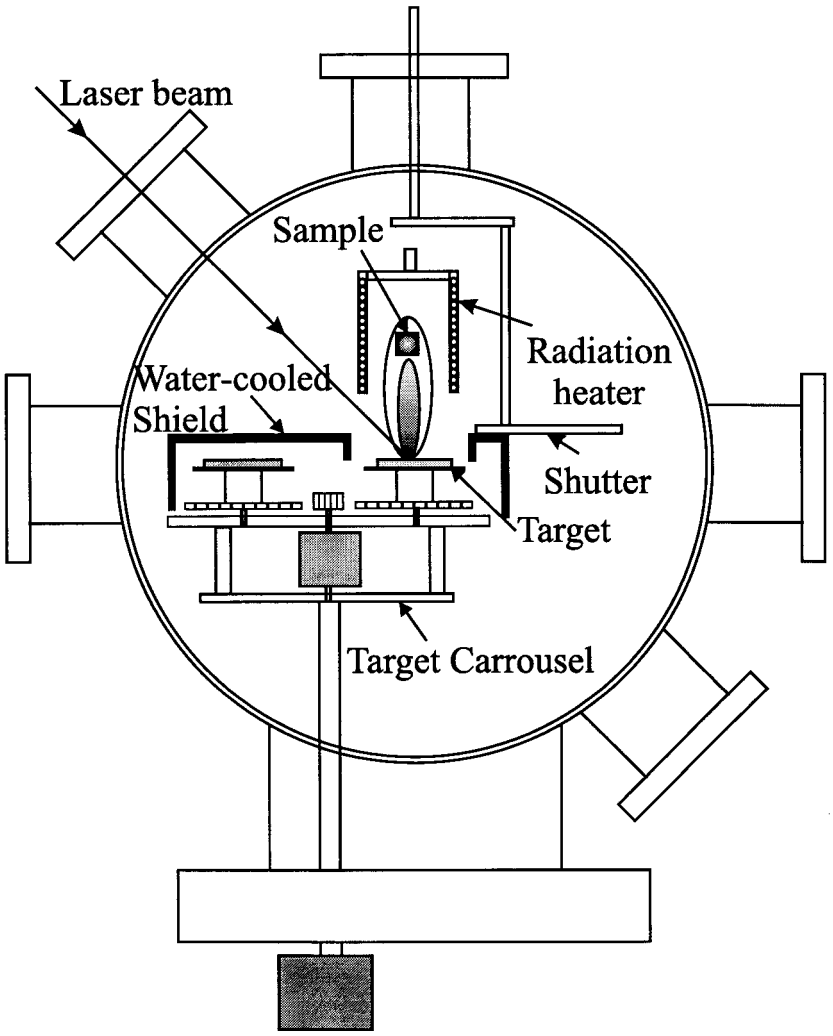

Figure 4.1 The Cambridge off-axis laser ablation system[10].

The system and surface morphology of the films prepared by it are described in more detail by Santiso *et al*[93].

The difference between on and off-axis laser ablation lies in the orientation of the substrate with respect to the plume. The substrate is parallel to the plume in an off-axis system, and perpendicular to the film in an on-axis system. Fewer large clusters of atoms reach the surface of the film in an off-axis system.

In Cambridge, the YBCO film thickness was calibrated by wet etching a step in the film with phosphoric acid ($H_3PO_{4(aq)}$), and measuring the step height with a profilometer to an accuracy of ±25nm. The STO deposition rate was assumed to be equal to the YBCO deposition rate. In Strathclyde, the deposition rates were determined independently for both the YBCO and the

STO. The films were ion milled (see section 2.3.2) in a system fitted with a mass spectrometer for endpoint detection. The thicknesses were measured with a Dektac profilometer to an accuracy of ±1nm.

4.3 Device fabrication

4.3.1 Photolithography

The majority of the films were patterned with the standard photolithographic techniques described in this section. The stages of patterning of the YBCO/STO bilayers are shown in Fig. 2.3.

The films were cleaned prior to patterning by ultrasonic stirring in acetone for 2 minutes. If the film surface was particularly dirty chloroform, then acetone and then propanol were used. The films were then airbrushed with acetone followed by propanol.

The following is a positive photoresist technique. Opaque areas of the mask are the regions where the photoresist remains on the film after patterning. Photoresist (AZ1529) was spun onto the film at 6000 RPM for 30 seconds. The film was then baked at 100°C for one minute. For features larger than 5μm, a Cannon projection mask aligner was used to expose the films for 3 minutes. The photoresist undergoes a chemical reaction when exposed to ultra violet light rendering it soluble in developer. After exposure, the resist was developed for 30 seconds in AZ developer diluted 4 parts developer to one part water.

The patterning of fine features (to 1μm) and alignment of the pattern to the grain boundary in the bicrystal required the use of a Carl Suss contact mask aligner. As a result of spinning, a thick layer of photoresist known as the edge bead forms around the edges of the film. The edge bead was first removed to achieve good contact between the mask and the film. Multiple exposures and subsequent developings were sometimes required to completely remove the edge bead. The film was exposed for 8 seconds in the Carl Suss. The resist was developed for between 15 and 45 seconds. The endpoint of the developing was detected visually.

4.3.2 Ion milling

After the resist had been patterned, ion milling was used to physically etch away the unwanted areas of the film. The Kaufman ion gun was powered with a Princeton Applied Research

power supply. The chamber was pumped down to less than $4x10^{-6}$mbar with a diffusion pump prior to milling. The film was milled in a 2% oxygen in argon gas mixture at a pressure of $2x10^{-4}$mbar. The beam current of the Ar^{+} ions was 10mA with a 500V accelerating voltage. The purpose of the oxygen gas was to enhance the etching rate by oxidising the debris from the areas of film being removed. The sample holder was cooled with water to minimise oxygen depletion from the YBCO film and grain boundary during milling. The angle of the step between the film and the substrate could be controlled by adjusting the angle of incidence of the ion beam to the substrate between 0° and 45°. The sample was rotated whilst being milled to ensure a uniform etch rate across its entire area.

The milling rate was calibrated by measuring step heights of patterned films with a profilometer. Typical milling rates at 0° incidence to the beam were 3.3 nm min^{-1} for STO and 5nm min^{-1} for YBCO. These rates approximately double at 45° incidence to the beam. The milling rate of the STO is two thirds of that of the YBCO. The milling rate was found to decrease by 1nm min^{-1} over a period of months. The milling rate recovered to its original value when the ion gun filament was replaced.

To ensure that the film had milled completely, it was checked that the resistance between two points on the bare substrate was greater than 1MΩ.

4.3.3 Patterning an YBCO/STO bilayer on a bicrystal

This section describes the additions required to the above techniques when patterning a film on a bicrystal. Resist was spun and baked as in section 4.3.1. Off-axis films had a layer of YBCO on their reverse side. This layer could cause difficulties with any subsequent electrical characterisation, so it was removed by etching in 2.5% phosphoric acid solution. The endpoint was detected visually after approximately 30 seconds when the film and substrate became translucent.

A grain boundary etch mask was then patterned in the film using the projection mask aligner as in section 4.3.1. The film edges could be removed by etching in phosphoric acid for bare YBCO films, but STO/YBCO bilayers required these regions to be removed by ion milling. STO does not etch in phosphoric acid. Care was taken not to overmill which would result in a step height large enough that the grain boundary and the film surface could not be brought into

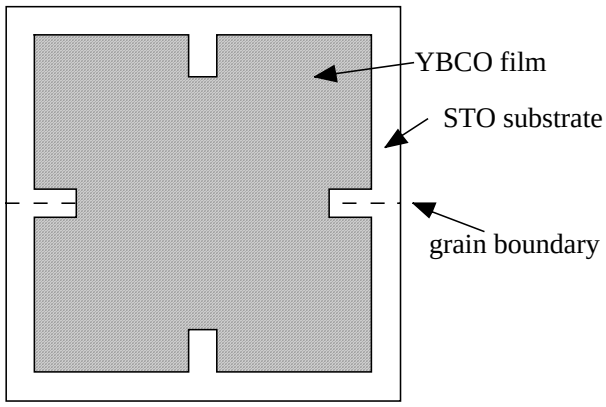

Figure 4.2 The film and the grain boundary after etching in hydrofluoric acid.

focus simultaneously in the contact mask aligner. The remaining resist was removed in acetone. Another layer of resist was spun and patterned into the grain boundary etch mask. Then, the STO bicrystal grain boundary was etched for 30 seconds in 7% hydrofluoric acid. The grain boundary was then visible in the substrate to enable the device pattern to be aligned to it. The film after the grain boundary has been etched is shown in Fig. 4.2.

Following this stage, the devices were patterned with the contact mask aligner and the film was ion milled as in sections 4.3.1 and 4.3.2. Next, holes were patterned over the areas of the film where contact pads were required and the STO layer was milled away in these regions. This enabled electrical contact to be made through to the YBCO. After this stage of patterning, it was checked that the resistance of an YBCO track was ~1 kΩ to ensure that the STO layer had been completely removed over the contact pads.

A diagram of the process is shown in Fig. 4.3.

4.3.4 Lift-off and gold contact pad deposition

To achieve the contact resistances necessary for low noise electrical characterisation of the devices, gold contact pads were deposited with the lift-off technique described below.

Holes were patterned in a layer of photoresist over the films, in the areas in which contact pads were required. The resist was slightly overdeveloped to ensure that there no resist remained in the regions where contact pads were required. Next, gold was deposited over the entire area of the film using dc sputtering. The chamber was pumped to below $5x10^{-5}$ mbar prior to gold deposition. The gold was sputtered at a pure argon pressure of $5x10^{-2}$mbar at 30W power. The gold deposition rate at this power is 3.3nm s^{-1}. Again, the sample holder was water cooled to

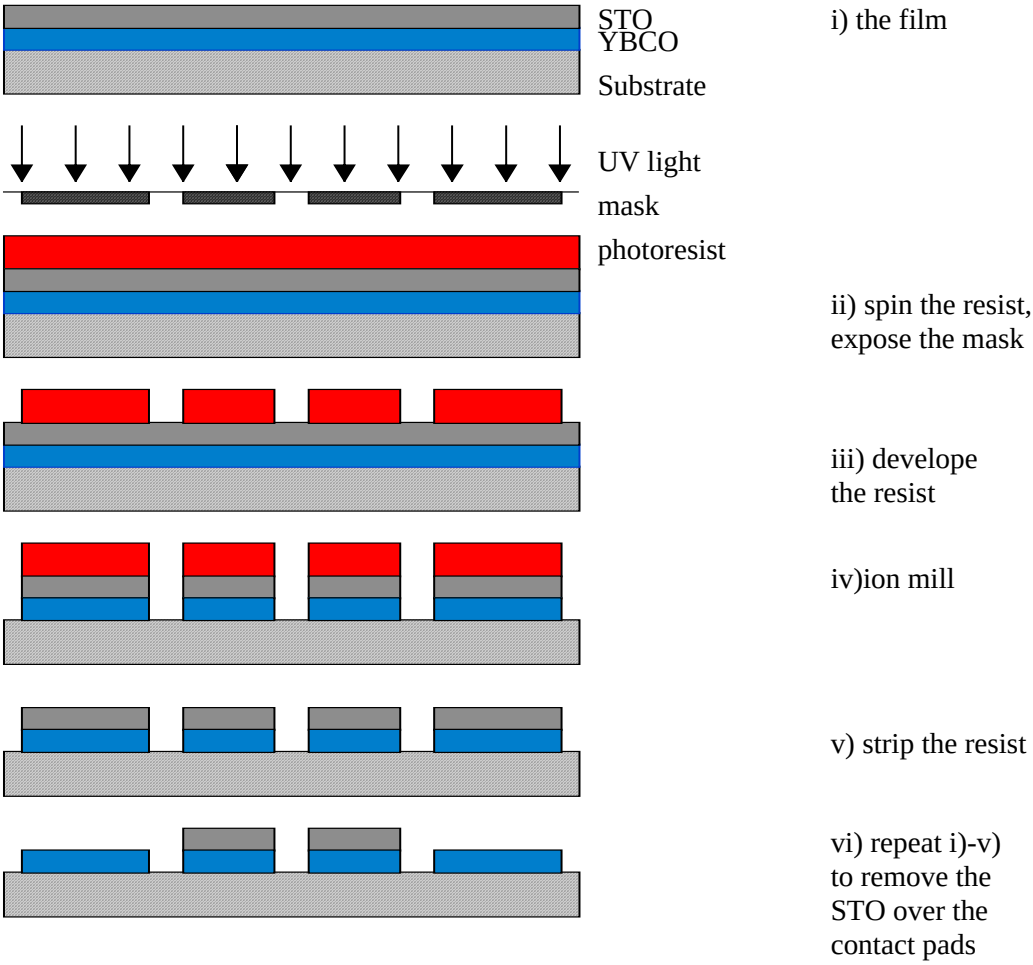

Figure 4.3 The stages of patterning of the YBCO/STO bilayer films (not to scale).

minimise oxygen depletion caused by heating during gold deposition. The resist was then stripped with acetone, leaving gold over the contact pads where there was no resist. A diagram of the lift-off process is shown in Fig. 4.4.

4.3.5 A hard masking process for thick films

The fabrication techniques described in sections 4.3.1 to 4.3.3 performed well for films up to 300nm thick. However, it was found to be impossible to pattern thicker films to high resolutions using photoresist. Mill times greater than one hour at 45° incidence to the beam led to the resist itself milling away. The resist was also found to etch faster at an edge, so narrow tracks disappeared first. It was desired to pattern a 200nm YBCO / 200nm STO bilayer film. Therefore the niobium masking technique described below was developed.

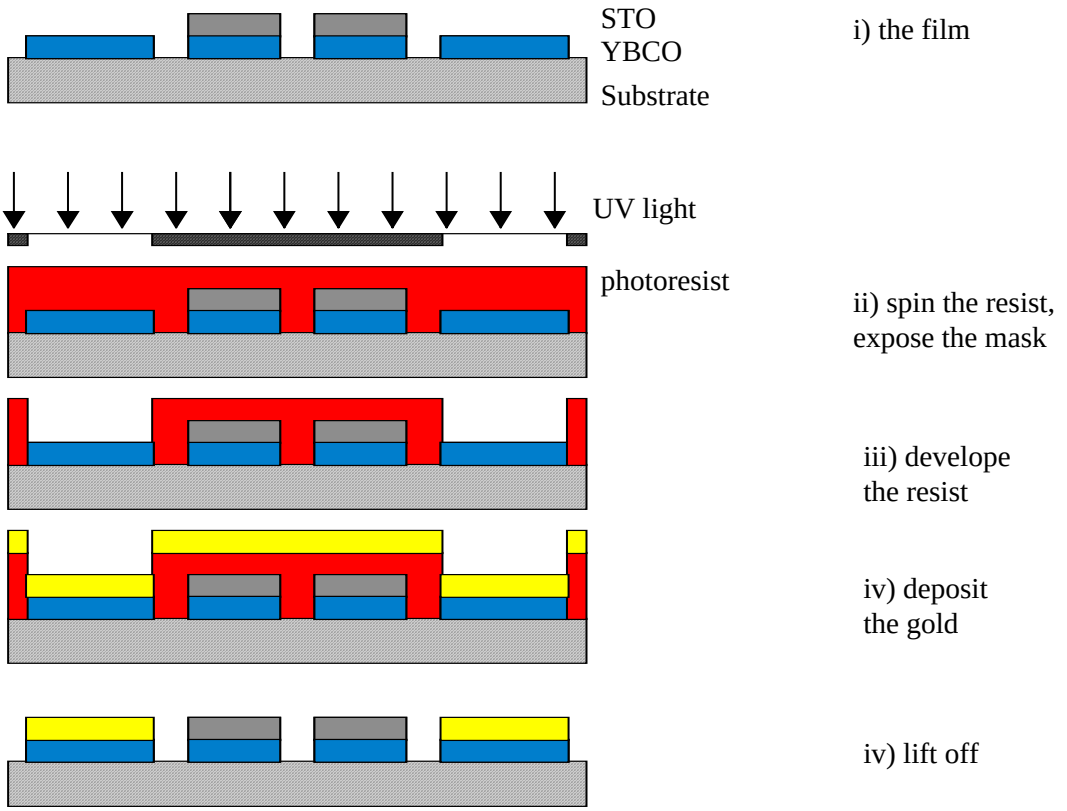

Figure 4.4 The lift-off process for gold contact pad deposition (not to scale).

The grain boundary in the substrate was exposed with the process described in section 2.3.3. The metal mask was deposited using a lift-off process. A negative resist or image reversal process was used for the patterning, where the resist underneath the opaque area of the mask is developed. The AZ5214 photoresist was spun at 4000 RPM for 30 seconds. The resist was then baked for 10 minutes at 80°C. The edge bead was removed. The resist was exposed through the required mask for 5 seconds in the contact mask aligner. The resist was then baked for a further 2 ½ minutes at 120°C. The resist was then flood exposed (with no mask) in the contact mask aligner for 25 seconds, and then developed for 30 seconds in 2 parts AZ developer to 1 part water solution.

A gold / niobium bilayer was sputter deposited onto the film. The gold was required to prevent any chemical reaction or diffusion of the niobium into the STO film. The gold was also necessary to provide an endpoint for subsequent carbon tetrafluoride (CF_4) plasma etching. The chamber was pumped overnight to a base pressure ~10^{-7}mbar. Prior to deposition the diffusion pump trap was filled with liquid nitrogen to further reduce the chamber pressure. The sample was milled for 30 seconds prior to deposition to clean its surface and improve the

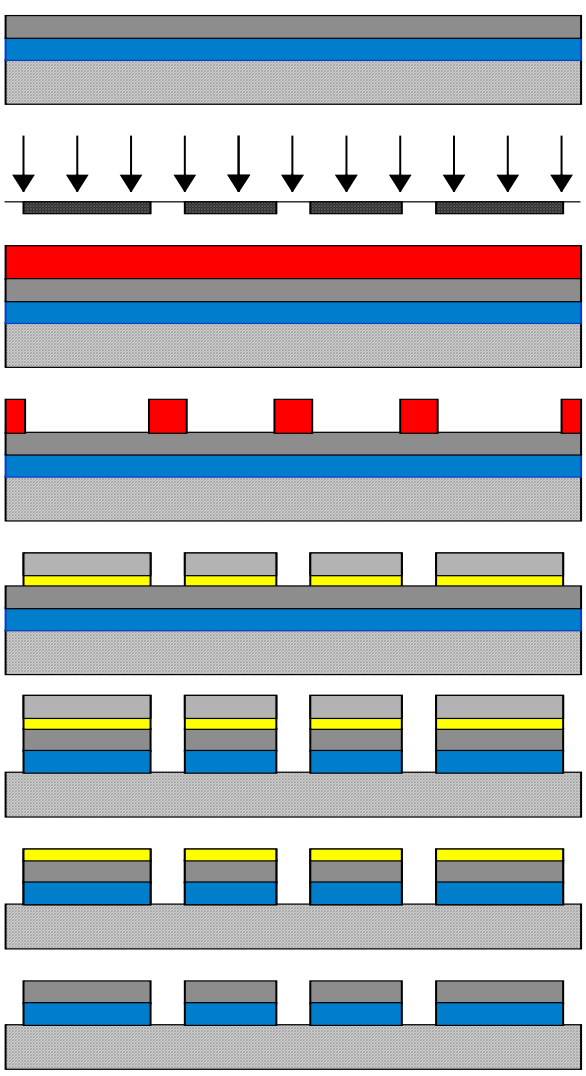

i) the film

ii) spin the resist, expose the mask

iii) develope the resist

iv)sputter Au Nb bilayer and lift off

v) ion mill

vi) CF_4 plasma etch to remove Nb

vii) $KI / I_{2(aq)}$ wet etch to remove Au

Figure 4.5 Image reversal using negative resist and a hard masking process for thick films (not to scale).

adhesion of the gold niobium bilayer. A 50nm gold film was deposited first, with the conditions described in section 4.3.4. The niobium was then sputtered for 15 seconds at a pressure of 2.3×10^{-3} mbar of pure argon with 75W power The argon pressure was then increased to 3.2×10^{-3} mbar and niobium was sputtered for 17 minutes. The niobium film thickness was 700nm.

The lift-off was performed by soaking in acetone for 2-3 hours. The sample was then ion milled for 75 minutes at 45° incidence to the beam. The mill rate of niobium is approximately the same as that of STO. The 700nm niobium film was therefore a sufficient mask for the longer mill time. The required 2µm features were reliably patterned in this way.

After milling, the remaining niobium was removed using CF_4 RF plasma etching. The base

pressure of the plasma etching chamber was 10^{-5}mbar. The sample was first cleaned for 1 minute in an oxygen plasma at a pressure of 0.25mbar with 50W incident and 7W reflected power giving a discharge voltage of 120V. The niobium was then removed by etching for 6 minutes in a 0.175mbar CF_4 plasma with the same power and a discharge voltage of 100V. The gold film is not etched by the CF_4, so this provided a natural endpoint for the process.

After the CF_4 etching, the chamber was flushed with argon and pumped to 10^{-3}mbar before opening, as CF_4 gas is toxic.

The gold was then removed by wet chemical etching for 30seconds in a solution of 4g potassium iodide and 1g iodine in 150ml water. The STO was then removed from the contact pads and gold contacts deposited using the same procedure as in sections 4.3.3 and 4.3.4. A diagram of the hard masking process is shown in Fig. 4.5.

Table 4.1 shows the film thicknesses of the various chips used in this study. The substrate were all 24° misorientated STO bicrystals, with the exception of Xros36 which was a 36.8° misorientated STO bicrystal.

Table 4.1 Film thicknesses

Chip Name	*YBCO thickness (nm)*	*STO thickness (nm)*	*Gold electrode thickness(nm)*
Subros	100	20nm capping layer	N/A
Xros24a	100	20	162
Xros24b	200	100	162
Xros24c	200	100	297
Xros24d	200	50	495
3tdev	200	200	594
Xros36	200	100	162
1D_res	200	50	594
Y998	100	None	N/A
Fiske	170	None	N/A

4.4 Electrical characterisation of devices

The samples were mounted using nail varnish onto chip carriers consisting of a copper block, a printed circuit board and a plug or socket. The samples were ultrasonically wire bonded to the chip carriers with 30μm diameter aluminium wire. The chip carrier was plugged into a probe which was dipped into a liquid helium dewar for electrical characterisation between 4.2K and 300K.

The measurement rig is shown in a block diagram in Fig. 4.6. The devices were current biased and the voltage and current were measured by a standard 4 point measurement technique. The low noise current source and voltage amplifiers were designed by Dr. Wilfred Booij. A Dell PC via a 16 bit National Instruments analogue to digital I/O card controlled the electronics. Current voltage characteristics were measured with LabVIEW software written by Dr. Gavin Burnell. The software also controlled the temperature controller, lock-in amplifier and voltage source.

The computer generated a 30Hz sinusoidal voltage, which was used to drive the current source. A second current source was used to drive Helmholtz coils to apply a magnetic field up to 100mT perpendicular to the direction of current flow through the junction. The ambient magnetic field was minimised with a μ-metal shield.

The EG&G 5302 lock-in amplifier enabled the direct measurement of differential resistance (or dynamic resistance) versus voltage curves. A 1kHz voltage with 5mV amplitude was generated by the lock-in amplifier. This signal was added to a slowly varying voltage ramp generated by the current source power supply. The amplitude of the 1kHz current applied to the device therefore changed depending upon the range of the current source. The lock-in measured the amplitude of the voltage across the device at 1kHz. The differential resistance could then be calculated with knowledge of the current source range and voltage amplifier gain. Variation of the current source range and voltage amplifier gain were found not to affect the differential resistance measurement. The differential resistance measurement was also not affected by changes in the frequency of the lock-in signal up to ~7kHz. Above 7kHz the amplitude of the voltage signal measured by the lock-in was reduced by passive RCR low pass filters in the probe.

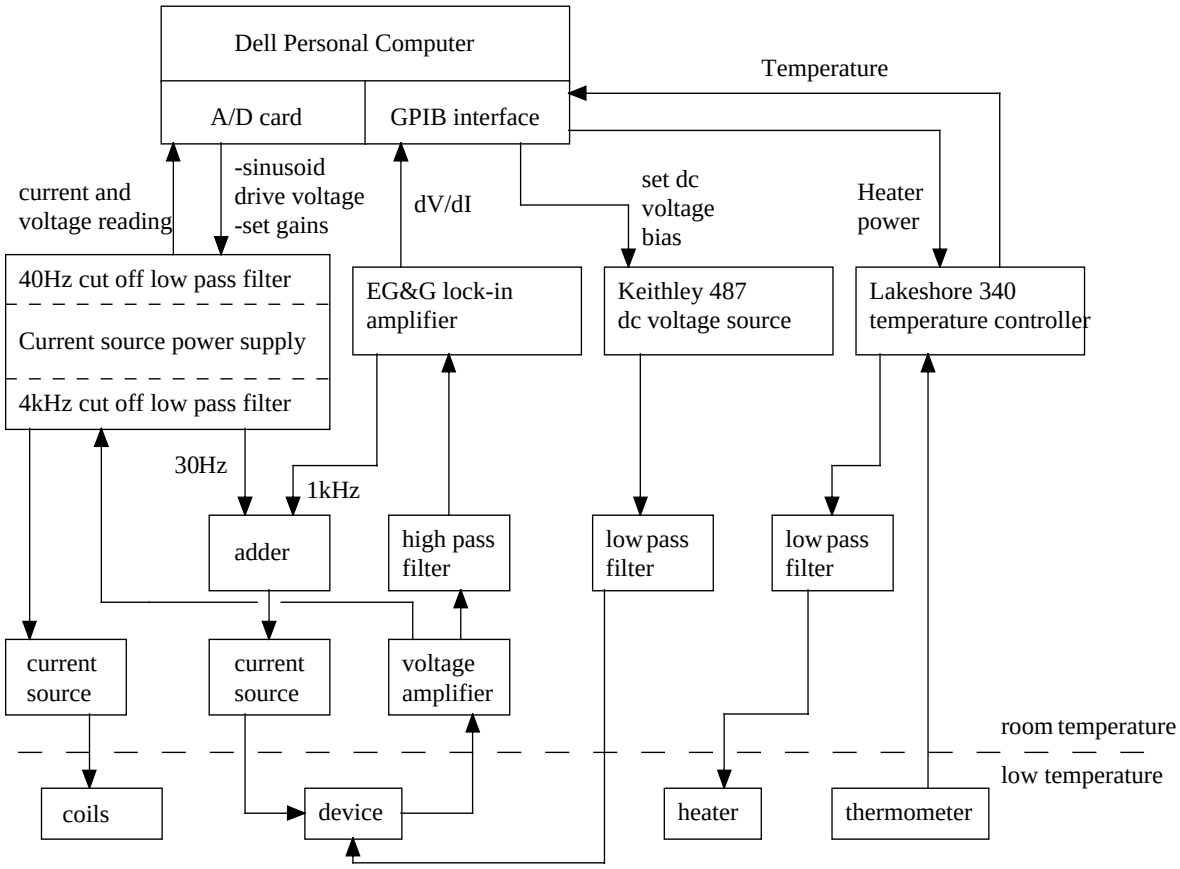

Figure 4.6. A block diagram of the electronics used for device measurement.

A Keithley 487 dc voltage source was used to voltage bias shunt capacitors and resonators on the sample being characterised.

The temperature of the sample was measured with a silicon diode temperature sensor with a Lakeshore 340 PID (proportional, integrating, differentiating) temperature controller. The calibration of the temperature sensor was checked in boiling liquid nitrogen at 77.4K and boiling liquid helium at 4.2K.

The Lakeshore temperature controller, the Keithley voltage source and the lock-in amplifier were connected to the computer with a GPIB card.

The peak to peak voltage noise of the system was 1μV. The following steps were taken to minimise the voltage noise. The current source and voltage amplifier power supply contained active low pass filters to minimise electromagnetic interference from the mains and from the A/D card. The current source and voltage amplifier were fixed to the probe itself. This

minimised the length of cable through which low level signals traveled, and thus reduced electromagnetic interference.

The heater was power supply was isolated from the ground of the measurement electronics.

The heater, thermometer and coil leads were made from twisted pairs of wires. This minimised inductive cross talk between these leads and the measurement lines. Each heater line was also filtered separately with a ferrite bead. The passive low pass RCR filters for the heater power supply and the voltage source were found to be essential for the correct measurement of Josephson junction critical currents and hysteresis. In the absence of these filters, the critical current was found to be significantly suppressed. For some devices with small critical currents (e.g. 60μA at 4.2K), this suppression could be up to 20μA. The upgrade of the measurement computer from an Apple Quadra to a Dell Pentium PC enabled the rapid measurement of thousands of critical currents. The absence of low pass filtering of the heater power supply was found to substantially increase the standard deviation of one thousand measurements of a device critical current.

Chapter 5: Josephson junctions with hysteretic current voltage characteristics at high temperatures

5.1 Introduction

This chapter describes the testing of grain boundary YBCO Josephson junctions shunted with an external capacitor. A capacitive shunt was used to obtain a junction with a hysteretic current voltage characteristic at a high temperature (T>50K). As described in Chapter 1, typical high T_c Josephson junctions have $\beta_c \approx 1$ at 4.2K and $\beta_c < 1$ at T>50K. The primary motivation behind fabricating a hysteretic junction at T>50K is that hysteresis is vital for the correct operation of a relaxation oscillation SQUID (ROS)[94,95].

First, the operation of the relaxation oscillation SQUID is described, followed by that of double relaxation oscillation SQUIDs. Next, previous experiments on both low T_c and high T_c hysteretic Josephson junctions is reviewed. Initial attempts to achieve coupling of the junction to co-planar and parallel plate external capacitors are discussed. Then, experiments where junctions were successfully coupled to external capacitors with hysteretic current voltage characteristics both at low and high temperatures are described. Simulations of junctions shunted with distributed impedances and lumped capacitances are performed. The feasibility of manufacturing relaxation oscillation SQUIDs from high T_c junctions is assessed.

5.2 The relaxation oscillation SQUID

A ROS consists of a SQUID made with hysteretic Josephson junctions shunted in parallel by an inductor L and a resistor R_b in series. However, unlike the dc SQUID, where a small change in magnetic flux produces a small change in read-out voltage, the ROS produces voltage pulses the frequency of which is determined by the applied magnetic field. An equivalent circuit for the ROS is shown in Fig. 5.1.

The ROS is operated at a constant current bias I_b slightly greater than twice the critical current of each junction. The cycle of operation is, starting from the point where the ROS has just switched into the voltage state:- (see also Fig. 5.2)

1. The current through the L-R_b combination slowly increases. The current through the SQUID decreases as the return branch of the IV curve is followed. The ROS remains in the voltage state.

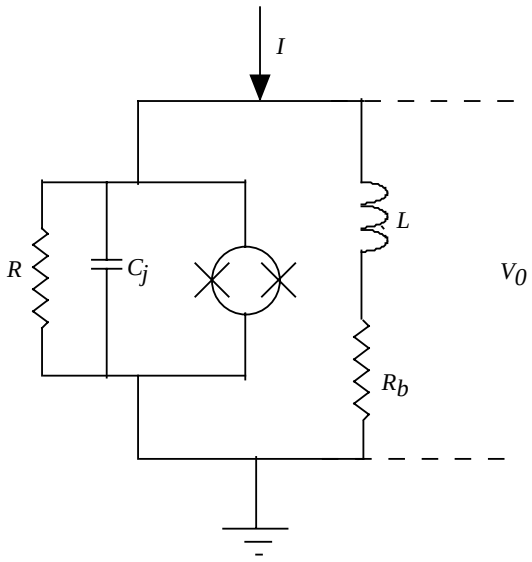

Figure 5.1 The equivalent circuit for a ROS

2. When the current through the SQUID reaches the return current of the junctions, the SQUID switches back into the superconducting state, so the voltage across the ROS is zero.

3. Now the current through the L-R_b combination decreases and the current through the SQUID increases until its critical current is reached at which point the SQUID returns to the voltage state and the cycle is repeated.

The frequency with which the cycle repeats is determined by the critical current of the SQUID, which is in turn determined by the magnetic flux through the SQUID (see Chapter 1). So, the ROS operates as a flux to frequency converter. By varying L, R_b and I_b the frequency of the oscillations can be varied from a few MHz up to 40GHz[95]. However,

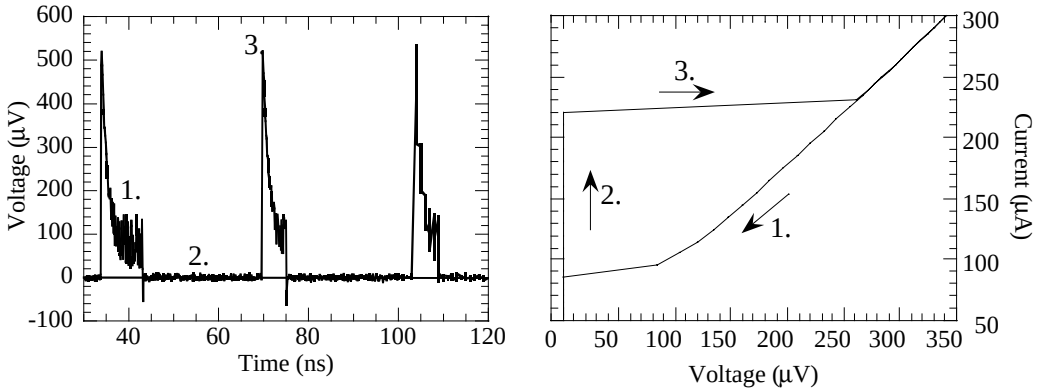

Figure 5.2 The voltage pulses measured from a ROS (R=0.659Ω, C_j=60pF, I_c=440μA, L=1nH, R_b=0.1Ω bias current 900μA) output and a hysteretic IV curve as a guide. (junction IV parameters and ROS parameters do not correspond.)

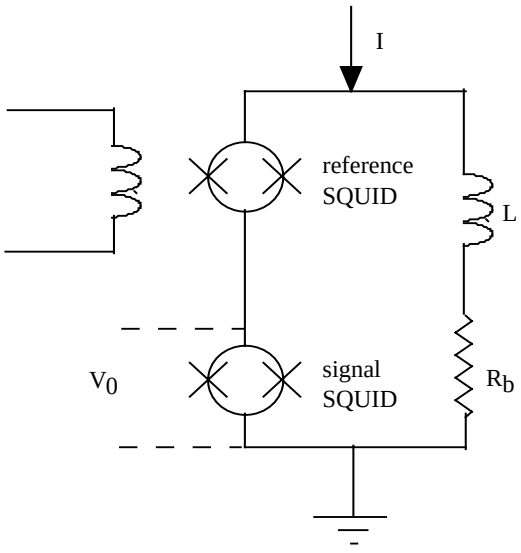

Figure 5.3. The equivalent circuit for a DROS.

it is important to choose R_b and I_b such that $V_\infty = R_b I_b < V_{min}$, where V_{min} is the voltage at which the SQUID switches back into the superconducting state, otherwise the oscillations will cease in the voltage state at stage 2 of the cycle[95].

More sophisticated devices based upon the ROS have also been demonstrated. A Double-ROS (DROS) is shown in Fig. 5.3 and consists of two SQUIDs in series shunted in parallel by an inductor and a resistor[95]. A reference flux is applied to one of the SQUIDs, and the dc voltage across the other (signal) SQUID is measured. The SQUID which has the lowest critical current participates in the relaxation oscillations. Either the average voltage of these oscillations is measured, or zero voltage, so the DROS acts as a critical current (or flux) comparator. Thus, the DROS can be read out digitally making it extremely useful for potentially unshielded SQUID imaging systems.

5.3 A survey of hysteretic junctions

5.2.1 Representative low T_C hysteretic junctions

Low T_c SIS tunnel junctions typically have a very high resistance (resistance area product ~ 100 - 1×10^4 $\Omega\ \mu m^2$) and also a high capacitance (~ 0.038 pF μm^{-2})[28]. The ideal SIS junction has $\beta_C \rightarrow \infty$[96]. Experimental investigations of these junctions were mainly concerned with verifying the predictions of the Stewart-McCumber phenomenological model of the Josephson junction IV characteristic, and also the form of $\beta_c(\alpha)$. Hansma *et al*[96] fabricated Sn-SnO-Sn junctions with a resistance area product of 6.1×10^4 $\Omega\mu m^2$ shunted with an Ag resistor

with a value between 1mΩ and 10Ω. The junctions had a capacitance of around 100pF, arising from the parallel plate structure formed by the junction and its electrodes, and the critical current was adjusted either by varying the temperature or by applying a magnetic field in order to change β_C between 80 and 1. The form of $\beta_c(\alpha)$ predicted by Stewart and McCumber was verified and agreement between the predicted and measured *IV* characteristics was obtained. The effect of current noise on $\beta_c(\alpha)$ was also examined and it was found that this suppressed the hysteresis – i.e. for a given β_c, α was increased in the presence of current noise.

The capacitively shunted variable thickness Pb microbridges described by Yeh *et al*[97] are more directly analogous to the experiments on grain boundary high T_c junctions described later in this chapter. A microbridge junction typically has β_c=0 and an external capacitor is required to produce hysteresis. Yeh *et al* measured junctions shunted with multilayer capacitors with a SiO / photoresist dielectric and either a normal Au or superconducting Pb top capacitor electrode, similar to the structures shown in Fig 5.7. The *IV* characteristics were measured before and after deposition of the capacitor structure and indeed the capacitor did give rise to hysteresis. However, hysteresis only occurred with a superconducting top electrode and the hysteresis was found to be much less than expected given a low frequency measurement of the capacitance. The explanation advanced for this behaviour was that at the Josephson frequency the junction sees a distributed impedance (Fig. 5.36) rather than a lumped capacitance (Fig. 5.8). For a distributed impedance the wavelength of the Josephson oscillations inside the capacitor is smaller the length of the capacitor itself. The shunt capacitance is reduced from its low frequency value because such a structure does not necessarily produce a -90° phase shift in the alternating current. Furthermore, losses in the transmission line further reduce the shunt capacitance. Also the geometry of the capacitive shunt was such that it also contained a significant shunt inductance.

5.3.2 High T_c hysteretic junctions

Josephson junctions manufactured from the high T_c materials (in the short limit where the current density is uniform across the junction) typically have a resistance area products of 1Ω μm^{-2} and specific junction capacitances of 1 pF μm^{-2} so in general $\beta_c \approx 1$[31,37,57,59,60,63,98-100]. This capacitance results from the intrinsic capacitance of the grain boundary, as discussed in section 2.4.2. This is in contrast to the low T_c SIS junctions which have much

larger resistance area products, and hence much greater β_c.Therefore, to make a hysteretic high T_c junction an external shunt capacitor of the type used by Yeh *et al*[97] is required, rather than the resistive shunt used by Hansma *et al*[96] to control β_c.

Of the YBCO grain boundary junctions shunted with an external capacitor the most convincing report has been that of Daly[100]. Here, multilayer shunt capacitors were deposited over YBCO step edge junctions on $LaAlO_3$ substrates. Two different dielectrics were used, $LaAlO_3$, which gave rise to a hysteretic IV at 67K with β_c=1.3, and $SrTiO_3$ which gave hysteresis at 4.2K with β_c=6. Control structures with no top electrode were also fabricated, and these did not have hysteretic *IV* characteristics which confirmed that the hysteresis was caused by the capacitor. However, the top electrode used was the normal metal Ag, in contrast to the result of Yeh *et al*. Again the hysteresis obtained was much less than that predicted assuming a lumped capacitance calculated from a low frequency measurement of the dielectric constant.

Dong[37,101] has fabricated YBCO SNS ramp edge junctions with a multilayer shunt capacitance, with a $SrTiO_3$ dielectric and an Au top electrode. The junctions themselves are similar to step edge junctions but with a small layer of Au deposited between the YBCO grains, with the aim of better control over the junction resistance. These devices show hysteresis at 77K with β_c=1.1. Lee *et al*[102] have fabricated hysteretic junctions using a YBCO film on a 36.8° $SrTiO_3$ bicrystal. The same multilayer capacitor geometry was used with a $SrTiO_3$ dielectric and a gold top electrode. However, hysteresis was observed only up to 30K with a maximum β_c of 4. Thus, it is questionable whether or not it is the shunt capacitor and not the grain boundary which is dominating the effective capacitance in this case.

Hysteretic junctions have also been reported in Tl compounds using a multilayer shunt capacitor and a step edge junction[103]. β_C in excess of 1000 was measured at 77K, but with a small critical current and a very high R_n (1kΩ). β_c=10 was reported for a trilayer c-axis junction made using Bi compounds with molecular beam epitaxy (MBE)[104]. However, these devices functioned as a Josephson junction only up to 30K, and MBE is a somewhat complex junction fabrication technique. The trilayer junctions of Fink *et al*[105] had β_c>100 up to 16K, but the superconducting top electrode used ($Ba_{1-x}K_xBiO_3$) had T_c=16K.

An array of YBCO junctions on a 24° $SrTiO_3$ bicrystal with β_c=2 were reported by Tarutani *et al*[106]. In this experiment the junctions were shunted by a co-planar capacitor in an attempt to

take advantage of the high dielectric constant of the $SrTiO_3$ substrate. However, as hysteresis was not observed above 40K it is again questionable whether or not this hysteresis was due to the shunt capacitor or the intrinsic grain boundary capacitance of the junctions.

5.4 Designs of shunt capacitor investigated

5.4.1 Co-planar shunt capacitance

The 'subros' mask was designed to add a co-planar shunt capacitance to a YBCO grain boundary junction on a $SrTiO_3$ bicrystal, taking advantage of the high dielectric constant of this material at low temperatures[54]. The mask design is shown in Fig. 5.4, together with a cross sectional view of the junction and capacitor showing the coupling of the electric field lines through the substrate. Also, the devices were designed to try and resolve the discrepancy between the Tarte result[59] and that of Beck[60] as to the contribution of the $SrTiO_3$ substrate to the junction capacitance (see section 2.4.2). Specifically, could the extra capacitance introduced from the superconducting wiring on the substrate used to measure the junction be large enough to introduce hysteresis into the junction IV curve?

The theoretical capacitance per unit length *C'* of the structure is given by (5.1)[107],

$$C' = \frac{\varepsilon_0(\varepsilon_R + 1)K(k')}{2K(k)} \tag{5.1}$$

where ε_R is the relative dielectric constant of the substrate and $K(k)$ is the complete elliptic

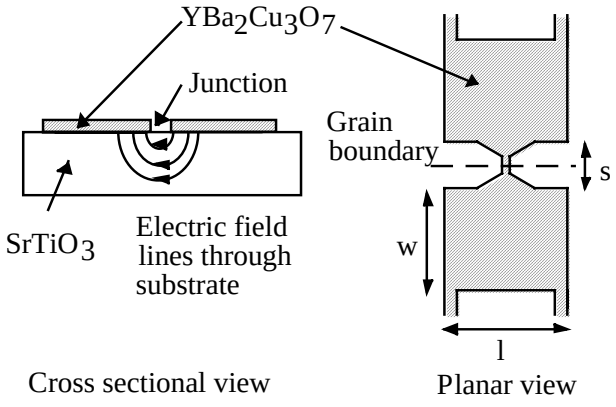

Figure 5.4 A cross sectional view showing the coupling of the electric field lines through the substrate, and the planar view of the mask design for the co-planar shunt capacitance.

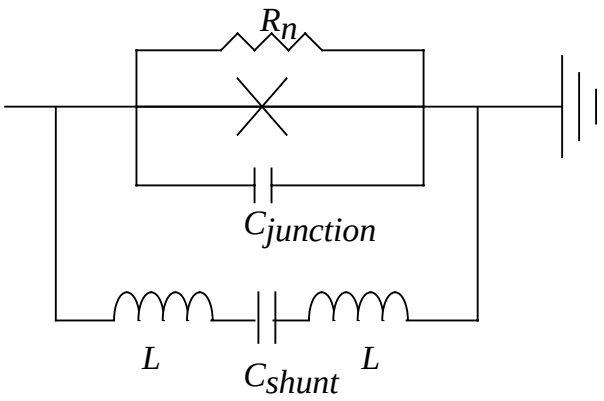

Figure 5.5 An equivalent circuit for the co-planar shunt capacitor. *L* represents the total inductance of the track, $C_{junction}$ and C_{shunt} are the intrinsic grain boundary capacitance and the external shunt capacitance respectively.

integral of the first kind with $k=s/(s+w)$ and $k'=(1-k^2)$. As shown in Fig. 5.4, *s* is the separation of the electrodes, *w* is the width of the electrodes and l is the length of the electrodes. The purpose of the 'bow tie' (the broadening of the track containing the junction towards the capacitor electrodes) as opposed to a simple rectangular track connecting the electrodes was to try and reduce the kinetic inductance of the track, which is inversely proportional to the width of the track[108] ($L_K=\mu_0 s\lambda_L^2/w_t h$, where w_t is the width of the junction and *h* is the film thickness). Hence, the bow tie maximises the width of the track and thus minimises the kinetic inductance. Lee *et al*[102] argued this inductance reduced the effective capacitance of the shunt, but did not use a bow tie structure. An equivalent circuit for a subros device is shown in Fig. 5.5, it is similar to that of Lee but without the resistance of the gold bridge connecting the two shunt capacitors.

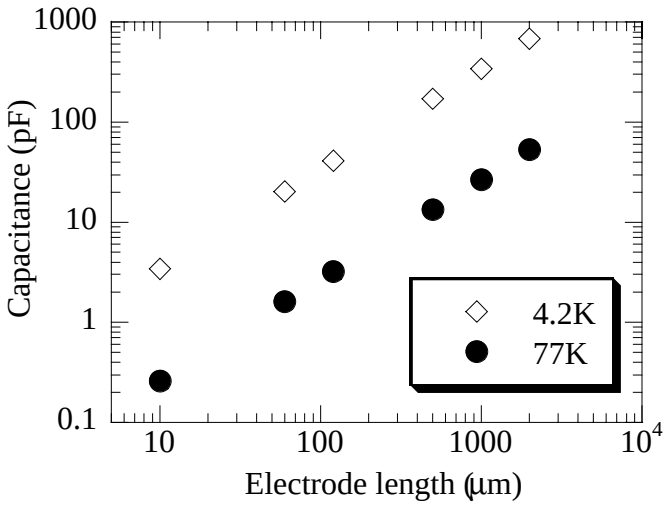

Figure 5.6 The expected shunt capacitance versus electrode length for the subros devices.

Six subros junctions were tested of width 2μm shunted by capacitor electrode lengths of 10, 60, 120, 500, 1000 and 2000μm respectively. Using low frequency measurements of the dielectric constant of bulk $SrTiO_3$ at 4.2K (ε_R=24000) and 77K (ε_R=1880)[54], Fig 5.6 shows a theoretical prediction of the shunt capacitance versus capacitor electrode length calculated using (5.1).

5.4.2 Multilayer shunt capacitance

The purpose of the 'xros' series of chips (and 3tdev) was to add a multilayer, parallel plate shunt capacitance to a YBCO grain boundary Josephson junction, in a similar manner to the shunt capacitors in refs [97,100,102]. The device design is shown in Fig. 5.7. The lengths of electrode *a* on the mask were 10, 25, 50, 75,100, 125, 150 and 175μm respectively. Junction widths of 2μm were investigated, as well as devices with and without a bow tie. A device was also patterned with no track across the grain boundary to enable the isolation resistance between the YBCO and the Au to be measured, which was found to be 0.7MΩ at 10Hz on xros24a. An equivalent circuit for an xros device is shown in Fig. 5.8.

The devices were ion milled at 45° with rotation to give rounded steps between the YBCO/$SrTiO_3$ and the substrate in order to obtain a continuous layer of gold over the entire width of the capacitor electrodes with the aim of minimising R_{bridge}. A crude prediction of the shunt capacitance (ignoring L, R_{bridge}) is given by $C=\varepsilon_0\varepsilon_R a^2/2d$ where ε_R and d are the

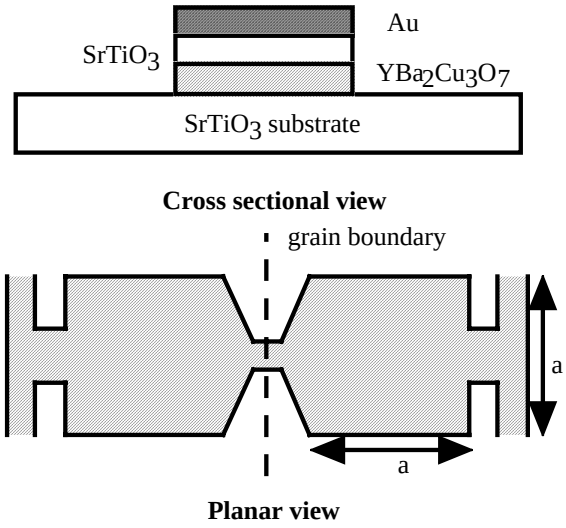

Figure 5.7 A cross sectional and planar view showing the parallel plate YBCO/$SrTiO_3$/Au capacitor structure of the xros devices.

dielectric constant and thickness of the thin $SrTiO_3$ film respectively, and a^2 is the area of one of the shunt capacitors.

5.4.3 Film thicknesses of the chips measured

Table 4.1 shows the film thicknesses of the various chips measured, which were subros, xros24a to d, xros36 and 3tdev. With the exception of xros36 where a 36.8° $SrTiO_3$ bicrystal substrate was used, all the chips were fabricated using 24° $SrTiO_3$ bicrystal substrates. In the text that follows, devices on a particular chip will be distinguished by the length of their shunt capacitor electrode.

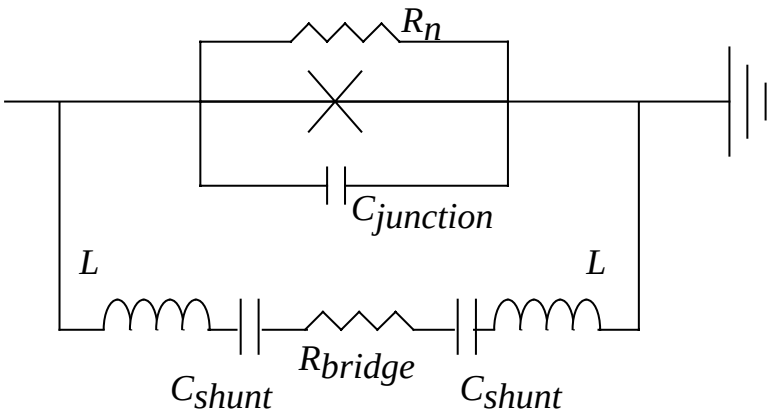

Figure 5.8 An equivalent circuit for the multilayer shunt capacitor.

5.5 Current Voltage Characteristics

5.5.1 Junctions with grain boundary capacitance dominant at all temperatures

5.5.1.1 Subros and xros24a – IV characteristics in absence of a magnetic field

Fig 5.9 shows IV characteristics for the 120μm junction on the subros chip measured at 15K and 77K. (Some measurements of subros were carried out by R. H. Hadfield[109].) It is representative of the IV curves measured for all of the devices on both subros and xros24a. At higher temperatures, noise rounding of the critical current step was observed. The normal state resistance (determined by measuring out to approximately 5xI_c and fitting an Ohmic line) was effectively temperature independent as expected for grain boundary junctions. The shape of the IV curves was in qualitative agreement with the predictions of the RCSJ model, as described in section 1.3.2.

However, no significant extra hysteresis was observed for any of the subros or xros24a devices at any temperature within the measured range from 4.2K up to the point where the critical current step was completely rounded away by noise. From the measured parameters of the device shown in Fig 5.9 (I_c=463μA, R_n=4.76Ω) and using the shunt capacitance from Fig 5.6 (41pF) the theoretical β_c was calculated to be 1320 using (1.16). For the subros junctions

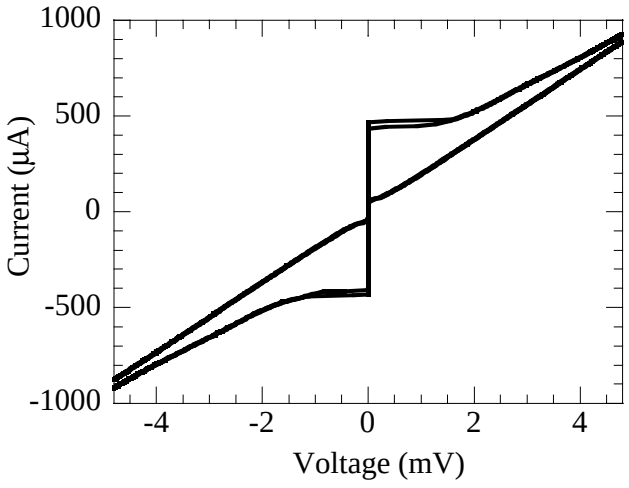

Fig 5.9 IV characteristics for the subros 120μm junction at 15K and 77K.

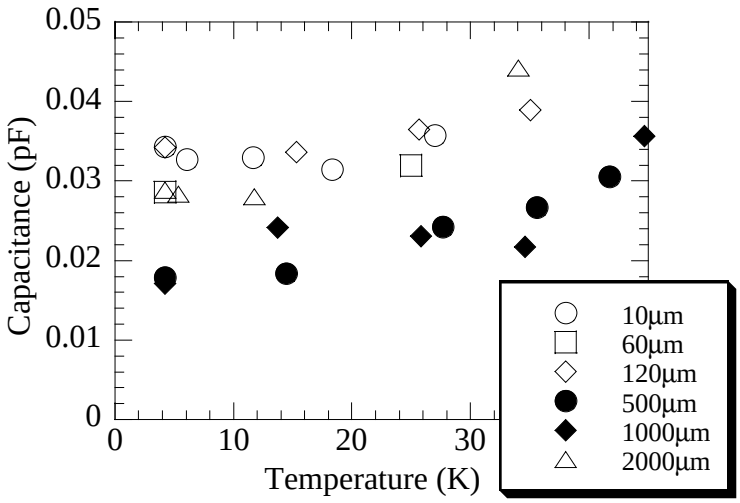

Figure 5.10 The effective shunt capacitance from the *IV* curve versus temperature for the subros junctions.

hysteresis was generally not present above 35K, and the highest temperature where β_c>1 was observed was 44K for the 1000μm device. For the xros24a junctions the situation was worse still, such that hysteresis was generally not observed above 20K and the highest temperature where β_c>1 was observed was 30K for the 175μm device.

From the hysteresis in the IV characteristic and using Zappe's approximation (1.17) the effective junction shunt capacitance could be calculated. This is plotted versus temperature for all the subros devices in Fig 5.10, and was found to be effectively independent of temperature.

The small values of shunt capacitance measured are typical of other measurements of the intrinsic capacitance of the grain boundary high T_c Josephson junctions (1 pF μm^{-2}) [31,57,59,60,63,98,99]. The capacitance also does not vary with the length of the shunt capacitor, which would be expected if the junction was coupled to the external capacitor, nor does it vary with temperature, which would be expected due to the dramatic decrease of the dielectric constant of bulk $SrTiO_3$ in this temperature range[54]. The capacitance of the grain boundary in a high T_c Josephson junction was found to be independent of temperature by Jansman *et al*[52]. Fig 5.11 shows the effective shunt capacitance plotted versus capacitor electrode width for the xros24a devices. Again the effective shunt capacitance is independent of the capacitor electrode width. Thus, the small values of β_c observed are believed to be solely due to the intrinsic capacitance of the grain boundary.

5.5.1.2 Fiske resonances in subros – further evidence for absence of coupling to external capacitor

The behaviour of all the devices in a magnetic field was investigated, and all showed a Fraunhofer type magnetic diffraction pattern of the junction critical current in good qualitative agreement with (1.26). Fig 5.12 shows the response of the 120μm device on subros.

When a magnetic field was applied to the junctions over a range between the first maximum and minimum in the Fraunhofer pattern, a resonance was observed in the *IV* characteristic at a particular voltage varying from 1.2mV for the 10μm device to 1.9mV for the 500μm device at 4.2K. The step appeared over a range of from 4.2K to 55K for the 10 and 120μm junctions and from 4.2K up to 45K for other junctions. Its position was found to be independent of temperature to within experimental errors. A series of *IV* curves at various magnetic fields, with V/R_n subtracted to emphasize the resonance, for the 10μm device at 15K are shown in Fig 5.13.

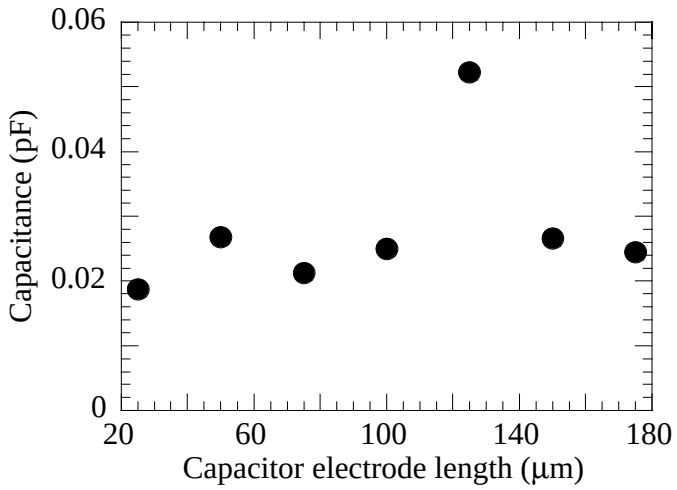

Figure 5.11. The effective shunt capacitance versus capacitor electrode length at 4.2K for the xros24a devices.

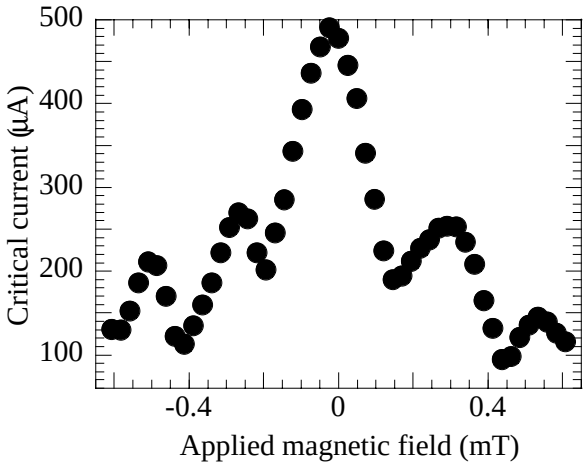

Figure 5.12. Critical current versus applied field for the 120μm junction at 15K.

The step is a Fiske resonance as opposed to a transmission line resonance or a flux flow resonance. It does not change position when the applied magnetic field is varied so it cannot be a flux flow resonance. The resonance only appears when a field is applied so it is unlikely to be a transmission line resonance which are present even in the absence of magnetic field[110]. Also, a transmission line resonance would propagate in the slit between the capacitor electrodes. Thus, its position would be expected to scale with capacitor electrode length which these resonances do not. Finally, based on a calculation using the dielectric constant of bulk $SrTiO_3$[54], (1.42) and (5.1) the transmission line resonance would be expected to be at a much lower voltage (<0.3mV) for all the devices in the temperature range over which the resonance appeared.

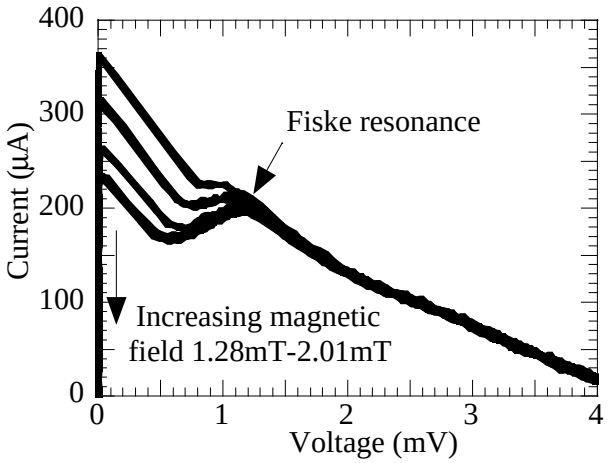

Figure 5.13. IV's at various magnetic fields for the 10μm device at 15K. The quasiparticle current V/R_n has been subtracted to emphasize the Fiske resonance

The capacitance per unit area calculated from the resonance position using (1.42) was found to agree with that determined from the hysteresis in the IV characteristic, assuming that the effective shunt capacitance is dominated by that from the grain boundary. The correlation is shown in Fig 5.13, and was obtained using the London penetration depth as a parameter equal to 220nm at 4.2K in (1.44). The approximation $\lambda_{eff} \sim \lambda_L^2/h$ was used for the limit where $\lambda_L >> h$. Although this limit was not strictly satisfied, it has been shown to be valid previously when extracting grain boundary capacitances from Fiske resonance data[59]. This value of the penetration depth lies midway between inductive measurements of the YBCO penetration depth of 140nm[22], and microwave resonator measurements giving 450nm[111] at 4.2K. The agreement between the two methods of calculating junction capacitance shows that there was no contribution to the shunt capacitance from the external capacitor. This would have resulted in a systematic difference between the results of the hysteresis and Fiske resonance methods of calculation. The agreement also indicates that heating effects were not responsible for the observed hysteresis.

In Fig. 5.14, the capacitance is plotted against the junction resistance and indeed is seen to scale with the junction resistance. This scaling is an intrinsic property of high T_c grain boundary Josephson junctions[98,99] and will be discussed further in Chapter 8.

5.5.1.3 xros36

The first attempt to improve the coupling of the junction to the external capacitor was made by increasing the misorientation angle of the bicrystal used from 24° to 36.8°. The possible

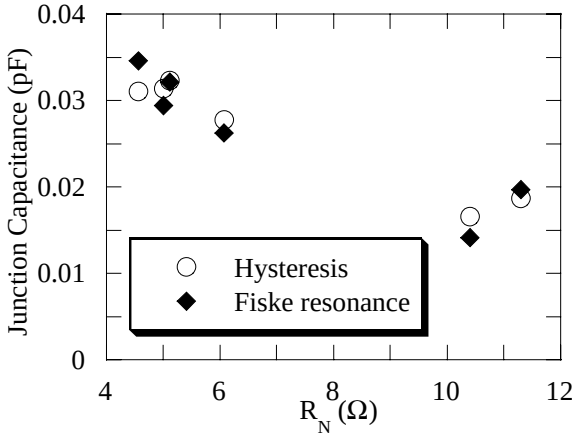

Figure 5.14 The correlation and scaling of junction capacitance with resistance for the subros devices.

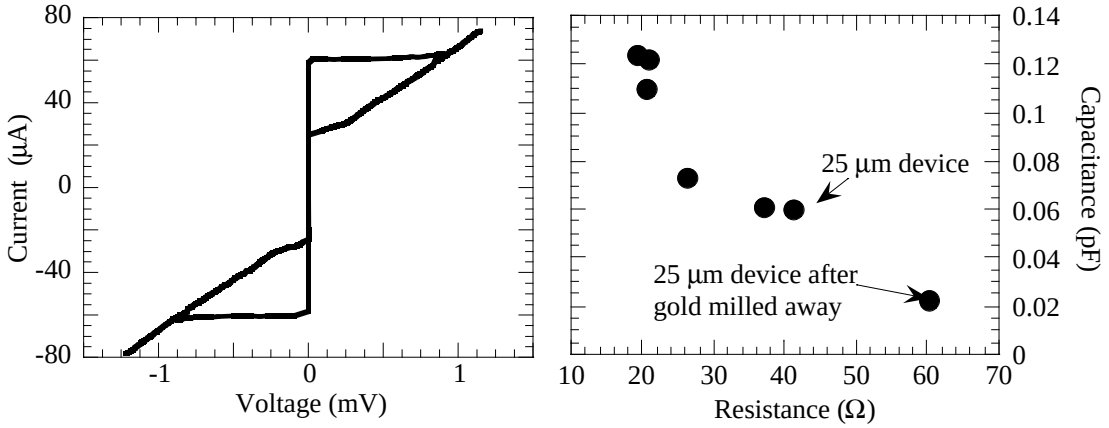

Figure 5.15. The *IV* curve of the 50μm device on xros36 (β_c=9.6, I_c=60μA, R_n=20.3Ω) and the scaling of capacitance with resistance for the xros36 devices.

benefit of this change was that the effect of the decrease in I_c (see section 2.4.1) on β_c should be more than compensated for by the increase in R_n, see (1.16).

The devices displayed significant hysteresis at 4.2K. The 50μm device had β_c=9.6, with I_c=60μA and R_n=20.3Ω, see Fig. 5.15. The junction critical currents were approximately a factor of 10 smaller than those of xros24a and subros and were not measurable above 45K despite a film T_c equal to 87.5K. The hysteresis persisted only up to 30K.

Neither β_c nor the effective capacitance from the hysteresis in the *IV* curve scaled with the length of the capacitor electrode. Also, the effective junction capacitance was again found to scale with junction resistance, see Fig. 5.15. Shown in Fig 5.15 is the capacitance of the 25μm device after removal of the Au top electrode, which continued to scale with the junction resistance. The increase in resistance is probably due to de-oxygenation of the grain boundary during the ion milling to remove this electrode. These two observations both indicate that the intrinsic grain boundary capacitance was again dominating the total shunt capacitance.

Plots of β_c calculated from the hysteresis in the IV curve using Zappe's approximation (1.17) versus I_c were obtained for the 25μm device (before Au electrode removal) by varying I_c with an applied magnetic field over a range of temperatures (see Fig 5.16). The relationship was found to be linear, and the gradient of the lines, which gives the effective capacitance, (see (1.16)) did not vary with temperature. (Within experimental error – each point in Fig 5.16 was taken from an average of 10 measured IV's. However, the small critical currents of the

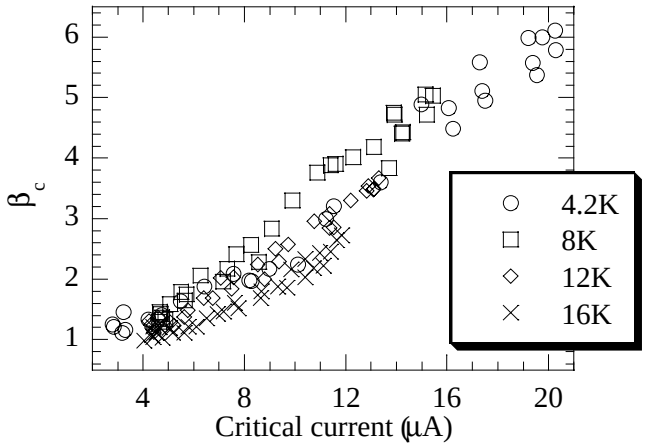

Figure 5.16 The variation of β_c with critical current at various temperatures for the 25μm device.

junctions made the measurement extremely sensitive to external sources of rf noise, which causes the scatter seen in Fig 5.16.)

5.5.2 Junctions with the external (multilayer) shunt capacitor dominant

5.5.2.1 Hysteresis at low temperatures

Figure 5.17 shows the *IV* characteristics at 4.2K of the 25μm device on 3tdev before and after the Au deposition of the top capacitor electrode. Two changes can be seen, firstly, the increase in hysteresis and secondly the appearance of a resonance. The resonance is believed to be a transmission line resonance since it was not present in the 'control' *IV* curve and was also present in the absence of an applied magnetic field, so it cannot be a Fiske resonance. Table 5.1 gives the parameters of this device. The slight increase in junction resistance and decrease in critical current can be attributed to heating of the sample, causing de-oxygenation of the grain boundary during patterning and Au sputtering.

Table 5.1. 3tdev 25μm device parameters at 4.2K before and after Au deposition.

*3tdev 25*μm device 4.2K	I_c (μA)	R_n (Ω)	β_c	C (pF)
Before Au deposition	163	11.0	1.35	0.022
After Au deposition	124	11.4	5.77	0.117

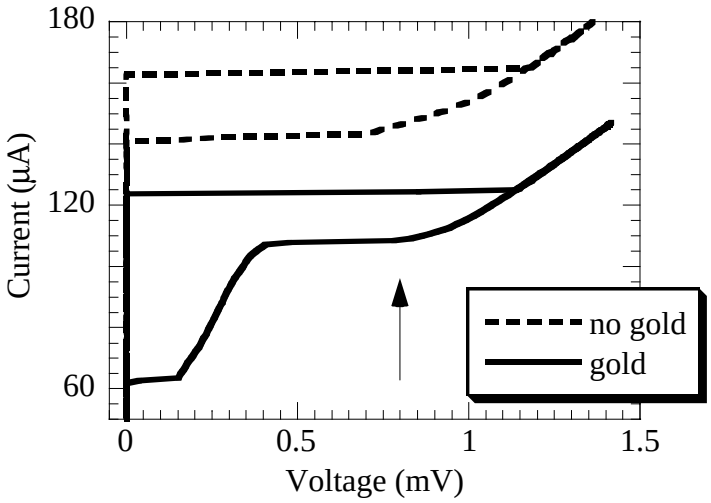

Figure 5.17. The IV characteristic of the 25μm device on 3tdev at 4.2K before and after Au deposition. The resonance is indicated by an arrow.

The increase in β_c and effective junction capacitance calculated from it shows that for this device the external shunt capacitor dominates the effective junction capacitance. However, the hysteresis observed is still much less than expected if the shunt capacitor is considered as a lumped circuit element. The dielectric constant of the 200nm $SrTiO_3$ film was calculated from the position of the resonance and was found to be 120 for this device, (see Chapter 7) giving a shunt capacitance of 1.66pF and β_c=81 using (1.16) and the measured I_c and R_n of the junction (Table 5.1).

In fact, the presence of the transmission line resonances indicates a possible explanation for this behaviour. For the resonances to be present, the wavelength of the Josephson oscillations in the external capacitor must be comparable to the length of the capacitor itself. So, it is not valid to treat the shunt capacitor as a lumped circuit element as in Figs 5.5 and 5.8, but instead it should be modelled as a distributed impedance, which reduces the effective capacitance of the external shunt. This was verified explicitly by repetition of the experiment that gave rise to Fig 5.16 and a plot of β_c versus the junction critical current was obtained for the 25μm device on 3tdev at 4.2K. Improvements in the measurement computer, software and electronics (see Chapter 4) meant that hundreds of critical currents and return currents could be measured rapidly, so each point in Fig. 5.18(b) corresponds to a distribution of critical currents and return currents such as that in Fig 5.18(a).

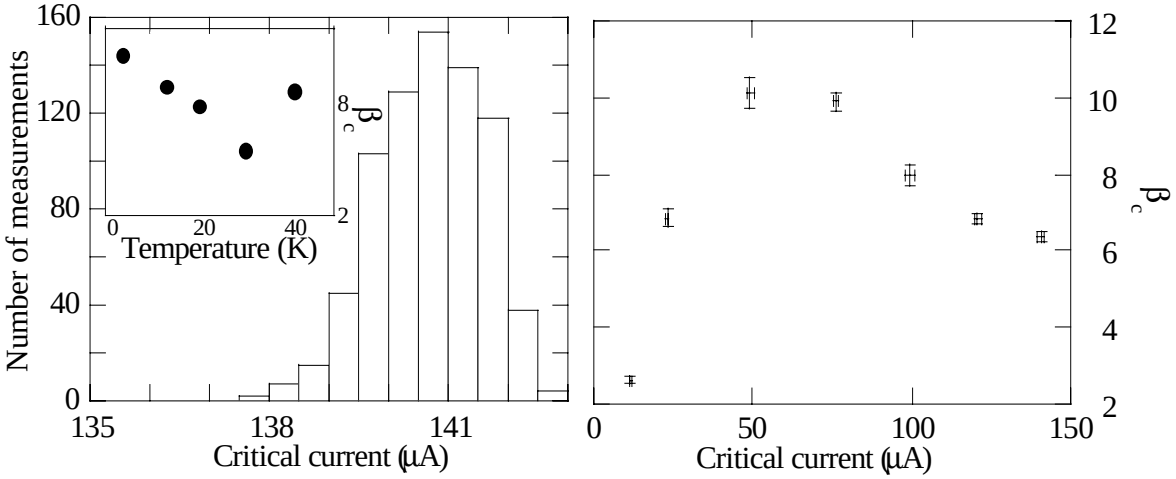

(a) **(b)**

Figure 5.18(a) The distribution of critical currents measured at 4.2K for the 25μm device on 3tdev. (b) The variation of β_c with I_c at 4.2K. The inset in (a) shows the variation of the maximum β_c with temperature. (These measurements were made after improvements had been made to the filtering of the probe heater power supply, so the critical current is slightly bigger than that in Fig. 5.17.)

By lowering the junction I_cR_n product the frequency at which the junction returns to the zero voltage state is reduced. Hence, the wavelength of the Josephson oscillations in the external shunt capacitor increases and the limit of a lumped shunt capacitance is approached, increasing the effective shunt capacitance. In contrast to Fig. 5.16, the non-linear relationship between I_c and β_c shown in Fig. 5.18 indicates that the effective shunt capacitance of the junction is varying with frequency.

However, as I_c is reduced towards zero, thermal noise suppression of the hysteresis dominates and β_c is once again reduced.

Figs 5.19 and 5.20 give further evidence that the dominant contribution to the effective capacitance is the external shunt capacitor. Fig 5.19, a graph of the effective capacitance versus shunt capacitor electrode length, shows that the junction capacitance has increased after the deposition of the gold top electrode. There is now a trend in the variation of effective capacitance with capacitor electrode length, but it is not what would be expected if the shunt capacitor were behaving as a lumped circuit element.

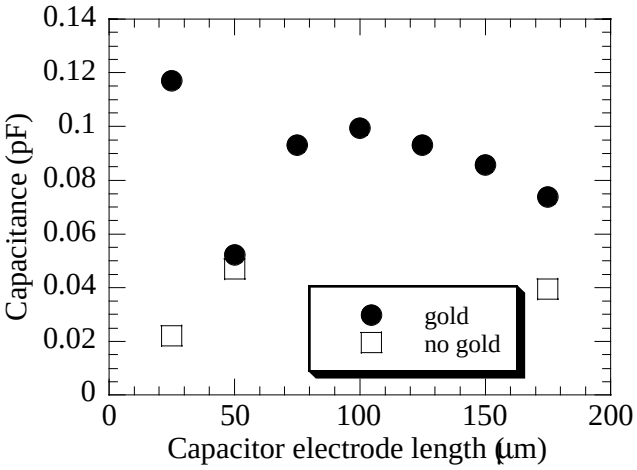

Figure 5.19. The variation of capacitance with capacitor electrode length before and after gold deposition for the 3tdev devices at 4.2K.

Fig 5.20 shows effective capacitance versus resistance for the 3tdev devices before and after deposition of the top capacitor electrode. For the junctions without a shunt capacitor, the same trend in effective capacitance versus resistance that was observed for the junctions where the grain boundary was the dominant contribution to the shunt capacitance is observed here also (see Figs. 5.14 and 5.15). However, for the junctions with an external shunt capacitor the effective capacitance increases with the resistance, i.e. in the opposite direction to that of the grain boundary trend.

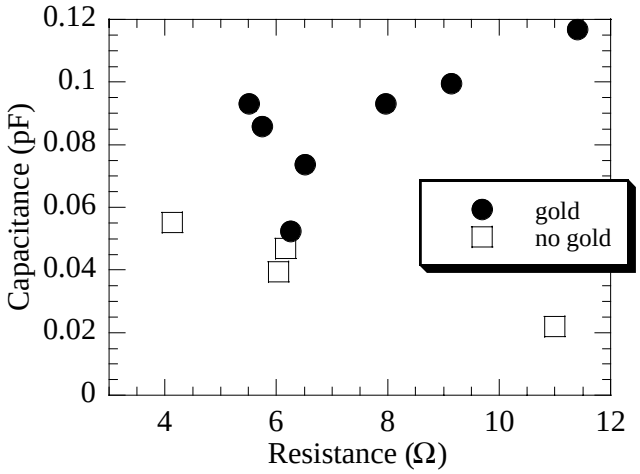

Figure 5.20. The scaling of capacitance with resistance before and after gold deposition for the 3tdev devices at 4.2K.

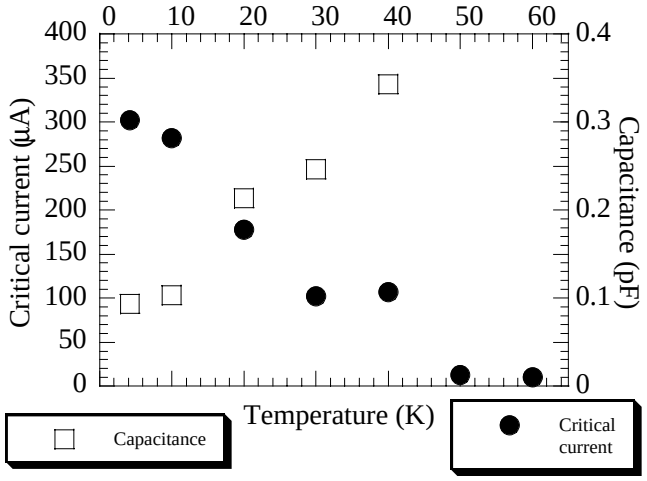

Figure 5.21. The variation of critical current and capacitance with temperature for the 75μm device on 3tdev.

In contrast to the junctions where the grain boundary capacitance was the dominant contribution to the effective capacitance, for these devices where the external shunt capacitor is dominant, the capacitance increases with temperature (see Fig 5.21).

The major drawback of the 3tdev devices was their low critical current. This is illustrated in Fig. 5.21, which shows critical current and capacitance versus temperature for the 75μm device, typical of the behaviour of all the devices on this chip. The most hysteretic junction at the highest temperature was the 25μm device, which had β_c=4.5, I_c=42.4±0.8μA, R_n=9.72Ω, C=0.37pF and α=0.55 at 41.5K. There was no hysteresis above 50K and the junctions had no measurable critical current above 60K, so the criterion of hysteresis above 50K for ROS operation was not fulfilled.

5.5.2.2 Hysteresis at high temperatures

Figure 5.22 shows the *IV* characteristics at 4.2K of the 50μm device on xros24d before and after Au deposition of the top capacitor electrode. Again, there are two changes, firstly the increase in hysteresis and secondly the appearance of resonances. The resonances are

Table 5.2 xros24d 50μm device parameters at 4.2K before and after Au deposition.

Xros24d 50μm device	I_c *(μA)*	R_n *(Ω)*	*C (pF)*
Before Au	2712	0.582	0.358
After Au deposition	2328	0.715	0.308

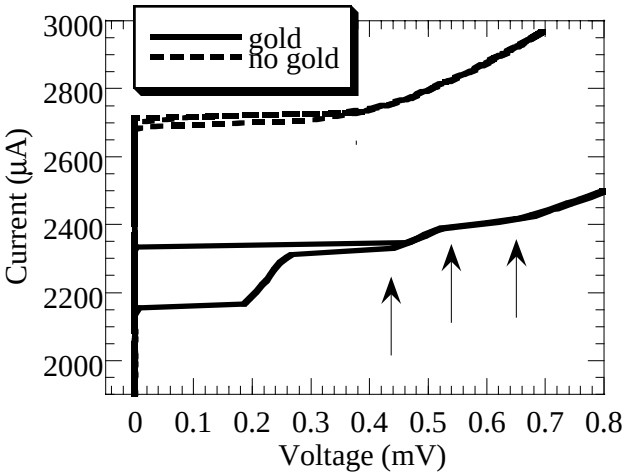

Figure 5.22 The IV characteristic of the xros24d 50μm device at 4.2K before and after Au deposition. Resonances are indicated by arrows.

transmission line resonances since they were not present in the 'control' *IV* curve and are present in the absence of a magnetic field. However, upon use of Zappe's approximation (1.17) and (1.16) to calculate the effective shunt capacitance, it was found that the capacitance had decreased on deposition of the top electrode (see Table 5.2).

Therefore, at 4.2K the grain boundary capacitance dominates the effective junction capacitance. However, for xros24b, c and d the hysteresis ($1<\beta_c<1.6$) was found to persist up to at least 55K for all the devices. For certain devices the temperature up to which hysteresis persisted was considerably higher, e.g. 72.3K for the xros24d 150μm device, the *IV* characteristic of which is shown in Fig 5.23.

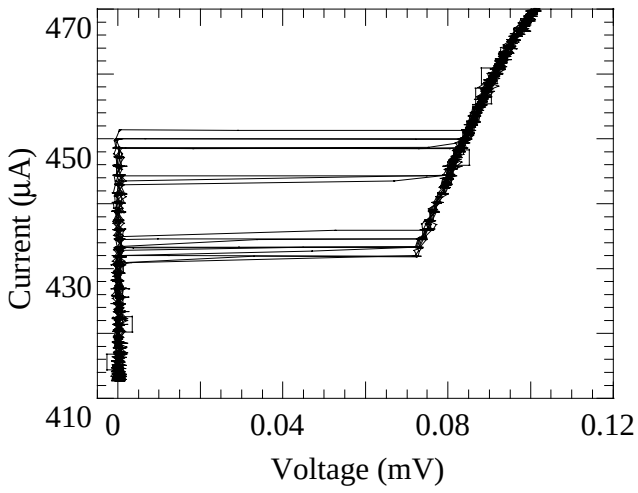

Figure 5.23 The IV characteristic of the xros24d 150μm device at 72.3K.

The distribution of critical currents and return currents shown in Fig. 5.23 is due to thermal and electromagnetic interference. The effective shunt capacitance of the xros24d 150μm capacitor at 72.3K was found to be 2.28pF, see Table 5.3. At 20K, the capacitance of the 150μm device was 0.48pF, and below 20K the 150μm device was not hysteretic. This temperature variation of the capacitance strongly indicates that the shunt capacitor was dominating the total capacitance at high temperatures. The 50μm device had a similar capacitance of 1.39pF at 68K. This represents a large increase over the grain boundary dominated capacitance of 0.308pF at 4.2K, and since the grain boundary capacitance is independent of temperature (see Fig. 5.10 and Jansman *et al*[52]) the increase is believed to be due to the external shunt capacitor. Fig 5.24 confirms this, showing a plot of capacitance versus resistance for the xros24d devices at 4.2K before Au deposition together with the 150μm device at 72.3K, which does not fit onto the trend.

So, at some temperature between 4.2K and 72.3K the dominant contribution to the capacitance changes from the grain boundary to the external shunt capacitor. This is particularly true in the case of the 150μm device which was not hysteretic below 20K.

Fig 5.25 shows a plot of capacitance versus capacitor electrode length for the xros24d devices at 21K and 61K (respectively the lowest and highest temperatures at which all the junctions had β_c>1). At 21K, the capacitance remains effectively constant for all sizes of capacitor, but

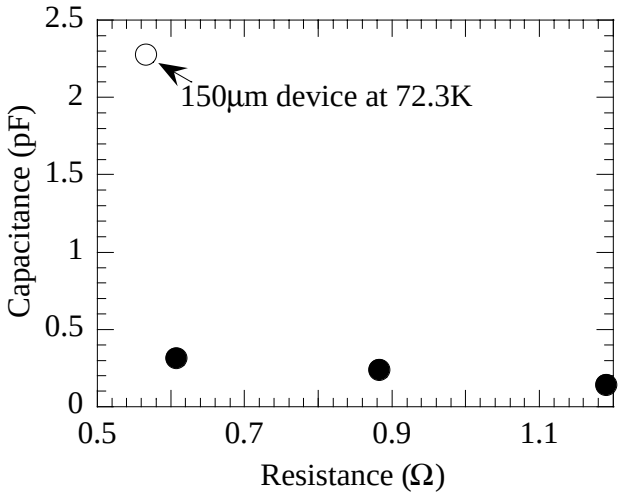

Figure 5.24. Capacitance versus resistance at 4.2K for hysteretic xros24d devices pre-Au deposition, together with the 150μm device with Au at 72.3K.

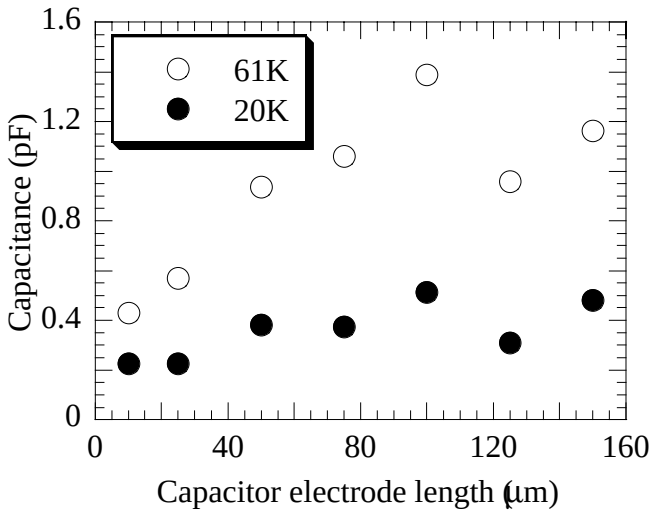

Figure 5.25. The variation of capacitance with capacitor electrode length for the xros24d devices at 20K and 61K.

at 61K there is some scaling of the capacitance with capacitor electrode size. The explanation for the saturation of the maximum value of the shunt capacitance is probably that the junction sees the larger capacitors as a distributed impedance. Given that the critical current and resistance of these devices were approximately equal, it would be expected that the wavelength of the Josephson oscillations inside the capacitor should also be equal. So, it is not beneficial to increase the size of the shunt capacitor beyond a certain limit at a given temperature.

To further demonstrate that the external shunt capacitance is dominating the effective capacitance of these junctions, Fig 5.26 shows a plot of capacitance versus temperature for the xros24d junctions. The capacitance increases with temperature, which is the behaviour observed for the 3tdev junctions where the external shunt capacitor dominated, as opposed to if the effective capacitance had been dominated by the grain boundary, in which case the capacitance would remain constant with increasing temperature. (see Fig 5.10, and Jansman *et al*[52]) The increase in capacitance with temperature shown in Fig. 5.26. is too large to be explained by errors introduced by Zappe's approximation (see Fig. 1.6).

The junctions on chips xros24b and c showed similar behaviour to that described above, and illustrated in Figs 5.22 to 5.26, although the maximum temperature at which hysteresis was observed was lower – 65K for the xros24b devices and 58K for the xros24c devices. The parameters of all the hysteretic junctions investigated are given in Table 5.3 below, as measured at the highest temperature for which β_c>1.

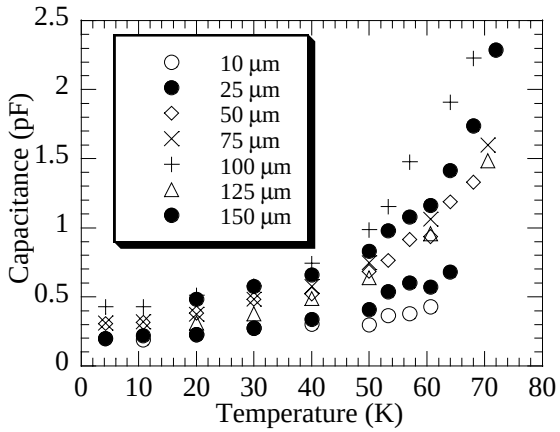

Figure 5.26. Capacitance versus temperature for the xros24d devices.

Table 5.3. A summary of the parameters of junctions on chips which had devices hysteretic at *T*>50K.

Chip	*Capacitor electrode length*	*T(K)*	I_c *(μA)*	R_n *(Ω)*	β_c	*C (pF)*
Xros24b	10	51	220	4.5	1.01	0.073
	50	65	210	3.6	1.18	0.140
	75	55	300	3.1	1.13	0.130
	100	42	100	9.8	1.12	0.038
Xros24c	10	51	310	1.8	1.21	0.40
	25	54	316	1.4	1.16	0.60
	50	53	220	1.1	1.01	1.17
	75	58	245	1.2	1.05	0.96
Xros24d	10	53	582	1.27	1.04	0.36
	25	61	279	1.46	1.03	0.56
	50	64	683	0.66	1.07	1.18
	75	71	447	0.68	1.03	1.60
	100	68	380	0.64	1.07	2.22
	125	71	341	0.81	1.01	1.48
	150	72	451	0.56	1.01	2.28

5.5.2.3 The effect of the bow tie.

On xros24c, junctions were patterned with and without bow-ties connecting them to the external capacitors. The effect of such a bow-tie on the McCumber parameter of the 10μm device is shown in Fig. 5.27. It can be seen that the bow tie both increases the effective shunt capacitance and increases the temperature up to which hysteresis persists. The I_cR_n product of these two junctions was equal at all the temperatures shown in the figure, so the increase in β_c must be attributed to the presence of the bow tie. The effect of the bow-tie can be interpreted in two ways, either as a reduction of the kinetic inductance of the track connecting the capacitor to the junction, or as an improvement of the impedance matching of the track containing the junction to the capacitor itself. When the bow-tie is absent there is a discontinuity in the inductance and capacitance per unit length of the structure when the track containing the junctions widens to the width of the capacitor electrode.

This confirms that one of the explanations in the literature[102], that the kinetic inductance of the track connecting the junction to the capacitor is a factor in determining the small β_c values that are observed.

5.6 Principle factors involved in the reduction of hysteresis

In order to gain a more thorough understanding of the results presented above, there are two questions which must be addressed. Firstly, why is there coupling of the junction to the shunt capacitor on some chips and not others, and secondly, for the chips where coupling to the

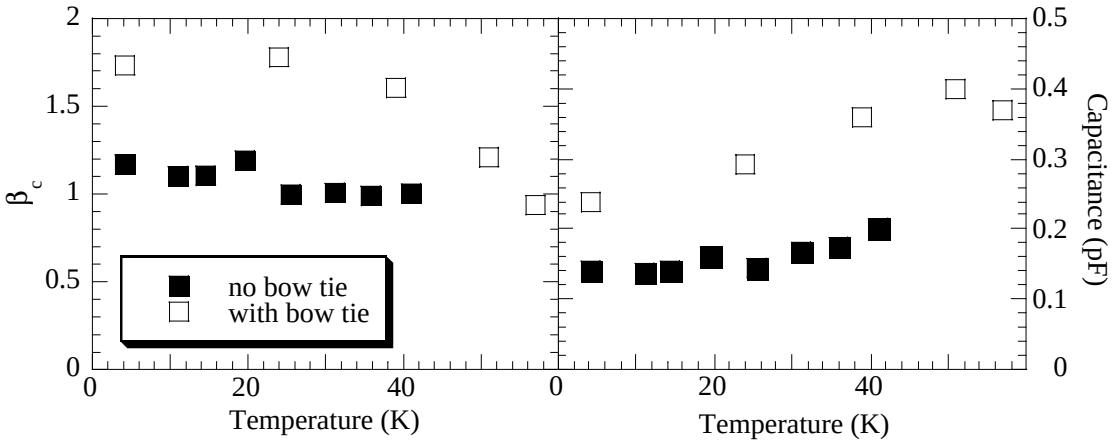

Figure 5.27. McCumber parameter and capacitance versus temperature for the xros24c 10μm device with and without a bow tie.

shunt capacitor is observed, why is the hysteresis so much less than what is expected from a simple calculation of the lumped capacitance?

5.6.1 The shunt capacitor as a distributed impedance, and impedance matching of the junction to the capacitor

The non-linear relation between β_c and I_c obtained at a given temperature for the 25μm device on 3tdev (see Fig 5.18(b)) strongly suggested that the external capacitor was behaving as a distributed impedance rather than the lumped capacitance required by the RCSJ model. Also, both Yeh *et al*[97] and Daly *et al*[100] have mentioned this as a possible reason why they did not observe as high β_c values as those they calculated based on the area of their capacitors. A modified equivalent circuit for all the devices is given in Fig 5.28. $Z(\omega)$ represents the complex impedance at angular frequency ω of an open ended transmission line formed by the propagation of Josephson oscillations in the cavity between the two capacitor electrodes. The impedance of such an open ended transmission line in the case where there are no losses, is given by[14],

$$Z = -jZ_0 \cot\left(\frac{2\pi a}{\lambda}\right) \tag{5.2}$$

where Z_0 is the characteristic impedance of the line, λ is the wavelength and a is the length of the resonator in the xros geometry (l for the subros geometry – see Figs. 5.7 and 5.4 respectively).

In the limit where $\lambda >> a$ the line behaves as a capacitive impedance as $Z \rightarrow -jZ_0\lambda/2\pi a$. So, the condition which must be fulfilled for the line to behave as a capacitor is $\lambda >> a$. The speed of

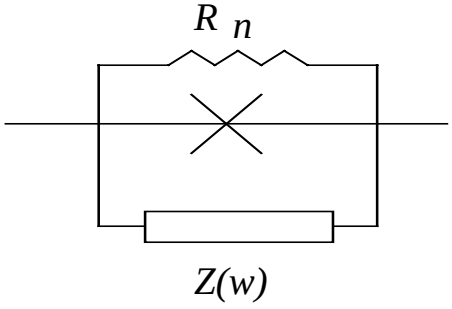

Fig 5.28. An alternative equivalent circuit for a Josephson junction shunted by an external capacitor.

propagation of electromagnetic waves in the cavity is given by $c=(L'C')^{1/2}$ where L' and C' are the inductance and capacitance per unit length of the transmission line respectively. By substituting this relation into $c=f\lambda$ (f is the frequency), and then using the ac Josephson relation (1.9), the wavelength of the Josephson oscillation propagating in the transmission line can be derived.

$$\lambda = \Phi_0 / V\sqrt{L'C'} \tag{5.3}$$

The voltage V at which the hysteretic IV curve of a Josephson junction switches from the critical current branch to the return current branch is given approximately by the I_cR_n product of the junction. Therefore, this is the voltage which should be used in (5.3).

Fig 5.29 gives a plot of the wavelength of the Josephson oscillation in the external capacitor versus temperature for the 10μm device on subros. The capacitance per unit length was determined from (5.1), using data for the variation of the dielectric constant of bulk $SrTiO_3$ with temperature from Neville *et al*[54]. The inductance per unit length was calculated from the formula derived by Enpuku *et al*[112] for a co-planar superconducting transmission line, with $\lambda_L(4.2)$=220nm (the parameter used to fit the capacitance determined from the hysteresis in the IV curves with that from the Fiske resonances) and using the two fluid model for the temperature dependence of the penetration depth (1.52). Up to 40K it can be seen that the length of the junction (2μm) is larger than the wavelength of the Josephson oscillations. The condition that the wavelength of the Josephson oscillations be much larger than the length of

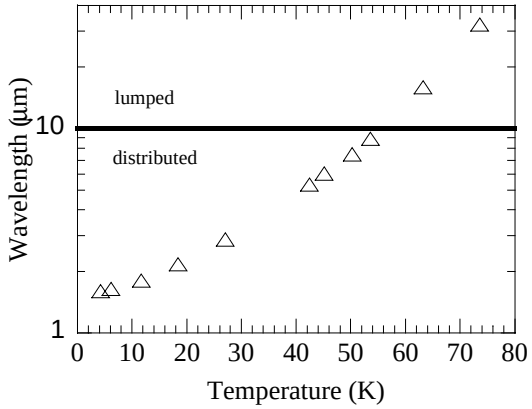

Figure 5.29. The wavelength of the Josephson oscillations in the external capacitor versus temperature for the 10μm device on subros. The solid line shows the length of the shunt capacitor electrode.

the capacitor is not fulfilled over any temperature range, although above 55K the wavelength is slightly larger than the electrode length, but even in this region no hysteresis due to the external shunt capacitor was observed. Similar curves were calculated for the other devices on subros.

For the junctions shunted with a multilayer capacitor, (5.4) and (5.5) were used to calculate the inductance and capacitance per unit length of the transmission line[113]. The expression (5.5) for the capacitance per unit length is that for a parallel plate capacitor. The inductance per unit length formula is also that for parallel plates. The magnetic field penetrates up to the skin depth in the gold and up to the penetration depth in the superconductor. The penetration depth is corrected as it is comparable to the film thickness. The correction is different to that for Fiske resonances (see section 1.4.2.1) as the resonator geometry and hence the magnetic field distribution is different.

$$L' = \frac{\mu_0}{a}\left(d + \delta_s + \lambda_L \coth\left(\frac{\lambda_L}{h}\right)\right) \tag{5.4}$$

$$C' = \frac{\varepsilon_0 \varepsilon_R a}{d} \tag{5.5}$$

In (5.4) and (5.5), d is the thickness of the dielectric, h is the thickness of the YBCO film, δ_s is the skin depth of the Au given by (1.48) and $\sigma(4.2K) = 4.2x10^7\ \Omega^{-1}m^{-1}$ is the conductivity of the Au, and λ_L is the London penetration depth of bulk YBCO. Once again the two fluid model was used for the temperature dependence of the penetration depth, but this time with λ_L=140nm[22] as Fiske resonances could not be distinguished from higher order tranmission line resonances for the junctions shunted with a multilayer shunt capacitor, so the fitting method used to determine λ_L for the subros film could not be repeated.

Fig. 5.30 shows a plot of the wavelength of the Josephson oscillations versus temperature for the 25μm device on 3tdev, where the external capacitor was found to be coupled to the junction, and for the 25μm device on xros24a, where the grain boundary was found to dominate the effective capacitance of the junction as calculated from the *IV* curve. As expected, the wavelength in the 3tdev device is larger than that in the xros24a device, explaining why coupling to the shunt capacitor was observed for the 3tdev device and not the xros24a device.

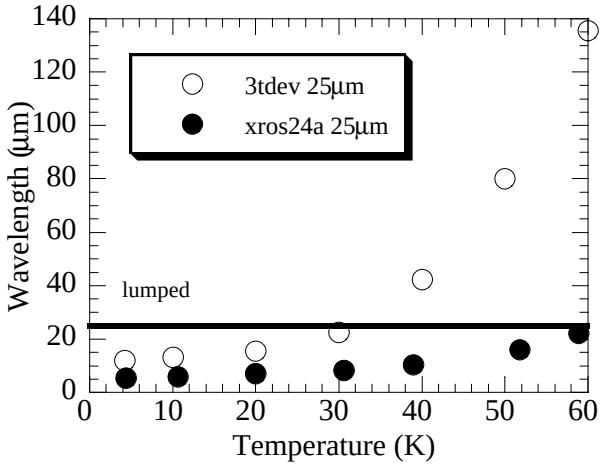

Figure 5.30. The wavelength of the Josephson oscillations in the external capacitor versus temperature for the 25μm device on 3tdev and xros24a. The solid line shows the length of the shunt capacitor electrode.

Fig 5.30 qualitatively explains the characteristic increase in capacitance calculated from the hysteresis in the *IV* curve with temperature observed for junctions that were coupled to the external capacitor (see Figs 5.21 and 5.26). As temperature increases, so the I_cR_n product decreases and λ increases. So, as the temperature rises the limit of $\lambda >> a$ is approached and the load impedance (5.2) becomes more capacitive.

The decrease in capacitance with capacitor size for the 3tdev devices at 4.2K shown in Fig 5.19 can also be qualitatively explained. The I_cR_n product of the 3tdev junctions was approximately equal at 4.2K, so the wavelength was also approximately equal (The *L'C'* product is independent of capacitor electrode length a.). Therefore, as capacitor electrode length increases $\lambda << a$ and the load impedance (5.2) becomes more inductive. However, as temperature increases the wavelength increases and so at T>65K it was junctions on xros24b, c, and d which had $a \geq 50\mu$m which were hysteretic.

It should be noted that (5.3) is an estimate of the wavelength at a particular frequency. It is clear from (5.2) and (5.3) that when $\lambda \approx a$ the effective capacitance varies with frequency, but the wavelength was determined only at the frequency equal to I_cR_n/Φ_0 for each junction, rather than the voltage at which the junction switches back to the zero voltage state.

But, Fig 5.30 raises a further issue. At high temperatures, the limit of $\lambda >> a$ is satisfied best, but no hysteresis was observed above 41K for the 25μm junction on 3tdev. The discrepancy is

illustrated again in Fig 5.31, showing the wavelength of the Josephson oscillations in the external capacitor versus temperature for the 50μm device on xros24a and b. Although the xros24b device coupled to the external capacitor, the wavelength is slightly larger in the xros24a device which did not couple to the external capacitor. There must be another mechanism controlling coupling to the external capacitor for these devices.

5.6.2 Thermal noise suppression of β_C

The second mechanism responsible for suppression of hysteresis, especially at high temperatures, is thermal noise suppression of both the junction critical current and the return current. White noise currents in the resistor cause premature excitations of the junction into the voltage state[114], and premature return to the zero voltage state from the return branch of the IV characteristic. Recently, Castellano *et al*[115] have carried out a detailed investigation of the return current distribution for Nb/AlO_x/Nb tunnel junctions, and similar return current distributions were observed for the junctions described here (see Fig. 5.18(a)). When k_BT becomes comparable to the maximum Josephson coupling energy $\Phi_0 I_c/2\pi$ the critical current step in the IV curve can be rounded off completely. The noise parameter Γ is defined as (see also section 1.3.2.3), and quantifies the effect of thermal noise. It is the ratio of the thermal

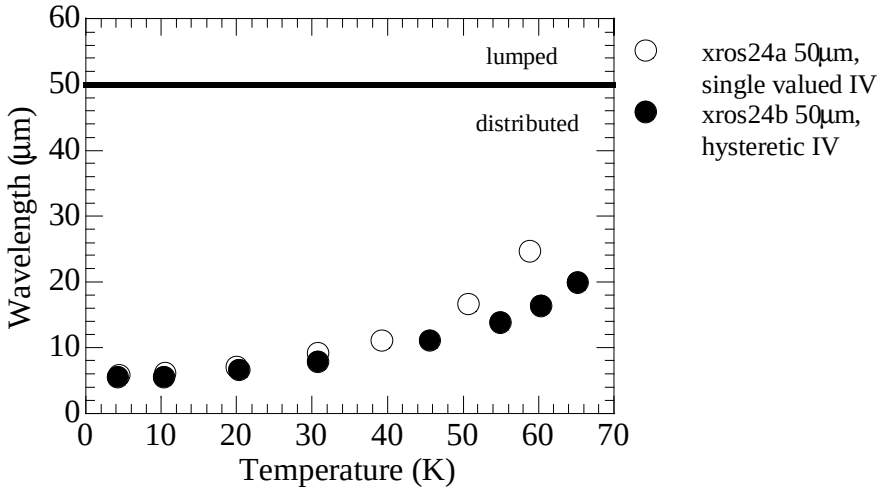

Figure 5.31. The wavelength of the Josephson oscillations in the external capacitor versus temperature for the 50μm device on xros24a and b. The solid line shows the length of the shunt capacitor electrode.

$$\Gamma = \frac{2\pi k_B T}{\Phi_0 I_c} \tag{5.6}$$

energy to the Josephson coupling energy, and the larger the Γ the greater the influence of thermal noise. The noise parameter is plotted versus temperature in Fig. 5.32 for the junctions which were most hysteretic at the highest temperature on each chip. It can be seen that the xros24a 50μm junction had a larger Γ than the xros24b 50μm junction so thermal noise, rather than the small wavelength of the Josephson oscillation in the xros24a junction was the primary cause of the absence of coupling to the external capacitor.

Fig. 5.33 shows noise parameter versus temperature for the xros24a and 3tdev 25μm devices, for which the wavelength of the Josephson oscillation was given in Fig. 5.30. In this case, the 3tdev device had a larger Γ but was hysteretic. However, the wavelength of the Josephson oscillations in the external capacitor was larger, so for these junctions this was the limiting factor in determining the presence or absence of coupling to the external capacitor.

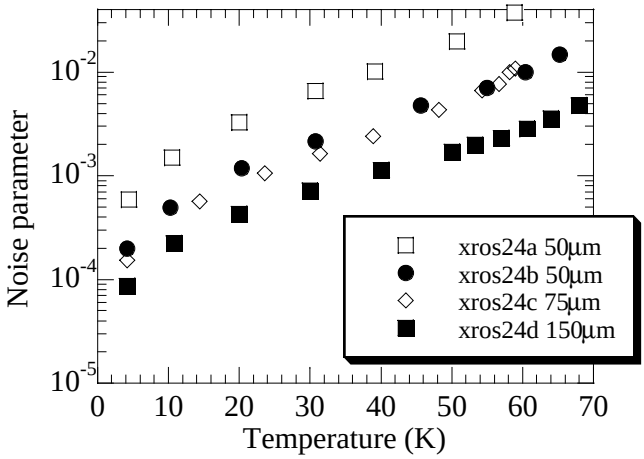

Figure 5.32 The variation of noise parameter with temperature for the most hysteretic junction at the highest temperature (for the chips which containing junctions which had β_c>1 at T>50K, with xros24a for comparison).

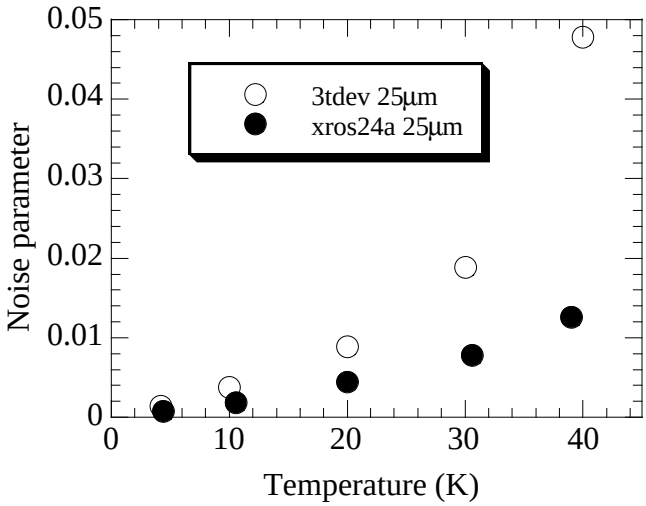

Figure 5.33. The variation of the noise parameter with temperature for the 3tdev and xros24a 25μm device.

5.6.3 The noise temperature calculated from the critical current distribution

The critical current distributions measured for the 3tdev 25μm device (see Fig. 5.18(a)) were analysed according to the method of Fulton and Dunkleberger[114] to try and determine the effective noise temperature. Assuming that the energy distribution of the junction before escape to the voltage state is near thermal, the lifetime τ of the junction in the zero voltage state when the junction is biased at a particular current I is given by (5.7).

$$\tau^{-1} = (\omega_J / 2\pi) e^{\frac{-E}{k_B T_N}} \tag{5.7}$$

Here, ω_J is the angular attempt frequency of escape from the potential well and T_N is the noise temperature. The form of the Josephson potential energy barrier E at a given current I is given by (5.8) [114],

$$E = (I_{c0}\Phi_0 / 2\pi)\left[x\left(2\sin^{-1}x - \pi\right) + 2\cos\left(\sin^{-1}x\right)\right] \tag{5.8}$$

where I_{c0} is the absolute junction critical current in the absence of thermal noise and $x=I/I_{c0}$. The expression (5.8) has the form of a tilted sinusoid. The measured current distribution gives a probability $P(I)$ that the junction will switch into the voltage state in the current interval between I and $I+\Delta I$. Since both the sweep frequency (30Hz) and the form of the current sweep were known (sinusoidal), the inverse lifetime could be related to $P(I)$ by (5.9) [114].

$$\tau^{-1} = \frac{dI}{dt}\frac{1}{\Delta I}\ln\left(\sum_{j=1}^{K} P(j) \Big/ \sum_{i=1}^{K-1} P(i)\right) \tag{5.9}$$

A current I was associated with a particular channel K, with K=1 corresponding to the maximum measured critical current. A plot of $\ln(\tau^{-1})$ versus E at various temperatures is shown in Fig. 5.34. The absolute critical current was taken to be the maximum measured value of the distribution. The data covers only a small fraction of the range of the Josephson potential energy barrier, which has a maximum depth (at x=0) of $4.7\text{x}10^{-20}$J or 3400K at a measurement temperature of 4.2K.

The curvature in some of the lines in this plot (e.g. 20.7K) indicates extrinsic (non-thermal) sources of noise[114]. The noise temperature T_N could then be determined from the gradient of these lines using (5.7), and the results are given in Table 5.4. The 41.5K data was non linear and is not included in Table 5.4. The higher the temperature, the smaller the maximum depth of the Josephson potential energy barrier and so the more significant non-thermal sources of noise become.

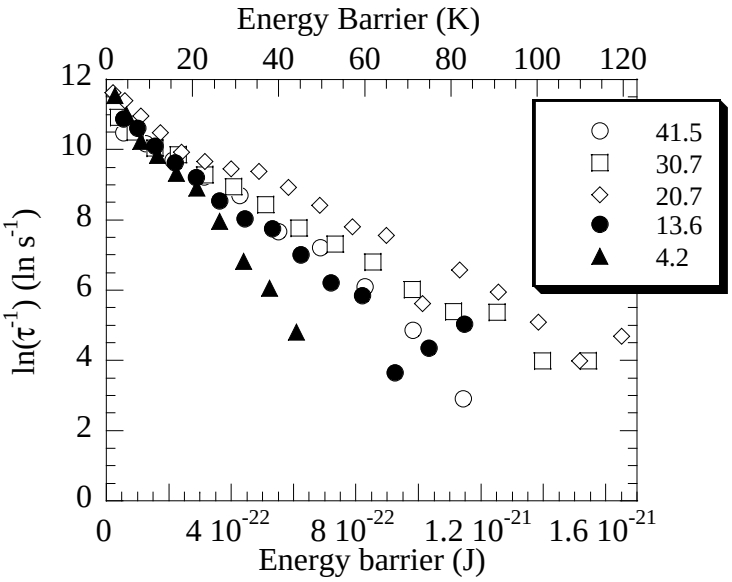

Figure 5.34. The inverse lifetime in the zero voltage state versus the Josephson potential energy barrier at various temperatures for the 3tdev 25μm device at various temperatures.

Table 5.4 The noise temperature and I_c calculated from Fig. 5.33.

Temperature T_M (K)	*Noise Temperature T_N (K)*	*Maximum measured I_c (μA)*	*I_c required for T_M=T_N (K)*
4.2	6.59	142.7	N/A
13.6	11.32	124.0	126.0
20.7	16.10	104.0	107.0
30.4	15.45	73.7	88.0

From Table 5.4 it can be seen that, at 4.2K, the noise temperature is greater than the measurement temperature. However, at higher temperatures, the noise temperature is less than the measurement temperature. This is clearly unphysical, and the most likely explanation is that the maximum measured critical current is less than the absolute critical current of the junction, leading to a systematic error in the calculation of *E*. Therefore, the I_c required for the noise temperature to equal the measurement temperature was calculated, and this gives a lower limit for the absolute critical current of the junction. As seen in section 5.5.2 there is significant suppression of the critical current at higher temperatures.

5.6.4 Simulations of hysteretic junctions

In order to confirm the validity of the factors that were believed to be controlling the coupling of the junction to the external capacitor, computer simulations were carried out using the program JSIM[116] with extensions written by Dr. C. Pegrum to enable the program to simulate hysteretic IV curves and voltage dependent resistances, and by Dr. J. Satchell[117] to add a stochastic noise current from any shunt resistors.

5.6.4.1 Thermal noise

To verify Zappe's approximation and the effect of thermal noise, a junction with a 300μA critical current was shunted with a lumped 1pF capacitor and various shunt resistances from 1.5 to 7Ω and simulated at temperatures of '0K' and 60K. The results are shown in Fig. 5.35. As expected, at 60K the critical current was reduced, by up to 40μA for the 7Ω resistor, and the return current was increased by up to 15μA. At 60K, for a given β_c, α is increased – i.e. the hysteresis was reduced. This is a reproduction of the experiments of Hansma *et al*[96] who

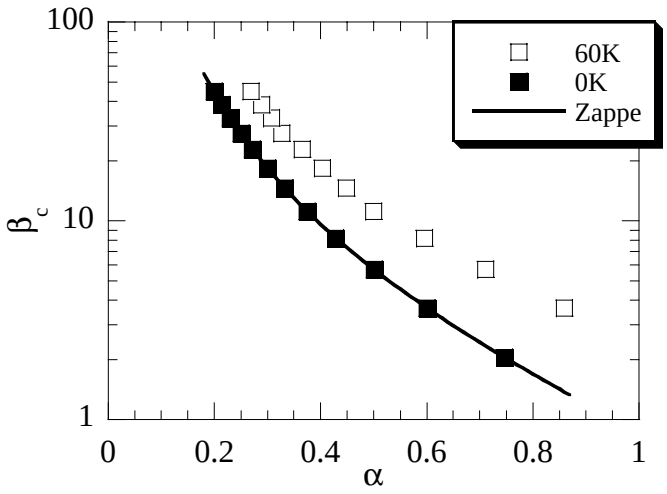

Figure 5.35 β_c versus α from Zappe's approximation, simulations at '0K,' and simulations at 60K.

were able to measure hysteretic junctions shunted with variable resistances by day and night to give more or less external noise respectively. The increase of α means that the effective shunt capacitance measured from the *IV* characteristic will be reduced at high temperatures.

5.5.4.2 Distributed impedance

The equivalent circuit given in Fig. 5.28 was tested using that given in Fig 5.36, modelling $Z(\omega)$ as a one dimensional lossy transmission line with inductance and capacitance per unit length given by 5.4 and 5.5 respectively.

Both *R'* and *G'* (the transmission line losses from the surface resistance of the YBCO and the Au and the dielectric losses in the $SrTiO_3$ respectively) are frequency dependent, and a patch for JSIM written by Dr. C. Pegrum enabled simulation of frequency dependent losses, by taking the last known value of the frequency from the previously determined voltage. The surface resistance of the gold is given by (1.49) and combining this with the skin depth δ_s from (1.48) and (1.9) gives (5.10).

$$R_{Au} = \left(\frac{\pi V \mu_0}{\sigma \Phi_0} \right)^{1/2} \tag{5.10}$$

For the gold conductivity σ a value of 3.8×10^7 $\Omega^{-1}m^{-1}$ at 60K was used. The YBCO surface

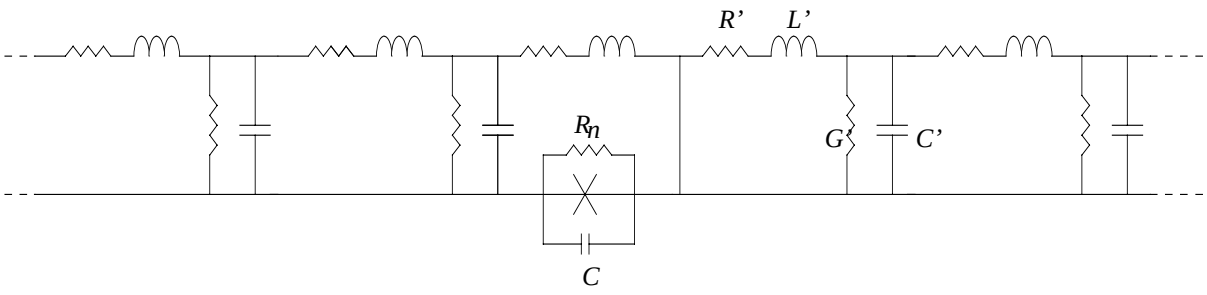

Figure 5.36 The junction shunted with a distributed impedance as investigated using simulations. (*C* and R_n are the junction grain boundary capacitance and normal state resistance respectively.)

resistance from (1.52) can be written as (5.11).

$$R_{YBCO} = k_{60}\left(\frac{V}{\Phi_0}\right)^2 \tag{5.11}$$

where k_{60} is a constant equal to $0.83\text{x}10^{-23}$ ΩHz^{-2}, as measured by Edstam *et al*[113] with a transmission line resonator coupled to a bicrystal YBCO Josephson junction (see Chapter 7). The resistance per unit length *R'* due to these losses is then given by (5.12)[118].

$$R' = \frac{l}{a}(R_{Au} + R_{YBCO}) \tag{5.12}$$

since the contributions from the YBCO and the Au add in series along the length of an element, but are seen in parallel across the width of an element.

It was evident from the simulations that the lower the losses in the inductor, the lower the suppression of observed hysteresis. From (5.10) and (5.11) and the plot of surface resistance versus junction voltage (frequency) in Fig 5.36 it can be seen that the crossover to where YBCO has a larger surface resistance occurs at 0.23mV at 60K. This voltage decreases with increasing temperature. Since the voltage at which the junctions switched back to the zero voltage state was typically around 0.2mV, it was believed not to be worthwhile to use YBCO as the top electrode.

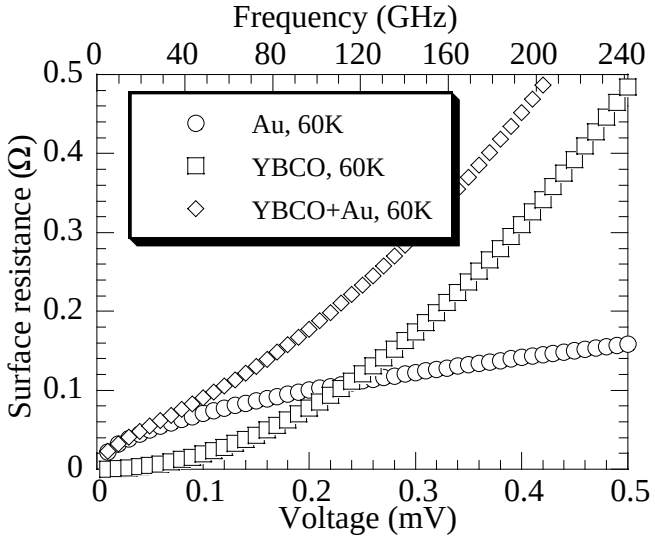

Figure 5.37 The surface resistance of Au and YBCO and their sum versus frequency and equivalent voltage at 60K(data interpolated from[113]).

The parameters used were nominally those of the xros24d 50μm junction at 60K. The absolute critical current was found to be 880μA, giving a measured critical current of 820μA (from a fit to the measured IV curve). The normal state resistance was 0.659Ω and the grain boundary capacitance was 0.3pF. Both 50 and 100 transmission line elements were used. A penetration depth of 159nm and a gold skin depth of 52nm were used to give an inductance per unit length from (5.4) of 0.0172 pH/2μm or 0.0088 pH/μm for a strip of capacitor of width 50μm. A relative dielectric constant of 40 (calculated from the position of the first resonance - see Chapter 7) gave a capacitance per unit length of 0.708pF/2μm or 0.354pF/μm. The values used for the surface resistance were those in Fig. 5.37 and *G'* was taken to be zero. The lumped capacitance *IV* assumed that the junction was shunted in parallel by two 50μm capacitors in series (C_{total}=17.7pF), which gives half that of the sum of all the *C'* elements used (C_{total} =35.4pF).

The results of a simulation of the circuit in Fig. 5.36 are shown in Fig. 5.38. It can be seen the effect of distributing the impedance is to reduce the hysteresis from that of the junction shunted by a lumped capacitance, although not by as much as was observed experimentally. To simulate the bow-tie, 5 elements of progressively increasing capacitance per unit length from 0.0272pF/2μm and decreasing inductance per unit length from 0.42pH/2μm were added onto either side of the junction. This was compared to a junction with 5 elements of C'=0.0272pF/2μm and L'=0.42pH/2μm followed by a discontinuous jump to

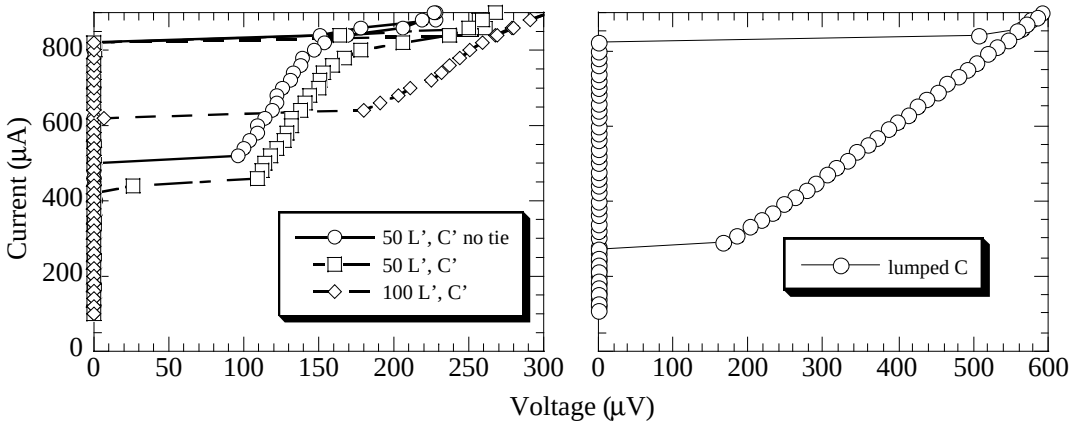

Figure 5.38 Simulations of the IV characteristic of a Josephson junction (nominally xros24d 50μm *T*=60K parameters) shunted with various distributed and lumped impedances.

C'=0.708pF/2μm and L'=0.0172pH/2μm. It is clear from Fig. 5.38 that the bow tie improves the couping of the shunt capacitor to the junction.

The line containing 100 elements gives less hysteresis than that containing 50 elements, as the limit of differential lengths of inductance and capacitance is approached. The 50 element line has an effective shunt capacitance of 2.9pF with a bow tie and 2.1pF without. The 100 element line has an effective shunt capacitance of 1.9pF, and the lumped shunt capacitance gives an effective shunt capacitance of 8.1pF, from the hysteresis in the IV curve.

Further simulations were carried out to elucidate the effect of non-zero *G'*, given in (1.53)[14]. *G'* is an admittance, so the effective loss resistance is its inverse. A typical measurement of the loss tangent of a $SrTiO_3$ thin film is 0.06[119], but this was carried out at 1GHz rather than the higher frequencies (hundreds of GHz) where the shunt capacitor was used here. However, this value of the loss tangent was found to completely suppress the hysteresis at 60K. A lower value of the loss tangent, 0.001, was investigated, but this too was found to completely suppress the hysteresis. Measurements from the literature[69,71,119-122] indicate that 0.001 is an unrealistically low value for the loss tangent of thin film $SrTiO_3$. The most plausible reason for this total suppression is probably that the simulation did not include enough transmission line elements.

These simulations serve only as a qualitative guide only to the experimental data. The width as well as the length of the capacitor electrode was comparable to the wavelength of the Josephson oscillations in the capacitor, but only a one dimensional transmission line was

simulated. The calculation of the surface resistance of the YBCO and the Au and of the dielectric losses in the $SrTiO_3$ did not include higher harmonics of the Josephson oscillations (see Fig. 1.3), which are most certainly present at voltages below the I_cR_n product of the junction.

However, the simulations verify that both thermal noise suppression of the critical current and the distributed nature of the shunt capacitor are both significant factors in the reduction of β_c observed from that predicted from a simple calculation of the lumped capacitance. A further factor was found to be dielectric losses in the $SrTiO_3$ film. Therefore, optimisation of the $SrTiO_3$ film to reduce the loss tangent to the lowest value reported in the literature[69] (0.005) should be considered to increase the hysteresis.

5.6.5 A comparison with hysteretic junctions in the literature

Table 5.5 gives a comparison of the data reported for other representative high T_c hysteretic junctions. The β_c value of 1.01 at 72K is comparable with that of Daly *et al*, who used a similar geometry of shunt capacitor. The β_c value achieved by Dong is considerably higher. Dong used a ramp edge SNS junction, as shown in Fig. 5.39. The junctions used by Dong

Table 5.5. Data from other studies of YBCO capacitively shunted Josephson junctions. *C* is that calculated from the hysteresis in the *IV* curve.

Junction type	*Dielectric*	*Capacitor area* (μm^2)	I_c (μA)	R_n (Ω)	β_c	C (pF)	T (K)	*Wavelength* (μm)	*Ref.*
Step edge on $LaAlO_3$	67nm $LaAlO_3$	220x220	160	1.4	1.3	4.3	67	215	Daly *et al*[100]
Step edge on $LaAlO_3$	80nm $SrTiO_3$	10x30	140	9.5	6	0.16	4.2	22	Daly *et al*[100]
Ramp edge SNS	100nm $SrTiO_3$	100x100	180	0.5	9.1	67	77	100	Dong[37]
Xros24d	50nm $SrTiO_3$	150x150	451	0.56	1.01	2.28	72	58	This work

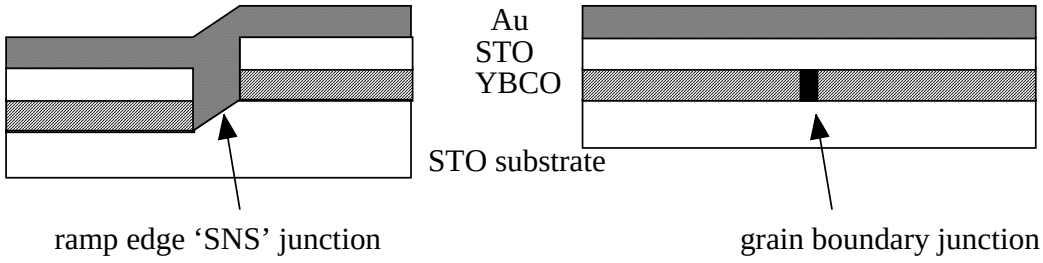

Figure 5.39 The ramp edge SNS junction geometry used by Dong[37] and the grain boundary junction investigated in this work.

enabled more efficient coupling of the Josephson oscillations to the gold top electrode, possibly eliminating the need for coupling structures such as the bow tie used in this work to impedance match the track containing the junction to the capacitor itself. However, Dong presents only one hysteretic *IV* curve and provides no explanation of the large β_c obtained. In all cases, the wavelength of the Josephson oscillations in the external capacitor is comparable to the size of the external capacitor.

5.7 ROS simulations

In order to establish whether or not an operational ROS could be constructed with the small amount of hysteresis observed, simulations were carried out to give *V(t)* for the circuit in Fig. 5.1 for the measured hysteretic junction parameters at high temperatures. The SQUID can be approximated as a single junction[95]. Fig. 5.40 shows a *V(t)* trace for the xros24d 50μm junction at 60K.

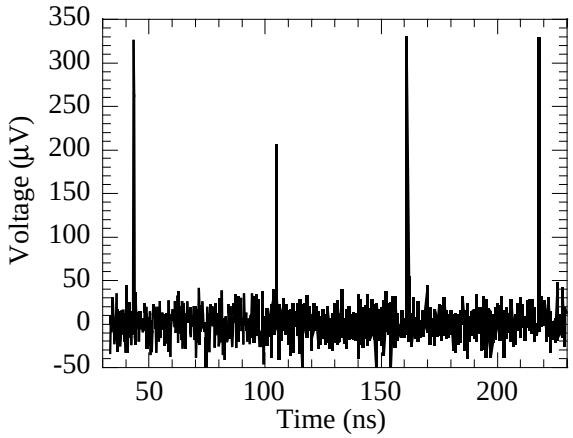

Figure 5.40. Simulated relaxation oscillations for the xros24d 50μm junction at 60K. The circuit parameters were (absolute) I_c=880μA, R_n=0.659Ω, C=1.8pF, L=1nH, R_b=0.1Ω and bias current I_b= 860μA. (thermally suppressed I_c=830μA, I_r=770μA)

The time spent in the zero voltage state T_0 and the voltage state T_V are given by[95],

$$T_0 = \frac{L}{R_b}\ln\left(\frac{I_b}{I_b - I_c}\right) \tag{5.13}$$

$$T_V = \pi\sqrt{LC} \tag{5.14}$$

Using these equations and the parameters from Fig. 5.41, T_0=33ns and T_V=0.13ns, in rough agreement with the simulated values. The pulses are narrow (<0.13ns) and thus would require a high bandwidth (tens of GHz) measurement system to be observed. A pre-amplifier (made from superconducting or conventional electronics) operating at low temperatures, would be required, or possibly a flip-flop which triggers on the pulses. However, for the data shown, the mean voltage is not significantly different from the noise voltage making the construction of a DROS from junctions with this small β_c value impossible.

5.8 Summary

Hysteretic junctions operating at high temperatures have been fabricated and tested. The highest temperature at which an *IV* characteristic for which β_c>1 was observed was 72.3K. A combination of factors is believed to be responsible for the absence of hysteresis at higher temperatures and the much lower β_c values than would be expected if the shunt capacitor was behaving as a simple lumped circuit element. The wavelength of the Josephson oscillations in the shunt capacitor is comparable to the dimensions of the shunt capacitor itself, so the junction sees a distributed impedance which has a lower effective capacitance than that of the equivalent lumped circuit element, and the impedance of the track containing the junction is mismatched to that of the external shunt. This was demonstrated both through simulations and calculations of the wavelength of the Josephson oscillations in the shunt capacitor for various measured devices with varying degrees of coupling to the shunt capacitor – devices with a longer wavelength had larger β_c values at higher temperatures. Junctions with an impedance matching structure (a 'bow tie') were found to be better coupled to the shunt capacitor than those without. At high temperatures, thermal noise suppression of the hysteresis was found to play a significant role, and it was shown that for two junctions with the same wavelength of Josephson oscillations the junction with the lower noise parameter was hysteretic at higher temperatures. From the measured distribution of critical currents, it was found that the

measured critical current was suppressed by up to 14.3μA The simulations also showed that the dielectric losses in the $SrTiO_3$ films used dramatically reduced the effective shunt capacitance of the structures.

Simulations showed that even with the small β_c values observed, it could be possible in principle to manufacture a working ROS, but due to the narrow pulses the measurement system would need to be very carefully designed.

Chapter 6: Single crystal strontium titanate characterisation using internal junction (Fiske) resonances

6.1 Introduction

The Josephson junction is a natural voltage tuned oscillator with 1mV (a typical YBCO grain boundary junction I_cR_n product at 4.2K - see section 2.4.2) equivalent to an oscillation frequency of 483GHz. Bulk STO is expected to exhibit a large variation of its permittivity ε_R in this angular frequency (ω) and temperature range. A comparison of the behaviour of thin film and single crystal $\varepsilon_R(\omega)$ could bring insight into the reduction of ε_R seen for thin film STO as compared to bulk STO as discussed in Chapter 3.

This chapter describes measurements of Fiske resonances in Josephson junctions of a series of different lengths on a single $SrTiO_3$ bicrystal. Initially, the aim of the experiment was to establish the influence of the strontium titanate substrate on the capacitance of the grain boundary. Subsequently it became apparent that a measurement of the dielectric constant of bulk single crystal strontium titanate could be made above and below the soft optic phonon frequency.

6.2 Mask Design

The subros chip described in Chapter 5 showed that parasitic capacitance from the STO substrate could not be made to be the dominant contribution to the capacitance of an YBCO grain boundary Josephson junction, since the size of shunt capacitor required to achieve the necessary McCumber parameter was greater than the wavelength of the Josephson oscillations in the capacitor. However, the geometry of the subros structure did not vary significantly

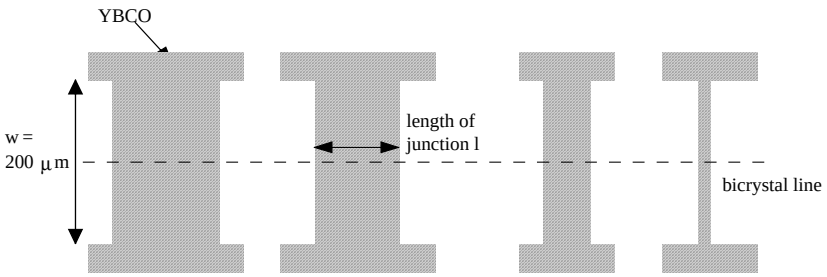

Figure 6.1 The series of tracks each containing a different junction length.

within 10μm on either side of the junction. To investigate the effect of the substrate on this length scale, a series of 11 junctions with 'lengths' (see Fig. 6.1) from 2 to 10μm, 15 and 20μm were patterned in a 170nm YBCO film deposited by off axis pulsed laser deposition on a 24.8º STO bicrystal substrate in Cambridge. The corrected junction lengths were measured in an optical microscope after patterning. *IV* measurements of the shorter junctions at 4.2K were made by E. Inglessi[123] and Dr. F. Kahlmann.

6.3 Current Voltage Characteristics and Fiske resonances

IV characteristics were measured over the temperature range in which resonances appeared, and in the range of magnetic fields between the first minima in the Fraunhofer modulation of the critical current. Fig. 6.2(a) shows the *IV* characteristic of the 2μm long junction at 4.2K, and Fig. 6.2(b) shows the IV characteristic of the same junction in a series of applied magnetic fields with the normal state current V/R_n subtracted. The resonance appeared only upon application of a magnetic field and did not change position with field and so it was assumed to be a Fiske resonance. By equating the capacitance found from the hysteresis to the capacitance per unit length from the position of the Fiske resonance (see section 5.4.1.2) the film penetration depth was found to be 208nm at 4.2K. As the longer junctions were not hysteretic, this method of penetration depth determination could not be applied, so it was assumed that this value of the penetration depth remained constant across the film.

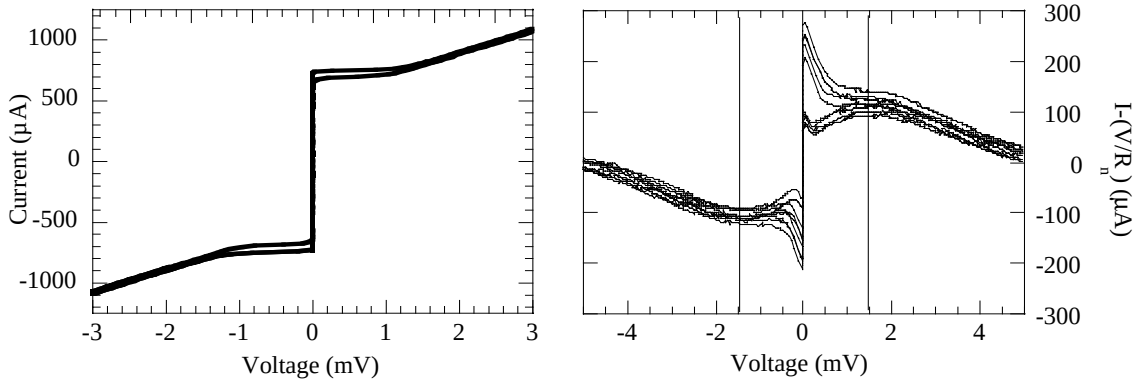

(a) **(b)**

Figure 6.2(a) The IV characteristic of the 2μm wide junction at 4.2K, and (b) the same junction in magnetic fields 235, 283, 331 and 379μT with a Fiske resonance indicated by lines at 1.5mV. The normal state current (V/R_n) has been subtracted.

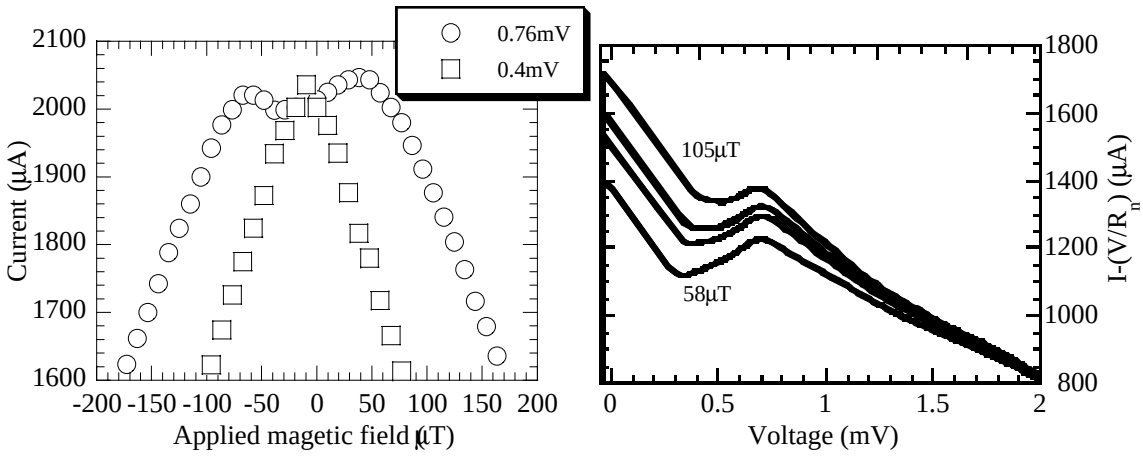

(a) **(b)**

Figure 6.3(a) The variation of current with magnetic field at and below the voltage of the first order Fiske resonance for the 5μm long junction at 15K. (b) IV curves with the normal state current subtracted for the same junction in the same range of applied magnetic field.

Fig. 6.3(a) shows the dependence of the current on magnetic field at and below the Fiske resonance voltage of the 5μm long junction at a temperature of 15K. The splitting of the zero field peak in the normal Fraunhofer pattern for the critical current modulation with magnetic field is characteristic behaviour at the Fiske resonance voltage (see Fig. 1.13). Fig 6.3(b) shows the excess current peak due to the Fiske resonance in the corresponding junction *IV* curve.

Fig 6.4 shows the position of the Fiske resonance versus applied magnetic field for various lengths of junction. It can be seen that, for most junctions, the position of the Fiske resonance

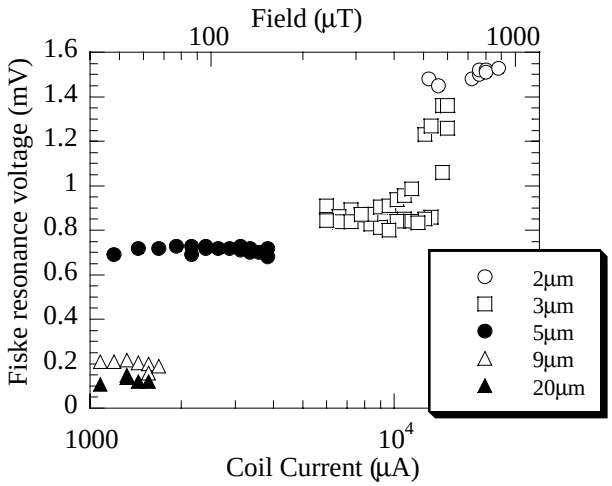

Figure 6.4. The voltage of the first order Fiske resonance versus magnetic field for various lengths of junction.

does not vary with field. Also, the Fiske resonance voltage decreases with increasing junction length, the behaviour expected from (4.17). This provides further evidence that the resonances are indeed Fiske resonances. There are two branches for the 3μm junction data, one which remains constant with applied field and one which increases. The branch which varies with field is believed to be a flux flow resonance or Eck peak, as described in section 1.4.2.2.

6.4 The Fiske resonance dispersion relation

6.4.1 A non-linear dispersion relation at 4.2K

Fig. 6.5 shows plots at 4.2K and 35K of inverse junction length versus Fiske resonance voltage for all the junctions where a resonance was observed. The error bars in the resonance voltage (where visible) arise from averaging over the magnetic field. This is effectively a dispersion relation for the transmission line formed by the junction cavity, and if the inductance and capacitance per unit length of the resonator were invariant with frequency, then this dispersion relation would be expected to be linear. However, at 4.2K the dispersion relation is non-linear and instead there are two branches, one with a higher gradient at low frequencies with a transition between 158GHz and 240GHz to a lower gradient branch at higher frequencies. Two branches in the dispersion relation were observed up to a temperature of 25K, but as can be seen from Fig. 6.5, the dispersion relation became linear again at 35K.

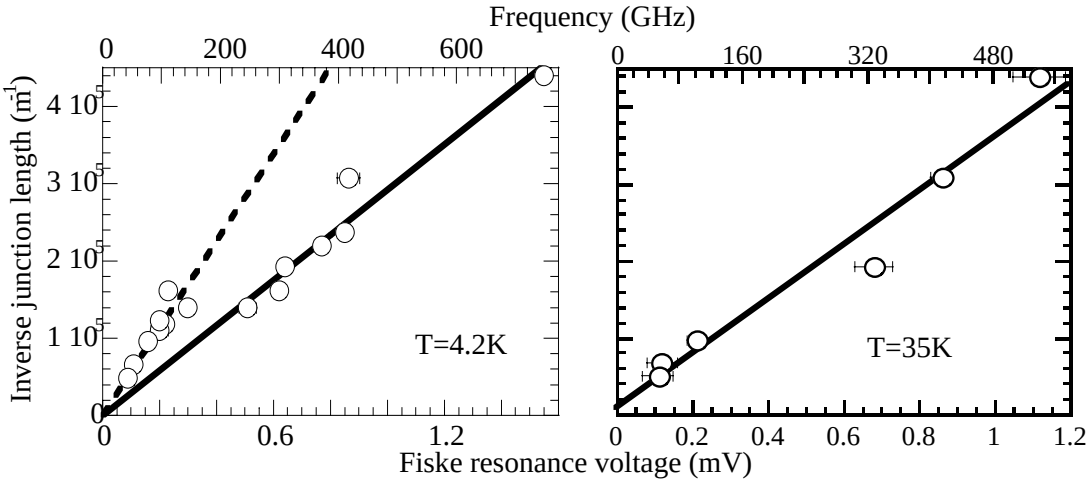

Figure 6.5. Inverse junction length versus the voltage of the first order Fiske resonance at 4.2K and 35K.

Assuming that the inductance per unit length L' remains constant across the film then the change in gradient must be due to a change in the capacitance per unit length C' of the resonator. L' was calculated to be 3.76pHμm^{-1} from the penetration depth of 208nm using (1.44). The penetration depth was comparable to the film thickness so it was corrected with $\lambda_{eff}=\lambda_L^2/h$. At 4.2K, C' was found to be 0.10±0.01pFμm^{-1} for the low frequency branch and 0.0240±0.0004pFμm^{-1} for the high frequency branch of the dispersion relation using (6.1), where V_1 is the voltage of the first order Fiske resonance (see section 1.4.2.1).

$$V_1 = \frac{\Phi_0}{2l\sqrt{L'C'}} \tag{6.1}$$

A comparison of capacitance per unit area versus resistance area product for these junctions with those on subros is shown in Fig. 6.6. Junction area is defined as film thickness times junction length. The specific junction capacitances calculated from the Fiske resonances above the transition are similar to those subros junctions with a similar resistance area product. Therefore, the capacitance of these junctions above the transition is dominated by the grain boundary. Below the transition, the junctions have a similar resistance area product but a much higher capacitance 'per unit area.' So, below the transition there must be a significant extra contribution to the total junction capacitance.

As shown in Fig 3.4 and (3.11), below ω_{TO} ε_{RSTO} suddenly rises from a negative value to a large positive value. The frequency of the transition in the dispersion relation in Fig 6.5 is believed to correspond to ω_{TO}. Below ω_{TO}, parasitic co-planar capacitance from the STO

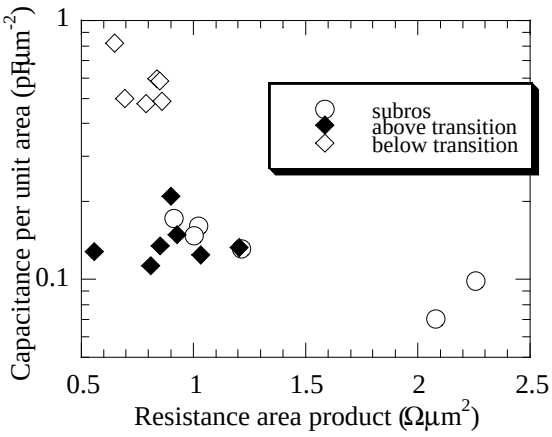

Figure 6.6. Capacitance per unit area versus resistance area product at 4.2K above and below the change in gradient of the dispersion relation, together with the data from subros.

substrate makes a significant addition to the total capacitance per unit length of the junction. This gives rise to the two branches with different gradients in the dispersion relation. The upper limit on the soft phonon frequency from the measured dispersion relation was 240GHz, and this is in reasonable agreement with the frequency of 270GHz measured by Vogt[77] for the lower frequency component of the soft optic phonon.

6.4.2 Temperature dependence of the dispersion relation

The voltages of the Fiske resonances below ω_{TO} increased with increasing temperature up to 25K, and this is shown in Fig. 6.7 for the 7, 8 and 10μm long junctions. This increase in the voltage of the first order Fiske resonance meant that the capacitance per unit length from the gradient of the lower branch of the dispersion relation decreased with increasing temperature. Table 6.1 shows the high and low frequency values of the junction capacitance per unit length, where C_{GB}' and C_{STO}' are the grain boundary and parasitic substrate contributions to the total junction capacitance per unit length respectively.

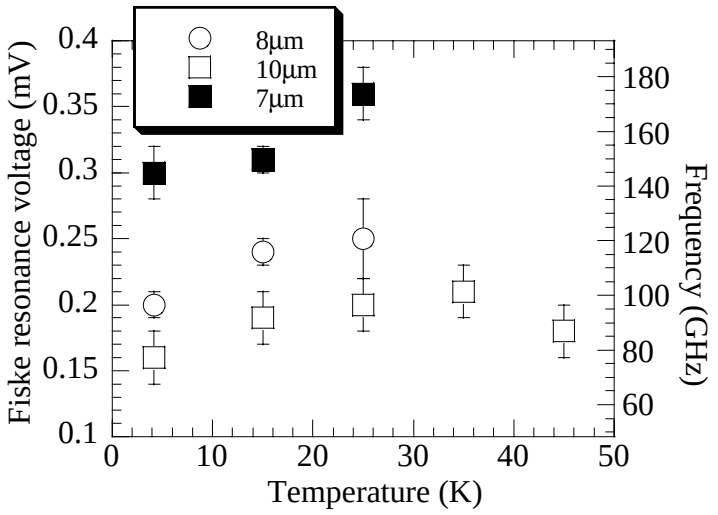

Figure 6.7. The variation of Fiske resonance voltage with temperature for the 7, 8 and 10μm long junctions.

Table 6.1 The high and low frequency junction capacitance per unit length.

Temperature (K)	*High frequency* C_{GB}' *(pFμm^{-1})*	*Low frequency* (C_{GB}'+ C_{STO}') *(pFμm^{-1})*
4.2	0.0240±0.0004	0.10±0.01
15	0.0260±0.0006	0.069±0.004
25	0.030±0.001	0.051±0.004

6.4.3 A fit to the dispersion relation

A fit was made to the Fiske resonance dispersion relation in Fig 6.5 using the transmission line propagation constant γgiven by (1.38). Above ω_{TO} the dielectric constant of the substrate ε_{RSTO} is negative (see (3.11) and Fig. 3.4). Therefore, above ω_{TO} the capacitance of the strontium titanate layer becomes negative and should reduce the overall capacitance per unit length of the resonator.

Tarte *et al*[57] showed that it is possible to separate the capacitance of the junction into two contributions. The grain boundary is modelled as a parallel plate capacitor. The co-planar capacitance from the substrate is conformally mapped onto a parallel plate capacitor structure. The tangential electric field must be continuous across the boundary. If the first electric field line in the substrate is linear, then this boundary condition is satisfied and the two contributions can then be added as if they were in parallel. The geometry is shown in Fig 6.8, which is a cross sectional view of the junction shown in Fig. 1.8. After the conformal mapping, the

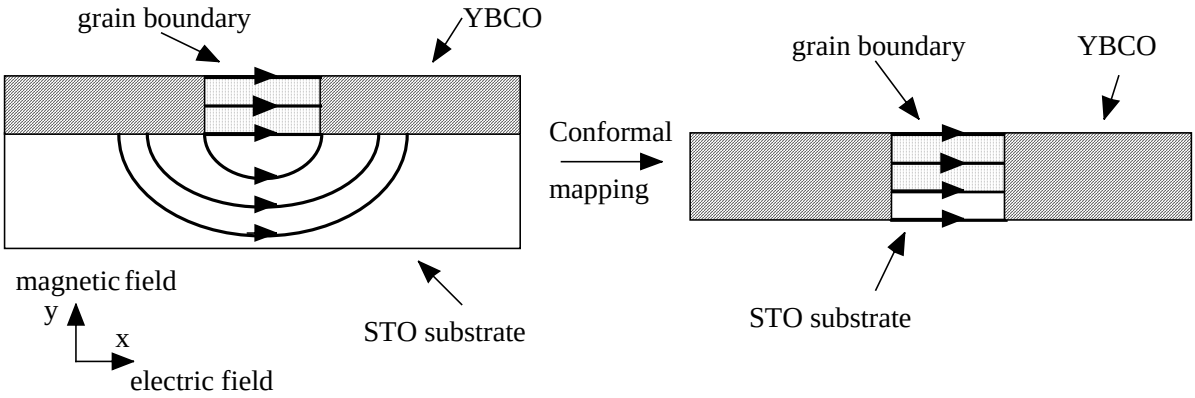

Figure 6.8. Cross sectional views of the resonator geometry measured. The resonance propagates into the page. The electric field lines in the grain boundary and the substrate are shown (not to scale).

structure is equivalent to that in Fig. 1.8, but the resonator now consists of two dielectrics.

It is also possible to separate the geometric inductance of the resonator into a contribution from the 'parallel plate' structure of the grain boundary and the co-planar stripline formed by the junction electrodes. However, the film thickness used is comparable to the penetration depth and thus the current due to the resonance penetrates the entire thickness of the film, so the kinetic inductance cannot be separated into two contributions from the substrate and the grain boundary. The relative magnetic permeability of the STO substrate is one. Therefore, the inductance of the resonator is not affected whether the STO substrate is present or absent and is therefore effectively frequency independent.

It was assumed that the inductance calculated from the fitting of the capacitance from the hysteresis in the IV curve to that from the Fiske resonance voltage for the 2μm junction was the total geometric and kinetic inductance per unit length of the resonator, and that this value was frequency independent and the same for all the junctions.

To take into account losses both in the YBCO grain boundary and the STO the wavenumber must be taken as the imaginary part of the transmission line propagation constant γ as defined in (1.38). C_{STO}' can be calculated using (5.1) or equivalently (2.1) for the capacitance per unit length of two co-planar strips. In (5.1), w is the 'width' of the track containing the junction and

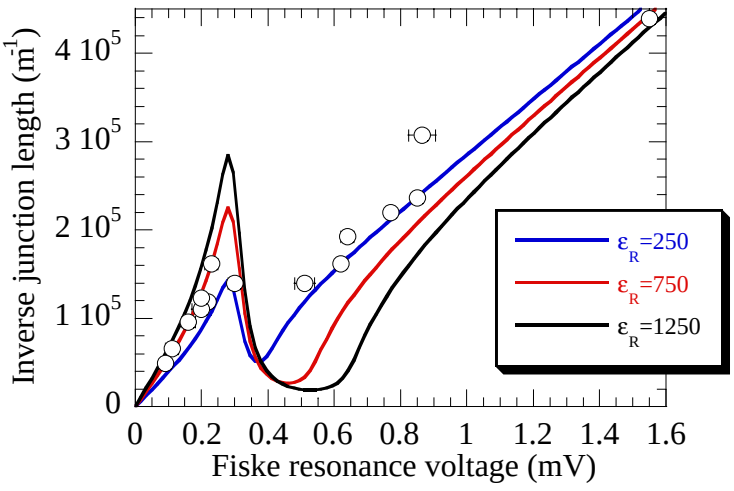

Figure 6.9. A fit to the Fiske resonance dispersion relation at 4.2K.

is equal to 200μm. The spacing of the capacitor electrodes, or *s* in (5.1), is the width of the cavity in which the Fiske resonances are propagating or approximately the thickness of the disordered region around the grain boundary, ~1nm[45]. The expression (3.11) for $\varepsilon_{RSTO}(\omega)$ was substituted into (5.1). Since (3.11) includes both real and imaginary parts of $\varepsilon_{RSTO}(\omega)$, this naturally takes into account dielectric loss in the STO, and (1.38) can be written as (6.2) where *R'* are the losses in the inductance per unit length of the resonator, and it is assumed that dielectric loss in the grain boundary is negligible compared to that from the STO.

$$k_x = \mathrm{Im}(\gamma) = \mathrm{Im}(((R'+i\omega L')(i\omega(C_{STO}'+C_{GB}'))^{1/2}) \tag{6.2}$$

The measured dispersion relation at 4.2K from Fig 6.5 was fitted to (6.2). The result is shown in Fig. 6.9, using the zero frequency dielectric constant $\varepsilon_{RSTO}(0)$ and the transverse optic phonon frequency ω_{TO} as the only variable fitting parameters. *R'* was determined from (5.11) with $k_{4.2}$=0.23x10^{-23}ΩHz^{-2}[113], $\varepsilon_{RSTO}(\infty)$=6[76] and η=30GHz[77]. The best fit to the dispersion relation was obtained when ω_{TO} was set equal to the frequency of the highest frequency resonance in the low frequency branch of the dispersion relation.. C_{GB}' was left constant over the entire frequency range of the dispersion relation and was set to 0.024pFμm^{-1} and *L'* was set equal to 3.76pHμm^{-1} (see section 6.4.1) .

The best fit is obtained for $\varepsilon_{RSTO}(0)$=750. However, it is not clear why no downward curvature is observed for junctions with Fiske resonances just above ω_{TO}. The measured dispersion relation above ω_{TO} is linear, with the speed of light independent of frequency and given by $(L'C_{GB}')^{-1/2}$. It is possible that the mode is propagating in the grain boundary unaffected by the negative dielectric constant of the STO. The STO losses dominated the YBCO losses in determining the shape of the dispersion relation.

The procedure was repeated for the dispersion relation at 15K and 25K, and the data obtained is summarised in Table 6.2. At 35K, not enough Fiske resonances were observed to draw any conclusions about the location of ω_{TO} or the value of $\varepsilon_{RSTO}(0)$. Table 6.2 shows that as expected from the Lyddane-Sachs-Teller relation (3.8), $\varepsilon_{RSTO}(0)$ decreases and ω_{TO} rises with increasing temperature. These are also the trends observed in $\varepsilon_{RSTO}(0)$ and ω_{TO} with

Table 6.2. The zero frequency dielectric constant and transverse soft optic phonon frequency of bulk STO at various temperatures from fits to the measured Fiske resonance dispersion relation, and measurements from the literature.

Temperature (K)	$\varepsilon_{RSTO}(0)$	$\varepsilon_{RSTO}(0)$ *Neville[54]*	ω_{TO} *(GHz)*	ω_{TO} *(GHz)Vogt[77]*
4.2	750	24123	145±10	390
15	500	18700	150±5	420
25	250	13935	170±10	450

temperature in both the zero frequency dielectric constant measurements (Fig 3.3) and the neutron scattering measurements of ω_{TO}(Fig 3.5). $B'=\varepsilon_{RSTO}(0)\omega_{TO}^2$ is found to be $6\pm1\text{x}10^{26}\text{s}^{-2}$, which is lower still than the Neville *et al*[54] calculation. This is to be expected, however, as both $\varepsilon_{RSTO}(0)$ and ω_{TO} are lower than previously measured values.

6.5 Further discussion

6.5.1 The measured values of the transverse soft optic phonon frequency and the zero frequency dielectric constant

Qualitatively, the behaviour of the measured Fiske resonance dispersion relations at 4.2K, 15K and 25K (see Figs. 6.5 and 6.9) supports the conclusion that parasitic capacitance from the STO substrate makes a significant contribution to the total junction capacitance per unit length only below ω_{TO}. The temperature dependence of ω_{TO} itself and ε_{RSTO} calculated from the measured dispersion relation are in rough agreement with previously measured values (see Table 6.2), and the trends follow the theoretical predictions. Quantitatively, however, possible reasons for the low values of both ω_{TO} and ε_{RSTO} as compared to measurements from the literature should be addressed.

The most likely explanation for the lowering of the bulk STO dielectric constant is the formation of structural domains during cooling past the cubic to tetragonal phase transition at 105K. In the absence of an applied electric field during cooling, tetragonal domains form with different c-axis orientation. Neville *et al*[124] have observed a resonance in the dielectric constant of multi domain STO as a function of frequency, between 1MHz and 10MHz, at 4.2K. The dielectric constant decreases from 24000 below this resonance to a value between 50 and 9000 depending on the orientation of the crystal. The resonance was believed to be

associated with oscillations of the ratio of the c to a-axis lattice parameters in the structural domains with different c-axis orientation. In a multi-domain crystal the domains must rotate in order to respond to changes in the applied electric field, but above a certain frequency determined by the spacing of the domains and the piezoelectric coupling between the induced polarization and the lattice strain, the domains are unable to respond to changes fast enough so the dielectric constant is reduced.

A further problem with determining absolute values of the dielectric constant from the measured dispersion relation is the co-planar geometry of the resonator. The electric field inside the STO is non-linear and passes across a grain boundary, so it is not clear in which direction with respect to the crystallographic orientation the dielectric constant is being measured. Low frequency dielectric constant measurements are carried out in well defined orientations with respect to the crystallographic lattice using a uniform, linear electric field, and vary from 25600 at 4.2K for <110> planes to 14100 at 4.2K for <111> planes[54]. The value of 750 at 4.2K from the Fiske resonance dispersion relation is a combination of these numbers averaged in a way in which it is not straightforward to separate into contributions from the different crystal planes. The same is true of the measured value of the transverse optic phonon frequency of 145GHz at 4.2K, which is measured across two grains with different orientations.

6.5.2 Fiske resonance dispersion relations in the literature

There have been several previous studies of Fiske resonances in YBCO grain boundary Josephson junctions of various lengths on STO bicrystal substrates. None have observed two branches in the dispersion relation. Tarte *et al*[59] measured junctions of various widths and different film thicknesses and found a linear dispersion relation with no branches at 4.2K. However, the lowest Fiske resonance voltage observed was 0.39mV, above the transverse optic phonon frequency of 0.3mV measured at 4.2K here. Medici *et al*[125] again measured junctions of various widths and obtained a linear dispersion relation with no branches, but the lowest Fiske resonance voltage observed was 0.3mV, again above the low frequency branch of the Fiske resonance dispersion relation measured here. Hence, both these studies are consistent with the dispersion relation presented in Fig. 6.5.

The most recent study of Fiske resonances in YBCO grain boundary Josephson junctions of

various widths on STO bicrystal substrates has been made by Navacerrada *et al*[126]. For the 50nm thick films which were studied, a linear dispersion with no branches was observed at 20K. The lowest frequency resonance was at 0.17mV, well into the low frequency branch of the dispersion relation in Fig. 6.5. This is in clear disagreement with the dispersion relation with two branches which was measured both at 15K and 25K. There is, however, a possible explanation for this apparent discrepancy. It has already been shown that the capacitance per unit area of the grain boundary varies with its resistance area product (see Fig. 3.14 for subros). Fig. 6.6 shows that for the junctions measured here the resistance area product is effectively constant at 4.2K, and therefore the capacitance per unit area of the grain boundary is effectively constant. This was a tacit assumption made in the fitting of the dispersion relation to (4.20). It is also assumed that the resistance area product does not vary significantly with temperature. The capacitance per unit area versus resistance area product at 20K for the junctions of Navacerrada *et al* is plotted in Fig 6.10, and there is a considerably larger spread in resistance area product for the junctions of Navaccerada *et al*, which would correspond to a wide variation in capacitance per unit area of the grain boundary. In particular, the longer junctions that might otherwise be in the low frequency branch of the dispersion relation have a very low grain boundary capacitance per unit area. Therefore, any branches in the Navacerrada dispersion relation are probably obscured by variations in the grain boundary capacitance per unit area.

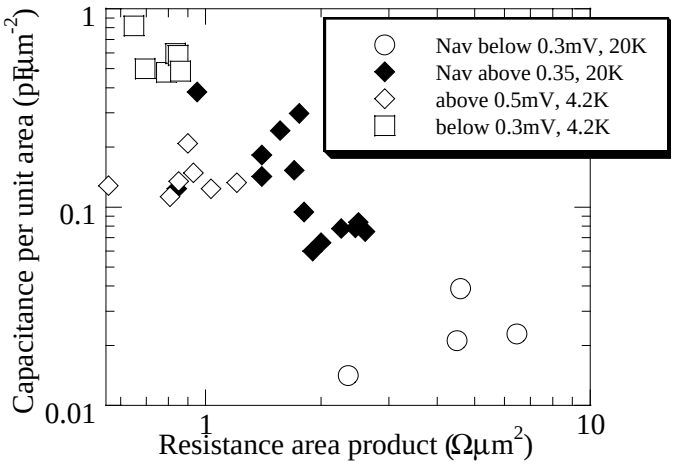

Figure 6.10. Capacitance per unit area versus resistance area product for the Navacerrada *et al*[126] junctions at 20K and for the junctions in this study at 4.2K.

6.5.3 Other possible causes of the step in the dispersion relation

It could be envisaged that the step in the dispersion relation in Fig. 6.5 was a consequence of the non-linear dynamics of the long Josephson junctions. However, as mentioned in section 1.4.2 a recent theoretical study of Fiske and flux flow resonances has found that the Fiske resonant voltages are unchanged and given by (6.1) whether the junction is in the long or short limit[17]. Also, at 4.2K the shortest junction was in the long junction limit, with l/λ_J=4 (the Josephson penetration depth λ_J is given by (1.30)). The Josephson penetration depth of the junctions was found to be independent of the junction length and equal to 480±50nm

The dispersion relation measured is that plotted in Fig. 1.11 from the sine-Gordon equation for the Josephson junction (1.32). Another possibility is that the two branches were caused by the plasma cut off frequency. The phase velocity of the two branches in Fig 6.5 is $1.6\text{x}10^6\text{ms}^{-1}$ below ω_{TO} and $3.3\text{x}10^6\text{ms}^{-1}$ above. The plasma frequency ω_p defined in (1.34) is given by c_J/λ_J, so below ω_{TO} it was greater than 5.5THz and above ω_{TO} it was greater than 11THz. The dispersion relation measured in Fig. 6.5 has no cut off frequency and is therefore that of Swihart modes propagating in the junction.

The fit to the dispersion relation ignored any frequency dependence of the capacitance of the grain boundaries in both the STO substrate and the YBCO. It has recently been proposed that the grain boundary in YBCO be modelled as a back to back Schottky barrier in a manner analogous to grain boundaries in semiconductors(see [127] and Chapter 9). Grain boundaries in silicon have a high capacitance at low frequencies because the built in voltage oscillates out of phase with the applied bias[128]. Grain boundaries in STO exhibit a similar high capacitance at low frequencies[129]. The built in voltage is due to trapped charge at the grain boundary. The capacitance is reduced at high frequencies because the relaxation time of the trapping and emission of charges at the boundary becomes too long to respond to the time dependence of the applied bias. The required relaxation time of the trapped charges from the dispersion relation in Fig. 6.5 would be $1/\omega_{TO}=6.9\text{x}10^{-12}$s. The relaxation time for silicon however, is $\sim10^{-3}$s, much larger than $1/\omega_{TO}$. Measurements of the $1/f$ noise in YBCO grain boundaries indicate that the relaxation time is also $\sim10^{-3}$s[130]. Frequency dependence of the grain boundary capacitance can therefore be ruled out as a cause of the step in the dispersion

relation in Fig. 6.5.

6.6 Conclusion

A series of junctions of various lengths on a bicrystal STO substrate was investigated. At temperatures up to 25K, two branches were observed in the Fiske resonance dispersion relation, with the low frequency branch corresponding to a larger capacitance per unit length. This was attributed to the frequency dependence of the dielectric properties of the STO substrate with frequency, and in particular the drop in dielectric constant at the transverse soft optic phonon frequency. By fitting the dispersion relation to that expected for a transmission line with two dielectrics in parallel, the dielectric constant of the STO was found to be 750 at 4.2K with a transverse soft optic phonon frequency of 145GHz. These values are lower than those found in the literature, and this is probably because of multiple structural domains in the STO below 105K and the non-linear fields in the STO resulting from the co-planar geometry used. For YBCO grain boundary junctions on bicrystal STO, parasitic capacitance from the substrate is only a significant contribution to the total junction capacitance below the transverse soft optic phonon frequency.

Chapter 7: Thin film strontium titanate characterisation with Josephson junctions coupled to external resonators

7.1 Introduction

As described in Chapter 6, the strontium titanate (STO) soft optic phonon was observed in the Fiske resonance dispersion relation of Josephson junctions on an STO bicrystal. Following this observation, it was decided to investigate the properties of thin film STO in the same frequency range using Josephson junctions coupled to external resonators. It was believed that high frequency measurements of the STO dielectric properties could bring insight into the differences in behaviour between thin film and bulk STO. In this chapter the theory relating to measurements of dielectric properties using Josephson junction driven resonators is discussed. Next, measurements of the dielectric constant of thin film STO are reported in the frequency range up to 1THz for a variety of geometries of resonator and a spread of film thicknesses. Tuning of the dielectric constant in this frequency range is also reported.

7.2 Josephson junctions coupled to external resonators

Previous research on Josephson junctions coupled to external resonators has focused primarily on the application of tunable microwave oscillators made from an array of junctions, phase locked with the aid of the transmission line[131]. The initial studies of high T_c grain boundary junctions coupled to external resonators were carried out by Edstam[132], with the aim of developing phase locked arrays of junctions[133]. The dielectric properties of silica have been determined at microwave frequencies using the technique[134]. In this section, first the theory relating to junctions shunted with general load impedances is discussed, followed by low and high T_c junctions coupled to external resonators. The theory has also been treated by Likharev[6].

7.2.1 Theory

As discussed in section 1.4.4, an external resonator causes a dip or peak to appear in the junction IV characteristic at the resonant frequency of the cavity. At this frequency a certain amount of microwave power is coupled out of the junction. For a lossless, one dimensional, transmission line coupled to an ideal (zero capacitance) resistively shunted Josephson junction,

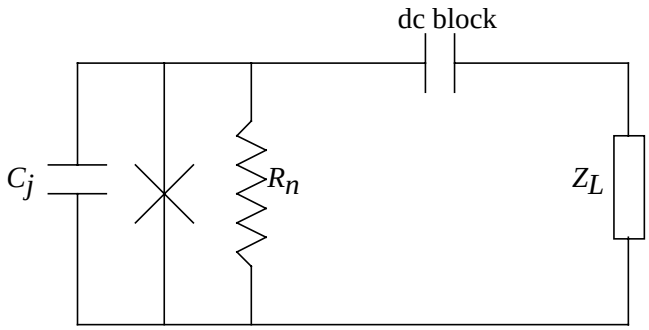

Figure 7.1 A Josephson junction shunted in parallel by a general load impedance.

the voltage V_n of the nth order resonance in the *IV* characteristic is given by,

$$V_n = \frac{n\Phi_0}{2l\sqrt{L'C'}} \tag{7.1}$$

where l is the length of the resonator and L' and C' are the inductance and capacitance per unit length of the resonator respectively.

Following Edstam *et al*[113,132,135], to properly describe the shape of the resonant structure in the *IV* curve the losses in the resonator must be taken into account, as well as the impedance matching between the junction and the resonator. The circuit shown in Fig. 7.1 is considered, which consists of a Josephson junction shunted in parallel by a resistor R_n, capacitor C_j and a general load impedance Z_L. The supercurrent I_{s0} generated by the oscillating voltages in the resistor is given by (7.2), from the RSJ model (see section 1.3.2).

$$I_{s0} = \sqrt{I_c^2 + \frac{V^2}{R_n^2}} - \left(\frac{V}{R_n}\right) \tag{7.2}$$

The Josephson junction is a dc to ac power converter and at a given voltage the microwave power generated is given by $I_{s0}(V)V$. For an infinite Z_L, this power is absorbed in the resistor giving (7.3). As discussed in section 1.3.2.1, the amplitude of the first harmonic of the Josephson oscillations is I_cR_n.

$$\frac{I_c^2}{2}R_n = I_{s0}(V)V \tag{7.3}$$

For a finite Z_L, however, microwave power is absorbed in the Z_L-R_n combination leading to a reduction ΔI_s in the voltage dependent supercurrent. This gives (7.4) for the power balance

condition.

$$\frac{I_c^2}{2}\mathrm{Re}\left(\frac{R_n Z_L}{R_n + Z_L}\right) = \left(I_{s0}(V) - \Delta I_s(V)\right)V \tag{7.4}$$

Combining (7.3) and (7.4) gives (7.5) for ΔI_s.

$$\frac{\Delta I_s}{I_{s0}} = \mathrm{Re}\left(\frac{1}{1 + Z_L/R_n}\right) \tag{7.5}$$

The argument leading to (7.5) can be repeated to give (7.6) to include the junction capacitance C_j.

$$\frac{\Delta I_s}{I_{s0}} = \mathrm{Re}\left(\frac{1 + Z_L/R_n - i\omega C_j Z_L}{(1 + Z_L/R_n)^2 + (\omega C_j Z_L)^2}\right) \tag{7.6}$$

The expressions (7.5) and (7.6) are valid for voltages above $I_c R_n$ where the Josephson oscillations are monochromatic. Below $V_c = I_c R_n$ (7.6) must be modified to take into account the amplitude of the higher harmonics of the Josephson oscillations (see Fig. 1.3) to give (7.7)[132],[6] where $v = V/V_c$. The relation (7.7) is valid if $|Z_L| > R_n(V_c/V)^3$.

$$\frac{\Delta I_s}{I_{s0}} = \frac{v}{\sqrt{1+v^2}}\mathrm{Re}\left(\frac{1 + Z_L/R_n - i\omega C_j Z_L}{(1 + Z_L/R_n)^2 + (\omega C_j Z_L)^2}\right) \tag{7.7}$$

The equations (7.5) and (7.6) are valid for small resistances and low or moderate capacitances, or when $\omega R_n C_j < 1$. This situation is usually the case for high T_c Josephson junctions which generally have small resistances and capacitances. When $\omega R_n C_j >> 1$, inductive loads which increase the effective impedance must be considered, since the large capacitance shorts out any microwave power generated by the junction. This is normally the case for low T_c tunnel junctions.

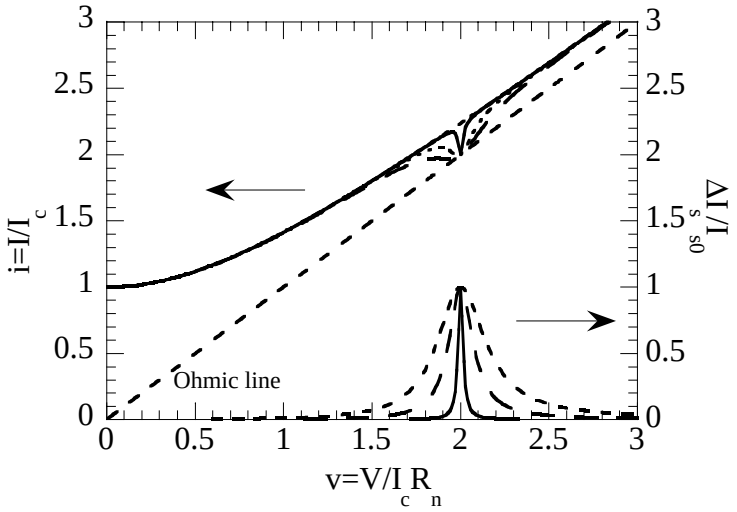

Figure 7.2. The *IV* curves (from (7.2) and (7.5)) and reduced voltage dependent supercurrent (from (7.5)) for a junction shunted by a series, lumped *LC* combination[132].

The effect of shunting a resistively shunted junction with a load impedance consisting of a lumped inductance L and capacitance C in series is shown in Fig. 7.2, for the case where $R_n<<(L/C)^{1/2}$. At resonance, the series LC combination impedance becomes real and finite (zero for a lossless components) and shorts the junction resistance to produce a dip in the IV curve, where the voltage dependent supercurrent has been completely suppressed such that $\Delta I_s/I_{s0}=1$. As $(L/C)^{1/2}$ approaches R_n, the width of the resonance increases. At other frequencies, the impedance of the resonator is large compared to the junction resistance so it has little effect on the junction IV curve. The resonance shown in Fig. 7.2 is known as a series resonance.

A more realistic case is that of a junction at the centre of an open ended transmission line of length l which has a load impedance of the form (7.8). An open ended transmission line has $Z_L=Z_0\coth(\gamma l)$[118]. The shunt impedance seen by the junction shown in Fig. 7.5 is that of two open ended transmission lines of length $l/2$ in series.

$$Z_L = 2Z_0 \coth\left(\frac{\gamma l}{2}\right) \tag{7.8}$$

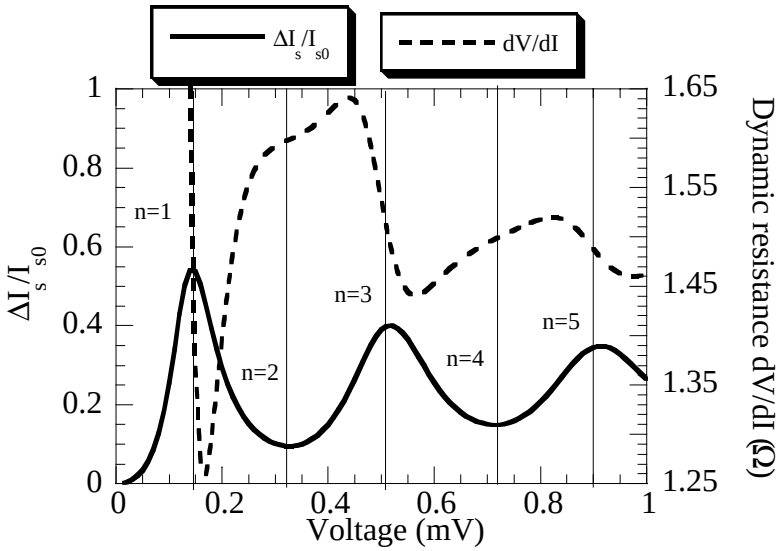

Figure 7.3 The normalised voltage dependent supercurrent and dV/dI versus voltage for a junction (I_c=100μA, R_n=1.46Ω) shunted with an open ended, low loss, transmission line with Z_L given by (7.8) and l=120μm. The series and parallel resonances are indicated by lines.

In (7.8), Z_0 is the characteristic impedance of the line, see (1.39), and γ is the propagation constant of the line, see(1.38). The normalised voltage dependent supercurrent and versus voltage (equivalent to frequency via the ac Josephson relation (1.9) from (7.6) is shown in Fig. 7.3. Also shown in Fig. 7.3 is the dynamic resistance dV/dI, which can be recovered with (7.2) followed by numerical differentiation.

The maxima in $\Delta I_s/I_{s0}$ in Fig 7.3 correspond to series resonances where the resonator has small, finite impedance so some microwave power is dissipated in the resonator and the voltage dependant supercurrent is suppressed. The minima are parallel resonances where the resonator has a large impedance, so most of the microwave power is dissipated in the resistor and the voltage dependent supercurrent is not affected. An alternative, equivalent, viewpoint of series and parallel resonances is to consider whether or not there is a node or antinode at the junction in the spatial distribution of current in the resonator. For an antinode, or a series resonance, microwave power can be coupled out and the junction can drive the resonator. However, for a node, there is no current variation at the junction, which cannot then drive the resonator, giving

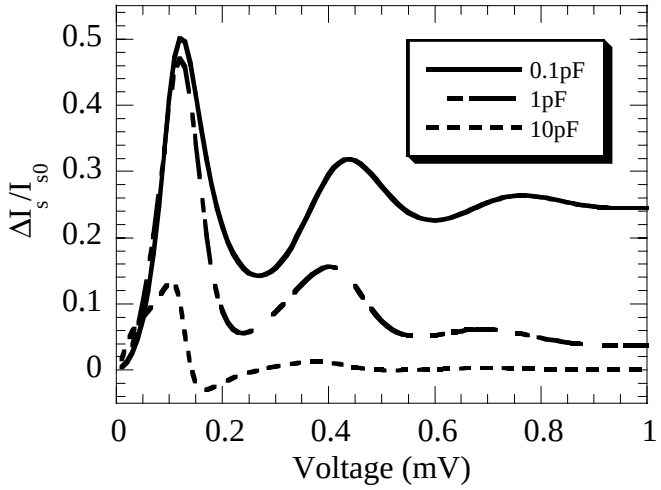

Figure 7.4 Normalised voltage dependent supercurrent for a junction coupled to the same transmission line as in Figure 7.3, for various junction capacitances and realistic transmission line losses.

rise to a parallel resonance. In the d*V*/d*I* curve, the series and parallel resonances are approximately halfway between the maxima and minima.

Fig 7.4 shows that the effect of increasing junction capacitance is to lower the resonant frequencies[113,132,136].

7.2.2 Low T_c junctions

Coupling of a Josephson junction to an external resonator was first achieved by Dayem and Grimes[30], who placed a superconducting point contact Josephson junction in a microwave cavity. Voltage steps were observed, at frequencies corresponding to the resonant frequencies of the microwave cavity. Subsequent studies have used microstrip transmission lines of the general geometry shown in Fig. 7.5, for a high T_c grain boundary junction, but with a low T_c tunnel junction replacing the grain boundary junction for the low T_c case. Olsson[134] used such a geometry with a Nb tunnel junction to determine the dielectric constant of SiO at frequencies between 13 and 103GHz with parallel type resonances. Bi *et al*[137] determined the surface resistances of Au, Nb, and Cu at frequencies up to 400GHz using series resonances and resistively shunted tunnel junctions. The surface resistances obtained were higher than expected for optimised thin films due to the lithography and patterning of the films necessary to manufacture the resonator.

Larsen *et al*[136] have carried out a more fundamental study of the physics of the interaction

between the junction and the resonator. As well as the parallel resonances corresponding to the fundamental frequencies of the resonator, sub-harmonic steps were also observed. These were believed to be generated by higher harmonics of the Josephson current, the amplitudes of which are shown in Fig. 1.3. The resonant voltages were at ~0.2mV, much less than the junction I_cR_n product of 3.3mV. The junctions were also in the limit where $\omega R_nC_j>>1$ (ωR_n-C_j=73). Larsen *et al* also found that the junction impedance determined from fitting to the shape of the resonance was considerably higher than that determined from a zero-bias conductance measurement, and were unable to explain this discrepancy.

7.2.3 High T_c bicrystal junctions

As mentioned above, the previous work on high T_c junctions coupled to external resonators has been carried out by Edstam[132]. YBCO grain boundary Josephson junctions on YSZ bicrystal substrates were used, with a SiO dielectric and either a Pb or Au top electrode, with the geometry shown in Fig. 7.5. The initial work[110] studied first order resonances only. It was demonstrated that the resonances were neither Fiske resonances (see section 1.4.2.1, section 5.5.1.2, Chapter 6) nor flux flow resonances. This was achieved by varying the length of the resonator and observing the decrease of resonance voltage with increasing resonator length, see (7.1).

The *IV* characteristics of the bicrystal junctions used by Edstam were quantitatively RSJ like. Therefore, it was straightforward to subtract the background voltage dependent supercurrent I_{s0} from the measured *IV* curves to obtain the frequency spectra of the change in voltage dependent supercurrent due to the resonator. The resonant voltages were greater than the junction I_cR_n product, and so could then be fitted to (7.5) using the impedance of an open ended transmission line as the load impedance, with the surface resistance of the YBCO as a parameter. Extremely good fits to (7.5) were obtained, and the YBCO surface resistance was determined between 50GHz and 1THz[113]. Edstam's thesis[132] also contains good fits to (7.7) for junctions with resonant voltages below the I_cR_n product.

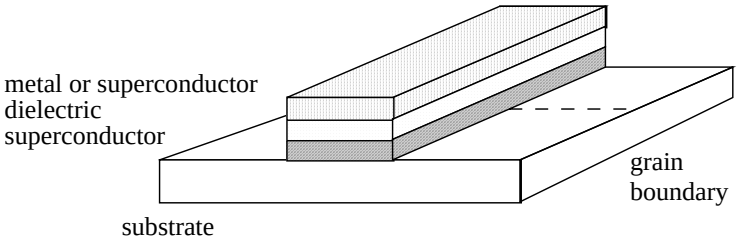

Figure 7.5. A grain boundary high T_c Josephson junction, shunted with an external transmission line.

Subsequent work focused on the determination of the YBCO surface resistance in the frequency range up to 1THz[113]. The YBCO penetration depth was measured at microwave frequencies[111]. The junction was coupled to a variety of both lumped and distributed resonator geometries[135]. In the latter case the theoretical spectrum of the normalised voltage dependent supercurrent fitted for the particular shunt impedance fitted well to the measured spectrum for all the geometries tested.

7.3 Mask design and films measured

The resonator designs tested are shown in Fig.7.6. All resonators had a cross section of the form in Fig. 7.6a, with a YBCO bottom electrode, various thicknesses of STO dielectric, and a gold top electrode. For the two dimensional resonators, electrode lengths *a* ranged from 25 to 175μm in 25μm increments. For the one dimensional resonators (1D_res), *a* ranged from 60μm to 160μm in 20μm increments. The junction width was kept at 2μm in all cases. The width *w* of the one dimensional resonator was defined by the gold top electrode and was equal to 4μm. For the two dimensional resonators, *a*=*w*. The contact pad next to the 3tdev resonators enabled the STO to be voltage biased with the YBCO as ground to test for tunability of the permittivity.

The wavelength λ_{1D} at resonance of the 1 dimensional resonator is given by (7.9), where *n* is a positive integer.

$$\lambda_{1D} = 2a/n \tag{7.9}$$

The wavelength λ_{2D} for the 2 dimensional resonators is given by (7.10), where both *n* and *m* are positive integers.

$$\lambda_{2D} = \sqrt{2}a\left(\frac{1}{n^2}+\frac{1}{m^2}\right)^{1/2} \tag{7.10}$$

From (7.9) and (7.10) it can be seen that the wavelength of the first order resonance is equal to twice the resonator length for both the 1 and 2 dimensional resonators.

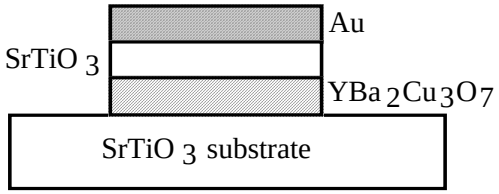

Figure 7.6a. The resonator cross section (not to scale).

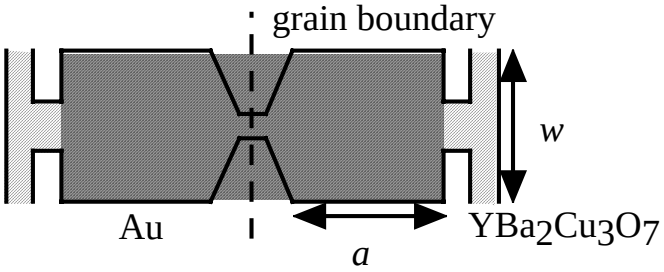

Figure 7.6b. Plan view of the xros two dimensional resonators (not to scale).

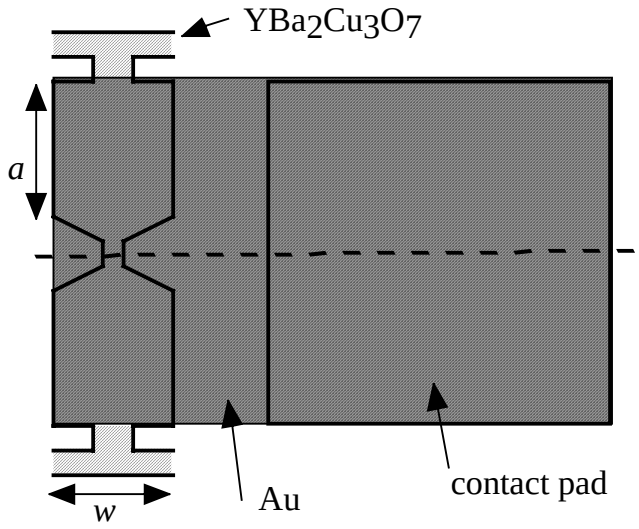

Figure 7.6c. Plan view of the 3tdev two dimensional resonators (not to scale).

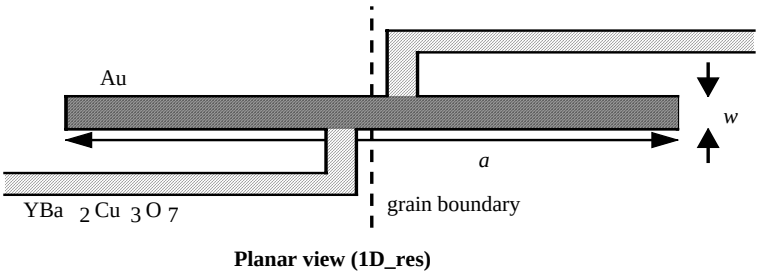

Figure 7.6d. Plan view of the linear one dimensional resonators (not to scale).

The capacitance per unit length of the resonators is given by (7.11).

$$C_1' = \frac{\varepsilon_0 \varepsilon_{RTF} w}{d} \tag{7.11}$$

The inductance per unit length of the one and two dimensional resonators is given by (7.12)[11].

$$L_1' = \frac{\mu_0}{w}\left[d + \delta_s + \lambda_L \coth\left(h/\lambda_L\right)\right] \tag{7.12}$$

Here, d is the thickness of the STO dielectric, δ_s is the skin depth of the gold (see section 1.4.5) and h is the thickness of the YBCO. The final term in (7.12) describes the magnetic field penetration into the superconductor when $h \sim \lambda_L$. The use of (7.11) and (7.12) for the capacitance and inductance per unit length ignores fringing fields at the edges of the resonator. The surface resistance of the gold $R_{s,Au}'$ is given by (7.13).

$$R_{s,Au} = \frac{1}{\sigma \delta_s} \tag{7.13}$$

σ is the gold conductivity, which is $4.2 \times 10^7\ \Omega^{-1}m^{-1}$ at 4.2K. The gold surface resistance is proportional to the square root of the frequency. In the two fluid model, the YBCO surface resistance $R_{s,YBCO}'$ is given by (7.14) (see section 1.4.5).

$$R_{s,YBCO} = k_{4.2}\omega^2 \tag{7.14}$$

The contributions add such that the resistance per unit length R' is given by (7.15).

$$R' = \frac{R_{s,Au} + R_{s,YBCO}}{w} \tag{7.15}$$

The conductance per unit length *G'* of the transmission line is calculated from the dielectric loss tangent and (1.53).

The thicknesses of the films used are given in Table 4.1. The xros24d and 1D_res films were deposited at the same time on a single 10x10mm bicrystal substrate, which was then cut in half and patterned. This ensured exactly the same film parameters for the two different resonator geometries.

7.4 Measurements of the dielectric properties of STO using Josephson junction driven resonators

7.4.1 A 50nm STO film with two different resonator geometries

Fig. 7.7 shows a plot of the *IV* characteristic of the xros24d 50μm resonator before and after the deposition of the gold top electrode. The resonances, indicated by arrows, appear only after the gold deposition, indicating that they are due to coupling of the junction to the external transmission line, and that they are neither Fiske resonances or flux flow resonances in the junction which would have been observed in the *IV* characteristic prior to gold deposition.

This point is emphasized further by Fig. 7.7, which shows the differential resistance (d*V*/d*I*) versus voltage for the 125μm device on xros24d measured before and after gold deposition. The first peak is due to noise rounding of the critical current step, and the subsequent peaks are

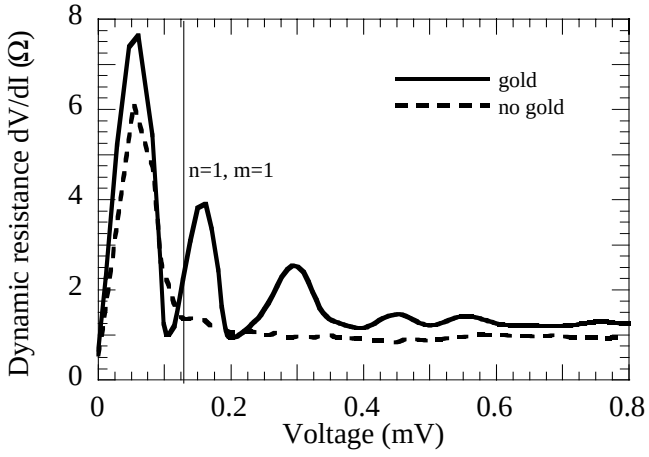

Figure 7.7. The dynamic resistance (d*V*/d*I*) versus voltage at 4.2K for the 125μm resonator on xros24d with and without a gold top electrode. The location of the first order (parallel) resonance is indicated.

the resonances in the *IV* curve, which again appear only after gold deposition. The resonant voltages also remained the same under an applied magnetic field, and decreased with increasing resonator length according to (7.1).

The dynamic resistance of the 160μm resonator on 1D_res at 40K with and without a small applied magnetic field is shown in Fig. 7.8. The resonant voltage was assumed to be halfway between the maxima and minima in the d*V*/d*I* curve. The *IV* characteristic is also shown, to indicate the corresponding position of the resonance on the *IV* curve. In some cases it was necessary to apply a magnetic field to observe the lower order resonances, as otherwise they were obscured by the switching from the zero voltage state. At high temperatures lower order resonances are obscured by the noise rounding in the *IV* curve.

It is crucial to correctly determine the orders of the resonances in order to be able to calculate ε_{RTF} for the films. As an example, equations (7.1), (7.9), (7.11) and (7.12) can be used to calculate ε_{RTF} from the 0.24mV resonance in Fig. 7.8. If the resonance is first order then ε_{RTF}=7.3 and if it is second order then ε_{RTF}=30.0, using the parameters given in Table 7.1.

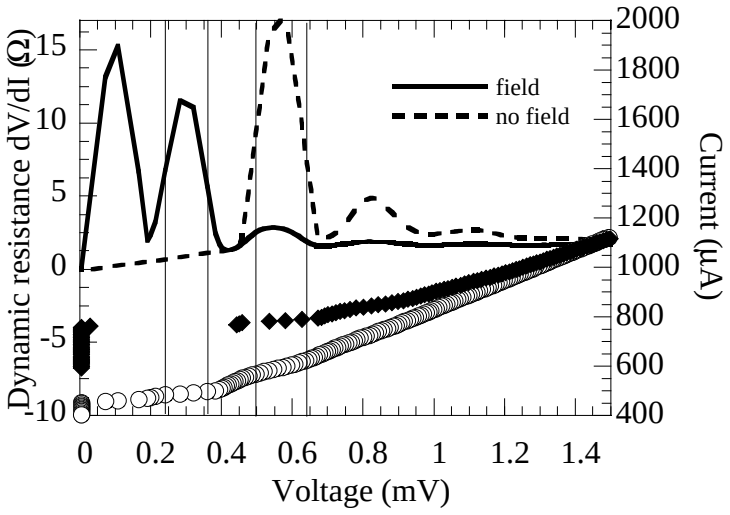

Figure 7.8 The dynamic resistance (dV/dI) and current versus voltage for the 160μm resonator on 1D_res at 40K, both with and with out an applied magnetic field. The first four resonances are indicated by lines.

Table 7.1 Parameters used for determination of ε_{RTF} and fitting of dynamic resistance versus voltage.

σ (40K) ($\Omega^{-1}m^{-1}$)	$R_{S,YBCO}$[138] (at 18.9GHZ, 40K) (mΩ)	Tan δ [119]	λ_L(40K) (nm) [22]	I_c (40K), in field (μA)	R_n (40K) (Ω)	C_j (4.2K) (pF)
4.07×10^{7}	0.5	0.06	143	451	1.62	0.09

Therefore, to distinguish whether the 0.24mV resonance was first or second order, the normalised voltage dependent supercurrent was simulated with (7.7). Substituting this result into (7.2) and differentiating numerically yields the dV/dI versus V curve. The junction was shunted with the load impedance for an open ended transmission line given by (7.8), again using the parameters from Table 7.1. The result of this curve fitting is shown in Fig 7.9 for the two different values of ε_{RTF}. For ε_{RTF}=7.3 the criterion $|Z_L|>R_n(V_c/V)$ is satisfied for V>0.37mV, and for ε_{RTF}=30.0 it is satisfied for V>0.48mV. The best fit is clearly obtained for ε_{RTF}=30, and reasonable agreement with the fit is obtained even for $|Z_L|<R_n(V_c/V)$, so the 0.24mV resonance is second order.

The first peak in the measured dV/dI in Fig. 7.9 is due to noise rounding of the critical current step and not the external resonator. The discrepancy between the experimental and the fitted dV/dI at high voltages is probably due to deviations of the junction behviour from the RSJ model.

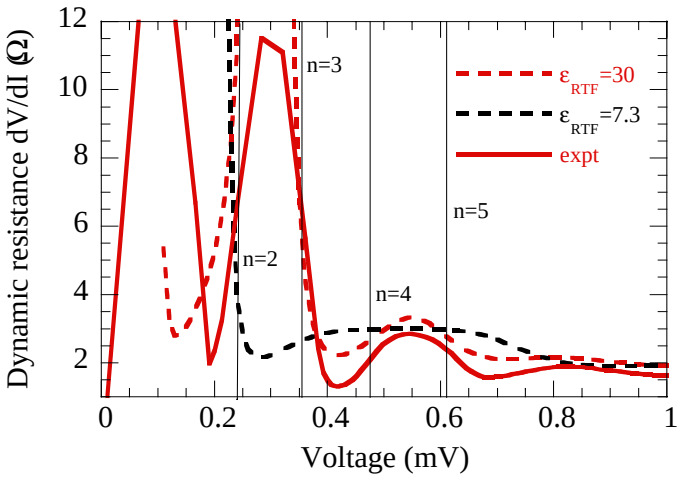

Figure 7.9 The dV/dI versus V curve of the 160μm resonator at 40K in a small magnetic field, with fits from (7.7) for two different values of ε_{RTF} (I_c=452μA, R_n=1.62Ω, C_j=0.17pF). The resonances are indicated by lines.

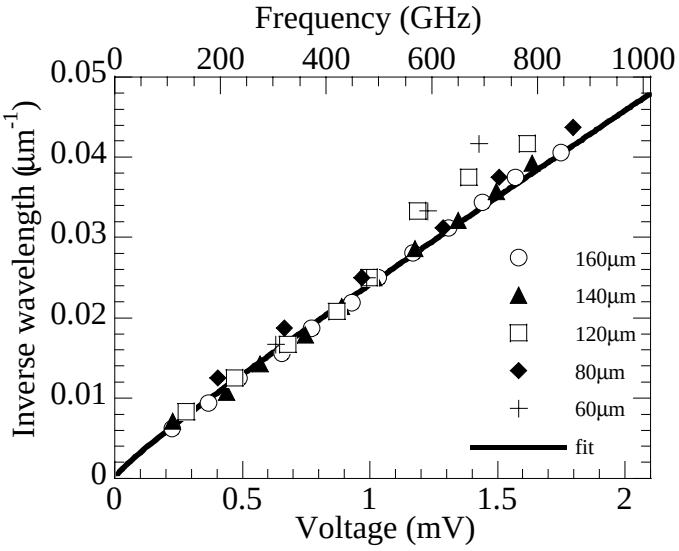

Figure 7.10 The 1D_res dispersion relation at 4.2K, and a fit to the dispersion relation from (1.38).

Once the orders of the resonances have been determined for one length of transmission line, the resonance orders for the lines of different length can be deduced from (7.1).

At 40K, it was possible to achieve reasonable fits to the measured dV/dI versus voltage curves for all the linear resonators measured with ε_{RTF} determined from one of the resonances and the parameters in Table 7.1. At lower temperatures where the junction I_cR_n products were larger, the criterion $|Z_L|>R_n(V_c/V)$ is satisfied only for voltages larger than most of the lower order resonances (e.g. 1.06mV for the 140μm resonator at 4.2K), and furthermore the junctions were more hysteretic, so the fits were not as good.

The dispersion relation for the linear resonators at 4.2K is shown in Fig. 7.10 It is seen to be linear over the entire frequency range observed, from 100GHz to 900GHz. The dispersion relation varied linearly with frequency over the entire temperature range measured, from 4.2K up to 75K above which temperatures resonances were no longer visible in the *IV* curves of any of the junctions. A fit to the dispersion relation using ε_{RTF}=35 (from averaging the dielectric constants calculated from each resonance) was obtained from the imaginary part of the complex propagation constant γ given by (1.38), and is also plotted in Fig. 7.10. The fit takes into account frequency dependence of the dispersion relation arising from the gold skin depth and the surface resistance of the gold and the YBCO. However, it can be seen that the dispersion relation still varies linearly with frequency in the range observed. The YBCO surface resistance at 4.2K was 0.1mΩ at 18.9GHz[138]. The shift to lower voltages of the

higher order resonances is probably due to discrepancies between the actual YBCO surface resistance and that of the parameter used.

The position of each resonance can now be used to calculate a value for ε_{RTF} with the parameters in Table 7.1 and the two fluid model temperature dependence of the penetration depth. For a given resonator length at a given temperature, ε_{RTF} for each order of resonance was averaged, and is plotted versus temperature in Fig. 7.11.

For the xros24d square resonators, the resonances are not at half integer wavelengths, see (7.10). Hence, (7.8) for the load impedance is no longer valid and fits to the dV/dI versus V curve such as that in Fig 7.9 were not obtainable. Also, exact determination of the wavelength from (7.10) for the higher order resonances was not possible, as the resonator was not a perfect square. However, the first order resonance, shown in Fig. 7.7 for the 125μm resonator at 4.2K with n=1 and m=1 in (7.10), has the same wavelength and therefore the same resonance voltage as the equivalent linear resonator. The dielectric constant calculated from the position of this resonance is plotted versus temperature in Fig. 7.11. The resonator length was assumed to be a plus 10μm, the length of the tapered section of junction track. This resonance has a current antinode in the centre of the square, with current nodes round the resonator edges and therefore at the junction. The length chosen gave best agreement with the dielectric constant from the linear resonators. No error bars are plotted for the two dimensional resonators, as only one resonance was used to determine this dielectric constant. With the exception of the 60μm resonator, the dielectric constants calculated from the linear resonators agree much better with each other than those from the two dimensional resonators, because it was possible to evaluate ε_{RTF} over the entire dispersion relation rather than from only the first order resonance.

The agreement between the dielectric constants calculated from the two different resonator geometries indicates that fringing fields at the edges of the resonators were not significant in the determination of the field distribution. This is assumed implicitly in the use of a distributed circuit model for a transmission line.

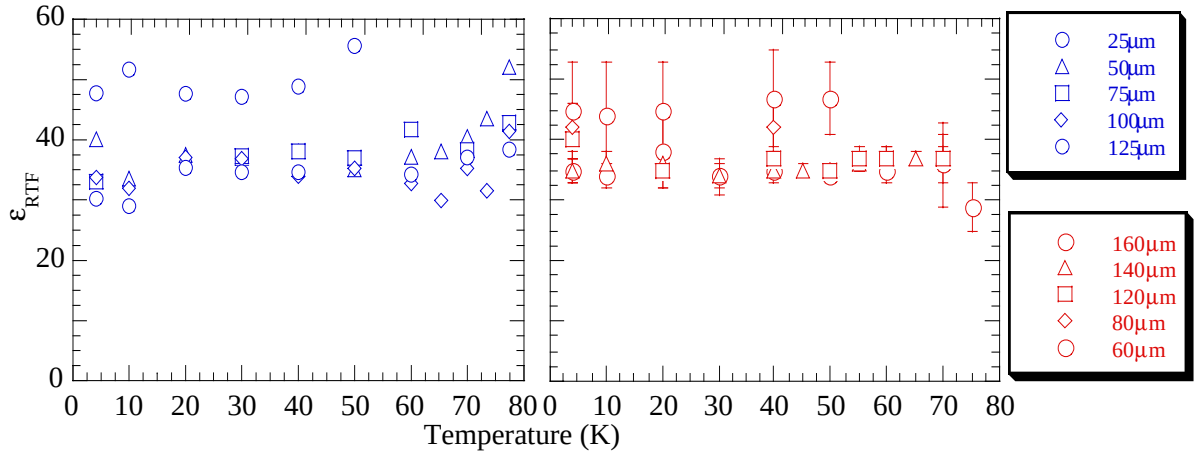

Figure 7.11. The dielectric constant of the 50nm STO film versus temperature from the positions of the 1D_res resonances (blue) and the xros24d first order resonances (red).

7.4.2 Further STO film thicknesses

The two further STO film thicknesses (100nm and 200nm) investigated were patterned with two dimensional square resonators. Dynamic resistance curves were measured for all the junctions over the temperature range for which resonances were visible. The dynamic resistance of the 50μm resonator on 3tdev at 4.2K is shown in Fig 7.12. Resonances are visible up to 0.91mV or 440GHz.

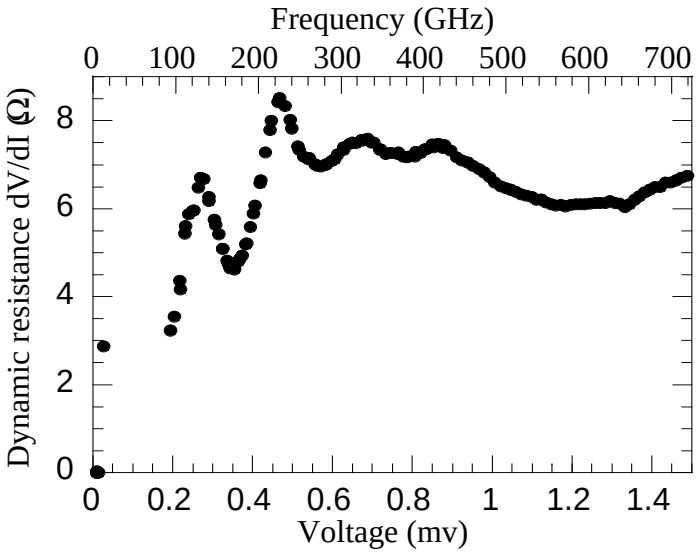

Figure 7.12. The dynamic resistance of the 50μm resonator on 3tdev, in a small magnetic field at 4.2K. (200nm STO)

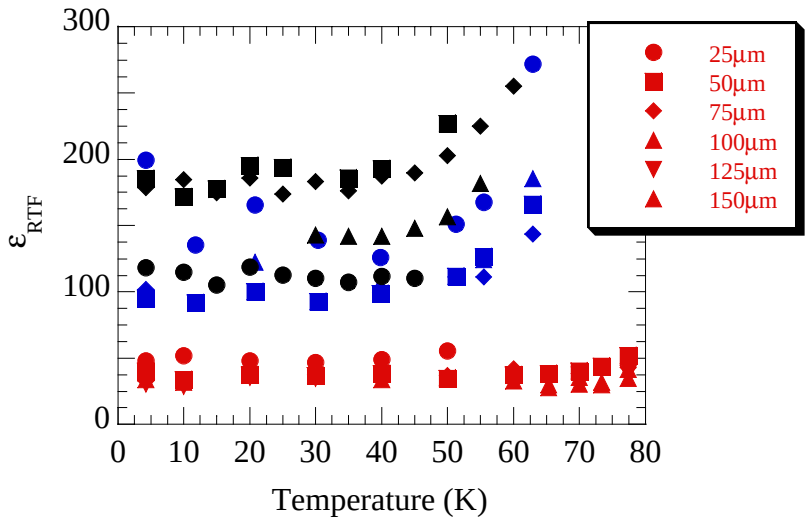

Figure 7.13. The variation of dielectric constant with temperature for the STO film thicknesses measured. The symbol shape indicates resonator size, and the 50nm thick films are red, the 100nm blue, and the 200nm black.

However, at 4.2K, only the 25, 50 and 75µm resonators on the 100 and 200nm films displayed definite first order resonances. The dispersion relation for these resonances could be extrapolated to predict the first order resonant voltages for the longer resonators. However, the predicted voltages were so low as to be obscured by the switching from the zero voltage state at low temperatures. As the wavelength of the higher order resonances was not clear, a dispersion relation with as many points as that in Fig 7.10 could not be plotted. The dispersion relation for the first order resonances observed was linear at all temperatures.

The dielectric constant calculated from the first order resonant voltages from the 2 dimensional resonators is plotted in Fig. 7.13. It can be seen ε_{RTF} from the 25µm resonators on the 100nm and 200nm films does not agree well with that from the larger resonators. The dynamic resistance at the resonance on the 25µm resonators changed rapidly for a small change in current. Its shape and position was therefore difficult to determine.

7.4.3 Tuning of the STO dielectric constant

The 3tdev resonators were patterned to allow the 200nm STO dielectric film to be voltage biased, as shown in Fig. 7.14 and Fig 7.6.

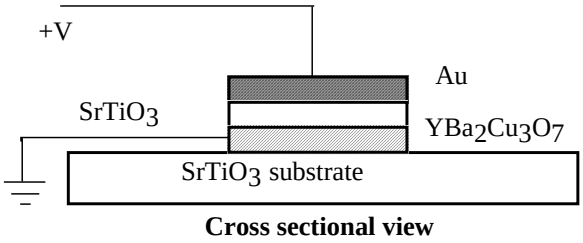

Figure 7.14. Voltage biasing of the STO dielectric on 3tdev.

Figure 7.15 shows the *IV* curve for the 50μm resonator at 30K for a series of different dielectric voltage biases. The resonant voltages can be seen to increase with increasing voltage bias. Since no magnetic field was applied in this measurement, the resonances can be neither Fiske resonances nor flux flow resonances. Furthermore, the critical current branch must be at 0V, which provides an absolute reference indicating that changing voltage offsets (from e.g., thermocouple e.m.f's) were not responsible for the change in position of the resonant voltages. The change in critical current from 176μA at 0V to 174μA at 1.8V is within experimental error (see Fig 5.18(a), showing the width of a distribution of repeated measurements of the critical current). Therefore, the increase in the resonant voltage with increasing dielectric voltage bias is believed to be due to tuning of the dielectric constant of the STO dielectric.

Fig 7.16 shows d*V*/d*I* versus *V* curves at 30K for the 50μm junction at various dielectric voltage biases. For these measurements, a small magnetic field was applied so that the critical current was suppressed and the junction followed the return branch of the *IV* characteristic shown in Fig. 7.15. The first order resonant frequency at 116GHz can be tuned to 90GHz at a dielectric voltage bias of -2V, and 140GHz at +2V.

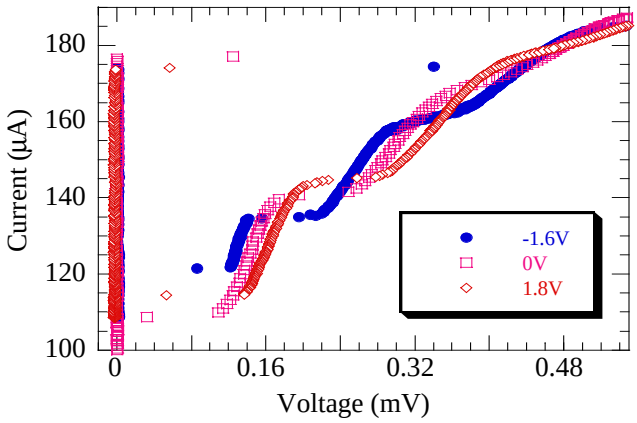

Figure 7.15. The *IV* curves for the 3tdev 50μm resonator at 30K for various dielectric voltage biases.

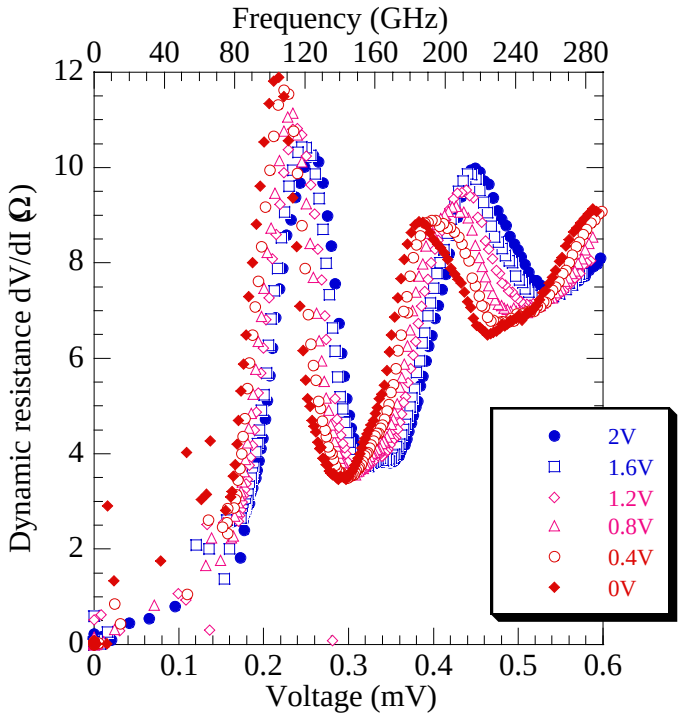

Figure 7.16 Dynamic resistance curves at various dielectric voltage biases for the 50μm resonator at 30K.

It is evident that the higher order resonant frequencies also tune with dielectric voltage bias. Above a dielectric voltage bias of ±2V, there was a significant leakage current (>5μA) through the dielectric which was apparent through asymmetry in the positive and negative value of the critical current. The measurement of the dielectric voltage bias above ±2V was therefore unreliable, and also current injection into Josephson junctions can give rise to flux flow resonances which change position with injection current[139].

Tuning of the resonant frequency with dielectric voltage bias was observed between 4.2K and 60K for the 50μm junction, and also at temperatures where the 25μm, 75μm, 100μm and 125μm resonators were tested. The first order resonant frequency of the 25μm resonator could be tuned between 237GHz and 284GHz for dielectric voltage biases of -1.6V and +2V, and the second order resonant frequency between 297GHz and 317GHz.

The dependence of ε_{RTF} on electric field and dielectric bias voltage at various temperatures is shown in Fig. 7.17. No hysteresis of $\varepsilon_{RTF}(E)$ was observed when the dielectric voltage bias was swept up and down between ±2V. No maximum was observed in $\varepsilon_{RTF}(E)$, due to the limitations imposed on the maximum possible dielectric voltage bias by the leakage current.

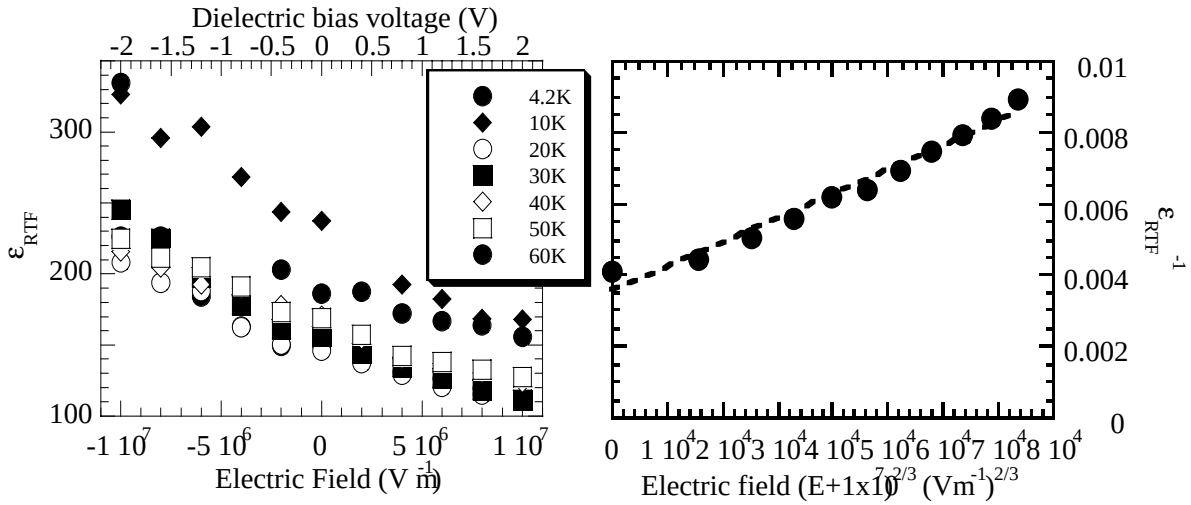

Figure 7.17 The tuning of ε_{RTF} with electric field (dielectric bias voltage) at temperatures from 4.2K to 60K, and a linear fit to ε_{RTF}^{-1} versus $(E+1x10^7)^{2/3}$ at 30K.

The shift in the maximum of $\varepsilon_{RTF}(E)$ away from 0V is believed to be due to the formation of a Schottky barrier between the Au top electrode and the STO, as discussed in section 3.4.3. Assuming that the maximum in $\varepsilon_{RTF}(E)$ occurs at $-1x10^7$ Vm^{-1} (2V), the data shown in Fig 7.17 could be fitted to either (3.5) or (3.6). For STO films with gold electrodes, 2V is a typical value for the shift in maximum of $\varepsilon_{RTF}(E)$ [83]. It was found that a linear fit was obtained when ε_{RTF}^{-1} was plotted versus $E^{2/3}$ rather than E^2, so the behaviour of $\varepsilon_{RTF}(E)$ is in the high field limit. There was too much scatter in the values of A_2 obtained to ascertain its temperature dependence. However, the maximum and minimum values obtained agreed with previous

Table 7.2 Measurements of A_2 from at various temperatures for both thin film and bulk STO.

Temperature (K)	$A_2(T)$ Vm^5 $(As)^{-3}$	*Reference*
10K	$4.6x10^9$ (minimum)	This work ~100GHz
30K	$1.7x10^{10}$ (maximum)	This work ~100GHz
4.2K	$8x10^9$	Bulk STO, Christen *et al*[83]
90K	$4x10^9$	Bulk STO, Christen *et al*[83]
295K	$1.2x10^{10}$	92nm STO, Abe and Komatsu[88]

measurements of both bulk and thin film STO (see Table 7.2), and as discussed in section 3.4.2 and from (3.12) only modification of $A_1(T)$ is required to model the size effect[87].

7.5 Discussion

7.5.1 Frequency dependence of ε_{RTF}

The fits obtained to the dynamic resistance of the junctions shunted with a linear resonator with a 50nm STO film required a frequency independent dielectric constant (see Fig. 7.9). The linear dispersion relation obtained between frequencies of 100GHz and 900GHz also showed that the dielectric constant was independent of frequency. This should be contrasted with the dispersion relation for the Fiske resonances, shown in Fig. 6.5 and Fig. 6.9, which required the dielectric constant of the single crystal STO to be strongly frequency dependent in the same frequency range. Therefore, for the 50nm STO film, the transverse soft optic phonon has hardened to a frequency well above 900GHz at 4.2K. This confirms the prediction of Zhou and Newns[74] that the soft optic phonon hardens in incipient ferroelectric thin films (see section 3.4.3). The absence of the soft optic phonon in the 50nm STO film is consistent with the far infra red ellipsometry experiments of Sirenko *et al*[140]. These experiments showed that the soft optic phonon hardened to 1.9THz at 4.2K in a 2μm thick STO film.

For the 100nm and 200nm STO films, resonances were observed up 340GHz and 440GHz respectively. Waves are not expected to propagate in STO just above the soft optic phonon frequency where the dielectric constant is negative, so these frequencies represent lower limits for the soft optic phonon frequencies in these films.

It can also be seen from Fig. 7.18 that for large YBCO surface resistances the resonant frequencies are lowered, particularly for higher order resonances. This effect is believed to be one of the causes of the discrepancy at high voltages between the fit to the dispersion relation for the linear resonators and the measured data, shown in Fig 7.10. This effect is also one of the causes of the spread in the values of the dielectric constant determined from each resonance in the dispersion relation from the linear resonators. For example, whilst the dielectric constant calculated from the second order resonance in the 160μm resonator at 40K was 30, and this gave a reasonable fit to the dynamic resistance curve, that calculated from

averaging all the resonances from all the resonator lengths in the dispersion relation was 34±4.

The errors on the measurement of the dielectric constant, for example 35±2 for the 160μm linear resonator at 4.2K, i.e. 6%, are too large to draw any conclusions about Curie-von Schweidler frequency dependence of the dielectric constant, which as discussed in section 3.4.4 leads only to a 7% decrease in the dielectric constant between 1mHz ad 20GHz. No Maxwell Wagner relaxation of the capacitance was observed for the linear resonators on the 50nm STO films between 100GHz and 900GHz. However, Hwang *et al*[89] do not rule out a Maxwell Wagner step at higher frequencies. The absence of a Maxwell Wagner step is therefore inconclusive as to whether or not the film is fully or partially depleted.

7.5.2 The magnitude of ε_{RTF}

There is too much scatter in the values of the dielectric constant obtained in Fig 7.13 to draw any quantitative conclusions about the size effect. However, it is clear that the 50nm STO film had a lower dielectric constant than the 100nm and 200nm films, indicating that the size effect was present, in agreement with the 490nm film thickness from the Zhou and Newns theory below which the size effect becomes significant (see section 3.4.3). The films measured had gold top electrodes. Therefore, the decrease of dielectric constant with film thickness observed

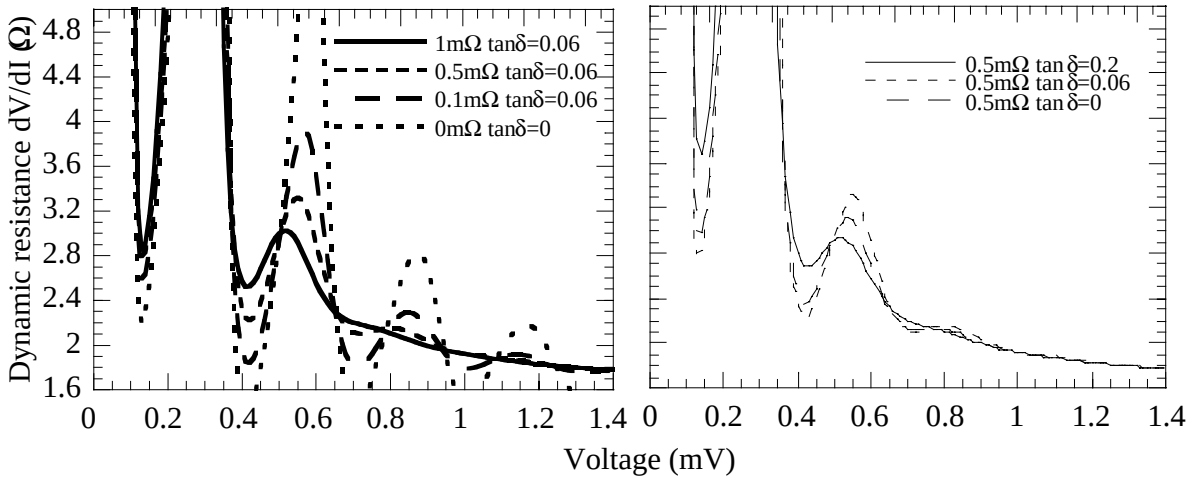

Figure 7.18. Dynamic resistance versus voltage curves for various YBCO surface resistances (values given at 18.9GHz) and STO loss tangents. The junction parameters are those from the 160μm linear resonator at 40K shown in Fig 7.9 (I_c=452μA, R_n=1.62Ω, C_j=0.17pF).

is consistent with the Vendik *et al*[86] prediction and the Hwang *et al*[89] experiment that the size effect occurs only in films with metallic electrodes.

For the 100nm and 200nm films, there is a possible increase of the dielectric constant with temperature, but the resonances were not observed to high enough temperatures to determine whether or not there was a peak..

The experiments on tuning of the dielectric constant showed that the values in Fig 7.13 were not the maximum of the dielectric constant, due to the effect of the Schottky barrier at the Au/STO interface. The maximum measured ε_{RTF} was 326 at 10K for the 50μm resonator with a –2V dielectric voltage bias and a 200nm STO film. The agreement of the values of χ(T) obtained with those from both thin film and bulk STO show that the Ginzburg-Landau-Devonshire theory for ferroelectrics described in section 3.2.2. is obeyed by the 200nm film.

The magnitude of the dielectric constant measured agreed reasonably well with values reported in the literature, although the dielectric constant for the 50nm film was low. Table 7.3 gives a comparison.

Similar structures to that used in 3tdev have been used to observe electric field effects on the Josephson junction critical current[141,142]. However, for the 3tdev devices no significant dependence of the junction critical current or the junction return current on the dielectric voltage bias was found.

Table 7.3 The dielectric constant of thin film STO.

ε_{RTF}	*Temperature (K)*	*Thickness (nm)*	*Frequency*	*Reference*
35±2	4.2	50	100-900GHz	160μm linear resonator, this work
326	10	200	95GHz, -2V bias	50μm square resonator, this work
1400	4.2	1000	1.5GHz	Dalberth *et al*[119]
120	4.2	100	10kHz	Christen *et al*[83]
280	295	92	100kHz	Abe and Komatsu[88]

It was not possible to determine the loss tangent of the STO film from the fits to the dynamic resistance versus voltage curves. This would have required the variation of two independent parameters which have the same effect on the dynamic resistance versus voltage curves, as shown in Fig. 7.18. An estimate of the loss tangent would have been possible had a independent measurement of the surface resistance of the YBCO films used been available. The YBCO was the dominant cause of resonator losses.

7.6 Conclusion

The dielectric constant of thin film STO has been measured at frequencies from 50GHz to 900GHz at temperatures from 4.2K to 77K, using a Josephson junction coupled to an external resonator. Reasonable agreement was obtained between the measured dynamic resistance versus voltage curve and that predicted from a junction shunted with a load impedance of an open ended transmission line resonator. For linear resonators, the dielectric constant of a 50nm STO film was found to be independent of frequency between 100GHz and 900GHz, and a typical value was 34±2 at 40K, calculated from each resonant voltage in the dispersion relation. This value was found to agree with that determined for another area of the 50nm film using a square resonator.

The frequency independence of the dielectric constant of the 50nm STO film indicated that the soft optic phonon had hardened, in agreement with theoretical predictions of an intrinsic dead layer in thin STO[74] films and recent infra red ellipsometry experiments[140].

The size effect was observed for the series of film thicknesses measured.

The dielectric constant of a 200nm STO film was found to be tunable at with a ±2V applied voltage bias between 246 and 111, at a frequency of around 100GHz. Reasonable agreement was found between the third order GLD parameter γ and that measured in previous experiments on both thin film and bulk STO.

Chapter 8: Capacitance as a probe of high angle $YBa_2Cu_3O_{7-\delta}$ grain boundary current transport

8.1 Introduction

From the point of view of applications the most disappointing aspect of the high T_c superconductors is the low critical current of bulk, polycrystalline samples. Soon after the discovery of the high T_c compounds it was experimentally proven that the limiting factor was the low critical current at the grain boundary[39]. More recently, progress has been made in enhancing the critical currents of grain boundaries by doping their electrodes[143,144] [145,146]. Most recently the critical current of the grain boundary itself has been enhanced selectively by preferential doping[147]. This is expected to have significant technological implications for the manufacture of high T_c cables.

However, a detailed physical understanding of the current transport in these grain boundaries is still lacking[145]. Various models have been proposed to explain grain boundary current transport in the high T_c superconductors[31,99,127]. Typically, the models are then invoked to explain scaling laws between the junction I_cR_n product and the critical current density[31], or between the junction critical current density and its resistance area product[148-150]. Scaling of junction capacitance per unit area with resistance area product has been observed previously[98], but has since been rarely commented upon. The capacitance has the possibility of being a useful probe of grain boundary current transport, as it is directly related to properties such as the width of the insulating barrier layer.

In this chapter, the models of grain boundary current transport in the high T_c superconductors are reviewed. The experimental data supporting each one is discussed. Then, scaling relationships are presented between the critical current density, resistance area product and capacitance per unit area measured for the doping enhanced junctions and from those in earlier chapters. Finally, each model is tested for its applicability to the measured experimental data.

8.2 Models of grain boundary current transport

There are two common features of all the models of grain boundary current transport. It is assumed that the high angle grain boundaries contain a narrow, insulating region along the

grain boundary. The presence of Fiske resonances and the large resistivites of the high angle grain boundaries provides supporting evidence for such an insulating layer. The supercurrent is assumed to cross this region by direct tunneling.

8.2.1 The intrinsically shunted junction model

The intrinsically shunted junction model proposed by Halbritter[151] assumed that there were two channels for quaisparticle current transport across the (YBCO) grain boundary, via direct or resonant tunneling. It was argued that the grain boundary consisted of a disordered, insulating region with a high density of localised states. This was a reasonable assumption since it was known that YBCO did not have a metallic phase and that oxygen disorder or depletion rendered YBCO insulating. The measured grain boundary resistivities were also typical of those of semiconductors. The carrier density in the cuprates (~10^{21} cm^{-3}[50]) is close to the metal insulator transition in 2 dimensions. The supercurrent transport was assumed to be dominated by direct tunneling across the barrier, since a Cooper pair cannot occupy a single localised state. The critical current density J_c of the barrier is therefore given by (8.1).

$$J_c \propto \exp(-2\kappa t_J) \tag{8.1}$$

In (8.1), t_J is the thickness of the barrier, R_n is its normal state resistance, A is the geometrical area of the junction (i.e. film thickness times junction width) and κ is a decay length given by,

$$\kappa = \left(\frac{2m\phi}{\hbar^2}\right)^{1/2} \tag{8.2}$$

where m is the effective mass of the charge carriers and ϕ is the height of the potential barrier. It was proposed that the quasiparticle current density J_N was dominated by resonant tunneling across the barrier, via a localised state at $t_J/2$, and given by (8.3).

$$J_N \propto \frac{1}{R_n A} \propto \exp(-\kappa t_J) \tag{8.3}$$

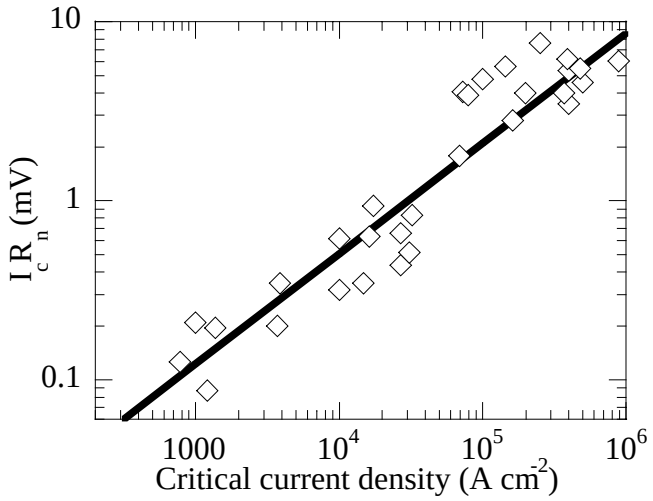

Figure 8.1 The scaling of I_cR_n product with J_c for YBCO grain boundary junctions with misorientation angles from 15° to 45° from Gross and Mayer[49,51,152]. The line is a fit to $I_cR_n \propto J_c^{0.6}$.

Combining (8.1) and (8.3) yields (8.4) for the scaling of the I_cR_n product with the critical current density or resistance area product.

$$I_cR_n \propto J_c^{1/2} \propto \left(1/R_nA\right) \tag{8.4}$$

The scaling of I_cR_n with J_c measured by Gross *et al*[49,51,152] for YBCO grain boundary junctions grown on STO bicrystals with misorientations from 15° to 45° is shown in Fig. 8.1. It was found that $I_cR_n \propto J_c^{0.6}$ in reasonable agreement with (8.4). Furthermore, for 90° basal faced tilt boundary junctions grown on MgO bicrystals Russek *et al*[153] found that $I_cR_n \propto (1/R_nA)^{0.85}$, also in reasonable agreement with the intrinsically shunted junction model prediction (8.4). The expressions (8.1) to (8.4) are justified in more detail by Halbritter[151,154]. Gross *et al*[31] have also showed that the scaling (8.4) was a universal property of all YBCO and BSCCO step edge and bicrystal junctions manufactured up to 1997.

The scaling of I_cR_n product with $J_c^{0.6}$ indicated that resonant tunneling dominated the quasiparticle transport across the grain boundary for the Gross and Mayer junctions, and that the intrinsically shunted junction model applied. However, the quasiparticle transport across the grain boundary could also be via direct tunneling, or via a combination of the two. In the case where the quasiparticle transport is dominated by direct tunneling, $J_c \propto (R_nA)^{-1}$ and I_cR_n is a constant. This is the behaviour observed in conventional low T_c SIS tunnel junctions where the

I_cR_n product is determined by the magnitude of the superconducting gap. Enpuku *et al*[148] fitted such a two channel quasiparticle transport mechanism to scaling of J_c with R_nA for their 24° to 36° misoriented YBCO bicrystal grain boundary junctions. It was found that at 77K direct tunneling dominated the quasiparticle transport mechanism.

If the grain boundary capacitance $C=\varepsilon_0\varepsilon_R A/t_J$, the intrinsically shunted junction model predicts (8.5) and (8.6) for the scaling of critical current density and resistance area product with capacitance per unit area.

$$J_c \propto \exp\left(-\frac{2\kappa\varepsilon_0\varepsilon_R A}{C}\right) \tag{8.5}$$

$$\frac{1}{R_nA} \propto \exp\left(-\frac{\kappa\varepsilon_0\varepsilon_R A}{C}\right) \tag{8.6}$$

In (8.5) and (8.6), ε_R is the dielectric constant of the barrier layer of the grain boundary.

Localised states in the barrier layer at the grain boundary would also give rise to a distribution of trapping times for carriers at the junctions. This leads to fluctuations of the grain boundary resistance and hence the critical current. The localised states are therefore a cause of the 1/*f* noise observed in the voltage noise power spectrum of SQUID's made from grain boundary junctions[155]. The lifetime of the localised states is too long to affect the grain boundary capacitance at the Josephson frequency.

8.2.2 The filamentary model

The filamentary model of current transport across the grain boundary was first suggested by Russek *et al*[153]. Subsequently, it has been developed further by Moeckly *et al*[98,99] and by Sydow *et al*[149,150].The model proposes that the grain boundary junction consists of two regions.

i) A thin, insulating barrier layer associated with the grain boundary itself.

ii) Regions of inhomogeneously oxygenated YBCO on either side of the barrier.

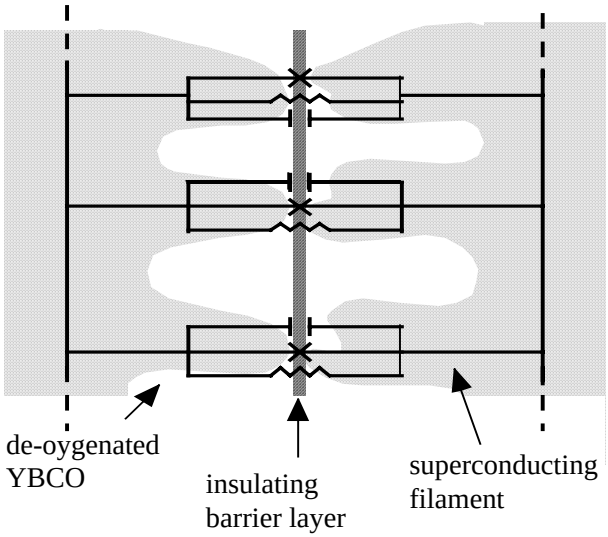

Figure 8.2 A schematic of the filamentary model of current transport across the grain boundary[99].

Superconducting filaments in the second region make contact to one another across the barrier layer. The grain boundary junction thus consists of an array of superconducting contacts. The junction critical current scales with the number of filaments. Resistive shunting arises from resonant or direct tunneling through the barrier layer. This occurs in areas where the filaments are separated by a sufficiently small distance such that the tunneling rate across the barrier is significant. Capacitive shunting of the junction comes about as the oxygen deficient areas of the second region act as an insulating dielectric. The model is shown schematically in Fig. 8.2, with the various RCSJ circuit elements in their correct positions.

As the number of filaments increases, so the critical current increases. The resistance decreases with the number of filaments. If a fraction y of the total junction area contains overlapping filaments, then $J_c = yJ_{c0}$, $R_nA = R_{n0}'/y$ and $C_s = yC_0$, where J_{c0}, R_{n0}' and C_0 are the critical current density, resistance area product and capacitance per unit area of a single filament. Eliminating y gives

$$J_c = {}^{J_{c0}R_{n0}'}\!\!\diagup\!\!_{R_nA} \tag{8.7}$$

$$J_c = \frac{J_{c0}}{C_{s0}} C_s \tag{8.8}$$

$$C_s = {}^{R_{n0}'C_{s0}}\!\!\diagup\!\!_{R_nA} \tag{8.9}$$

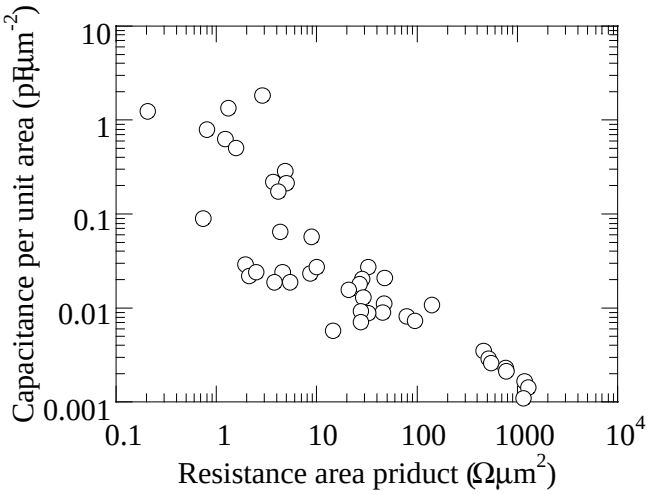

Figure 8.3 The scaling of capacitance per unit area with resistance are product for 90° basal faced tilt grain boundary junctions reported by Moeckly and Buhrman[98,99].

where C_s is the capacitance per unit area of the grain boundary. These expressions can be simply deduced by considering the consequences of increasing the number of filaments in contact across the grain boundary.

Moeckly and Buhrman[98,99] reported correlation of the capacitance per unit area with the resistance area product of their 90° basal faced tilt grain boundary junctions, as shown in Fig. 8.3.

The strongest evidence for the influence of oxygen disordered regions in the current transport across the grain boundary comes from oxygen annealing experiments. Sydow *et al*[149,150] studied the effects of repeated anneals at 500°C in ozone of bicrystal YBCO grain boundary junctions with a 24° misorientation. The anneals increased I_c and decreased R_n whilst the I_cR_n product remained constant. Only by annealing in an inert gas was it possible to reproduce scaling $I_cR_n \propto J_c^{0.6}$ as observed by Gross *et al*, shown in Fig. 8.1. It was established that there were two regions in the I_cR_n versus J_c plot. For $J_c<10^4$ A cm^{-2}, $I_cR_n \propto J_c^{0.6}$, but for $J_c>10^4$ A cm^{-2}, I_cR_n is constant and on the order of 1mV. This behaviour is shown in Fig. 8.4. The result was reproduced using electromigration instead of annealing.

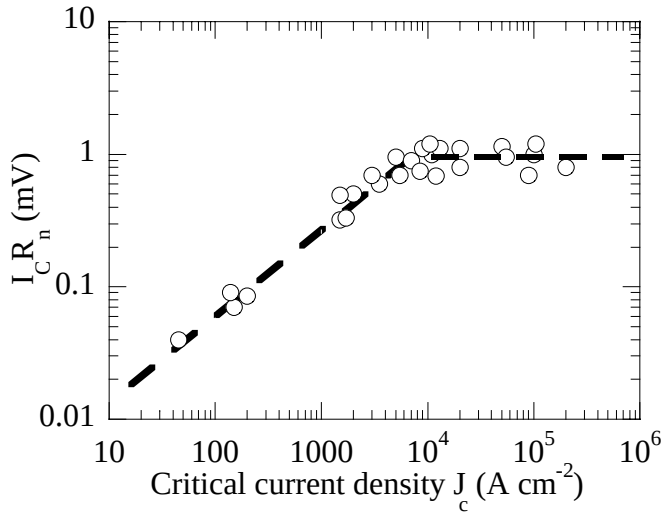

Figure 8.4 The saturation of I_cR_n product with J_c after annealing in ozone, from Sydow *et al*[150].

The I_cR_n saturation was believed to be the limiting effect of the insulating barrier layer. The ozone anneals increase the oxygenation of the second region containing the superconducting filaments and so increases the number of filaments. This increases I_c and reduces R_n, but the I_cR_n product is an intrinsic property of the barrier layer and so remains constant. The $I_cR_n \propto J_c^{0.6}$ scaling is observed when none of the YBCO adjacent to the barrier layer is fully oxygenated. The volume of oxygen deficient YBCO spreads outwardly from the barrier layer in a non-uniform manner. In this scaling region, very few or no superconducting filaments are in close contact across the grain boundary.

It should be noted that the junctions for which scaling of capacitance per unit area with resistance area product was observed in Fig. 8.3 fell into the saturated I_cR_n product region of Fig. 8.4. The relationships (8.7)-(8.9) are valid only when the I_cR_n products of the grain boundary junctions are saturated.

The dependence of the critical current density with position along the junction can be recovered by taking the inverse Fourier transform of the Fraunhofer pattern for the variation of critical current with applied magnetic field. For a grain boundary junction, the critical current density has been found to be inhomogeneous on a length scale of ~0.2μm[156]. It was found that for certain 5μm wide 24° YBCO grain boundary junctions the current was found to flow only in a 2μm wide area of the grain boundary. The critical current density has been shown to be inhomogeneous on the order of nanometres by measuring its correlation function[157]. These results also support the filamentary model of current transport across the grain

boundary.

8.2.3 Band bending

The band bending model of current transport across high angle grain boundaries in the high T_c superconductors was proposed by Mannhart and Hilgenkamp[127]. They were motivated by the success of a band bending model derived by Gurevich and Pashitskii[43] in explaining the dependence of critical current on grain boundary misorientation angle for low angle grain boundaries.

Mannhart and Hilgenkamp[127] also reviewed limitations of the intrinsically shunted junction and filamentary models. It was claimed by Mannhart and Hilgenkamp that there was no clear evidence for the existence of localised states with the required density, or that the quasiparticles could undergo a resonant tunneling conduction process via a single localised state. It was also stated there was no compelling evidence that there were layers at the grain boundary which had sufficient oxygen depletion to transform the cuprates into their insulating phases.

Models based upon oxygen deficiency also could not explain the universality of the scaling behaviour of the current transport properties of the cuprates. For example, YBCO and BSCCO grain boundaries were both shown to obey $I_cR_n \propto J_c^{0.6}$, by Gross *et al*[31]. However, when pressure is applied parallel to the a-axis of the unit cell of single crystal YBCO, T_c falls, but when the pressure is applied parallel to the b-axis T_c rises by approximately the same amount[43]. YBCO has anisotropic in plane presssure derivatives. In contrast, BSCCO has isotropic in plane pressure dervatives. The cuprates differ also in their dependence of T_c on oyxygen concentration, so why should the scaling behaviour of grain boundary current transport be a universal property?

A model was therefore proposed based upon the structural properties of the grain boundary rather than upon oxygen inhomogeneities. It was assumed that an insulating region could be formed within the conducting phase at the grain boundary in an analogous manner to the behaviour of silicon grain boundaries. The grain boundary is modelled as two back to back Schottky barriers. This model is well established for grain boundaries in semiconductors[158]. At the centre there is the insulating dislocation array.

Here, the periodicity of the crystal lattice is interrupted and the chemical bonds are re-arranged and charge trapping sites are formed. This gives rise to a difference in the work function from that of the bulk material. Away from this region depletion layers are formed where the charge carrier density is reduced from that of the bulk material on the scale of the depletion length l_{TF}. Therefore bending of the electronic band structure occurs at the grain boundary, as shown in Fig. 8.5. The depletion length is given by (8.10),

$$l_{TF} = \left(\frac{2\varepsilon_0 \varepsilon_R V_{bi}}{en} \right)^{1/2} \tag{8.10}$$

where ε_R is the YBCO dielectric constant, V_{bi} is the height of the potential barrier at the interface and is also known as the built in voltage, e is the electronic charge and n is the charge carrier density. The built in voltage depends on the carrier concentration and the density of trapping sites at the grain boundary. Using $\varepsilon_R \approx 10$, $n \approx 4.5 \times 10^{21} cm^{-3}$ and $V_{bi}=0.1V$ it is found that $l_{TF} \approx 0.16nm$.

The depletion length is therefore on the same length scale as the coherence length in the a-b plane of the YBCO. The order parameter in the cuprates is very sensitive to changes in the carrier density, so the depletion regions at the grain boundary will influence its superconducting properties. The carrier density is close to the two dimensional metal insulator

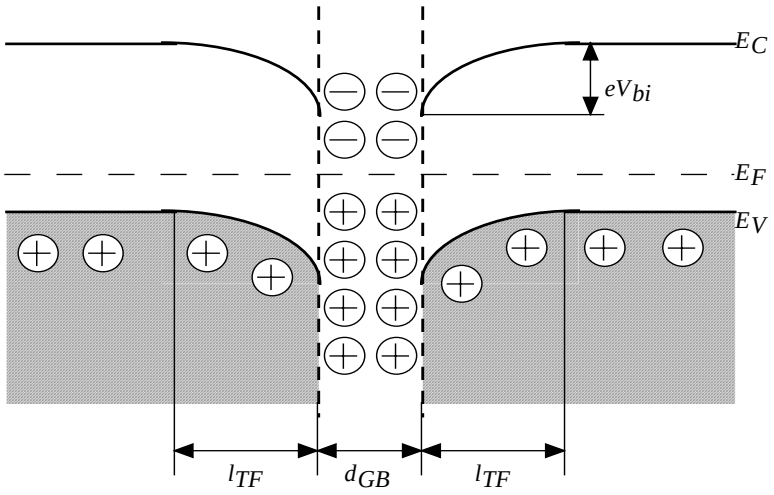

Figure 8.5 Bending of the electronic band structure at the grain boundary[143]. E_C, E_F and E_V represent the energies of the conduction band, the Fermi level and the valence band respectively.

transition, so it is possible that in the depletion regions the YBCO can be driven into its antiferromagnetic insulating phase.

The model is consistent with electric field experiments where a voltage bias was applied to a gate dielectric above the junction. The electric field caused a small decrease in the junction critical current[141]. However, a quantitative prediction of the magnitude of the decrease in the critical current with electric field has not been made from the band bending model. The electric field effect on the grain boundary critical current has also been attributed to the piezoelectric effect in the dielectric (STO). It was proposed that the piezoelectric distortion of the STO crystal lattice changed the width of the grain boundary[142].

Mannhart and Hilgenkamp[127] estimated the capacitance per unit area of the grain boundary from the band bending model. The electronic width t_J was assumed to be

$$t_J = d_{GB} + 2l_{TF} \tag{8.11}$$

where d_{GB} is the structural width of the grain boundary equal to 0.4nm from STEM measurements[45]. If the depleted layer is assumed to be insulating throughout its entire length and assuming ε_R=10, this gives 0.12pF μm^{-2} in reasonable agreement with previous measurements (see Fig 4.15). The resistance area product of the grain boundary was estimated with the Wentzel-Kramers-Brillouin (WKB) approximation to give (8.12) for the resistance of a reactangular potential barrier of height $\phi = eV_{bi}$.

$$R_n A = \frac{4\pi\hbar t^2 \exp(2\kappa t_J)}{e^2(1+2\kappa t_J)} \tag{8.12}$$

Using 0.1V for V_{bi} and an effective mass of 4.5 times the electronic mass for the charge carriers gives $0.29nm^{-1}$ for the decay length with (8.2). The electronic width of the grain boundary t_J is 0.72nm from (8.9) and (8.10), giving $4\Omega\mu m^2$ for the resistance area product, again in reasonable agreement with the measured values.

The transport mechanism across the grain boundary is tunneling in the band bending model. Therefore, the I_cR_n product should be constant and $J_c \propto (R_nA)^{-1}$. If the electrons carrying the supercurrent travel across the insulating region by direct tunelling then (8.5) holds for the variation of critical current density with capacitance per unit area for a given carrier

concentration. However, its key success lies in the qualitative explanation it provides for doping experiments on grain boundary critical currents.

Studies of the normal state and superconducting properties of Ca-doped YBCO thin films, $Y_{1-x}Ca_xBa_2Cu_3O_{7-\delta}$, were carried out by Kucera and Bravman[159]. It was demonstrated that Ca-doping reduced T_c to 73.9K for x=0.3, the solubility limit of Ca in YBCO. Assuming that the holes from the Ca are transferred directly to the CuO planes, the overdoping for x=0.3 should be 0.15 holes per CuO plane greater than the equilibrium value of 0.16 holes per CuO plane for x=0. The overdoping for x=0.3 was found to be 0.015 holes per CuO plane greater than the equilibrium value, based on conductivity and thermopower measurements. This lack of overdoping was caused by the compensation of the Ca doping by oxygen vacancies. An empirical formula was deduced relating the maximum critical temperature T_{cmax} to that at hole concentration n_{CuO} per copper oxide plane $T_c(n_{CuO})$.

$$\frac{T_c(n_{CuO})}{T_{\mathrm{cmax}}} = 1 - 82.6(n_{CuO} - 0.16)^2 \tag{8.13}$$

In (8.13), T_{cmax} is the maximum critical temperature of a film with a given calcium concentration at optimal oxygen doping.

Schmehl *et al*[144] studied the effect of Ca-doping on the grain boundary current transport properties. It was thought that Ca-doping could modify the charge carrier density and the built in voltage at the grain boundary thus changing its effective electronic width. The critical current density at 4.2K was found to increase with x up to x=0.3. At x=0.3, the critical current density was more than an order of magnitude larger than the x=0 value. There was a corresponding decrease in the the resistance area product which at x=0.3 was an order of magnitude less than the value at x=0. A reduction in T_c with increasing x was also found, corresponding to the overdoping of the charge carriers. Using (8.10) it was determined that there was a 5% change in l_{TF} from the increase in hole concentration at x=0.3, which was not sufficient to explain the order of magnitude increase in the critical current density (see (8.3)). It was speculated that the increase in the critical current density was due to an alteration of V_{bi} caused by Ca ions embedded at the grain boundary. The critical current increase with x can therefore be qualitatively explained within a band bending model.

However, Ca doping could modify the film microstructure in such a way as to reduce the

structural width of the grain boundary d_{GB}. A reduction of the grain size was observed with increasing x.

A detrimental effect of the Ca-doping was the reduction in the T_c of the Ca-doped films, accompanied by a reduction in the critical current density of the grains themselves at high temperatures (77K). Hammerl *et al*[147] sought to address this problem by growing multilayers consisting of Ca-doped and undoped films. The Ca was expected to diffuse preferentially along the grain boundary during film growth. The grain boundary in the undoped film would become doped with Ca, raising its critical current. This was found to be the case, and doped / undoped multilayers were found to have grain boundary critical current densities at 77K approaching those found in undoped grain boundaries at 4.2K.

8.3 Results

8.3.1 Introduction

A large volume of capacitance, resisitance and critical current data was available from the 'control' measurements of the junctions coupled to external capacitors and resonators described in Chapters 5 to 7. Ca-doped YBCO films on 24° STO bicrystals were obtained from the Augsburg group with x=0, 0.1, 0.2 and 0.3. These films were patterned into 2 to 5μm wide junctions and measured by James Ransley[160].

The critical and return current of each junction was obtained visually from its *IV* curve, using the current where the measured voltage became significantly greater than the noise voltage. The capacitance was obtained using Zappe's approximation (see section 1.3.2.2). The resistance was obtained by fitting a straight line to the *IV* curve at biases greater than 5 times the critical current. Junction widths were determined in a calibrated optical microscope, within a 10% error.

8.3.2 Calcium doped grain boundaries

The *IV* characteristics of the Ca doped grain boundary junctions were RCSJ like. Fraunhofer modulation of the critical current with an applied magnetic field was observed. For each x value, at least one grain boundary junction had an *IV* curve with β_c>1. The hysteretic portion of the *IV* curve of the 3μm wide junction for the x=0.2 film is shown in Fig. 8.6.

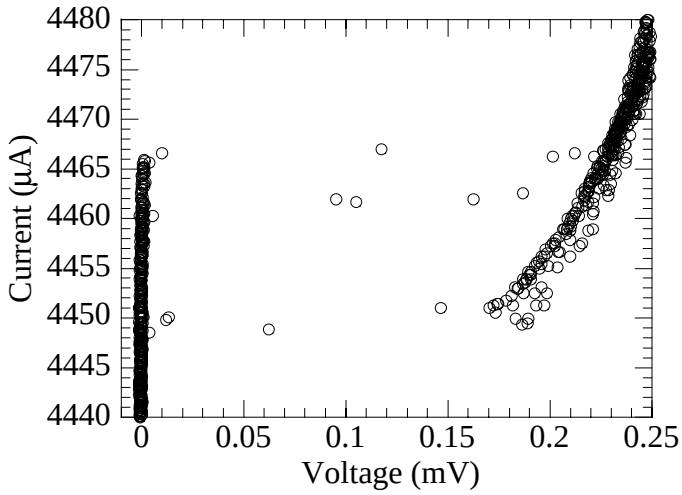

Figure 8.6 The hysteretic portion of the *IV* curve at 4.2K of the nominally 3μm wide junction for the x=0.2 calcium doped film. (I_c=4467μA, R_n=0.37Ω and C=0.46pF)

The variation of film critical temperature, critical current density, resistance area product and capacitance per unit area with calcium concentration x is shown in Figs. 8.7 to 8.10 respectively. The dependence of T_c on x is similar to that measured by Kucera and Bravman[Kucera, 1995 #26] for films with "optimal" oxygen doping, with the x=0.2 film having the lowest T_c.

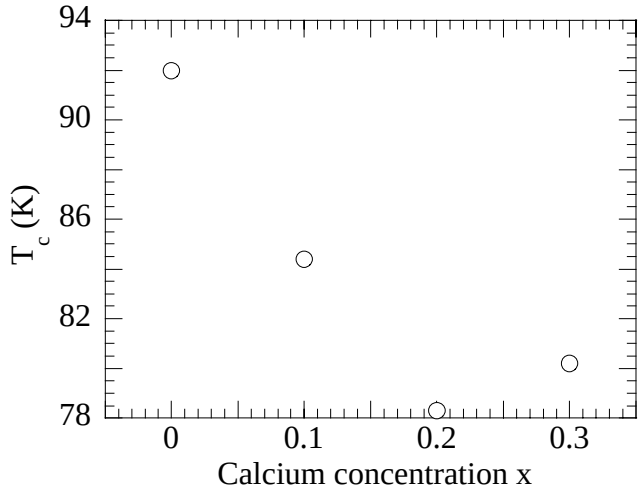

Figure 8.7 Film T_c versus calcium concentration x.

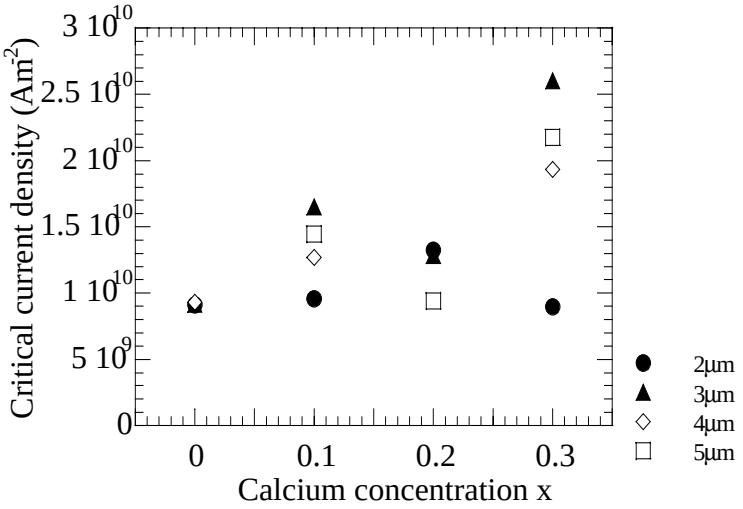

Figure 8.8 Junction critical current density at 4.2K versus calcium concentration for various junction widths.

The critical current density increases with calcium concentration, with the exception of the x=0.2 film. No increase of the critical current density with calcium concentration is observed for the 2μm wide junctions. A possible explanation for this is oxygen diffusion out of the grain boundary during film patterning. This would be a more significant effect for the narrowest junction. The trend is the same as that observed by Schmehl *et al*[144]. However, the critical current densities of the x=0 junctions are higher (~$1x10^{10}Am^{-2}$ compared to ~$2x10^{9}Am^{-2}$) and those of the x=0.3 junctions are lower (~$2x10^{10}Am^{-2}$ compared to a maximum of ~$6x10^{10}Am^{-2}$) than the junctions of Schmehl *et al*. The films in this study were patterned by

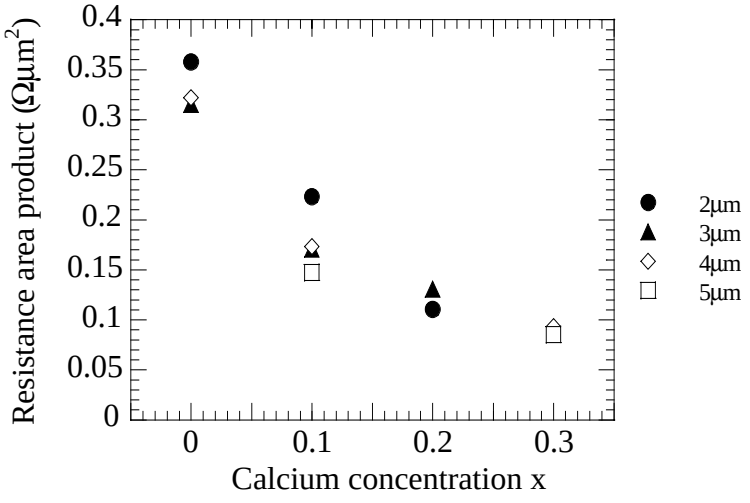

Figure 8.9 Junction resistance area product at 4.2K versus calcium concentration for various junction widths

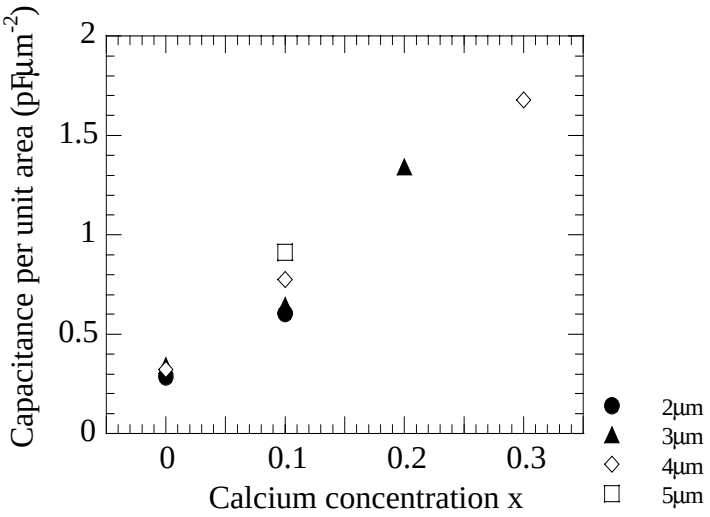

Figure 8.10 Junction capacitance per unit area at 4.2K versus calcium concentration for various junction widths.

Ar^+ ion milling rather than wet etching in acid. It is possible that sample heating in a vacuum during ion milling leads to oxygen depletion of the grain boundary. This may reduce the critical current of the junctions with a higher calcium concentration.

The resistance area product of the junctions decreases with calcium concentration as observed by Schmehl *et al*[144]. The x=0 junctions in this study had a lower resistance area product and the x=0.3 junctions had a higher resistance area product than the Schmehl *et al* junctions. The x=0.2 concentration fits onto the trend and there is no dependence of resistance area product on junction width.

The capacitance per unit area of the grain boundary increases with calcium concentration as shown in Fig. 8.10. The band bending model prediction for the capacitance per unit area of the grain boundary can be derived from $C/A=\varepsilon_0\varepsilon_R/t_J$ and (8.10) and (8.11), giving (8.14) for the inverse capacitance per unit area.

$$\frac{A}{C}=\frac{d_{GB}}{\varepsilon_0\varepsilon_R}+2\left(\frac{V_{bi}}{\varepsilon_0\varepsilon_R en}\right)^{1/2} \tag{8.14}$$

It can be seen from (8.14) that there are 4 possible parameters determining the capacitance per unit area which could vary with calcium concentration. These are the structural width of the grain boundary d_{GB}, the dielectric constant ε_R of the $Y_{1-x}Ca_xBa_2Cu_3O_{7-\delta}$, the density of charge trapping sites at the grain boundary and the carrier concentration n. The dielectric constant is

Table 8.1. The effective electronic width of the *x*=0.3 grain boundary

ε_R	*5*	*20*	*30*	*100*
t (nm)	0.03	0.11	0.16	0.52

assumed to be the same in the disordered region of the grain boundary as in the remainder of the film. A lower limit of 0.1nm is available for d_{GB} from STEM imaging of the grain boundary[45]. The dielectric constant must therefore be at least 20, otherwise the effective electronic width of the *x*=0.3 grain boundary calculated from its specific capacitance of 1.67pF μm^{-2} becomes smaller than its structural width, as shown in Table 8.1.

The voltage at which the *x*=0.2 and 0.3 junctions switched back to the zero voltage state was less than 0.3mV. This is the voltage equivalent to the soft optic phonon frequency below which the STO substrate makes a significant contribution to the junction capacitance per unit area (see Chapter 6). It is therefore possible that for the *x*=0.2 and 0.3 junctions parasitic capacitance from the STO substrate makes a significant contribution to the total capacitance. The capacitances per unit area of the *x*=0.2 and 0.3 junctions (see Fig 8.10) are comparable to those of the junctions where the STO contributed to the capacitance per unit area (see Fig. 6.6). However, it is clear from Fig. 8.9, Fig 8.10 and Fig. 8.14 that the capacitance per unit area of the doped grain boundaries scales with their resistance area product. The substrate would give a constant contribution to the capacitance per unit are regardless of the doping of the grain boundary, so the capacitance would not be expected to scale with the resistance.

8.3.3 I_cR_n product versus critical current density

The junction I_cR_n product at 4.2K for the grain boundaries measured is plotted versus the critical current density in Fig. 8.11, together with the Hilgenkamp and Mannhart data[42]. The 24° grain boundaries have a saturated I_cR_n product. This behaviour is characteristic of the filamentary model when there are filaments in direct contact across the insulating, structurally disordered barrier layer. Improving the oxygenation of the region in contact with the barrier layer increases the critical current and reduces the resistance leaving the I_cR_n product constant. The absence of scaling of the I_cR_n product with J_c indicates that direct tunneling of the quasiparticles across the barrier layer is the dominant transport mechanism where the superconducting filaments are in contact.

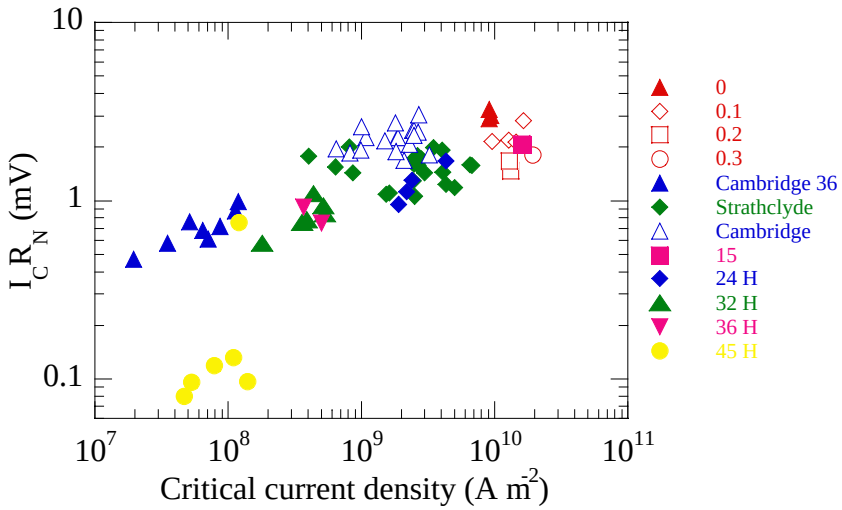

Figure 8.11. The scaling of I_cR_n product with critical current density at 4.2K. The grain boundaries have 24° misorientation unless indicated. The Augsburg doped films are in referred to by their calcium concentration is given. The Hilgenkamp and Mannhart data is also plotted, and indicated with an H in the legend[42].

There is some decrease of the I_cR_n product with J_c for the 36° grain boundaries. In the context of the filamentary model this could be caused by an absence of superconducting filaments across the grain boundary. However, the width of the disordered region of the grain boundary increases with misorientation angle[45], and this could also cause the reduction in the I_cR_n product. The d-wave order parameter suppression of the critical current also increases with grain boundary misorientation angle[47,148]. There is not enough variation in the I_cR_n product to determine whether the scaling is real or part of the intrinsic scatter in the data.

It can also be seen from Fig. 8.11 that for a given critical current density the junctions in the films grown in the off axis pulsed laser deposition system in Cambridge had a larger I_cR_n product than those grown in the on axis system in Strathclyde.

8.3.4 Critical current, reistance and capacitance scaling relationships

The resistance of the junctions was found to be temperature independent. The critical currents decreased linearly with temperature. The variation of junction capacitance with temperature is discussed in Chapter 5. The capacitance was temperature independent for junctions where the grain boundary capacitance was the dominant contribution to the total capacitance. None of the undoped junctions returned to the zero voltage state at voltages less than 0.3mV. Therefore, the STO substrate could not increase the capacitance determined from the hysteresis in the *IV*

curves for any of the undoped junctions.

The scaling of critical current density with resistance area product at 4.2K for the 24° misorientated grain boundary junctions is shown in Fig 8.12.

The data fit to the power law $J_c \propto (R_n A)^{-0.87}$, plotted in Fig. 8.12. The combination of the saturated (constant) $I_c R_n$ product and the similarity of the fitted power law to (8.7) point towards the filamentary model of current transport across the grain boundary, with direct tunelling of the Cooper pairs and the quasiparticles across some fraction of the grain boundary area. The power law is inconsistent with the intrinsically shunted junction model expression (8.4) which predicts $J_c \propto (R_n A)^{-2}$.

The critical current density was also found to scale approximately inversely with the resistance area product at 60K, indicating no substantial change in the quasiparticle transport mechanism with temperature.

The critical current density is plotted versus the capacitance per unit area of the grain boundary at 4.2K in Fig 8.13. The critical current density is approximately linearly proportional to the capacitance per unit area in agreement with the prediction (8.8) of the filamentary model of current transport.

In order to test whether a tunneling transport mechanism across the grain boundary could be responsible for the scaling in Fig. 8.13, the barrier height ϕ can be estimated by fitting (8.5) to

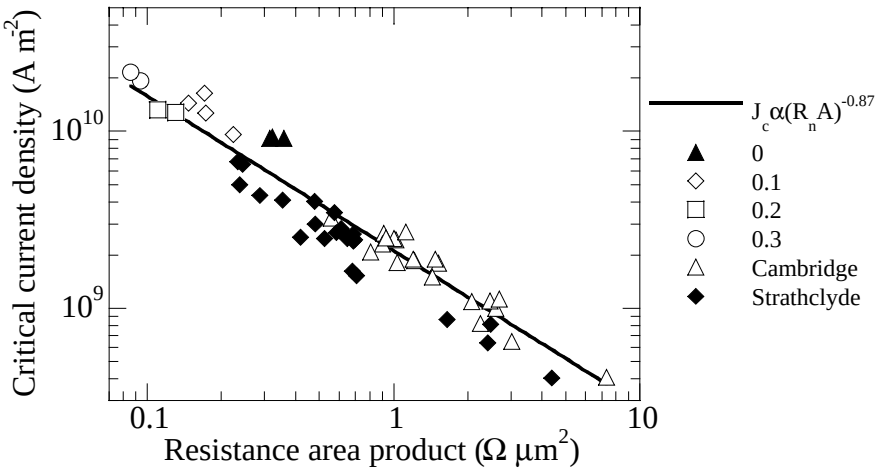

Figure 8.12. Critical current density versus resistance area product at 4.2K for the 24° misoriented grain boundary junctions.

the data. The variation of critical current with capacitance in (8.5) is that predicted by both the intrinsically shunted junction model and the band bending model of grain boundary current transport. The effective mass of the charge carriers was assumed to be 4.5 times the electron mass. If ε_R=30, then ϕ=1meV, and ε_R=5 gives ϕ=34meV. These barrier heights are both comparable to k_BT =6meV at 77K, and would imply that the resistance area product should be temperature dependent. An independent estimate of ϕ can be determined from the angular dependence of J_c measured by Hilgenkamp and Mannhart[42], along with the structural width of grain boundaries with different misorientations measured with TEM by Browning *et al*[45]. The plot of J_c versus θ in Fig 2.6 can be converted to J_c versus d_{GB} and fitted to (8.3) if $t \approx d_{GB}$ ($0.1 < d_{GB} < 0.8$nm for $15° < \theta < 45°$). This gives $0.25 < \phi < 0.37$eV, much larger than ϕ from the critical current versus capacitance data. It is also clear from the tunneling fits from (8.5) shown in Fig. 8.13 that the critcal current density does not vary exponentially with the capacitance per unit area (regardless of the value of the barrier height) as predicted by a tunneling model. Therefore, current transport by tunneling across the entire geometric area of the grain boundary is an unrealistic explanation for the critical current with capacitance scaling observed.

The grain boundary capacitance per unit area varies approximately inversely with the resistance area product, as shown in Fig. 8.14, again following the prediction of the filamentary model. Tunneling of the quasiparticles across the entire geometric area of the

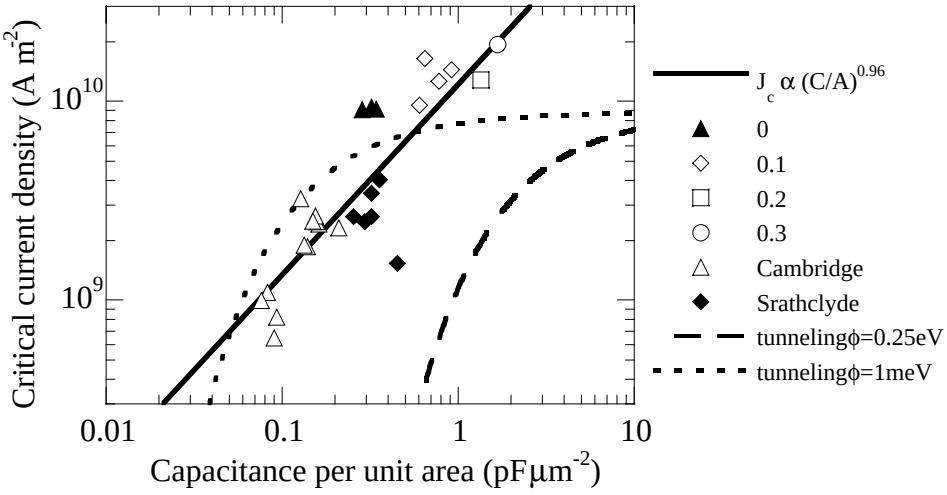

Figure 8.13. Critical current density versus capacitance per unit area for the 24° misorientated grain boundary junctions at 4.2K, together with fits from (8.5) for ϕ=0.25eV and ϕ=1meV.

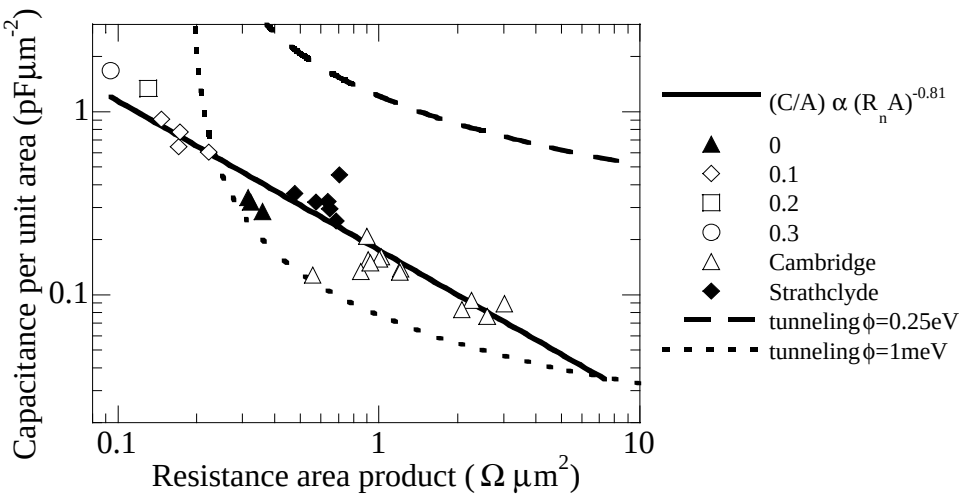

Figure 8.14. Capacitance per unit area versus resistance area product of the 24° grain boundary junctions at 4.2K, together with fits from (8.6) for ϕ=0.25eV and ϕ=1meV.

grain boundary can again be ruled out with a numerical argument. The variation in the capacitance per unit area indicates that the barrier thickness has changed by an order of magnitude. An order of magnitude change in thickness should bring about a change in the resistance area product by at least 3 orders of magnitude if (8.1) or (8.12) were being obeyed. The resistance area products observed changed by less than 2 orders of magnitude. Whether or not the barrier height is realistic, the capacitance per unit area does not vary exponentially with the resistance area product as predicted by a tunneling model such as (8.6).

The scaling of grain boundary capacitance with resistance area product is common to all grain boundaries in the cuprate superconductors on substrates with a wide range of dielectric permittivities, as shown in Fig. 8.15. The increase in capacitance at low frequencies caused by the $SrTiO_3$ substrate described in Chapter 6 falls within the scatter in this graph.

8.4 Further Discussion

8.4.1 The scatter in grain boundary parameters

The critical current density, resistance area product and capacitance per unit area of the grain boundaries varied over at least one order of magnitude for a single mis-orientation angle. There are various possible causes of this scatter. Microstructural defects in STO bicyrstals have been correlated with changes in grain boundary critical current density and

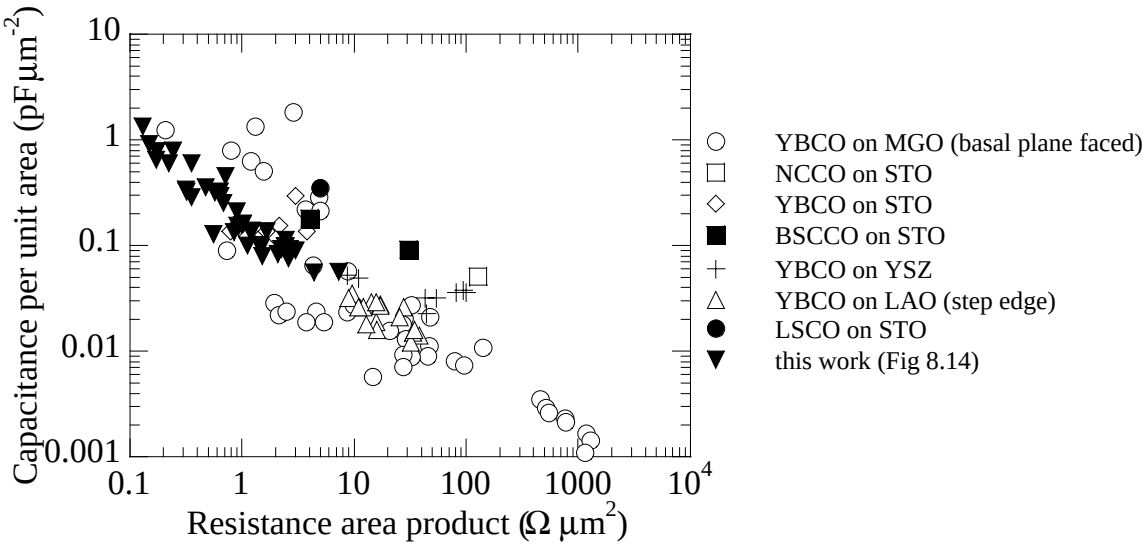

Figure 8.15. The global scaling of capacitance per unit area with resistance area product (at 4.2K) for grain boundary junctions, bicrystal unless otherwise indicated. Data for YBCO on MgO (single grain boundaries in polycrystalline films)[99], NCCO on $SrTiO_3$[161], YBCO on $SrTiO_3$[59], BSSCO on $SrTiO_3$[162,163],YBCO on yttria stabilised zirconia[63], YBCO on $LaAlO_3$ (step edge)[164], LSCO on $SrTiO_3$[165].

resistance[166]. The defect distribution along the $SrTiO_3$ bicrystal line was found to be inhomogeneous on a scale of ~1μm. Defects were found to lead to meandering ofthe YBCO grain boundary by up to 0.8μm from the bicrystal line. The electrical characteristics of these junctions showed no critical current and strong temperature dependence of the resistance, which was not observed for any junctions in this study. Junctions with a moderate defect density in the $SrTiO_3$ showed I_c=2μA at 63K compared to I_c=380μA at 77K for defect free junctions. Some of the junctions in this study did not show a critical current at 77K (e.g. xros24a, 3tdev). Therefore it is possible that defects in the $SrTiO_3$ bicrystal led to some of the scatter observed.

The film growth of YBCO takes place through the nucleation of 3 dimensional islands. These islands will not follow the grain boundary line exactly, but instead will meander or facet leading to changes in the grain misorientation angle from that of the substrate. This therefore leads to some scatter in the grain boundary critical current[45].

Annealing experiments such as those carried out by Sydow *et al*[150] show the importance of oxygenation in controlling the properties of the grain boundary. Differences in the oxygen content of the grain boundaries could contribute to the scatter observed in the critical currents,

resistances and capacitances.

It is also clear from Fig 8.12 and Fig 8.14 that there were systematic differences in the junction properties depending on the geometry of the pulsed laser ablation system used to deposit the films. In general the grain boundaries in the off axis films deposited in Cambridge had a lower critical current and capacitance and a higher resistance than those films deposited by on axis laser ablation.

8.4.2 The evidence for filaments

It is clear from the saturation of the I_cR_n product (Fig 8.11), the linear increase of critical current with capacitance(Fig 8.13) and the power law decrease of capacitance with resistance (Fig 8.14) that a filamentary model is required to explain grain boundary current transport. However, there is little evidence from microscopy of the grain boundaries that such filaments exist. A combination of grain boundary faceting and d-wave pairing has been shown to lead to an inhomogenous critical current density across the grain boundary[47] (see also section 2.4.1). There is also evidence for inhomogenous critical current density across the grain boundary from deviations from the Fraunhofer modulations of the critical current with a magnetic field[156]. So, there is evidence for superconducting filaments, or supercurrent transport across only a part of the geometric area of the grain boundary. However, d-wave pairing cannot directly influence the normal state resistance of the grain boundary.

Different types of facet are associated with different structural widths of the grain boundary[45]. It is possible that the high angle facets correlate with regions of large structural width of the grain boundary and low angle facets correspond to regions of small structural width of the grain boundary. The high angle facets would then have a large resistance, a small capacitance and possibly reversal of the direction of flow of the supercurrent. The low angle facets would have a small resistance, a large capacitance and a high critical current density. This would enable scaling of the critical current with the capacitance and the resistance due to the variation in structural width of the grain boundary at different facets.

8.4.3 The evidence against filaments

The filamentary model is also unable to provide a satisfactory explanation for the global scaling of capacitance with resistance for grain boundaries in the cuprates shown in Fig. 8.15.

The model postulates that the variations in capacitance and resistance are due to variations in the oxygen distribution at the grain boundary. However, as discussed in section 8.2.3 the pressure derivative of the critical temperature differs for YBCO and BSCCO, so why so should the oxygen kinetics be the same?

It can be seen from Fig. 8.11 that the critical current density varies over nearly two orders of magnitude for those grain boundaries with a 24° misorientation angle. Within the context of the filamentary model, this would require the effective area of oxygenated YBCO in contact with the barrier layer at the grain boundary to vary between ~1% and 100% of the total area of the grain boundary. It is not clear how diffusion of oxygen could result in the highly non uniform oxygen distribution required for e.g. 90% effective area in contact. Furthermore, it is not clear why saturation of the critical current density is not observed at a point where nearly 100% of the barrier layer is in contact with fully oxygenated YBCO.

8.4.4 Variable barrier thickness

The models described in section 8.2 assumed an insulating region at the centre of the grain boundary with a constant barrier thickness. Linear scaling of the capacitance per unit area with the critical current density has been observed for low T_c SIS tunnel junctions, which would be expected to have an exponential dependence analagous to (8.5)[167]. The linear scaling was attributed to variations in the thickness of the barrier layer. A fraction x of the barrier area was assumed to have thickness t_J and a fraction (1-x) thickness $2t_J$. The total capacitance per unit area is given by (6.14) assuming that the contributtions add in parallel. The capacitance per unit area of a layer of thickness t_J is C_{s0}.

$$C_s = \frac{\varepsilon_0 \varepsilon_R (x+1)}{2d} = \frac{C_{s0}(x+1)}{2} \tag{6.14}$$

The critical current density and resistance area product are assumed to be dominated by transport across regions of thickness t_J. This gives (6.15) and (6.16) for the scaling of capacitance with critical current density and resistance area product R_n', where J_{c0} and R_{n0}' are the critical current density and resistance area product of regions of thickness t_J.

$$C_s = \frac{C_{s0}}{2}\left(1+\frac{J_c}{J_{c0}}\right) \tag{6.15}$$

$$C_s = \frac{C_{s0}}{2}\left(1+\frac{R_{n0}'}{R_n'}\right) \tag{6.16}$$

Variations in the grain boundary thickness could arise from the faceting of the grain boundary[45]. The data in Fig. 8.13 gives C_{s0}=0.08pFμm^{-2} and J_{c0}=6.3x10^8 Am^{-2}, and that in Fig. 8.14 gives C_{s0}=0.052pFμm^{-2} and R_{n0}'=4.65Ωμm^2. These values represent maxima for the capacitance and the critical current density and a minimum for the resistance area product. The range over which the capacitance, critical current and resistance area product vary is much larger than these limits. A larger variation of the thickness, such as *t* and 10*t*, could explain the larger maxima of the critical current density and the capacitance per unit area This gives C_{s0}=0.4pFμm^{-2} and J_{c0}=5.7x10^9 Am^{-2}, large enough to cover the undoped films. Other mechanisms, such as a change in the barrier height due to a change in the density of trapping states at the boundary could further increase the critical current density of the doped films.

8.5 Conclusion

The critical current density and capacitance per unit area of 24° grain boundaries in YBCO have been shown to increase with calcium doping. The resistance area product was shown to decrease. The scaling of the critical currrent with resistance and capacitance, and of capacitance with resistance of the grain boundaries demonstrates that current transport does not occur over the entire geometric area of the grain boundaries. A tunneling model alone was shown to give an unrealistic barrier height when applied to the critical current versus capacitance data. Therefore a filamentary model is required to explain grain boundary current transport, but there are severe drawbacks to a model based on oxygen deficiency at the grain boundary alone.

It is clear that capacitance is an important probe of grain boundary current transport, as it is directly related to the thickness of the insulating barrier layer at the grain boundary.

Chapter 9: Conclusion

The first aim of this thesis was to manufacture hysteretic grain boundary $YBa_2Cu_3O_{7-\delta}$ Josephson junctions at temperatures higher than 50K. The junctions were shunted with a multilayer $YBa_2Cu_3O_{7-\delta}$/SrTiO3/Au parallel plate capacitor. The highest temperature at which hysteresis was achieved was 72.3K with a McCumber parameter of 1.01, for a junction with a critical current of 450μA and a resistance of 0.56Ω at this temperature. The shunt capacitor consisted of two 150μm^2 square capacitors in series, with a 50nm $SrTiO_3$ dielectric. However, the hysteresis measured was much less than that predicted from a calculation of the lumped parallel plate capacitance. This was attributed to two causes; the wavelength of the Josephson oscillations was comparable to the size of the shunt capacitor itself, so the junction sees the capacitor as a distributed impedance and thermal noise suppression of the hysteresis. For the 150μm^2 capacitor at 72.3K the wavelength of the Josephson oscillations was 58μm. A measurement of the critical current distribution showed that the critical current at 30K was suppressed from 88μA to 73μA. The McCumber parametes achieved were comparable to others reported in similar structures[100] and the causes of the smaller than expected McCumber parameter were analysed. Simulations showed that it would be possible to make a relaxation oscillation SQUID from a device with a McCumber parameter of 1.01.

It was found during the investigation of Josephson junctions coupled to external capacitors that further work was needed to establish why the $SrTiO_3$ substrate, with its high dielectric constant of 24000 at 4.2K, did not influence the capacitance of the grain boundary junctions grown on it. Therefore, a series of grain boundary $YBa_2Cu_3O_{7-\delta}$ junctions of different lengths was patterned onto a $SrTiO_3$ bicrystal. The measured Fiske resonance dispersion relation had two branches, one with a high capacitance at low frequencies and a low capacitance branch at high frequencies. This behaviour was caused by the frequency depedence of the dielectric constant of the bulk $SrTiO_3$ in the region of the transverse soft optic phonon. The bulk $SrTiO_3$ dielectric constant decreases at frequencies greater than that of the transverse soft optic phonon. From the measured dispersion relation the bulk dielectric constant of the $SrTiO_3$ was found to be 750 at 4.2K and the soft optic phonon frequency was 145GHz. These values are both lower than previous measurements of the $SrTiO_3$ dielectric constant of 24000 at 4.2K and 390GHz for the frequency of the transverse soft optic phonon. This discrepancy was attributed to the formation of multiple structural domains in the strontium titanate. This result provides an explanation for

the absence of a contribution to the junction capacitance from the $SrTiO_3$ substrate observed by Tarte *et al*[57,59]. In this case, the junctions all had Fiske resonances above the frequency of the soft optic phonon in $SrTiO_3$ at 4.2K and thus the substrate could not add to the junction capacitance. The improved understanding of the influence of the $SrTiO_3$ substrate on the jucntion capacitance enabled the use of the grain boundary capacitance as a probe of the current transport across the grain boundary. Furthermore, the experiment provides a direct measurement of the dielectric properties of bulk $SrTiO_3$ in this frequency and temperature range, allowing a contrast with the subsequent measurements on thin film $SrTiO_3$.

The dielectric constant of a series of thicknesses of thin film $SrTiO_3$ was measured using Josephson junctions coupled to external resonators. Diffierent resonator geometries gave the same dielectric constant for a given $SrTiO_3$ film thickness. In contrast to the behaviour of bulk $SrTiO_3$, the dielectric constant of a 50nm $SrTiO_3$ film was found to be frequency independent between 100GHz and 900GHz. The soft optic phonon had hardened to a frequency greater than 900GHz. This is consistent with recent theoretical predictions of the existence of an intrinsic dead layer between an incipient ferroelectric film and a metal electrode[74] and the subsequent hardening of the soft optic phonon[140]. The films exhibited the size effect, with their dielectric constant being dependent on the film thickness. The 200nm $SrTiO_3$ film had a dielectric constant of 200 for a 50μm resonator and the 50nm film 34±4. The dielectric constant of the 200nm film was found to be tunable with an electric field between 245 and 112 at 116GHz, consistent with the Ginzburg-Landau-Devonshire theory of ferroelectrics. The technique has been demonstrated in investigations of fundamental dielectric properties of ferroelectrics in the frequency range from 100GHz to 900GHz and the temperature range from 4.2K to 70K. The experiment could be adapted straightforwardly to measure other perovskite ferroelectrics with a lattice parameter compatible with $YBa_2Cu_3O_{7-\delta}$. The method is also useful for routine on chip dielectric characterisation in structures similar to final device designs.

For the junctions on 24° bicrystals, the capacitance per unit area of the grain boundary was found to scale linearly with its critical current density and was inversesly proportional to its resistance area product. Models based on current transport across the grain boundary by tunneling such as the band bending model[127] or resonant tunneling[31] alone cannot be invoked as an explanation for this scaling. A model in which current does not flow over the

entire geometric area of the grain boundary is required. Such a model could be based on optimally oxygen doped $YBa_2Cu_3O_{7-\delta}$ filaments in contact across the boundary[149], or by a model where the structural width varies along the length of the grain boundary. The grain boundary capacitance was shown to be extremely valuable as a probe of grain boundary current transport, as it is directly related to the structural width of the grain boundary.

Publication List

1. P. F. McBrien, W. E. Booij, G. Burnell, F. Kahlmann, M. G. Blamire, E. J. Romans, C. M. Pegrum and E. J. Tarte, “Ferroelectric characterisation using Josephson junctions,” submitted to IEEE Transactions on Applied Superconductivity and presented at ASC 2000.

2. P. F. McBrien, R. H. Hadfield, W. E. Booij, A. Moya, F. Kahlmann, C. M. Pegrum and E. J. Tarte, “The capacitance of superconducting films with strontium titanate and other substrates,” Physica C, in press.

3. P. F. McBrien, W. E. Booij, F. Kahlmann, M. G. Blamire, E. J. Tarte, E. J. Romans and C. M. Pegrum, “Measurements of the dielectric properties of strontium titanate at submillimetre wavelengths using Josephson junction driven oscillators,” Superconductor Science and Technology, 1999, vol. 12, pp819-21 and presented at ISEC 1999 and CMMP 1999.

4. P. F. McBrien, R. H. Hadfield, W. E. Booij, A. Moya, M. G. Blamire, E. J. Tarte, J. Clark and C. M. Pegrum, “Josephson junctions with hysteretic current voltage characteristics at high temperatures,” IEEE Transactions on Applied Superconductivity, 1999, vol. 9, pp3468-3471 and presented at ASC 1998 and CMMP 1998.

5. E. J. Tarte, P. F. McBrien, J. H. T. Ransley, F. Kahlmann and J. Evetts, “Capacitance as a probe of high angle grain boundary transport in oxide superconductors,” submitted to IEEE Transactions on Applied Superconductivity and presented at ASC 2000.

6. E. J. Tarte, P. F. McBrien, E. Inglessi, F. Kahlmann, W. E. Booij and M. G. Blamire, “The capacitance of grain boundaries in high temperature superconducting thin films,” Physica B, 2000, vol. 284, pp628-9.

7. F. Kahlmann, W. E. Booij, M. G. Blamire, P. F. McBrien and E. J. Tarte, “The performance of high-Tc dc SQUID magnetometers with resistively shunted inductances compared to unshunted devices,” submitted to IEEE Transactions on Applied Superconductivity and presented at ASC 2000.

8. F. Kahlmann, W. E. Booij, M. G. Blamire, P. F. McBrien, E. J. Tarte, N. H. Peng, C. Jeynes, E. J. Romans and C. M. Pegrum, “Transfer function and noise properties of

$YBa_2Cu_3O_{7-\delta}$ direct-current superconducting-quantum-interference-device magnetometers with resistively shunted inductances," Applied Physics Letters, 2000, vol. 77, pp567-9.

9. F. Kahlmann, W. E. Booij, M. G. Blamire, P. F. McBrien, N. H. Peng, C. Jeynes, E. J. Romans, C. M. Pegrum and E. J. Tarte, "High-T_c dc SQUID magnetometers in $YBa_2Cu_3O_{7-\delta}$ thin films with resistively shunted inductances," Institute of Physics Conference Series, vol. 167(2), pp437-440 and presented at EUCAS 1999.

10. F. Kahlmann, W. E. Booij, M. G. Blamire, P. F. McBrien, N. H. Peng, C. Jeynes and E. J. Tarte, "Integrated resistors in $YBa_2Cu_3O_{7-\delta}$ thin films suitable for superconducting quantum interference devices with resistively shunted inductances," Institute of Physics Conference Series, vol. 167(2), pp473-476 and presented at EUCAS 1999.

11. W. E. Booij, C. A. Elwell, E. J. Tarte, P. F. McBrien, F. Kahlmann, D. F. Moore, M. G. Blamire, N. H. Peng and C. Jeynes, "Electrical properties of electron and ion beam irradiated $YBa_2Cu_3O_{7-\delta}$," IEEE Transactions on Applied Superconductivity, 1999, vol. 9, pp2886-9 and presented at ASC 1998.

References

[1]B. D. Josephson, "Possible new effects in superconductive tunneling," Phys. Lett. **1,** 251-253 (1962).

[2]Anderson, "Probable observation of the Josephson Superconductive tunnel effect," Phys. Rev. Lett. **10,** 230-232 (1963).

[3]R. P. Feynman, *The Feynman Lectures on Physics* (Addison-Wesley, Reading, USA, 1965).

[4]W. C. Stewart, "Current voltage characteristics of Josephson Junctions," Applied Physics Letters **12,** 277-280 (1968).

[5]D. E. McCumber, "Effect of ac impedance on dc current-voltage characteristics of superconductor weak-link junctions," J. Appl. Phys. **39,** 3113-3118 (1968).

[6]K. K. Likharev, *Dynamics of Josephson Junctions and Circuits* (Gordon and Breach Science Publishers, Reading, 1986).

[7]T. P. Orlando and K. A. Delin, *Foundations of applied superconductivity* (Addison-Wesley, Wokingham, UK, 1990).

[8]H. H. Zappe, "Minimum current and related topics in Josephson Tunnel junction devices," J. Appl. Phys. **44,** 1371-1377 (1972).

[9]Barone and Paterno, *Physics and applications of the Josephson effect* (Wiley-Interscience, New York, 1982).

[10]D. J. Kang, *High Tc dc SQUID Magnetometers* (PhD. Thesis, University of Cambridge, 1998).

[11]T. Van Duzer and C. W. Turner, *Principles of superconductive devices and circuits*, 2nd ed. (Prentice Hall, New York, 1999).

[12]M. Tinkham, *Introduction to Superconductivity* (McGraw-Hill, 1996).

[13]Swihart, "Field solution for a thin film superconducting strip transmission line," J. Appl.

Phys **32,** 461-469 (1961).

[14]R. E. Collin, *Foundations for microwave engineering* (McGraw-Hill, New York, 1966).

[15]Fiske, "Temperature and magnetic field dependence of the Josephson tunneling current," Rev. Mod. Phys. **36,** 221-222 (1964).

[16]Kulik, "Theory of "steps" of voltage current characteristics of the Josephson tunnel current," JETP Lett. **2,** 84-87 (1965).

[17]M. Cirillo, N. Gronbech-Jensen, M. R. Samuelsen, M. Salerno, and G. Verona Rinati, "Fiske modes and Eck steps in long Josephson junctions: Theroy and experiment," Phys. Rev. B **58,** 12377-12384 (1998).

[18]J. G. Bednorz and K. A. Muller, "Possible High Tc Superconductivity in the Ba-La-Cu-O system.," Z. Phys. B. **64,** 189 (1986).

[19]M. K. Wu, J. R. Ashburn, C. J. Torng, P. H. Hor, R. L. Meng, L. Gao, Z. J. Huang, Y. Q. Wang, and C. W. Chu, "Superconductivity at 93K in a new mixed phase Y-Ba-Cu-O compound system at ambient pressure.," Phys. Rev. Lett. **58,** 908-910 (1987).

[20]J. Rossat-Mignod, L. P. Regnault, C. Vettier, P. Burlet, J. Y. Henry, and G. Lapertot, "Investigation of the spin dynamics in $YBa_2Cu_3O_{6+x}$ by inelastic neutron scattering," Physica B. **169,** 58-65 (1991).

[21]S. W. Tozer, A. W. Kleinsasser, T. Penney, D. Kaiser, and F. Holtzberg, "Measurement of anisotropic resistivity and Hall Constant for single crystal $YBa_2Cu_3O_{7-\delta}$," Phys. Rev. Lett. **59,** 1768-1771 (1987).

[22]C. W. Schneider, R. E. Somekh, J. E. Evetts, D. J. C. Walker, I. M. Watson, F. Baudenbacher, S. N. Mao, X. X. Xi, Q. Li, C. Kwon, T. Venkatesan, R. G. Humphreys, N. G. Chew, R. Gross, and A. Beck, "Inductive measurements of $\lambda(T)$ of bare YBCO films and the proximity effect in YBCO/normal metal bilayers," IEEE Trans. Appl. Supercon. **5,** 1432-1435 (1995).

[23]T. Datta, in *Concise encyclopedia of magnetic and superconducting materials*, edited by J.

E. Evetts (Pergamon Press, 1992)

[24]C. C. Tsuei, J. R. Kirtley, C. C. Chi, L. S. Yu-Jahnes, A. Gupta, T. Shaw, J. Z. Sun, and M. B. Ketchen, "Pairing symmetry and flux quantization in a tricrystal superconducting ring of $YBa_2Cu_3O_{7-\delta}$," Phys. Rev. Lett. **73,** 593-596 (1994).

[25]D. A. Wollman, D. J. Van Harlingen, J. Giapintzakis, and D. M. Ginsberg, "Evidence for d_{x2-y2} pairing from the magnetic field modulation of $YBa_2Cu_3O_7$-Pb Josephson junctions," Phys. Rev. Lett. **74,** 797-800 (1995).

[26]S. R. Bahcall, "Boundary effects and the order parameter symmetry of high-T_c superconductors," Phys. Rev. Lett. **76,** 3634-3637 (1996).

[27]R. R. Schulz, B. Chesca, B. Goetz, C. W. Schneider, A. Schmehl, H. Bielefeldt, H. Hilgenkamp, J. Mannhart, and C. C. Tsuei, "Design and realisation of an all d-wave dc π-superconducting quantum interference device," Appl. Phys. Lett. **76,** 912-914 (2000).

[28]Hypres, "Niobium design rules," http://www.hypres.com (2000).

[29]R. W. Moseley, W. E. Booij, E. J. Tarte, and M. G. Blamire, "Direct writing of low T-c superconductor-normal metal-superconductor junctions using a focused ion beam," Appl. Phys. Lett **75,** 262-264 (1999).

[30]A. H. Dayem and C. C. Grimes, "Microwave emission from superconducting point contacts," Appl. Phys. Lett. **9,** 47-49 (1966).

[31]R. Gross, L. Alff, A. Beck, O. M. Froehlich, D. Koelle, and A. Marx, "Physics and technology of high temperature superconducting Josephson junctions," IEEE Trans. Appl. Supercon. **7,** 2929-2935 (1997).

[32]A. J. Pauza, W. E. Booij, K. Herrmann, D. F. Moore, M. G. Blamire, D. A. Rudman, and L. R. Vale, "Electron-beam damaged high-temperature superconductor Josephson junctions," J. Appl. Phys. **82,** 5612-5632 (1997).

[33]F. Kahlmann, A. Englehardt, J. Schubert, W. Zander, C. Buchal, and J. Hollkott, "Superconductor-normal-superconductor Josephson junctions fabricated by oxygen

implantation into $YBa_2Cu_3O_{7-\delta}$," Appl. Phys. Lett. **73,** 2354-2356 (1998).

[34]W. E. Booij, A. J. Pauza, E. J. Tarte, D. F. Moore, and M. G. Blamire, "Proximity coupling in high-T-c Josephson junctions produced by focused electron beam irradiation," Phys. Rev. B. **55,** 14600-14609 (1997).

[35]F. Kahlmann, W. E. Booij, M. G. Blamire, P. F. McBrien, E. J. Tarte, N. H. Peng, C. Jeynes, E. J. Romans, and C. M. Pegrum, "Transfer function and noise properties of $YBa_2Cu_3O_{7-\delta}$ superconducting interference device magnetometers with resistively shunted inductances," Appl. Phys. Lett. **77,** 567-569 (2000).

[36]D.-J. Kang, W. E. Booij, M. G. Blamire, and E. J. Tarte, "Performance of high-T-c superconducting quantum interference devices with resistively shunted inductances," Appl. Phys. Lett. **73,** 3929-3931 (1998).

[37]Z.-W. Dong, *High Tc Superconducting thin film devices* (PhD. Thesis, University of Delft, Netherlands, 1995).

[38]I. Takeuchi, P. A. Warburton, Z. Trajanovic, C. J. Lobb, M. A. Bari, W. E. Booij, E. J. Tarte, and M. G. Blamire, "Fabrication of in-plane aligned a-axis oriented $YBa_2Cu_3O_{7-x}$ trilayer Josephson junctions," Appl. Phys. Lett **69,** 112-114 (1996).

[39]P. Chaudhari, J. Mannhart, D. Dimos, C. C. Tsuei, J. Chi, M. M. Oprysko, and M. Scheuermann, "Direct measurement of the superconducting properties of single grain boundaries in $YBa_2Cu_3O_{7-\delta}$," Phys. Rev. Lett **60,** 1653-1656 (1988).

[40]L. R. Vale, R. H. Ono, J. Talvacchio, M. G. Forrester, B. D. Hunt, M. S. Dilorio, K. Yang, Y., and S. Yoshizumi, "Long term stability of YBCO-based Josephson junctions," IEEE Trans. Appl. Supercon. **9,** 3382-3385 (1999).

[41]D. Dimos, P. Chaudhari, and J. Mannhart, "Superconducting transport properties of grain boundaries in $YBa_2Cu_3O_{7-\delta}$," Phys. Rev. B. **41,** 4038-4049 (1990).

[42]H. Hilgenkamp and J. Mannhart, "Superconducting and normal-state properties of $YBa_2Cu_3O_{7-\delta}$ bicrystal grain boundary junctions in thin films," Appl. Phys. Lett. **73,** 265-267

(1998).

[43]A. Gurevich and E. A. Pashitskii, "Current transport through low-angle grain boundaries in high-temperature superconductors," Phys. Rev. B **57,** 13878-13893 (1998).

[44]R. D. Redwing, B. M. Hinaus, M. S. Rzchowski, N. F. Heinig, B. A. Davidson, and J. E. Nordman, "Observation of strong to Josephson coupled cross over in 10^0 $YBa_2Cu_3O_x$ bicrystal junctions," Appl. Phys. Lett. **75,** 3171-3173 (1999).

[45]N. D. Browning, J. P. Buban, P. D. Nellist, D. P. Norton, M. F. Chisholm, and S. J. Pennycook, "The atomic origins of reduced critical currents at [001] tilt grain boundaries in $YBa_2Cu_3O_{7-\delta}$ thin films," Physica C **294,** 183-193 (1998).

[46]I.-F. Tsu, S. E. Babcock, and D. L. Kaiser, "Faceting, dislocation network structure, and various scales of heterogeneity in a $YBa_2Cu_3O_{7-\delta}$ low-angle [001] tilt boundary," J. Mater. Res. **11,** 1383-1397 (1996).

[47]H. Hilgenkamp, J. Mannhart, and B. Mayer, "Implications of $d_{x\hat{}2-y\hat{}2}$ symmetry and faceting for the transport properties of grain boundaries in high-T_c superconductors," Phys. Rev. B **53,** 14586-14593 (1996).

[48]J. Mannhart and H. Hilgenkamp, "Wavefunction symmetry and its influence on superconducting deivces," Supercond. Sci. Tech. **10,** 880-883 (1997).

[49]R. Gross, P. Chaudhari, M. Kawasaki, and A. Gupta, "Superconducting transport characteristics of $YBa_2Cu_3O_{7-\delta}$ grain boundary junctions," IEEE Trans. Magn. **27,** 3227-3230 (1991).

[50]K. A. Delin and A. W. Kleinsasser, "Stationary properties of high-critical-temperature proximity effect Josephson junctions," Supercon. Sci. Tech **9,** 227-269 (1996).

[51]R. Gross, C. P., M. Kawasaki, and A. Gupta, "Scaling behaviour in electrical transport across grain boundaries in $YBa_2Cu_3O_{7-\delta}$ superconductors," Phys. Rev. B **42,** 10735-10737 (1990).

[52]A. B. M. Jansman, M. Izquierdo, J. Flokstra, and H. Rogalla, "Resonances and hysteresis

in inductively shunted high-Tc SQUIDS," Institute of Physics Conference Series **158,** 707-710 (1997).

[53]D. Winkler, Y. M. Zhang, P. A. Nilsson, E. A. Stepantsov, and T. Claeson, "Self-induced resonances in YBCO bicrystal grain-boundary Josephson-junctions," Physica B **194,** 1771-1772 (1994).

[54]R. C. Neville, B. Hoeneisen, and C. A. Mead, "Permittivity of SrTiO3," J. Appl. Phys. **43,** 2124 - 2131 (1972).

[55]J. Krupka, R. G. Meyer, M. Kuhn, and J. H. Hinken, "Dielectric properties of single crystals of Al_2O_3, $LaAlO_3$, $NdGaO_3$, $SrTiO_3$ and MgO at cryogenic temperatures.," IEEE Trans. Microwave Theory Tech. **42,** 1886-1890 (1994).

[56]H. Scheel, M. Berkowski, and B. Chabot, "Problems in epitaxial growth of high temperature superconductors.," Journal of Crystal Growth **115,** 19-30 (1991).

[57]E. J. Tarte, M. G. Blamire, W. E. Booij, G. Burnell, R. E. Somekh, G. A. Wagner, and J. E. Evetts, "Intrinsic capacitative shunting of bicrystal Josephson junctions," extended abstracts of 6th International Conference on Superconducting Electronics,Berlin **2** (1997).

[58]K. Nakajima, K. Yokota, H. Myoren, J. Chen, and T. Yamashita, "Field effects on the dielectric property Of YBCO bicrystal grain- boundary junctions," IEEE Trans. Appl. Supercon. **5,** 2861-2864 (1995).

[59]E. J. Tarte, G. A. Wagner, R. Somekh, F. Baudenbacher, P. Berghuis, and J. E. Evetts, "The capacitance of bicrystal Josephson junctions deposited on $SrTiO_3$ substrates," IEEE Trans. Appl. Supercon. **7,** 3662-3665 (1997).

[60]A. Beck, A. Stenzel, O. M. Froehlich, R. Gerber, R. Gerdemann, L. Alff, B. Mayer, R. Gross, A. Marx, J. C. Villegier, and H. Moriceau, "Fabrication and superconducting transport properties of bicrystal grain boundary Josephson junctions on different substrates," IEEE Trans. Appl. Supercon. **5,** 2192 (1995).

[61]H. R. Yi, D. Winkler, and T. Claeson, "Junction parameters of $YBa_2Cu_3O_7$ step-edge junctions on $LaAlO_3$ substrates from Fiske resonances," Appl. Phys. Lett. **66-70,** 1677-1679

(1995).

[62]Y. M. Zhang, D. Winkler, G. Brorsson, and T. Claeson, "Parallel-plate resonators In $YBa_2Cu_3O_7$ bicrystal grain boundaries," IEEE Trans. Appl. Supercon. **5,** 2200-2203 (1995).

[63]D. Winkler, Y. M. Zhang, P. A. Nilsson, E. A. Stepantsov, and T. Claeson, "Electromagnetic properties at the grain-boundary interface of a $YBa_2Cu_3O_{7-\delta}$ bicrystal Josephson-junction," Phys. Rev. B. **72,** 1260-1263 (1994).

[64]D. E. Kotecki, J. D. Baniecki, H. Shen, R. B. Laibowitz, K. L. Saenger, J. J. Lian, T. M. Shaw, S. D. Athavale, C. Cabral, P. R. Duncombe, M. Gutsche, G. Kunkel, Y.-J. Park, Y.-Y. Wang, and R. Wise, "$(Ba,Sr)TiO_3$ dielectrics for future stacked capacitor DRAM," IBM J. Res. Develop. **43,** 367-382 (1999).

[65]J. F. Scott, "Ferroelectric memories," Physics World**,** 46-50 (1995).

[66]R. W. Simon, "HTS Technology for wireless communications," Extended Abstracts of International Conference on Superconducting Electronics, Berkeley. (unpublished)**,** 6-11 (1999).

[67]A. T. Findikoglu, Q. X. Jia, X. D. Wu, G. J. Chen, T. Venkatesan, and D. W. Reagor, "Tunable and adaptive bandpass filter using a nonlinear dielectric thin film of $SrTiO_3$," Appl. Phys. Lett. **68,** 1651-1653 (1996).

[68]M. J. Lancaster, J. Powell, and A. Porch, "Thin-film ferroelectric microwave devices," Supercond. Sci. Tech. **11,** 1323-1334 (1998).

[69]P. Petrov, E. F. Carlsson, P. Larsson, M. Friesel, and Z. G. Ivanov, "Improved strontium titanate multilayers for microwave application: Growth and properties," J. Appl. Phys. **84,** 3134-3140 (1998).

[70]K. A. Muller and H. Burkard, "$SrTiO_3$: An intrinsic quantum paraelectric below 4K," Phys. Rev. B. **19,** 3593-3602 (1979).

[71]D. Fuchs, C. W. Schneider, R. Schneider, and H. Rietschel, "High dielectric constant and tunability of epitaxial strontium titanate thin film capacitors," J. Appl. Phys. **85,** 7362-7369

(1999).

[72]C. Ang, A. S. Bhalla, R. Guo, and L. E. Cross, "Dielectric loss of $SrTiO_3$ single crystals under direct current bias," Appl. Phys. Lett. **76,** 1929-1931 (2000).

[73]M. E. Lines and A. M. Glass, *Principles and applications of ferroelectrics and related materials* (Clarendon Press, Oxford, 1977).

[74]C. Zhou and D. M. Newns, "Intrinsic dead layer effect and the performance of ferroelectric thin film capacitors," J. Appl. Phys. **82,** 3081-3088 (1997).

[75]F. Jona and G. Shirane, *Ferroelectric Crystals* (Pergamon Press, Oxford, 1962).

[76]L. Ryen, X. Wang, U. Helmersson, and E. Olsson, "Determination of the complex dielectric function of epitaxial $SrTiO_3$ films using electron energy-loss spectroscopy," J. Appl. Phys. **85,** 2828-2834 (1999).

[77]H. Vogt, "Refined treatment of the model of linearly coupled anharmonic oscillators and its application to the temperature dependence of the zone centre soft mode frequencies of $KTaO_3$ and $SrTiO_3$," Phys. Rev. B **51,** 8046-8059 (1995).

[78]A. S. Barker, "Temperature dependence of the transverse and longitudinal optic frequencies and charges in $SrTiO_3$ and $BaTiO_3$," Phys. Rev. **145,** 391-399 (1966).

[79]Y. Yamada and G. Shirane, "Neutron scattering and nature of the soft optical phonon in $SrTiO_3$," J. Phys. Soc. Japan **26,** 396-403 (1969).

[80]P. A. Fleury and J. M. Worlock, "Electric field induced Raman scattering in $SrTiO_3$ and $KTaO_3$," Phys. Rev. **174,** 613-623 (1968).

[81]R. A. Cowley, "The phase transition of strontium titanate," Phil. Trans. R. Soc. Lond A **354,** 2799-2814 (1996).

[82]Y. A. Boikov and T. Claeson, "High tunability of the permittivity of YBa2Cu3O7-delta/SrTiO3 heterostructures on sapphire substrates," J. Appl. Phys. **81,** 3232-3236 (1997).

[83]H. M. Christen, J. Mannhart, E. J. Williams, and C. Gerber, "Dielectric properties of

sputtered $SrTiO_3$ films," Phys. Rev. B. **49,** 12095-12104 (1994).

[84]C. Basceri, S. K. Strieffer, A. I. Kingon, and R. Waser, "The dielectric response as function of temperature and film thickness of fiber-textured (Ba,Sr)TiO_3 thin films grown by chemical vapour deposition," J. Appl. Phys. **82,** 2497-2504 (1997).

[85]O. G. Vendik and S. P. Zubko, "Modeling the dielectric response of incipient ferroelectrics," J. Appl. Phys. **82,** 4475-4483 (1997).

[86]O. G. Vendik, Z. S. P., and L. T. Ter-Martirosayn, "Experimental evidence of the size effect in thin ferroelectric films," Appl. Phys. Lett. **73,** 37-39 (1998).

[87]S. K. Streiffer, C. Basceri, C. B. Parker, S. E. Lash, and A. I. Kingon, "Ferroelectricity in thin films: The dielectric response of fibre-textured $(Ba_xSr_{1-x})Ti_{1+y}O_{3+z}$ thin films grown by chemical vapour deposition," J. Appl. Phys **86,** 4565-4575 (1999).

[88]K. Abe and S. Komatsu, "Measurement and thermodynamic analyses of the dielectric constant of epitaxially grown $SrTiO_3$ films," Jpn. J. Appl. Phys. **32,** L1157-L1159 (1993).

[89]C. S. Hwang, B. T. Lee, C. S. Kang, K. H. Lee, H.-J. Cho, H. H. Hideki, W. D. Kim, S. I. Lee, and M. Y. Lee, "Depletion layer thickness and Schottky type carrier injection at the interface between Pt electrodes and (Ba, Sr)TiO_3 thin films," J. Appl. Phys. **85,** 287-295 (1999).

[90]G. W. Dietz, M. Schumacher, R. Waser, S. K. Streiffer, C. Basceri, and A. I. Kingon, "Leakage currents in $Ba_{0.7}Sr_{0.3}TiO_3$ thin films for ultrahigh-density dynamic random access memory," J. Appl. Phys. **82,** 2359-2364 (1997).

[91]J. D. Baniecki, R. B. Laibowitz, T. M. Shaw, P. R. Duncombe, D. A. Neumayer, D. E. Kotecki, H. Shen, and Q. Y. Ma, "Dielectric relaxation of $Ba_{0.7}Sr_{0.3}TiO_3$ thin films from 1mHz to 20GHz," Appl. Phys. Lett. **74,** 498-500 (1998).

[92]B. H. Hoerman, G. M. Ford, L. D. Kaufmann, and B. W. Wessels, "Dielectric properties of epitaxial $BaTiO_3$ films," Appl. Phys. Lett. **73,** 2248-2250 (1998).

[93]J. Santiso, A. Moya, and F. Baudenbacher, "Stoichiometry and surface morphology of

$YBa_2Cu_3O_7$ thin films prepared by off-axis laser ablation," Supercond. Sci. Tech. **11,** 462-466 (1998).

[94]D. J. Adelerhof, H. Nijstad, J. Flokstra, and H. Rogalla, "(Double) relaxation oscillation SQUIDs with high flux to voltage transfer: Simulations and experiments," J. Appl. Phys. **76,** 3875-3886 (1994).

[95]M. Van-Duuren, *Advanced relaxation oscillation SQUIDS* (PhD. Thesis, University of Twente, Netherlands, 1997).

[96]P. K. Hansma, G. I. Rochlin, and J. N. Sweet, "Externally shunted Josephson junctions: Generalized weak links," Phys. Rev. B. **4,** 3003-3014 (1971).

[97]J. T. C. Yeh and R. A. Buhrman, "Capacitively shunted variable thickness microbridges," Appl. Phys. Lett. **31,** 362-365 (1977).

[98]B. H. Moeckly and R. A. Buhrman, "Josephson properties of basal-plane-faced tilt boundaries in $YBa_2Cu_3O_{7-\delta}$ thin films," Appl. Phys. Lett. **65,** 3126-3128 (1994).

[99]B. H. Moeckly and R. A. Buhrman, "Electromagnetic Properties Of $YBa_2Cu_3O_{7-\delta}$ Thin-Film Grain- Boundary Weak Links," IEEE Trans. Appl. Supercon. **5,** 3414 (1995).

[100]K. P. Daly, J. F. Burch, R. Hu, A. E. Lee, J. Luine, and C. Pettiette-Hall, "Capacitively shunted, hysteretic YBCO step-edge junctions," IEEE Trans. Appl. Supercon. **3,** 2345-2348 (1993).

[101]Z.-W. Dong, P. Hadley, and J. E. Mooij, "High IcRn products and hysteretic behaviour of YBCO/Au/YBCO Josephson junctions.," Physica C **235-240,** 3243-3424 (1994).

[102]S.-G. Lee, Y. Huh, and Y. Hwang, "Effect of capacitive shunt on current-voltage characteristics of high T_c Josephson junctions," IEEE Trans. Appl. Supercon. **9,** 3472-3474 (1999).

[103]J. S. Martens, V. M. Hietala, T. E. Zipperian, G. A. Vawter, D. S. Ginley, C. P. Tigges, T. A. Plut, and G. K. G. Hohenwarter, "Fabrication Of TlCaBaCuO step-edge Josephson-junctions with hysteretic behaviour," Appl. Phys Lett. **60,** 1013-1015 (1992).

[104]G. F. Virshup, M. E. Klausmeierbrown, I. Bozovic, and J. N. Eckstein, "Hysteretic, high-T_C Josephson-Junctions using heterostructure trilayer films grown by molecular-beam epitaxy," Appl. Phys. Lett. **60,** 2288-2290 (1992).

[105]R. L. Fink, M. Thompson, C. Hilbert, and H. Kroger, "Hysteretic josephson-junctions from $YBa_2Cu_3O_{7-\delta}/SrTiO_3/Ba_{1-x}K_xBiO_3$ trilayer films," Appl. Phys. Lett **61,** 595-597 (1992).

[106]Y. Tarutani, H. Hasegawa, T. Fukazawa, and K. Takagi, "Measurement of the critical current distribution for the resistively shunted junctions," J. Appl. Phys. **83,** 5000-5002 (1998).

[107]K. C. Gupta, R. Garg, and L. J. Bahl, *Microstrip lines and slotlines* (Artech House, Dedham, MA, 1979).

[108]Meservey, "Measurements of the kinetic inductance of superconducting linear structures," J. Appl. Phys. **40,** 2028-2034 (1969).

[109]R. H. Hadfield, *Part III Project Report* (Unversity of Cambridge, 1998).

[110]J. Edstam, P.-A. Nilsson, E. A. Stepantsov, and H. K. Olsson, "100GHz oscillations on a monolithic high T_C chip," Appl. Phys. Lett **62,** 896-898 (1993).

[111]J. Edstam and H. K. Olsson, "London penetration depth of YBCO In the frequency range 80-700 GHz," Physica B **194,** 1589-1590 (1994).

[112]K. Enpuku, T. Maruo, and T. Minotani, "Effect of large dielectric constant of $SrTiO_3$ substrate on the characteristics of high T_C dc superconducting quantum interference device," J. Appl. Phys. **80,** 1207-1213 (1996).

[113]J. Edstam and H. K. Olsson, "Josephson broad-band spectroscopy to 1 Thz," Appl. Phys. Lett. **64,** 2733-2735 (1994).

[114]T. A. Fulton and L. N. Dunkleberger, "Life time of the zero voltage state in Josephson tunnel junctions," Phys. Rev. B **9,** 4760-4768 (1974).

[115]M. G. Castellano, G. Torrioli, F. Chiarello, C. Cosmelli, and P. Carelli, "Return current in hysteretic Josephson junctions: Experimental distribution in the thermal activation regime," J.

Appl. Phys. **86,** 6405-6411 (1999).

[116]E. Fang and T. Van-Duzer, Extended Abstracts of the 1989 International Superconducting Electronics conference**,** 407-410 (1989).

[117]J. Satchell, "Limitations on HTS single flux quantum logic," IEEE Trans. App. Sup. **9,** 3841-3844 (1999).

[118]S. Ramo, J. R. Whinnery, and T. Van Duzer, *Fields and waves in communication electronics* (John Wiley, New York, 1984).

[119]M. J. Dalberth, R. E. Stauber, J. C. Price, C. T. Rogers, and D. Galt, "Improved low frequency and microwave dielectric response in strontium titanate thin films grown by pulsed laser ablation," Appl. Phys. Lett. **72,** 507-509 (1998).

[120]D. Galt, J. C. Price, J. A. Beall, and T. E. Harvey, "Ferroelectric thin film characterisation using superconducting microstrip resonators," IEEE Trans. Appl. Supercon. **5,** 2575-2578 (1995).

[121]J. Sok, J. S. Lee, and E. H. Lee, "Tunability and loss tangent of ferroelectric $SrTiO_3$ films in YBCO superconducting resonator," Supercon. Sci. Tech. **11,** 875-879 (1998).

[122]A. B. Kozyrev, T. B. Samoilova, A. A. Golovkov, E. K. Hollmann, D. A. Kalinikos, V. E. Loginov, A. M. Prudan, O. I. Soldatenkov, D. Galt, C. H. Mueller, T. V. Rivkin, and G. A. Koepf, "Nonlinear behaviour of thin film strontium titanate capacitors at microwave frequencies," J. Appl. Phys. **84,** 3326-3332 (1998).

[123]E. Inglessi, *Part III Project Report* (University of Cambridge, 1999).

[124]R. Neville, B. Hoeneisen, and C. A. Mead, "Anomalous resonance of strontium titanate," J. Appl. Phys. **43,** 3903-3905 (1972).

[125]M. G. Medici, J. Elly, M. Razani, A. Gilabert, F. Schmidl, P. Seidel, A. Hoffman, and I. K. Schuller, "Effect of photodoping on the Fiske resonances of $YBa_2Cu_3O_X$ grain boundary Josephson junctions," Jnl. Superconduct. **11,** 225 (1998).

[126]M. A. Navacerrada, M. L. Lucia, and F. Sanchez-Quesada, "Electromagnetic properties

and He^{+} irradiation effects on $YBa_2Cu_3O_{7-x}$ grain-boundary Josephson junctions," Phys. Rev. B **61,** 6422-6427 (2000).

[127]J. Mannhart and H. Hilgenkamp, "Possible influence of band bending on the normal state properties of grain boundaries in high-T_C superconductors," Mater. Sci. Eng. B **56,** 77 (1998).

[128]C. H. Seager and G. E. Pike, "Anomalous grain-boundary capacitance in silicon," Appl. Phys. Lett. **37,** 747-749 (1980).

[129]Y. Yamaoka, "$SrTiO_3$ based boundary layer capacitors," Ceram. Bull. **65,** 1149-1152 (1986).

[130]A. Marx, U. Fath, L. Alff, and R. Gross, "Correlation of critical current and resistance fluctuations in bicrystal grain boundary junctions," Appl. Phys. Lett. **67,** 1929-1931 (1995).

[131]M. Darula, T. Doderer, and S. Beuven, "Millimetre and sub-mm wavelength radiation sources based on discrete Josephson junction arrays," Supercond. Sci. Tech. **12,** R1-R25 (1999).

[132]J. Edstam, *Josephson junctions: Oscillators and broadband spectrometers at frequencies up to 1THz* (PhD. Thesis, Chalmers University of Technology, Sweden, 1994).

[133]J. Edstam and H. K. Olsson, "Mutual phase locking of two high T_C Josephson junctions from 0.2 to 1Thz," Appl. Phys. Lett. **64,** 2587-2589 (1994).

[134]H. K. Olsson, "Dielectric constant of evaporated SiO at frequencies between 13 and 103GHz," IEEE Trans. Magn. **25,** 1115-1118 (1989).

[135]J. Edstam and H. K. Olsson, "Integrated high-T_C microstrip resonators and components In the frequency range 5-1000GHz," Physica B **194,** 117-118 (1994).

[136]A. Larsen, H. Dalsgaard-Jensen, and J. Mygind, "Self-induced steps in a small Josephson junction coupled to a mulitmode resonator," Phys. Rev. B. **43,** 10179-10190 (1991).

[137]B. Bi, K. Wan, W. Zhang, S. Han, and J. E. Lukens, "Josephson junction driven submillimeter wave microstrip resonator," IEEE Trans. Appl. Supercon. **1,** 145-149 (1991).

[138]N. Klein, N. Tellman, H. Schulz, K. Urban, S. A. Wolf, and V. Z. Kresin, "Evidence of two-gap s-wave superconductivity in $YBa_2Cu_3O_{7-x}$ from microwave surface impedance measurements," Phys. Rev. Lett. **71,** 3355-3358 (1993).

[139]F. Lombardi, U. Scotti di Uccio, Z. Ivanov, T. Claeson, and M. Cirillo, "Flux flow in $YBa_2Cu_3O_{7-\delta}$ grain-boundary Josephson junctions with a four-terminal configuration," Appl. Phys. Lett. **76,** 2591-2593 (2000).

[140]A. A. Sirenko, C. Bernhard, A. Golnik, A. M. Clark, J. Hao, and X. X. Xi, "Soft-mode hardening in $SrTiO_3$ thin films," Nature **404,** 373-375 (2000).

[141]B. Mayer, J. Mannhart, and H. Hilgenkamp, "Electric field controllable Josephson junctions of high quality in high-T_c superconductors," Appl. Phys. Lett. **68,** 3031-3033 (1996).

[142]M. Windt, H. Haensel, D. Koelle, and R. Gross, "On the nature of the electric-field effect on $YBa_2Cu_3O_{7-\delta}$ grain boundary junctions employing epitaxial $SrTiO_3$ gate insulators," Appl. Phys. Lett. **74,** 1027-1029 (1999).

[143]C. W. Schneider, R. R. Schulz, B. Goetz, A. Schmehl, H. Bielefeldt, H. Hilgenkamp, and J. Mannhart, "Tailoring of high-T_c Josephson junctions by doping their electrodes," Appl. Phys. Lett. **75,** 850-852 (1999).

[144]A. Schmehl, B. Goetz, R. R. Schulz, C. W. Schneider, H. Bielefeldt, H. Hilgenkamp, and J. Mannhart, "Doping-induced enhancement of the critical currents of grain boundaries in $YBa_2Cu_3O_{7-\delta}$," Europhys. Lett. **47,** 110-115 (1999).

[145]H. Hilgenkamp, C. W. Schneider, R. R. Schulz, B. Goetz, A. Schmehl, H. Bielefeldt, and J. Mannhart, "Modifying the electronic properties of interfaces in high-T_c superconuductors by doping," Physica C **326-327,** 7-11 (1999).

[146]H. Hilgenkamp, C. W. Schneider, B. Goetz, R. R. Schulz, A. Schmehl, H. Bielefeldt, and J. Mannhart, "Grain boundary critical currents - a new perspective," Supercon. Sci. Tech. **12,** 1043-1045 (1999).

[147]G. Hammerl, A. Scmehl, R. R. Schulz, B. Goetz, H. Bielefeldt, C. W. Schneider, H.

Hilgenkamp, and J. Mannhart, "Increasing grain boundary critical currents in high-T_c superconductors at 77K," submitted to Nature (2000).

[148]K. Enpuku, T. Minotani, F. Shiraishi, and S. Ohta, "Transport and noise properties of high-T_c bicrystal junctions," Supercond. Sci. Tech. **12,** 792-794 (1999).

[149]J. P. Sydow, M. Berninger, R. A. Buhrman, and B. H. Moeckly, "Effect of oxygen content on YBCO Josephson junction structures," IEEE Trans. Appl. Supercon. **9,** 2993-2996 (1999).

[150]J. P. Sydow, M. Berninger, R. A. Buhrman, and B. H. Moeckly, "On the characteristic voltage of highly oxygenated YBCO grain boundary junctions," Supercond. Sci. Tech. **12,** 723-725 (1999).

[151]J. Halbritter, "Pair weakening and channels at cuprate interfaces," Phys. Rev. B. **46,** 14861-14871 (1992).

[152]R. Gross and B. Mayer, "Transport processes and noise in $YBa_2Cu_3O_{7-\delta}$ grain boundary junctions," Phys. C **180,** 235-242 (1991).

[153]S. E. Russek, D. K. Lathrop, B. H. Moeckly, R. A. Buhrman, D. H. Shin, and J. Silcox, "Scaling behaviour of $YBa_2Cu_3O_{7-\delta}$ thin film weak links," Appl. Phys. Lett. **57,** 1155-1157 (1990).

[154]J. Halbritter, "Extrinsic or intrinsic conduction in cuprates: Anisotropy, weak and strong links," Phys. Rev. B **48,** 9735-9746 (1993).

[155]M. Kawasaki, P. Chaudari, and A. Gupta, "1/f noise in $YBa_2Cu_3O_{7-\delta}$ grain boundary junctions," Phys. Rev. Lett. **68,** 1065-1068 (1992).

[156]M. Carmody, B. H. Moeckly, K. L. Merkle, and L. D. Marks, "Spatial variation of the current in grain boundary Josephson junctions," J. Appl. Phys **87,** 2454-2459 (2000).

[157]O. M. Froehlich, H. Schulze, A. Beck, R. Gerdemann, B. Mayer, R. Gross, and R. P. Huebener, "Supercurrent density correlation function of $YBa_2Cu_3O_{7-\delta}$ grain boundary

Josephson junctions," IEEE Trans. Appl. Sup. **5,** 2188-2191 (1995).

[158]F. Greuter and G. Blatter, "Electrical properties of grain boundaries in polycrystalline semiconductors," Semicon. Sci. Technol. **5,** 111-137 (1990).

[159]J. T. Kucera and J. C. Bravman, "Transport characteristics of calcium doped $YBa_2Cu_3O_{7-\delta}$ thin films," Phys. Rev. B. **51,** 8582-8590 (1995).

[160]J. Ransley, CPGS Report, University of Cambridge, 2000.

[161]S. Kleefisch, L. Alff, U. Schoop, A. Marx, R. Gross, M. Naito, and H. Sato, "Superconducting NCCO bicrystal grain boundary junctions," Appl. Phys. Lett. **72,** 2888-2890 (1998).

[162]U. Frey, M. Blumers, M. Basset, J. C. Martinez, and H. Adrian, "Transport properties and lower critical field of BSCCO Josephson junctions," Institute of Physics Conference Series **158,** 563-565 (1997).

[163]T. Amrein, M. Seitz, D. Uhl, L. Schultz, and K. Urban, "Thin film BSCCO Josephson junctions and direct current superconducting quantum interference devices on (001) SrTiO3 bicrystals," Appl. Phys. Lett. **63-65,** 1978 (1993).

[164]H. R. Yi, M. Gustafsson, D. Winkler, E. Olsson, and T. Claeson, "Electromagnetic and microstructural characterization of $YBa_2Cu_3O_7$ step edge junctions on (001) $LaAlO_3$ substrates," J. Appl. Phys. **79,** 9213 - 9220 (1996).

[165]A. Beck, O. M. Froehlich, D. Koelle, R. Gross, H. Sato, and M. Naito, "LSCO bicrystal grain boundary Josephson junctions," Appl. Phys. Lett. **68-70,** 3341 (1996).

[166]E. B. McDaniel, S. C. Gausepohl, C.-T. Li, M. Lee, J. W. P. Hsu, R. A. Rao, and C. B. Eom, "Influence of $SrTiO_3$ bicrystal microstructural defects on $YBa_2Cu_3O_7$ grain boundary Josephson junctions," Appl. Phys. Lett. **70,** 1882-1884 (1997).

[167]H. S. J. Van Der Zant, R. A. M. Receveur, T. P. Orlando, and A. W. Kleinsasser, "One-dimensional parallel Josephson-junction arrays as a tool for diagnostics," Appl. Phys. Lett. **65,** 2102-2104 (1994).